



POLITECNICO DI MILANO
DEPARTMENT OF CHEMISTRY MATERIALS
AND CHEMICAL ENGINEERING
DOCTORAL PROGRAMME IN MATERIALS ENGINEERING

**MATRIX FUNCTIONALISATION AND INNOVATIVE CONTROL
SCHEMES AS METHODS TO OPTIMISE ACTUATION IN
SMA/ELASTOMER SOFT SYSTEMS**

Doctoral Dissertation of:
Fabio Lazzari

Supervisor:
Prof. Simone Pittaccio
Prof. Chiara Castiglioni

Tutor:
Prof. Chiara Bertarelli

The Chair of the Doctoral Program:
Prof. Chiara Bertarelli

2023 – XXXV Cycle

Abstract

The present research project aims to investigate different methods to optimise the functionality of soft actuators based on Shape-Memory Alloys (SMA). This class of actuators, deemed of interest for their compactness, bio-compliance and high energy density, generally display limitations particularly in the bandwidth (cycling frequency) and controllability, due to heat-transfer-related effects.

This research consists in a thorough study of the interaction between the SMA active element and an enveloping elastomeric matrix that serves as an interface towards the external environment. The main research question is whether and how functionalising the matrix and establishing specialised control schemes that take the matrix into account may serve to improve SMA-based actuation. The methods include different models ranging from lumped-parameter to multi-physical finite element (FEM) ones, developed to gain insight in the complex interplay of material properties, physical dimensions and control strategies that determines the rates of heating and cooling of the system.

The thesis also describes a method to produce and characterise poly-dimethylsiloxane (PDMS) rubber modified with graphene showing the effectiveness of carbon fillers in adjusting heat transport properties for this application. Finally, the work reports about the design, fabrication and testing of an operational SMA/elastomer actuator (a gripper) as a proof-of-concept of applicability of matrix functionalisation in optimising the working characteristics of SMA in soft actuators.

In conclusion, the thesis demonstrates that the role of the matrix is very important in SMA/elastomer soft actuators. The dependency of the actuator functionality on material properties such as heat conductivity is not simple, but is strongly mediated by the relative dimension of the components and the control strategy plays a fundamental part in establishing the dynamic working properties of the system. Matrix functionalisation with graphene is feasible and can be effectively integrated in designs as a means to optimise actuation. It is hoped that in future these results will prove robust in the design of optimised soft actuators for a whole range of different uses.

Sommario

Il presente progetto di ricerca si propone di studiare diversi metodi per ottimizzare la funzionalità di attuatori morbidi basati su leghe a memoria di forma (SMA). Questa classe di attuatori, ritenuti interessanti per la loro compattezza, bio-conformità e alta densità di energia, presentano generalmente limitazioni in particolare nella larghezza di banda (frequenza di ciclaggio) e nella controllabilità, a causa degli effetti legati al trasferimento di calore. Questa ricerca consiste in uno studio approfondito dell'interazione tra l'elemento attivo SMA e una matrice elastomerica avvolgente che funge da interfaccia verso l'ambiente esterno. La principale domanda di ricerca è se e come la modifica della matrice e la creazione di schemi di controllo avanzati che tengano conto della matrice possano servire a migliorare l'attuazione basata sulle SMA. I metodi includono diversi modelli, da quelli a parametri concentrati a quelli a elementi finiti multifisici (FEM), sviluppati per ottenere informazioni sulla complessa interazione tra le proprietà dei materiali, dimensioni fisiche e strategie di controllo che determinano le velocità di riscaldamento e raffreddamento del sistema.

La tesi descrive anche un metodo per produrre e caratterizzare il polimero polidimetilsilossano (PDMS) modificato con grafene, che mostra l'efficacia dei riempitivi di carbonio nella regolazione delle proprietà di trasporto del calore per questa applicazione. Infine, il lavoro riporta la progettazione, la fabbricazione e il collaudo di un attuatore SMA/elastomero (una pinza) come prova dell'applicabilità della modifica della matrice nell'ottimizzazione delle caratteristiche di funzionamento della SMA negli attuatori morbidi. In conclusione, la tesi dimostra che il ruolo della matrice è molto importante negli attuatori morbidi SMA/elastomero. La dipendenza della funzionalità dell'attuatore da proprietà del materiale come la conducibilità termica non è semplice, ma è fortemente mediata dalla dimensione relativa dei componenti, e la strategia di controllo gioca un ruolo fondamentale nello stabilire le proprietà di funzionamento dinamico del sistema. La funzionalizzazione della matrice con il grafene è fattibile e può essere efficacemente integrata nei progetti come mezzo per ottimizzare l'attuazione. Si spera che in futuro questi risultati si dimostreranno robusti nella progettazione di attuatori morbidi ottimizzati per un'intera gamma di usi diversi.

Contents

Abstract.....	3
Sommario	5
Contents.....	7
1. Introduction to shape-memory soft actuation.....	11
1.1. Soft actuation technologies: opportunities and limitations	11
1.2. Soft actuators based on shape-memory alloys	13
1.3. Optimisation techniques for shape-memory alloy soft actuation.....	16
1.4. Gaps to be filled	20
2. Objective and approach.....	21
2.1. Objective	21
2.2. Approach.....	21
3. Shape memory alloys: physics, models and control	25
3.1. Metallurgy and phenomenology of NiTi-based shape memory alloys.....	26
3.1.1. Pseudoelasticity and shape memory effects	28
3.1.2. Binary and ternary NiTi-based systems: NiTi and NiTiCu alloys	31
3.1.3. Thermal treatments.....	34
3.2. Modelling of the shape memory effect.....	35
3.2.1. A look into SMA modelling approaches.....	35
3.2.2. Summary of the evolution of phenomenological models.....	37
3.2.3. Brinson (1993) model.....	39
3.3. Techniques for the automatic control of SMAs	41
3.4. Conclusions	44
4. Selection and optimisation of the shape memory wire	45
4.1. Specifications and choice of the wire diameter.....	46
4.2. Initial material selection.....	47
4.3. Shape setting and ageing process	48

4.4.	Final selection of the SMA material and of the optimal heat treatment.....	51
4.5.	Testing of functional actuation capability and material parameter identification	58
4.6.	Conclusions	61
5.	Matrix modification	62
5.1.	Introduction	62
5.2.	Choice of the polymer matrix.....	63
5.3.	Choice of the fillers	67
5.3.1.	Selection criteria for GNPs as polymer matrix fillers	67
5.3.2.	GNP selection and characterisation.....	70
5.4.	Preparation of the GNP/PDMS composite.....	73
5.4.1.	Preparation of the composite samples: dispersion of GNP in the PDMS matrix	74
5.4.2.	Characterisation of the modified silicone samples	76
5.5.	Conclusions	85
6.	Numerical models of the multimaterial actuator	86
6.1.	Definition of the reference actuator for the present study	87
6.2.	Constitutive modelling the SMA wire.....	88
6.2.1.	Modified Brinson model for the SMA	89
6.2.2.	Tuning of the constitutive SMA model parameters.....	95
6.3.	Modelling of Joule’s effect in the SMA wire.....	96
6.4.	Modelling of the multimaterial interaction in the SMA/PDMS actuator	97
6.4.1.	Mechanical interaction	97
6.4.2.	Thermal interactions and material properties	98
6.4.3.	Different implementations of multimaterial heat transfer for the 0-D and 1-D simulations	99
6.4.4.	Lumped parameter implementation of the SMA/Matrix heat transfer	99
6.4.5.	Distributed parameter implementation of the SMA/Matrix heat transfer	102
6.5.	Materials tabulated parameters.....	104
6.6.	Basic testing and comparison of the model implementations	105

6.6.1.	Cross-validation of the numerical models.....	105
6.6.2.	Considerations about the experimental validation of the models.....	113
6.7.	Conclusions.....	114
7.	Advanced control strategy for the multimaterial actuator.....	115
7.1.	State variable estimation of a soft SMA-based actuator	116
7.1.1.	Discussion on the EKF performance.....	118
7.2.	Concept of a variable PID controller based on state variables estimation	122
7.2.1.	Range of operation and test protocol.....	123
7.2.2.	Configuration of a standard PI controller.....	124
7.2.3.	Development of the non-linear variable PI controller	125
7.3.	Results and discussion.....	129
7.3.1.	Comparison of the variable and standard PI controllers, driving the actuator with a non-modified matrix.....	129
7.3.2.	Effect of the matrix modification in conjunction with the variable PI controller ..	134
7.4.	Towards the application of the advanced control with a real system.....	136
7.5.	Conclusions	137
8.	Numerical analysis: functionalisation and system dimensioning	139
8.1.	Test procedure	140
8.2.	Physical parameters expected to affect performance	142
8.3.	Results and discussion.....	144
8.3.1.	Complete actuation cycle starting with the system stabilised at $T_0 = 25\text{ }^\circ\text{C}$	144
8.3.2.	Complete actuation cycle starting with the system stabilised at $T_0 = 56\text{ }^\circ\text{C}$	166
8.4.	Possible expansions of the parametric study.....	176
8.5.	Conclusions	176
9.	Proof-of concept actuator: The Orca gripper	178
9.1.	General concept of the gripper and dimensioning.....	178
9.2.	Actuator fabrication.....	181
9.2.1.	Shape setting of the SMA element.....	181

9.2.2.	Spring characterisation	183
9.2.3.	Production of the Orca gripper by stepwise moulding-and-assembling.....	185
9.3.	Actuator characterisation and assessment of the effects of optimisation	188
9.3.1.	Testing set-up and protocol	189
9.3.2.	Results of the comparison	190
9.4.	Future developments	192
9.5.	Conclusions	193
10.	Conclusions	194

CHAPTER 1

Introduction to shape-memory soft actuation

Soft actuators can be defined as systems composed of one or more than one highly deformable material or composite that can be activated by external stimuli to produce mechanical work (forces/torques and/or displacements) [1].

The strong level of functional integration is one of the reasons why soft actuators are now perceived as interesting new technologies to be developed, but the main focus of interest is for their adaptability to interact with other systems and the environment in a superior way, compared to their rigid counterparts. In fact, soft actuators are expected to have a greater ability to produce and withstand large strains, achieve motion with multiple degrees of freedom with complex functionalities, emulate biological systems, and match tissue characteristics. For these reasons, they have a potential to revolutionize healthcare, wearable devices, manufacturing and robotics [2]–[4].

1.1. Soft actuation technologies: opportunities and limitations

The methods to obtain soft actuators can be different and currently include, on the one hand, using smart materials that can directly generate actuation once they receive the right stimulus (e.g. heat, light, pressure, chemical stimuli, and electric or magnetic fields) [5]; in this case, the relevant materials provide both the structure and the function to the actuator. On the other hand, it is possible to exploit materials only for their very large deformability, or other soft-structural characteristic, and employ separate sources of energy (pneumatic, hydraulic, ...) to implement the actuation [6]; in such cases the materials condition the output of the actuator, by allowing soft interfacing to other systems, adding compliance and making multiple degrees of freedom available.

The problem with many soft self-actuating materials is that they derive their properties from basic phenomena, which are sometimes difficult to control, may change with time, or need very intense stimuli. This is the case with most polymeric smart actuators. For instance, electro-active (electrostrictive) polymers (EAP) display interesting ranges of force and deformability, but generally require extremely high voltages to operate (ca. 10-100 MV/m) [7]. The ionic artificial muscles, which operate with lower voltages (1-7 V) are dependent on the use of ionic solutions (electrolytes) that permeate the polymer, and which can make the system quite difficult to integrate in safe devices, especially for health-related applications[1]. Something similar happens with ionic polymer-metal composites, which are more complex to make than other types of (multi)materials; although their strains can be higher than 3 % with stresses as high as 30 MPa, after initial displacement their position tends to drift, and so some steady current is needed to fix position [7]. Another class of materials is conductive polymers whose electromechanical coupling is pretty low ($< 1\%$), pushing the limits of power supply and making medium-large scale applications challenging [5]. Carbon-nanotube composites can generate high stiffnesses but their elongations are very limited, so that they may not be among the best performers for most macroscopic soft actuation applications [7].

Considering non-self-actuating technologies, pressure-driven fluidic systems can be considered very interesting devices because they produce high forces and have the potential to be lightweight; however, they cannot be considered self-standing actuators because they do not integrate a transducer: they typically require connection to a relatively large external pump or compressor, so the whole system tends to be bulky and impractical for portable or wearable applications [8].

In between self- and non-self-actuating solutions there are those soft actuators integrating Shape Memory Alloys (SMAs). This class of materials are characterised by a very-large-strain reversible martensitic transformation; they can recover their original shape or size upon reverse transformation into austenite [9]. Considering the most important factors for a soft actuator [1], SMA produce high strains and force, can operate in different environments, are small (have high specific energy), their flow stress can be modulated, are biocompatible (e.g. Ni-Ti based compositions), can be made mechanically anisotropic, and can be used as both actuators and temperature sensors. In the design of soft actuators, they are employed as the actuating material providing the opportunity to develop compact, light, flexible and silent

devices [10]. SMAs do not need any external heater, since their conductivity enables direct Joule heating through the material itself, producing thermal activation intrinsically; furthermore, this characteristic allows them to be powered by batteries [11].

Conversely, the main drawback of SMAs for soft actuation is probably the limited bandwidth that is a consequence of the thermodynamic nature of the stimulus required for their function [9]. In particular, the cooling part of an action cycle can be rather slow if left to natural heat dissipation. Fatigue life can be long but is strongly dependent on the level of actuation stress and strain. [12] SMAs are materials with strongly nonlinear and hysteretic properties in terms of at least stress-strain, temperature-strain and temperature-resistivity relationships. This fact is a great challenge when approaching the closed-loop control of their actuation, especially if the aim is to follow precise paths and speeds.

1.2. Soft actuators based on shape-memory alloys

Despite their nature of metallic material, SMAs possess very large deformability, and they are often used in soft actuators in the shape of thin elements (wires, springs, thin films). Their coupling with other soft materials like deformable polymers can provide new opportunities to implement better interfaces between the SMA and the outside world, condition the direction and path of the actuation, generate appropriate bias or recovery forces, needed in cyclic actuation. For these reasons SMA and above all the widely used nickel-titanium (NiTi) based compositions, are becoming of great appeal for the fabrication of soft robotic systems.

SMA wires and springs can be applied in different types of structure and with a different positioning of the SMA material, obtaining different performances (Figure 1) [13].


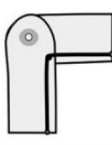
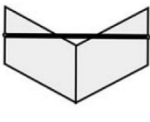


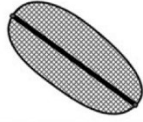
						
Structure type	Mechanical joint	Mechanical joint	Flexural hinge	Polymer	Polymer	Mesh
SMA positioning	External	Embedded	External	External	Embedded	External
Performance using SMA spring	Good	Excellent	Good	Good	Excellent	Very good
Performance using SMA wire	Poor	Excellent	Very poor	Poor	Excellent	Very poor

Figure 1 - Summary of the applicability of the SMA wires and SMA springs to different types of structures [13].

The SMA element in the form of a wire exerts a high force but it does not give rise to high displacements. In the spring configuration, the SMA element exerts less force but it has a much greater displacement.

For this reason, the straight wire is often incorporated in polymeric matrices to obtain non-linear deformations. By embedding the SMA wire inside a polymeric matrix, out of the neutral plane, bending of the entire matrix can be obtained (Figure 2a)[14].

Multiple SMA wires can be incorporated for the purpose of achieving motion such as twisting [15] or coupled bend-twist deformation [16].

It is possible to build rotational actuators by integrating several wires in a soft cylindrical matrix obtaining a wrist-like device (Figure 2b-c) [17], or embedding a SMA wire into a 3D-printed helical structure [18].

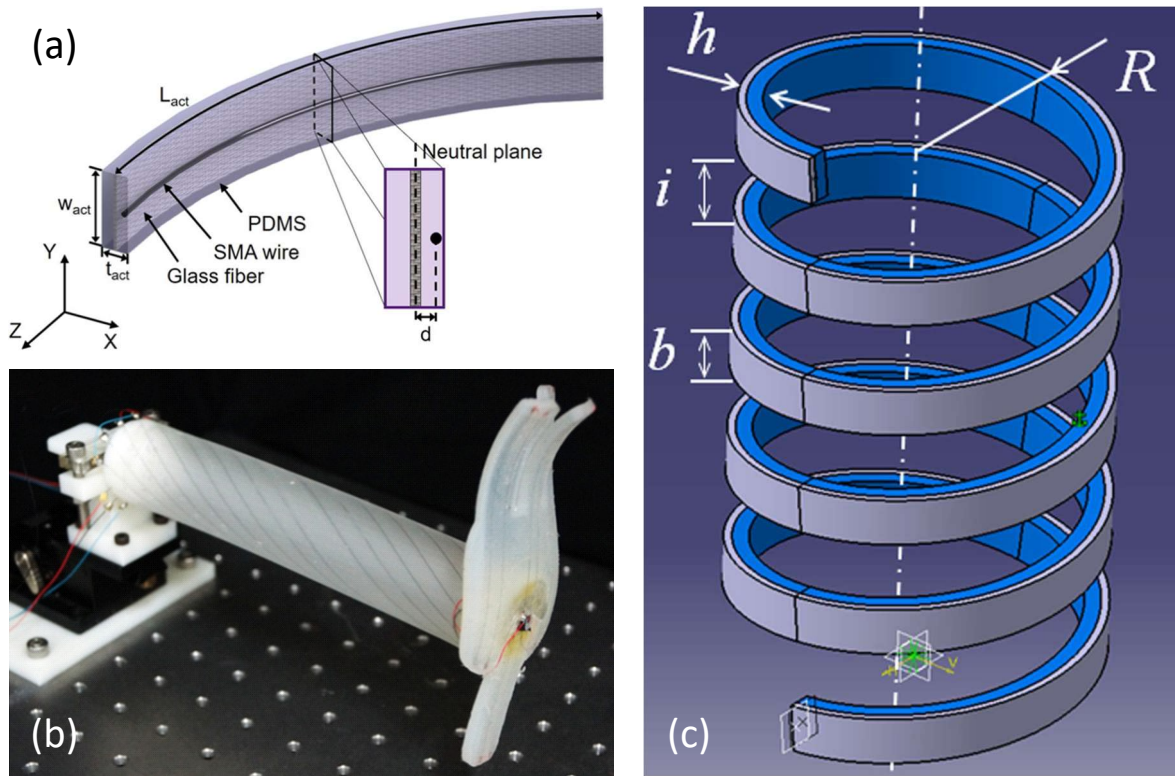


Figure 2 - Straight SMA wires can be incorporated in polymeric matrices to obtain non-linear deformations. By embedding the SMA wire out of the neutral plane of the polymeric matrix a bending actuator can be obtained (a)[14]. Wrist-like device obtained by integrating several wires in a soft cylindrical matrix (b)[17]. Rotational actuator build embedding a SMA wire into a 3D-printed helical structure (c)[18].

A number of applications can be found in published literature, where these structures are used to build modular devices. Here, we shall list some devices exemplifying different design and fabrication strategies.

Tendons. A prototype of a robotic hand was developed using four tendon-driven soft composite fingers and a thumb (Figure 3a). Grasping capabilities of the device were demonstrated with various objects of diverse shapes [19].

Bent wires. In [20], a modular device based on a bent wire configuration was designed inspired by a starfish. The robot was tested in different situations and for different purposes. It can be implemented to obtain terrestrial locomotion or to swim underwater. Furthermore, it has been used to manipulate objects of different shapes and rigidity (Figure 3b).

Hinged structures. Robotic soft grippers have great interest thanks to their superiority over conventional rigid grippers when they are used to grab fragile objects or objects with irregular shapes. These devices often have modular structures that integrate SMA actuators with one or multiple hinges [14], [21], [22].

Springs. Alternatively, it is common to find examples of devices in which SMA elements are externally attached to a soft structure. Often, these devices make use of SMA elements in the spring configuration.

The most complete examples report the creation of modular devices inspired by a worm [23] and an octopus (Figure 3c) [24], [25]. The OCTOPUS robot was the first example of a soft robot that has the ability to move and manipulate objects underwater [26].

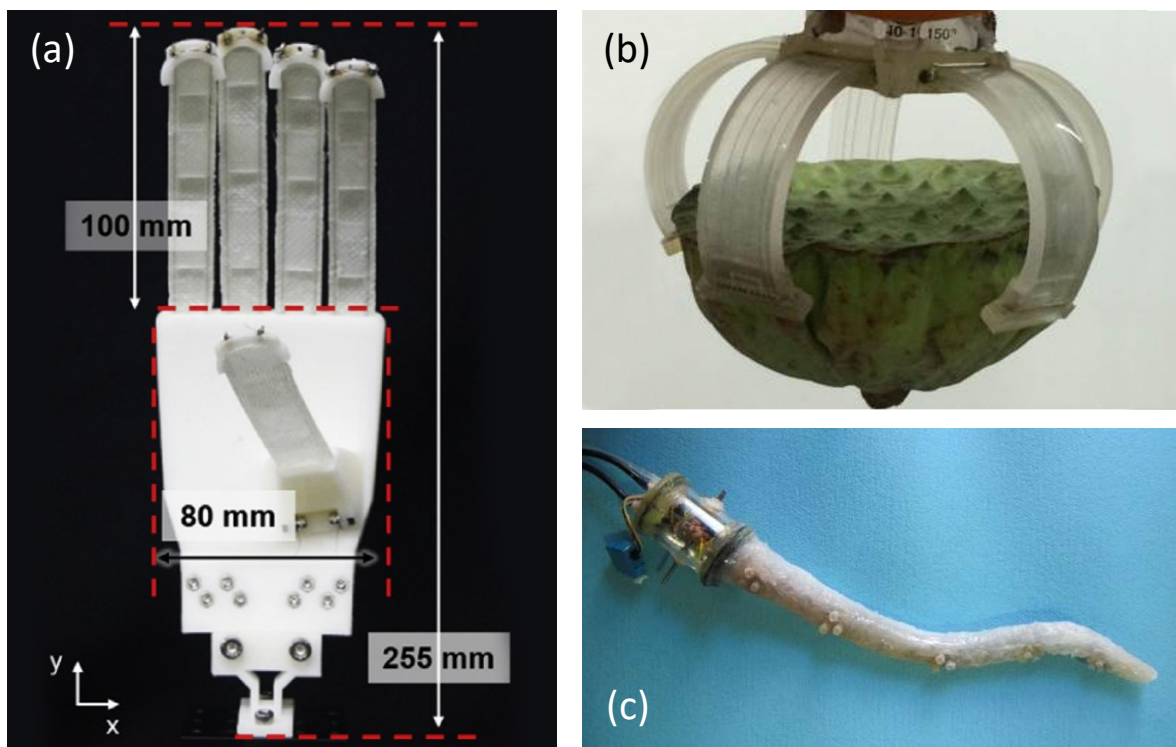


Figure 3 - Prototype of a robotic hand with four tendon-driven soft composite fingers and a thumb (a)[19]. Modular soft robot used to manipulate an object (b)[20]. SMA-based soft actuating unit inspired to the octopus muscular hydrostat (c)[25].

In [27], a device inspired by a worm was created by 3D printing, which contains 3 SMA coils. The soft body design allows for right and left bending in addition to up-and-down bending to achieve locomotion. The translational movement in a pipe was obtained by a biomimetic robot with peristaltic motion, inspired by the motion generated by the bowels. It has nine independently controlled SMA springs and a silicone rubber skin [28].

Even from this short overview, it is clear that the SMA elements in different configurations can produce a variety of practical effects, from grasping to locomotion, allowing at the same time displacement and force to be applied along single or multiple degrees of freedom.

1.3. Optimisation techniques for shape-memory alloy soft actuation

As expressed at the end of Section 1.1, SMA-based technologies, besides their undeniable advantages, also display limitations, particularly linked to their bandwidth and efficiency. Different methods for optimising SMA-based soft actuators can address various aspects of their design and implementation. Next, we shall provide a brief overview of the main directions of development.

The most widely researched improvements are certainly linked to the mechanical aspects.

Bias force. A certain level of bias force must be present in most SMA-based soft actuators to enable their mechanical reset. While bias optimisation has been carefully modelled for stiff systems in order to aid the design phase [29], only few works deal with the conditioning effect of soft matrices. The effect of the bias force in soft systems can be used to guide motion along precise paths and optimise the stroke of the device. The bias force can be modulated for example acting on the geometry of the device and the thickness of the rigid elements contained within it [30].

Stiffness and matrix mechanics. In [31], efficient stiffness modulation of soft actuators is accomplished by changing the geometry and layout of the rigid segments within the structure. In this research, a broad range of bending, twisting, and extensional deformations have been realized through accurate placement of 3D-printed elements made of materials with different tensile moduli.

The optimisation of the actuator size and material selection can be aided by modelling the complete system [32]. An example of this approach is provided in [14]. A bending actuator, in which the initial curvature is imposed by a special double casting procedure can be used

to improve the maximum grasping force and the maximum bending angle of the actuator. The paper demonstrates that the effect of the initial curvature on the maximum bending angle of the actuator can be accurately predicted using multimaterial modelling.

In [33], Liu et al proposed a SMA-based soft robotic gripper with variable stiffness and a high grasping force designed to grab heavy objects stably. The device is based on the use of paraffin (wrapped in an elastomeric membrane), which is activated alternately to the SMA element. When heating the paraffin to the liquid state, the gripper, being at low stiffness, can be easily actuated by heating SMA wire to carry out a grasping operation. Conversely, when the paraffin is cooled and resolidified, high stiffness is obtained, and the soft gripper can keep configurations firmly and stably increasing the maximum grasping force to about 10 times. Furthermore, for long holding times, the proposed gripper can reduce energy consumption in comparison to actuators where the SMA element must be kept heated. The drawbacks of this system are the very long actuation times. In fact, the time required by the device to change from low stiffness to high stiffness was demonstrated to be 380 s, and the time required for the reverse process was 70 s.

The integration of functional materials is certainly an interesting development idea but it needs to be optimised. For instance, there is an obvious need to account for appropriate constitutive law to describe complex systems. It has been stated it will be useful to employ models more complex than (hyper-)elasticity. Plasticity or fatigue laws received little attention in the community but are key to predict the reliability of soft robots. An issue related to that is the problem of mixing different materials in the same robot to create specific behaviours. Then, regarding the inclusion of various kinds of actuation, multiphysics model are needed to couple the mechanics of the robot with heat transfer for SMA [34].

Matrix thermal properties. Given the thermodynamic nature of the stimulus needed to actuate SMAs the heat-transfer related aspect of these devices is of paramount importance. In order to optimise their behaviour, it is useful to study the effect that an embedding matrix has on the thermomechanical behaviour of a SMA element incorporated inside it. One might think that given the insulating nature of polymeric matrices, their use could worsen the performance of SMA-based soft devices decreasing heat dissipation rates. This is not entirely true. In fact, the SMA/polymer interface can allow the heat to dissipate at a faster rate than in air [30], exploiting conductive rather than convective transport. However, it is reported that the device decreases its performance in sequential actuation cycles. The main reason is overheating of the matrix that is in contact with the wire.

With the aim of addressing this problem, a thin actuator has been created in [11] composed of two layers of conductive polymer (2.2 W/mK), in which a silicone rubber film containing a U-shape SMA wire is inserted. The device is a lightweight and highly dynamic SMA-based actuator designed to obtain a flexural response. The effect of the conductive layers has not been evaluated due to the absence of a non-thermally enhanced device to compare against. The experimental tests obtained by continuously actuating the device with a constant period and duty cycle, showed that the temperature of the SMA at the end of each cycle increases as the number of actuation cycles increases. In [35], analytical and numerical analyses on the same device concept were conducted with the aim of evaluating the impact on the thermal and mechanical efficiency of the size and number of SMA wires in the actuator. The tests showed that electrical-to-mechanical energy conversion efficiencies can be improved by increasing wire diameter and wire count. However, it is useful to point out that the thermal interface between the two materials has not been taken into consideration, and that it is not excluded that it may influence the thermal behaviour during cooling. The device was modified in another work [36], embedding liquid metal microdroplets in the sealing elastomer at various volume ratios in order to study its influence on the actuator properties. The device characterisation showed that as the liquid metal volume ratio increases the actuation frequency increases too, but the peak curvature change generated decreases. Instead, the maximum blocking force has very limited change with increases in the liquid metal volume ratio.

Sensorisation. Soft actuating devices can also be functionalised by the use of sensors. For instance, piezoelectric transducer (PZT) flexure sensors can be easily inserted into a device, whose matrix is shaped by filling with silicone rubber a 3D printed mould (Figure 4a) [37]. In some implementations based on piezoresistive sensors, such as [38], the displacement is nonlinear with the measured (voltage) signal and affected by artefacts related to the temperature increase due to the Joule heating of the SMAs.

Measurements conducted by capacitance liquid-metal sensors have a good linear relationship with the curvature of an actuator on which they are applied (Figure 4b) [39].

In [40], one-shot additive manufacturing of a soft robotic finger equipped with 3D printed sensing systems (a strain gauge for the bending sensing and a capacitive force sensor for the object detection) is obtained. The sensors were manufactured using a conductive thermoplastic polyurethane (CTPU) in the same printing cycle as the finger (Figure 4c).

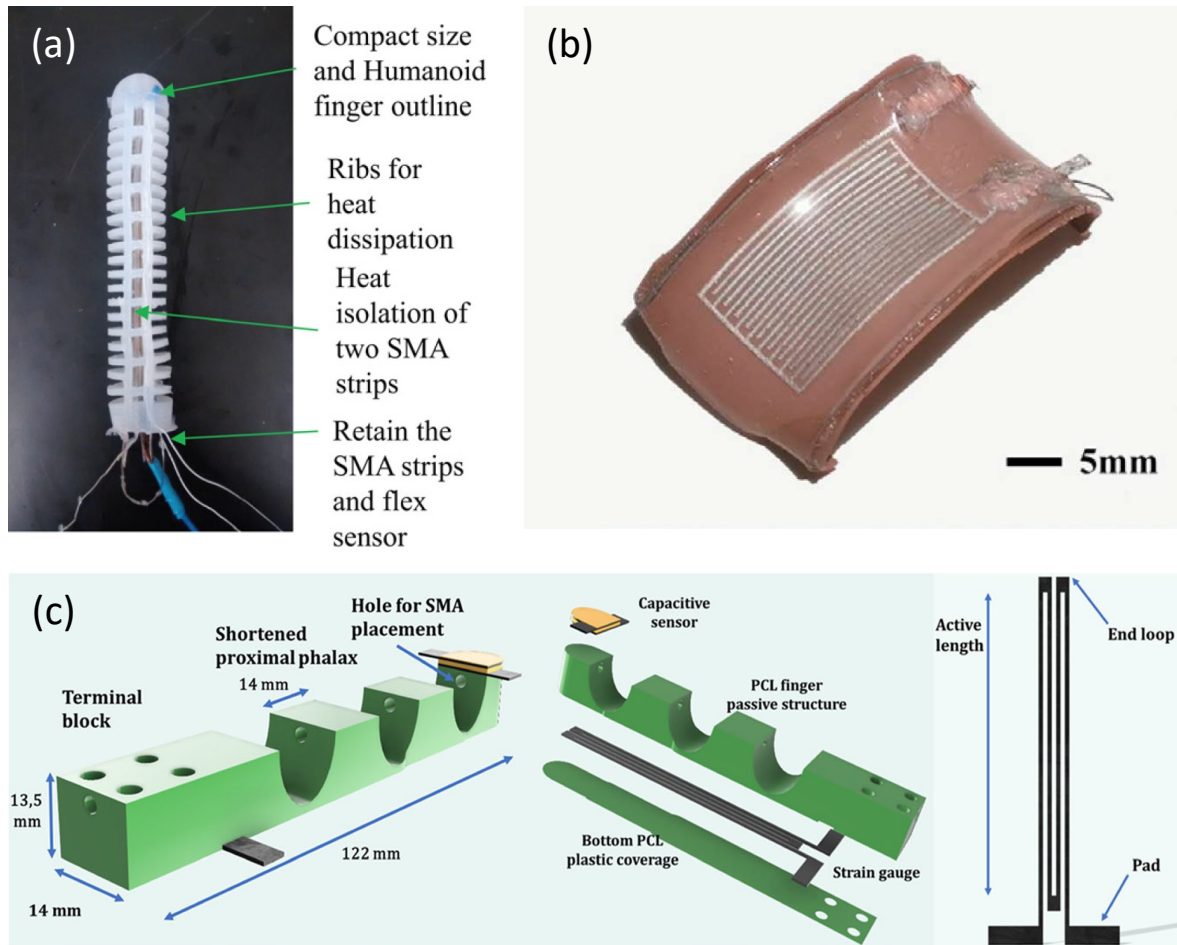


Figure 4 – SMA-soft robotic finger integrating a piezoelectric flexure sensor (a)[37]. Capacitive strain sensor built by spraying liquid metal on a silicone rubber layer using a paper mask (b)[39]. 3D-printed finger equipped with two sensors. The first one is a strain gauge sensor placed in the bottom part of the device. The second one is used as a force/contact sensor and is placed on the tip of the finger (c)[40]

Control algorithms. Strategies specifically aimed at optimising the power consumption of the SMA element in soft actuators are scarcely present in the literature. Some works show how it is possible to optimise the electric power consumption through the use of a PWM-based activation in SMA wires [41], [42].

Automatic control strategies of SMA soft actuators are often only partially able to account for the complex material phenomenology: they are typically implemented for the sole purpose of functional verification or device characterisation, and simply based on standard controllers (e.g. PID controller) rather than advanced ones [43]. More complex strategies have been used in some cases, for instance to control an actuator composed of SMA wires inserted in a Bowden cable [44], [45]. However advanced, the control of a system in which

the SMA wire does not make good contact with the surrounding matrix is not representative of the more common systems, in which the wire is embedded in the polymer matrix.

Lastly, control strategies useful to optimise efficiency and reduce energy consumption of the complete SMA-based soft actuators are completely absent in the literature.

1.4. Gaps to be filled

The optimisation problem, as the analysis of the literature suggests, is still a matter of importance for the implementation of high-performance SMA-based actuators: this means especially improving the efficiency, the bandwidth and the controllability.

Previous work often addresses separately the effects of SMA property tuning, advanced control strategies, or – rarely – matrix modification. It is difficult to find published papers investigating not only the roles of such specific techniques, but also the effects of their interactions. Nevertheless, it is expected that those factors can interact. This approach will characterise the present work, as is explained in Chapter 2.

Another important aspect, that can impact soft actuator performance through its ability to be controlled, is the possibility of developing embedded sensors. While this direction of improvement will not be fully investigated in this work, some of the results obtained will be discussed in view of some possible future implementation along those lines.

CHAPTER 2

Objective and approach

2.1. Objective

The aim of this research project is to investigate different methods to optimise the functionality of soft actuators based on Shape-Memory Alloys (SMA). This class of actuators, deemed of interest for their compactness, bio-compliance and high energy density, generally display limitations particularly in the bandwidth (cycling frequency) and controllability due to heat-transfer-related effects. This research consists in a thorough study of the interaction between the SMA active element and an enveloping elastomeric matrix that serves as an interface towards the external environment. The main research question is whether and how functionalising the matrix and establishing specialised control schemes that take the matrix into account may serve to improve SMA-based actuation.

2.2. Approach

In order to answer our research question, I have adopted a multi-layered approach including:

1. Material optimisation and modification procedures, to optimise shape memory alloy properties and enhance the heat-transport and mechanical characteristics of the matrix;
2. Different mathematical models ranging from lumped parameter to multi-physical finite element (FEM) ones to gain insight in the complex interplay of material properties, size and control strategies that determines the rates of heating and cooling, and the energy flow in the system;
3. The creation of an advanced model-based and state-estimator-equipped closed-loop control algorithm that takes into account the behaviour of the SMA and the matrix;

4. The development of a proof-of concept SMA-based soft actuator to verify the practical applicability of the investigated optimisation methods, with a focus on assessing the effect of additional functional materials in supporting and improving the action and control of the SMA.

As a result of this research I derive some indications or guidelines for an optimised design of SMA-based soft actuators.

The structure of the thesis, schematically represented in Figure 5, is as follows:

In Chapter 1, the literature review concerning soft actuators is presented, reporting the strengths and weaknesses of the SMA-based soft actuators, and highlighting the aspects of their development that need further optimisation.

In Chapter 2, the goal of the work is presented together with an outline of the methods that have been developed to achieve it.

In Chapter 3, an overview of the physical characteristics of SMA materials is reported, together with the state of the art of their modelling and their automatic control. This analysis of the intrinsic behaviour and functioning mechanisms of SMAs is provided as a reference and to set a starting point for the research of the new processes and methods developed in the thesis.

In Chapter 4, I present the procedures employed to select, optimise and characterise an SMA wire for the current project.

In Chapter 5, a poly-dimethylsiloxane (PDMS) matrix modified with graphene nanoparticles (GNPs) is produced and characterised in order to assess the effectiveness of carbon fillers in adjusting heat transport properties for this application.

In Chapter 6, a simple soft actuator (a SMA wire embedded in a PDMS matrix) is defined as the reference case study. I present the various models developed on that concept, which are the at basis of the optimisation process and the search of general design principles. The material parameters used in the models are identified from the experimental measurements carried out in the previous chapters.

In Chapter 7, an advanced scheme for the closed-loop control of SMA-based soft actuators is proposed. The implementation makes use of a Kalman-based estimator algorithm, which, through the modelling of the actuator, supplies a variable PID controller with the useful information to manage the non-linearities of the system.

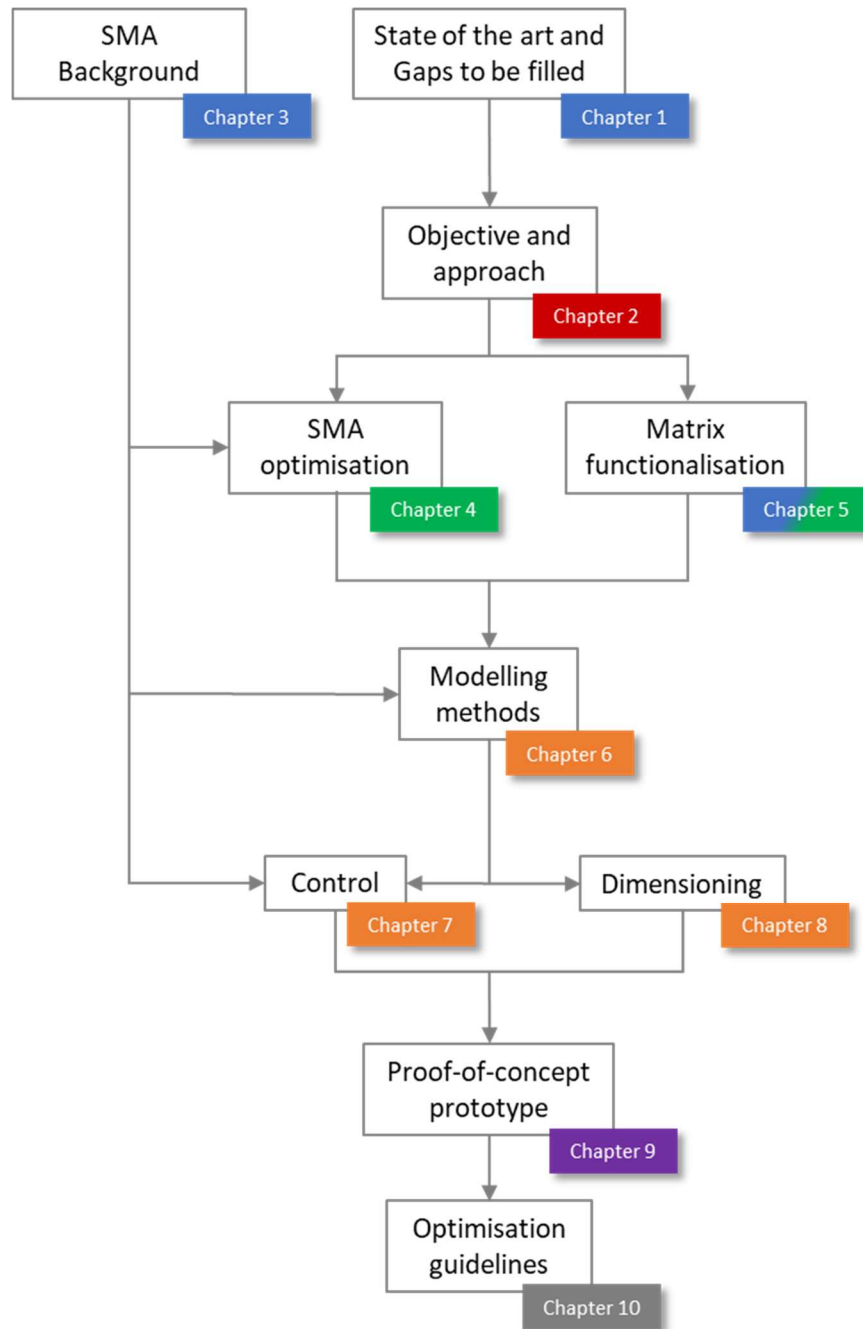


Figure 5 - Scheme of this thesis project. The sections in which the literature review is presented are highlighted in blue. The state of the art of SMA-based soft robots led to formulate the rationale of the thesis (red). The contribution made to this thesis work started with the study and optimisation of SMA and soft materials (green). Subsequently, numerical methods were developed and used to study the optimisation of SMA-based soft robots (orange). The development of a proof-of-concept actuator was conducted to verify the applicability of matrix functionalisation (purple). Finally, the conclusions of the work with the original contributions are presented (grey).

In Chapter 8, finite element modelling is used to predict the influence of the modified elastomeric material properties and morphology on the thermomechanical behaviour of the SMA. The study also focusses on the influence of the thermal interface between the elastomeric matrix and the embedded SMA wire on the performance of the soft device.

In Chapter 9, an operational SMA/PDMS+GNPs actuator is designed, fabricated and tested as a proof-of-concept of applicability of matrix functionalisation, and advanced control as design principles to optimise the working characteristics of SMA in soft actuators.

Finally, in Chapter 10, I draw the conclusions and claim my original contributions.

CHAPTER 3

Shape memory alloys: physics, models and control

Shape Memory Alloys (SMAs) are a type of smart material that is increasingly being used in various fields of application because of their peculiar functional properties, such as:

- *Pseudo-Elasticity (PE)*: when the SMA is initially at a temperature higher than a characteristic temperature, it has the ability to recover large deformations of up to 8-10% with no residual strains. Most of the deformation and shape recovery occur at constant stresses.
- *One-way Shape Memory Effect (SME)*: when the SMA is below a characteristic temperature displays low stiffness, is very deformable, and the accumulated strains are maintained when the load is removed. Subsequently, when heated above a certain other characteristic temperature, it can recover the pseudo-plastic deformations and regain its original shape.
- *Two-Way Shape Memory Effect (TWSME)*: in addition to the one-way effect that is displayed upon heating, some SMAs have in addition the ability to recover a pre-determinate shape in response to cooling; This effect is exhibited by certain compositions when pre-conditioned with special thermomechanical training treatments.

The shape memory effect is the focal point of interest for the present work because it is the basis for the use of SMAs as the actuating element in soft devices.

The Section 3.1 describes SMAs, providing an overview of their martensitic transformations and related phenomena. Some information on the compositions of interest and their characteristics will also be presented.

In Section 3.2, we shall analyse the state of the art of mathematical modelling of the SMA behaviour. Modelling the shape memory effect is a necessary step to obtain a complete model of the multimaterial soft system, which is the object of this thesis. Furthermore, as a new automatic control system for the multimaterial actuator will also be developed in this thesis work, some interesting published techniques used for the automatic control of SMAs are analysed in Section 3.3.

3.1. Metallurgy and phenomenology of NiTi-based shape memory alloys

Shape memory alloys are a class of metallic materials whose functional properties are due to a solid-state phase transformation that occurs by nucleation and growth of the martensitic phase from a parent austenitic phase. The martensitic transformation is a first-order, non-diffusive transition between the two main crystallographic phases. In SMAs, it is largely crystallographically reversible. Non-diffusive transformations do not modify the composition of the parent phase, but only its crystalline structure by rearrangement of atoms in short-range cooperative motion. Moreover, non-diffusive transformations are considered athermal since they do not progress at a constant temperature and the amount of the new phase depends only on temperature, not time. Finally, the martensitic transformation is crystallographically reversible, when the transformation proceeds in both directions with the exact restoration of the lattice structures, and without the creation of defects, which happens if the phases are accommodated elastically (without dislocations). Even so, some energy loss occurs during the transitions, due to internal and transformation-related friction. The effect of this energy loss on the material behaviour is that all the cyclic working paths that involve phase transition display hysteresis.

In SMAs, martensite can be produced by a temperature variation or stress-induced. Martensite is the phase stable at low temperatures or high stresses, while austenite is stable at high temperatures. It is possible to define some characteristic temperatures for the thermally-induced martensitic transformation (Figure 6). Taking into account the direct transformation, M_s (martensite start) temperature marks the beginning of the transformation

into martensite, while M_f (martensite finish) temperature indicates the end of it. In the same way, A_s and A_f (austenite start and finish) are defined for the inverse transformation.

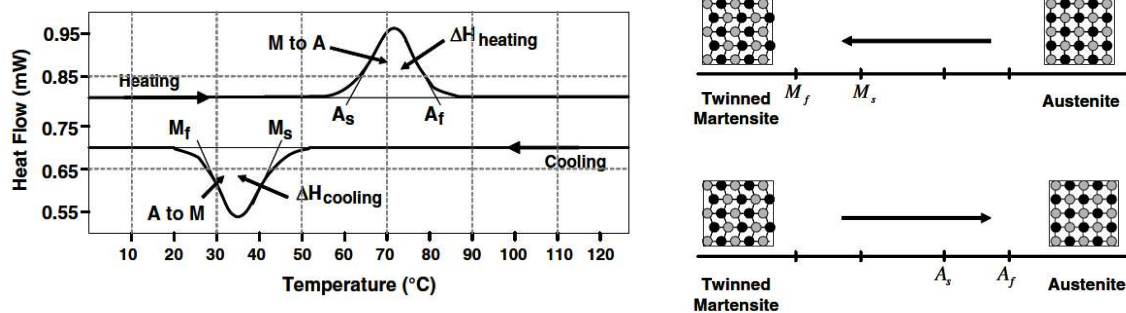


Figure 6 - In SMAs, it is possible to define some characteristic temperatures for the martensitic transformation. The DSC curve (left) shows the transformation temperature and the associated latent heat of transformation during heating and cooling. The diagram (right) shows the temperature-induced phase transformation of an SMA in absence of mechanical loading. [46]

Since the crystal lattice of the martensitic phase has lower symmetry than the one of the parent austenitic phase, several variants of martensite, with different orientations, can be formed from the same parent phase crystal (Figure 7).

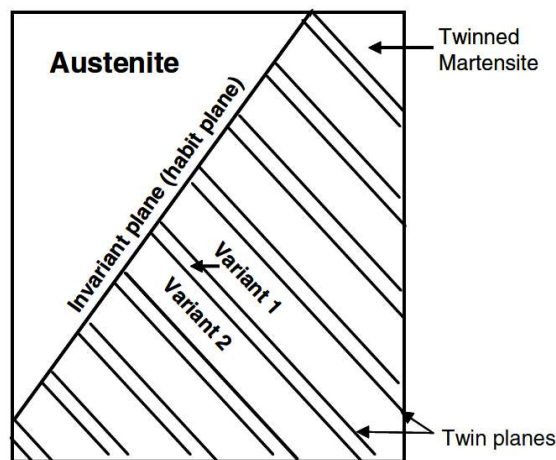


Figure 7 – Schematic of the austenite/martensite interface [46].

Generally, the martensite formed by cooling the austenite and in unstressed condition, is multi-variant and is characterised by a self-accommodated twinned structure. Twin boundaries are very mobile, so low energy is necessary to induce their motion. Consequently, upon application of an external stress, the variants, which are best aligned with the stress grow at the expense of the misaligned ones. This process shifts the balance of self-accommodation towards the most favourable variants and causes the detwinning of the martensite (Figure 8).

material behaviour is extremely non-linear and hysteretic. Indeed, when the load is applied to the material in the austenitic state, the elastic limit is overcome and a plateau at quasi-constant stress is induced. This happens due to the gradual transformation of austenite into detwinned martensite induced by stress. Then, upon unloading, the deformation is completely recovered passing through a plateau corresponding to a lower level of stress. This happens because the most stable structure above A_f (austenite) is gradually restored as the martensite-stabilising effects of the external load are reduced.

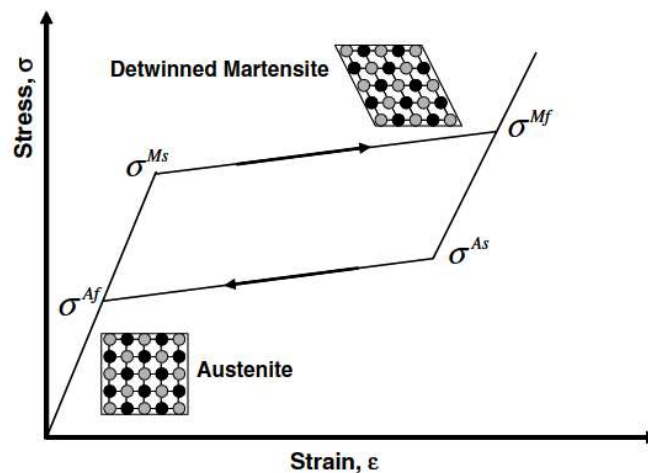


Figure 9 – Schematic of a pseudoelastic stress-strain diagram [46]. The elastic regions (full austenite at low strains and full detwinned martensite at high strains) are separated by the plateau region, which corresponds to stress-induced phase transformations.

3.1.1.2. One-way shape memory effect

When a mechanical load is applied to the SMA in the twinned martensitic phase i.e. at a temperature lower than M_f , the material exhibits a macroscopic deformation that is retained after the removal of the load. This happens because the application of the mechanical load induces the detwinning of the martensite by reorienting some variants present in the material. The SMA maintains this detwinned structure until it is heated above A_s temperature and the reverse phase transformation from detwinned martensite to austenite starts. When the temperature reaches A_f the initial shape of the material is completely recovered. Then, if the SMA is cooled down to a temperature below M_f , the direct transformation occurs and leads to the formation of twinned martensite again without any shape change (Figure 10).

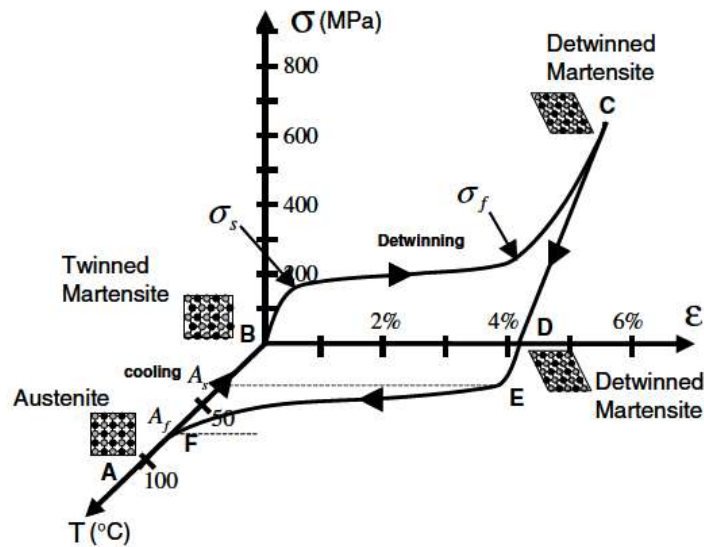


Figure 10 – Stress-strain-temperature data exhibiting the shape memory effect for a typical NiTi SMA [46].

For SMA-based actuation applications it is necessary to “memorise” a reference shape through a shape-setting thermal treatment. Most actuators are based on shapes like the straight wire, helical spring, flat spring or bending elements, such as beams or laminas. Moreover, the actuator function is deployed when the shape recovery process happens against a constraint, so that the partially constrained recovery can give rise to high specific forces and/or produce the displacement of loads [48]. Finally, cyclic actuation can be aided by external bias forces that can be exploited to re-deform the material upon cooling.

3.1.1.3. Two-way shape memory effect

For some SMA compositions, it is possible to perform a pre-conditioning through specific thermomechanical cycling procedures to obtain a further shape memory effect towards a different shape upon cooling (Figure 11). While the reference shape for austenite is set by heat treatment, the reference shape for detwinned martensite is memorised through a repeated thermomechanical process that imprints specific deformation paths based on the stabilisation of preferred martensitic variants. In this way, this two-way effect does not require an external bias force to deform the material when it is in the martensitic state. Indeed, the shape of the material changes between two reference shapes only driven by heating and cooling. In this case, both the deformations and the forces involved are lower than the ones in the one-way shape memory effect.

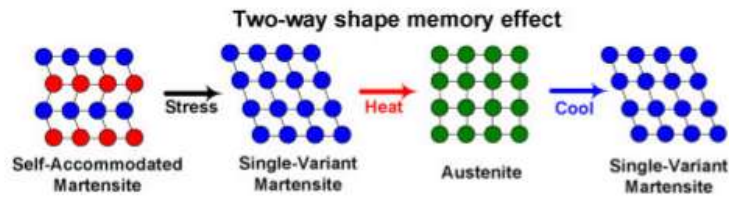


Figure 11 – Demonstration of two-way shape memory effects. The TWSME causes the martensite to adopt a more "single variant" configuration as compared to the one-way shape memory effect, which causes the martensite to typically return to a self-accommodated structure after cooling from austenite. Certain habit plane variants are favoured due to locally oriented internal stresses, and the martensite undergoes shape change upon cooling from austenite. [49]

3.1.2. Binary and ternary NiTi-based systems: NiTi and NiTiCu alloys

NiTi-based alloys are the most widely studied SMAs systems and they are the functional materials of interest for the present study. NiTi-based SMAs include binary alloys, composed only of Ni and Ti, and ternary alloys, when another metallic element substitutes a certain amount of Ni or Ti.

NiTi binary alloys can follow two different paths of martensitic transformation, i.e. directly from the B2 cubic austenite structure to the monoclinic B19' martensite or passing through an intermediate transition. In the latter case, the first-step is the R-phase transformation, which generates a rhombohedral phase (Figure 12). This intermediate product is characterised by a lattice cell which, unlike the one of monoclinic martensite, is similar to the cubic cell of austenite. Therefore, the R-phase transformation generates smaller deformation strains, and exhibits lower hysteresis and higher stability than the second-step transformation into the B19' martensite.

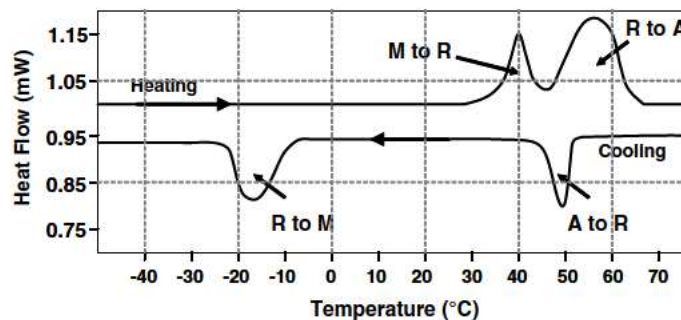


Figure 12 - A DSC curve for a Ni-rich NiTi SMA showing the two-stage transformation from austenite to martensite [46].

On the other hand, for some ternary NiTi-based alloys including NiTiCu it is possible to observe an intermediate transformation into an orthorhombic martensite, with the B19 structure, before the transition into monoclinic martensite.

Finally, it is important to highlight that the occurrence of a particular transformation path in NiTi-based alloys depends on the composition, and on the thermo-mechanical treatments applied.

Considering more in detail the binary NiTi system, its cubic phase is stable down to room temperature as observed in the phase diagram of this intermetallic compound (Figure 13). However, below 923 K, the cubic phase exists only when Ni content ranges from 50 to 50.5% since the stoichiometric range for cubic phase stability becomes narrow. Within this composition range, the increase of the content of Ni or Ti leads to different properties. Alloys with an excess of Ni have a pseudoelastic behaviour at room temperature and even below and an increase in the Ni content causes a decrease of the transformation temperatures. Conversely, Ti-rich alloys have higher critical temperatures and, at room temperature, they exhibit shape memory effect. Moreover, both Ni-rich alloys and the equiatomic NiTi alloys that have been subjected to thermomechanical treatments undergo the two-step martensitic transformation that involves the R-phase formation as intermediate transition. On the other hand, the Ti-rich alloys and the equiatomic alloys that have been annealed completely or solubilised exhibit the single stage transformation from the cubic austenite to the monoclinic martensitic phase.

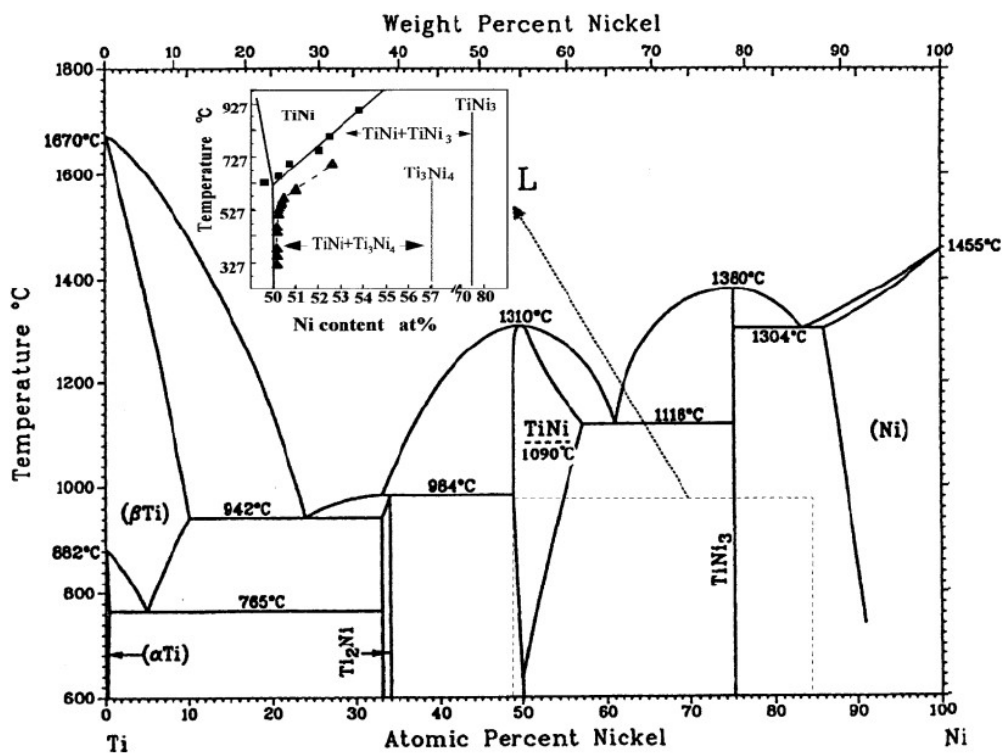


Figure 13 – Phase diagram of a Ti-Ni alloy, to which the phase equilibrium between the B2 and Ti₃Ni₄ phases are added [50].

Considering instead the ternary systems, the Cu addition in substitution of a percentage of Ni affects the transformation path and the associated shape memory properties. Generally, NiTiCu displays shape memory effect at room temperature and if the amount of Cu ranges between about 7 % and 15 %, it exhibits the two-step martensitic transformation cubic \rightarrow orthorhombic \rightarrow monoclinic (Figure 14). The transition temperature of the first step is quite stable, while by increasing Cu content the offset temperature of the second step from orthorhombic to monoclinic phase decreases. Furthermore, when Cu exceeds 15 %, the second step does not occur, even at extremely low temperatures, i.e. liquid nitrogen one.

Another comparison between NiTi and NiTiCu systems concerns the hysteresis of the first-step transformation of ternary alloys and the one of the single-step transition of certain binary alloys compositions. While the hysteresis of the B2 \rightarrow B19 transformation in a binary Ti-Ni alloy is more than 40 K, that of the Ti-Ni-10 Cu (at%) alloy is 11 K and the recoverable strain is more than 3 %. Thus the B2 \rightarrow B19 transformation is useful for applications as actuators. Unfortunately, Cu addition exceeding 10at% embrittles the alloy and spoils the formability [51].

Mechanically, NiTiCu alloys have smaller hysteresis in pseudoelasticity, and lower flow stresses, which are connected with a to the increased ease of interface movement during the transformation determined by Cu substitution for Ni.

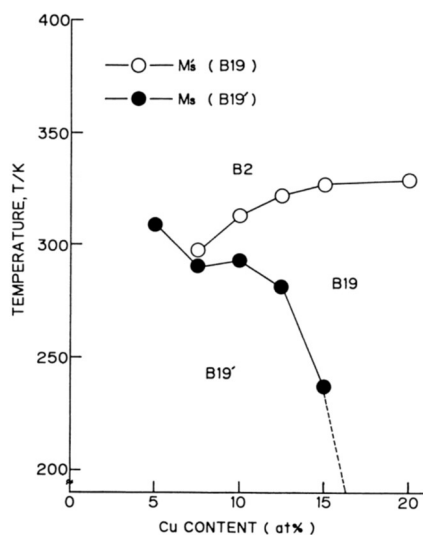


Figure 14 - Cu-content dependence of transformation temperatures in NiTiCu alloys [50].

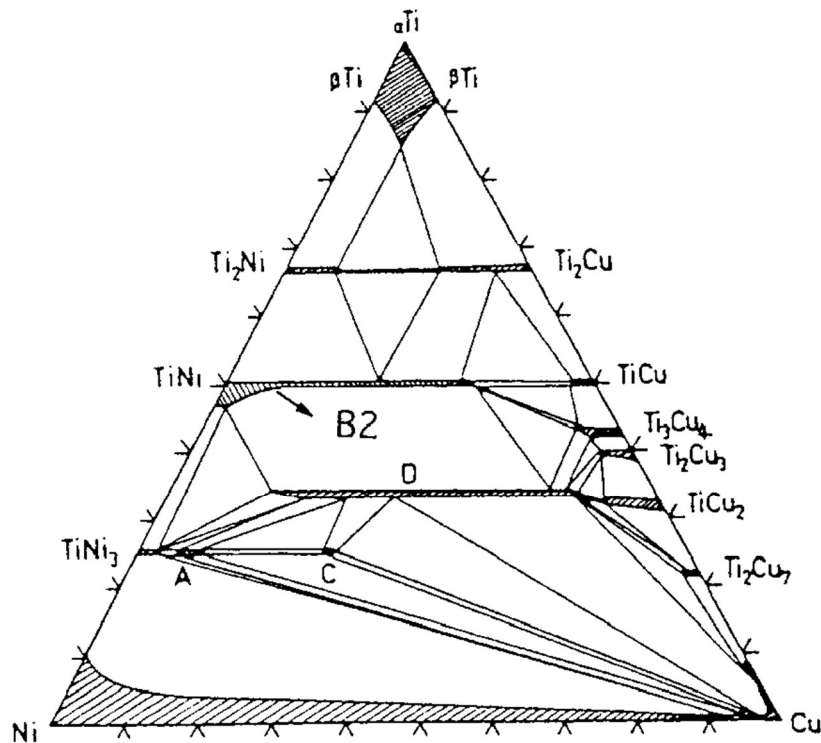


Figure 15 – Ti-Ni-Cu phase diagram at 870 °C [52]

3.1.3. Thermal treatments

Thermal treatments are extremely important for the tuning of the martensitic transformation temperatures, stresses and reversibility, particularly for Ni-rich NiTi alloys. This peculiarity arises from the equilibrium between the NiTi phase and metastable coherent Ni₄Ti₃ precipitates. Indeed, during the ageing thermal treatment, the precipitation reaction occurs and its products are frozen in by quenching. As a result, the obtained microstructure contains a certain amount of secondary Ni₄Ti₃ which, by subtracting Ni, deplete the matrix of Ni. In this way, the transformation temperatures increase with the aging time until a constant value is reached. Moreover, higher aging temperatures, that are not effective for the precipitation of the Ni₄Ti₃ phase lead to comparatively lower transformation temperatures [50].

In addition, thermal treatments are crucial for the shape-setting procedures when it is necessary to form the SMA for specific applications. Shape-setting is carried out at temperatures between 325 and 500 °C and the duration is between 5 and 30 minutes. During the heat treatment, firstly the work hardening, that would prevent phase interface mobility, is reduced. Then, the formation of precipitates starts and the residual internal stresses derived from the shaping are gradually minimised upon increasing of the treatment duration. After

that, the SMA is quenched; the final microstructural configuration will be retained as the preferred crystalline orientation of the parent phase due to pinning by the remaining dislocation network and secondary phases, enabling the shape recovery effects [53].

Even though substitution of Cu for Ni affects the transformation behaviour in many respects, the basic mechanisms discussed are also valid for the NiTiCu ternary system. Regarding ageing, it is worth mentioning that Cu addition (substituting Ni) hinders Ni₄Ti₃ precipitation and thus is effective for avoiding *M_s* temperature changes due to differences in cooling speed. *M_s* sensitivity to composition is also very much reduced by Cu addition [51].

3.2. Modelling of the shape memory effect

3.2.1. A look into SMA modelling approaches

There are countless SMA models in the literature that are based on a variety of methodologies. A first subdivision allows to distinguish the methods based on a microscopic approach from the macroscopic ones.

To describe the behaviour of the SMA, microscopic models start with microstructural features at the lattice or grain-crystal level, such as phase nucleation, interface motion, and martensite twin growth. Most of them are based on molecular dynamics or the Landau-Devonshire free energy. The majority of these models use appropriate volume-averaging techniques to capture the overall effect in the SMA and are based on the concept of a unit cell or Representative Volume Element (RVE). These models are capable of describing SMA behaviour at the highest level, but they are typically very large and complex, requiring powerful computers in order to produce accurate results [54].

On the other hand, as the name implies, macroscopic models aim to represent the SMA response at a macroscopic scale (typically > 100 μm). The macroscopic effects are taken into account using the suitable approximations and assumptions. Phenomenology and the application of thermodynamic principles are the two most important aspects of this modelling approach. While some models have a framework that is based on thermodynamics, others heavily rely on phenomenology and assume that the laws of thermodynamics are satisfied a priori. Without explicitly taking into account the underlying physics, another class of models attempts to reproduce the hysteretic input-output

relationship employing various hysteresis operators to predict a specific stress-strain-temperature response.

The macroscopic approaches are the most suitable for our purpose and therefore will now be explored. They can be subdivided into three main groups: those based on hysteresis, free energy, and the phenomenological ones.

The hysteretic response of the SMAs can be modelled by establishing a suitable input-output model that describes the hysteresis observed between a forcing function and the response variable. Generally, these kinds of models are used for the description of the behaviour of ferroelectric and magnetic materials and can be found in the literature about control. In the work by Smith et al. [55], this hysteresis approach is deeply investigated for SMAs modelling and two different groups of models are identified on the basis of the operator that tracks the SMA response. The first class of models is the Preisach type, which integrates the response of individual relays switching between two fixed states. In the case of SMAs, it corresponds to the type of transformation. Critical values of the driving forces are prescribed that trigger the switching in both directions. In literature, it is possible to find some studies [56], [57] that follow this approach to describe the hysteresis related to pseudoelasticity and shape memory effect. Among the advantages of these models there is the ease to describe return point memory and inner loops. The second group of models are of the Duhem-Madelung type, and describe the hysteresis in an incremental way. This approach adopts two different differential operators for the loading and unloading paths to describe the material response. For instance, Ivshin and Pence [58] describe the hysteresis of SMAs using this approach. Thanks to its simplicity, this approach is employed in the real-time control of SMA-based devices and to predict inner-loop response. However, the approach is not completely reliable when it is necessary to take into account effects including the two-way shape memory, the presence of multiple variants and hysteresis changes.

In free-energy-based models, a suitable form of potential or free energy that represents the state of the system is identified. A more consistent effort is made to describe the phase-transformation-related effects either as changes in free energy or through a generalised constitutive function, such as a dissipation potential. The type of free energy depends on the choice of state or field variables., so possible choices are the Gibbs free energy or phenomenological Landau-Devonshire forms.

As proposed in [59] and [60], the free energy of SMA can be decomposed as:

$$\text{Free energy} = \text{Exchange energy} + \text{Mechanical energy} + \text{Thermal energy} + \text{Latent heat}$$

where, in particular, the exchange energy is a function of the phase volume fraction. It usually determines the nature of the transformation kinetics through the dissipation potential, and also the nature of hysteresis and memory in the material response

Typically, just the interaction between Martensite and Austenite is taken into account and the interaction between individual variants of Martensite is ignored. Examples of multi-variant martensite models, for instance, derive from the Müller-Achenbach-Seelecke approach [61].

The key characteristic of phenomenological models is the separation of the driving forces and the kinetics (evolution) of phase transformation from the constitutive stress-strain-temperature relationship. A good number of phenomenological models can be found in literature, and this is certainly due to their ease of use and good ability to describe the macroscopic SMA response, at least in a 1-D setting.

These models differ according to the choice of internal variables and the description of their evolution in terms of thermo-mechanical driving forces. A σ - T phase diagram is often used to identify the active zones of transformation and the dead zones. Appropriate evolution functions are defined in each active zone to calculate the progress of the phase transformation.

In the next section, some interesting examples of this approach will be further described, also showing how incremental developments ultimately led to compact and robust formulations that facilitate the use of phenomenological models as SMA actuator design tools.

3.2.2. Summary of the evolution of phenomenological models

Approaching to the study of SMA pseudoelasticity, Tanaka et. al. [62] made the basic assumption that the thermomechanical process of the SMA material can be fully expressed by three major state variables: strain, temperature and martensite volume fraction. That was one of the first models to use only the stress-induced martensitic fraction (ζ) as an internal variable.

The relationship between the state variables stress σ , strain ε and temperature T in the terms of the martensite volume fraction ξ , is expressed by the following constitutive equation:

$$\sigma - \sigma_i = [D(\xi)(\varepsilon - \varepsilon_i) + \Omega(\xi)(\xi - \xi_i) + \Theta(T - T_i)] \quad 3.1$$

$$D(\xi) = D_A + \xi(D_M - D_A) \quad 3.2$$

$$\Omega(\xi) = -\varepsilon_L D(\xi) \quad 3.3$$

where D is the total elastic modulus, which is a linear combination of the elastic moduli of martensite and austenite, respectively D_M and D_A , proportionally to the total martensitic fraction ξ ; Ω is the transformation tensor and Θ is the thermoelasticity modulus, ε_L is the maximum residual strain; the subscript i indicates the initial value of the variable at the start of the transformation.

The transformation kinetic laws describe the variation of the martensitic fraction ξ as a function of the current temperature and stress:

if $[(T > M_F) \wedge (C_M(T - M_S) < \sigma < C_M(T - M_F))]$ *then*

$$\xi = 1 - e^{a_M(M_S - T) + b_M \sigma} \quad 3.4$$

if $[(T > A_S) \wedge (C_A(T - A_F) < \sigma < C_A(T - A_S))]$ *then*

$$\xi = 1 - e^{a_A(A_S - T) + b_A \sigma} \quad 3.5$$

where a_A , a_M , b_A and b_M are material constants, dependent on the transition temperatures A_S , A_F , M_S and M_F , and on the Clausius-Clapeyron coefficients C_A and C_M .

Liang C. et al. modified the phase kinetics from an exponential to a cosine-based function [63], in order to obtain a better fit to the experimental data:

if $[(T > M_F) \wedge (C_M(T - M_S) < \sigma < C_M(T - M_F))]$ *then*

$$\xi = \frac{1 + \xi_{Si}}{2} + \frac{1 - \xi_{Si}}{2} \left\{ \cos \left[\frac{\pi}{M_S - M_F} \left(T - M_F - \frac{\sigma}{C_M} \right) \right] \right\} \quad 3.6$$

if $[(T > A_S) \wedge (C_A(T - A_F) < \sigma < C_A(T - A_S))]$ *then*

$$\xi = \frac{\xi_i}{2} \left\{ \cos \left[\frac{\pi}{A_F - A_S} \left(T - A_S - \frac{\sigma}{C_A} \right) \right] + 1 \right\} \quad 3.7$$

The following improvement to this same model was provided by Brinson, whose formulation has achieved great success and has been at the basis of several applications and implementations.

3.2.3. Brinson (1993) model

Brinson et. al. [64] proposed a modified model based on the Tanaka-Liang framework in order to account for the shape memory effect by splitting the martensitic phase fraction into two parts: temperature-induced twinned fraction (ξ_T) and stress-induced detwinned fraction (ξ_S). This differentiation of the phase fractions is used to capture stress/strain recovery, and is based on the assumptions that the twinned martensite does not contribute to the recovery stress.

The constitutive law of Brinson's model is a modified version of Tanaka's [62], described by eq. 3.1, accounting for the two martensite variants (self-accommodated vs. detwinned).

The relationship between stress, strain, and temperature is described by:

$$\sigma - \sigma_i = [D(\xi)\varepsilon - D(\xi_i)\varepsilon_i + \Omega(\xi)\xi_S - \Omega(\xi_i)\xi_{S_i} + \theta(T_1 - T_{1_i})] \quad 3.8$$

$$D(\xi) = D_A + \xi(D_M - D_A) \quad 3.9$$

$$\Omega(\xi) = -\varepsilon_L D(\xi) \quad 3.10$$

where the subscript S refers to the stress-induced part of the martensitic fraction (which directly impacts on the transformation strain).

The phase diagram in Figure 16 was constructed to describe phase transformation involving austenite and the two martensite types, depending on the position of its inner state in the σ - T plane.

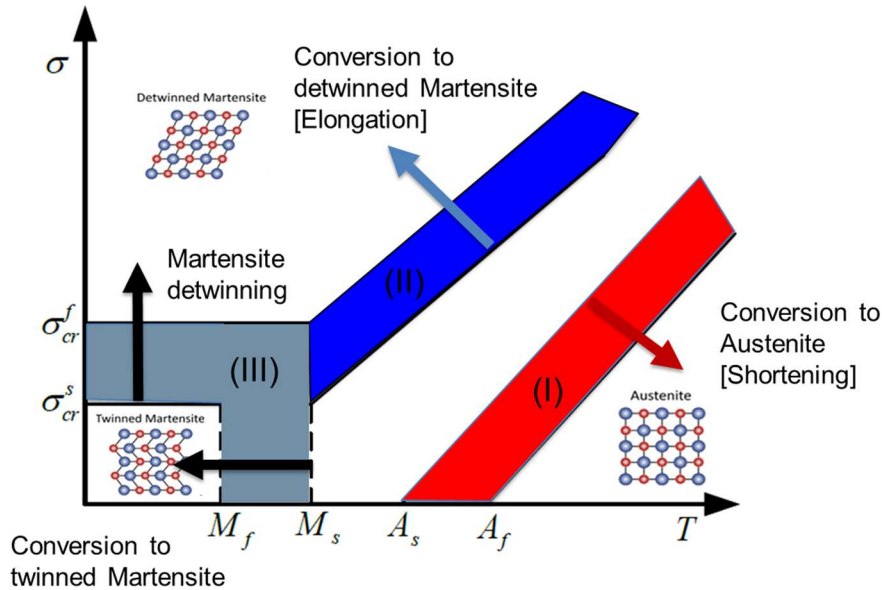


Figure 16 – SMA phase plane with critical stress-temperature boundaries (straight lines). The three highlighted zone bounded by the critical lines, and the corresponding arrows, define limits and directions of the transformations. The kinetic laws take effect only within the transformation zones.

The transformation kinetic laws from Liang C. et al. [63], are modified by Brinson as follows:

(I) Conversion to Austenite:

if $[(T > A_S) \wedge (C_A(T - A_S) < \sigma < C_A(T - A_S))]$ then

$$\xi = \frac{\xi_i}{2} \left\{ \cos \left[\frac{\pi}{A_F - A_S} \left(T - A_S - \frac{\sigma}{C_A} \right) \right] + 1 \right\} \quad 3.11$$

$$\xi_S = \frac{\xi_{S_i}}{\xi_i} \xi \quad 3.12$$

$$\xi_T = \frac{\xi_{T_i}}{\xi_i} \xi \quad 3.13$$

(II) Conversion to detwinned Martensite:

if $[(T > M_S) \wedge (\sigma_S^{cr} - C_M(T - M_S) < \sigma < \sigma_F^{cr} - C_M(T - M_S))]$ then

$$\xi_S = \frac{1 + \xi_{S_i}}{2} + \frac{1 - \xi_{S_i}}{2} \cos \left\{ \frac{\pi}{\sigma_S^{cr} - \sigma_F^{cr}} [\sigma - \sigma_F^{cr} - C_M(T - M_S)] \right\} \quad 3.14$$

$$\xi_T = \frac{\xi_{T_i}}{1 - \xi_{S_i}} (1 - \xi_S) \quad 3.15$$

(III) Martensite detwinning and conversion to twinned Martensite:

if $[(T < M_S) \wedge (\sigma_S^{cr} < \sigma < \sigma_F^{cr})]$ then

$$\xi_S = \frac{1 + \xi_{S_i}}{2} + \frac{1 - \xi_{S_i}}{2} \cos \left[\frac{\pi}{\sigma_S^{cr} - \sigma_F^{cr}} (\sigma - \sigma_F^{cr}) \right] \quad 3.16$$

$$\xi_T = \frac{\xi_{T_i}}{1 - \xi_{S_i}} (1 - \xi_S) + \Delta_{T\xi} \quad 3.17$$

if $[(M_F < T < M_S) \wedge (T < T_0)]$ then

$$\Delta_{T\xi} = \frac{1 + \xi_{T_i}}{2} \left\{ \cos \left[\frac{\pi}{M_S - M_F} (T - M_F) \right] + 1 \right\} \quad 3.18$$

else

$$\Delta_{T\xi} = 0 \quad 3.19$$

This form of the kinetic equations is able to model the coexistence of twinned and detwinned martensite fractions and the processes leading to their transformation into one another or into austenite. Note, in particular, the (constant) parameters σ_S^{cr} and σ_F^{cr} expressing the critical stresses, between which twinned martensite detwins. Also note the introduction of the parameter $\Delta_{T\xi}$, which accounts for the transformation of residual austenite into twinned martensite by cooling in the zone below M_S and between σ_S^{cr} and σ_F^{cr} .

This formulation of the phenomenological model does not explicitly account for other effects of much consequence for real actuators, such as partial cycles (inner loops) and two-way shape memory.

3.3. Techniques for the automatic control of SMAs

Various techniques for the automatic control of SMA actuators directly exposed to air can be found in literature, ranging from linear controllers, to strategies employing the use of non-linear control design. The most commonly used control variable is the position (e.g. elongation or curvature of the actuator), but examples can be found using for the feedback loop the force exerted by the actuator [65], the electrical resistance [66] or the temperature [67].

An overview of the most common types of controllers will now be given, exploiting some particular works as examples of the use of different techniques, including modelling of the SMA behaviour, to optimise the controller action.

PID (Proportional-Integral-Derivative) controllers are very common, due to their applicability in various fields. These controllers are effective and easy to implement, but may not be robust to disturbances [68]. Furthermore, in a linear PID it may be difficult to tune the error gains for the control of nonlinear and time-varying SMA actuators.

The use of a saturated PI controller (no derivative part) can help reducing the error and improving tracking frequency [69]. Adaptive PID controllers can help in rejecting overshoots, though with some chattering problems. [70].

Another strategy involves the use of a PID controller associated with an inverse hysteresis compensator. Liu et. al. [71] developed a self-sensing PWM (Pulse Width Modulation) controller including a feedforward inverse compensator (Figure 17), modelling the SMA hysteresis with the use of a Duhem differential model. The PID controller is supported by the inverse compensator, in which the hysteresis model represents the major and minor hysteresis loops; a temperature dynamics model computes the required input power to heat up the SMA actuator, and an actuator force model accounts for the strain energy required to deform the actuator. This strategy has demonstrated good improvement in the position tracking, but its effectiveness depends on the precise knowledge of the ambient temperature and the material properties.

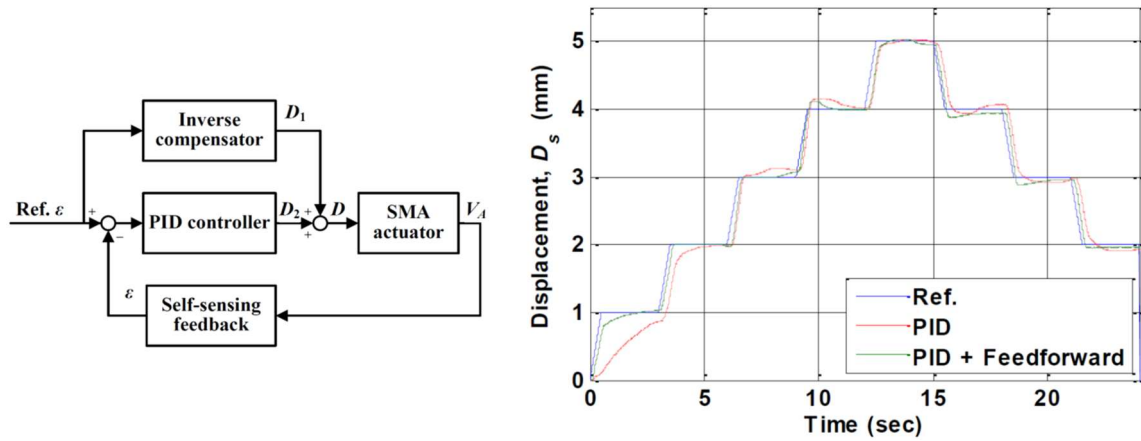


Figure 17 – Schematics of a self-sensing PWM controller including a feedforward inverse compensator (left). Experimental verification of the effectiveness of this control technique for a multi-step reference input (right) [71].

Another common technique involves the tuning of PID parameters via fuzzy logic. A combination of the error and its derivative can be used to modify the proportional, integral and derivative gains via the Mamdani rule-based process [66].

When employed in complex models, fuzzy-logic controller (FLC) is a nonlinear approach that is valued for its robustness and usability [72]. However, when complex strategies are necessary, its implementation has the disadvantage of requiring high computational power [73], [74].

Nonlinear algorithms, such as Variable Structure Control (VSC) and its subclass Sliding Mode Control (SMC), are another form of control system that appears frequently in literature. These techniques utilise a switching control law to drive and maintain the nonlinear plant's state trajectory onto a user-specified surface in state space.

Together with the SMC technique, VSC is very popular in controlling SMA systems, thanks to its resilience against parametric uncertainty and external disturbances. However, the main problem, shared by both algorithms, is the presence of control chattering. Furthermore, their robustness is not ensured during the reaching phase, in which the sensitivity to disturbance decreases.

The integral SMC (ISM) technique allows certain improvements in the reaching phase, ensuring that SMC is insensitive to the starting conditions. It is obtained imposing the sliding mode throughout a system's response from the beginning [75]. Also the Fuzzy SMC algorithm can improve initial offset tracking and it proved to be efficient thanks to its disturbance rejection capability [76].

A Sliding Mode Controller can be designed by using a NARX (nonlinear autoregressive network with exogenous inputs) neural network to obtain a black-box model of the actuator. This method uses SMAs' input-output data and use autoregressive algorithms to model the behaviour. In some cases, modelling accuracy is lower than 80% particularly in situations where there are abrupt changes in the input signals (for example in case of impulse or step input) [77].

All model-free controllers, based on the use of neural networks, fuzzy systems and neuro-fuzzy structures, need to learn the inverse model of the hysteresis via the input and the output measurements. The advantage of these methods is that they can be used to model complex and multidimensional systems. However, these black box-based controllers require a large amount of experimental data.

The opposite is true for model-based controllers. These controllers are developed using a set of equations specifically modelling the physical behaviour of the system; therefore, representative models of SMA wires are used.

The model of the complete system can be used as an additional feedback to a VSC controller to improve the position tracking. In the work by Elahinia et al. [78], Liang's SMA model has been used to describe the SMA behaviour. In that work, it has been experimentally verified that this controller is fast and robust in the face of parameter uncertainties and unmodelled dynamics, capable of rejecting disturbances.

Modelling of the system can also be useful in order to incorporate in the controller loop estimators for unmeasured variables.

For example, based on the input-output feedback-linearisation method, a nonlinear controller has been developed by Abiri et al. in order to control the output force of a SMA spring actuator [79]. First, the state-space model of the actuator, based on Brinson's SMA model, was verified by some open loop experimental tests. The controller implementation has been tested using the simulated actuator, which allows exploiting a complete knowledge of all the state variables that can be included in the control loop. The authors conclude their paper by observing that, in order to be able to test the controller on a real system, a nonlinear observer would be required to estimate the state variables that cannot be measured directly (such as the martensite fractions). That is left for future investigation.

Zhang et al. proposed a modified feedback-linearisation scheme for the control of the displacement d , consisting of three parts: feedback linearisation block, active modelling and outer-loop controller [80]. In this control scheme (Figure 18), a Kalman filter estimates the state vector $x = (T - T_{amb}, d, \dot{d})^T$ and the corresponding modelling errors $f = (f_1, f_2, f_3)^T$, considered as constant and noisy unknown parameters. Compared to conventional State Feedback Control (SFC), the proposed AM-SFC has reduced the absolute tracking error, thanks to active modelling, capable to eliminate the negative influences caused by the uncertainties in SMA dynamics.

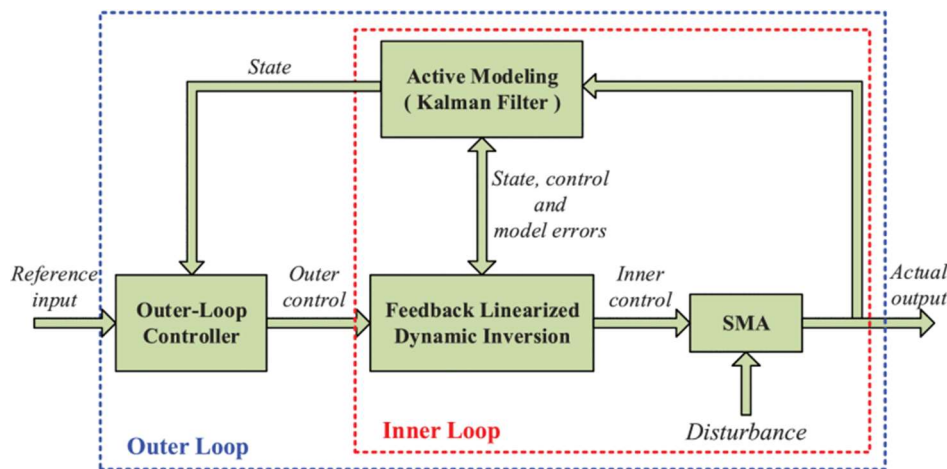


Figure 18 – Scheme of a modified feedback linearisation control consisting of three parts, feedback linearisation, active modelling and outer-loop controller [80]

3.4. Conclusions

In this background chapter, I have shown the peculiar characteristics of shape memory alloys, highlighting their unique functional characteristics and their complex behaviour.

They will be at the core of the study that I present in this thesis. The possibility to select the most promising composition, optimise its inherent nonlinear hysteretic properties and address its combination with other materials to produce improved soft actuators will be assessed by simulations and experiments in the next chapters.

Here, I tried to summarise some of the most relevant prior knowledge about modelling and control strategies, which will be essential to tackle the intermediate goals that I shall pursue, providing a brief overview of those works that I have considered and selected as sources of inspiration for my proposed solutions.

CHAPTER 4

Selection and optimisation of the shape memory wire

Every time SMAs are employed for a particular application, it is important to optimise their functional properties in order to comply with the required working conditions, and the field of soft actuation is no exception. Among the main factors affecting SMA performance there are the element shape, the alloy composition, the level of cold working, the characteristics of the heat treatment, and the process of (thermo)mechanical conditioning. From the analysis of the literature in Section 1.2, and considering the advantages in terms of forces, different loading conditions, high surface to volume ratio and possibility to be formed into varied shapes, the SMA in the form of a wire was selected as reference design element in this project. As described in Section 3.1 the composition of a shape memory alloy affects its transformation ranges. In this work of thesis, we decided to consider binary and ternary compositions based on the NiTi e NiTiCu systems, which are well-established alloys with good functional properties, and are easily available on the market. Following a short-listing of the wires at our disposal, cold drawing has been applied to the most promising batches. With a suitable reduction in the wire cross-section, the grain size is maintained or refined, and a suitable work hardening (increase in dislocation density) is produced. Not only does the presence dislocations result in strengthening, but the internal elastic stresses developing around the dislocations also produce pinning of the microstructure and help material shape recovery by facilitating the reverse martensitic transformation from martensite to austenite. Alongside the mechanical processing, the ageing treatment is also fundamental: it is employed to set SMA wire into the desired reference shape, and to optimise the mechanical behaviour at the same time. This process, combined with cold-working, has a great influence on the material transformation parameters, such as the transformation temperatures.

Mechanical conditioning was used to stabilise the cyclic behaviour of several different samples, that were then mechanically tested, in order to compare their characteristics, select an optimised wire and determine its properties.

4.1. Specifications and choice of the wire diameter

The aim of this work is to investigate generalisable aspects in the optimisation of SMA-based soft robots to be used at room temperature. For this reason, it is essential to choose a material that has transformation temperatures compatible with this requirement, i.e. that will be martensitic in ambient conditions, and austenitic above room temperature. Furthermore, the temperature required for the wire to transform into austenite phase under a reasonable load must be compatible with the thermal working range of the soft matrix, and must be as low as possible, to avoid wasting energy. Moreover, a small hysteresis can help obtain a fast transformation and limit energy losses.

Regardless of the exact characteristics of the soft actuator, a SMA wire contained within it as a functional element will have to display an optimal shape-setting and a good cycling stability.

Furthermore, we shall require that the material should have a recoverable transformation strain in the range of, or somewhat higher than 2 % at 200 MPa. For an actuator the size of some centimetres, this specification is expected to enable the achievement of strokes in the range of up to some millimetres, and the displacement of masses of several tens or hundreds of grams, depending on the loading direction. Requiring the material to work at larger strains or stresses may limit its fatigue life [12].

Finally, considering the combined effects of supply power density and wire surface-to-volume ratio on heat transfer, it is easy to see that, for decreasing wire diameters, both the energy expenditure required for heating up the wire into the austenitic range and the time required for cooling it down into the martensitic one decrease. At the same time, for a given stress sustained by the wire, wires of larger diameter can manage higher forces.

In the light of this preliminary analysis, it was decided that a diameter of 0.65 mm would account for most aspects. Furthermore, a wire with this diameter can be suitable for working both in tensile and in bending conditions, expanding the validity of some conclusions of this work to the fabrication of different types of soft actuators.

4.2. Initial material selection

Four materials batches, of various compositions (NiTi and NiTiCu) and in the form of wires, were identified in the repository of CNR-ICMATE as having nominal (labeled) A_s temperatures above approximately 60 °C. As a further constraint, the diameters were chosen large enough to be able to carry out the subsequent cold drawing process. In order to make a first selection, the actual transformation temperatures were investigated. In order to be characterised by Differential Scanning Calorimetry (DSC) without defects, specimens from each of the four batches were solution-annealed. This particular heat treatment, conducted at very high temperature (say, above $0.6 \cdot T_m$, where T_m is the melting temperature) for a long time duration (one or several hours), aims to relax all internal stresses, bring all the material into the austenitic phase, dissolve secondary phases and precipitates, and reduce the number of defects. Practically, specimens of these materials were cut from a larger coil and placed in a quartz vial. To reduce reactions with the air, in particular with oxygen, vacuum was created in the vial before it was filled with argon. After being sealed, the vial was heated to 800°C in a kiln, and after 60 minutes, it was quickly removed and broken in a water bath to rapidly quench the samples.

Calorimetric analyses were conducted with TA Q100 DSC with decreasing and increasing temperature ramps at 15 °C/min, scanning the -40–140 °C range. The measured transformation temperatures of the four samples are listed in Table 1. Wires S1 and S2 had martensitic transformation temperatures too low for use at room temperature. For this purpose, M_f temperature ought ideally to be higher than room temperature. Moreover, it is important to highlight that for the conventional cold-worked and aged materials the thermal hysteresis between the transformation temperatures is increased, with lowered M_f and raised A_f . For this reason, only SCu1 (NiTiCu₆) and S4 (NiTi) wires have been deemed suitable for our purposes. Furthermore, these two wires have an A_f temperature that is not too high for use inside polymeric matrices. Finally, it can be noted that the hysteresis of the SCu1 (NiTiCu₆) wire is clearly lower than the others (all NiTi compositions). This is a typical effect of the Cu substitution (for Ni), which is also known to produce a decrease in the transformation stresses and an overall increase in the transformation temperatures [50].

Table 1 - Details of the four wires procured. In addition to the characteristic temperatures for the martensitic transformation, the temperature values at which the peak of the phase transformation is positioned are reported (subscript p). The temperatures were obtained by DSC after solution-annealing treatment (all temperatures are reported in °C). SCu1 and S4 were finally selected for the next heat treatment step.

ID	ϕ [mm]	Mf	Mp	Ms	As	Ap	Af	DeltaH	Producer code
S1	1	7,1	13,1	20,7	38,5	46,5	50,4	33,4	S46/06
S2	1,3	14,7	25,7	34	48,8	62	68,9	36,3	S35/07
SCu1	1	46,9	53,4	62,3	65,1	73,8	79,5	20,4	Kyokalloy
S4	1	55,2	65,9	78	87,5	103,2	112,7	37,3	S3/07

4.3. Shape setting and ageing process

The two selected wires were supplied from the producer in cold-drawn state, and then they were required for our study to be further cold drawn to the desired diameter of 0.65 mm. Since the two selected materials have the same starting diameter of 1 mm, the same procedure for cold drawing was adopted to reach a final cross-section reduction of 42 %.

The as-received wires were first thermally annealed at 680 °C for 10 minutes and then the diameter was reduced by 0.05 mm steps down to 0.85 mm. Then a further thermal annealing was necessary before the final stepwise cold reduction of the diameter down to 0.65 mm. Ageing was carried out in an electric kiln at four different temperatures (430 °C, 445 °C, 460 °C, 475 °C).

To estimate the optimal duration for each ageing temperature, I used a method we developed in a previous work for 1 mm Ni-rich NiTi wires [81]. Briefly, the specimen electric resistance is monitored during an extended heat treatment at a set temperature: the appearance of typical features in the measured signal mark the achievement of optimal ageing, in terms of mechanical properties, functional stability, and shape setting.

According to that method, a constant test current equal to 1 A was injected into each specimen during ageing and the resulting voltage was measured continuously for the entire treatment duration (1800 s). The jig used for heat treatments is shown in Figure 19. It held the wires taut under a nominal strain of 3 %.

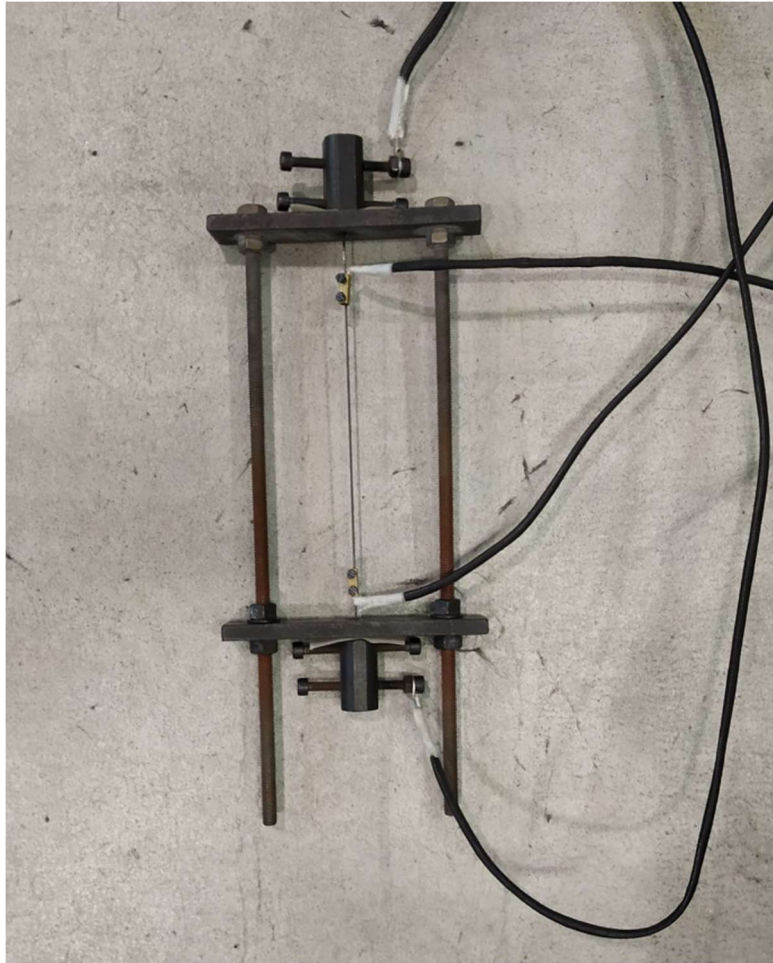


Figure 19 - The jig employed to heat treat (ageing) the SMA wires.

The electric resistance signals that have been calculated are shown in Figure 20 for SCu1 specimens and in Figure 21 for S4 ones. A critical latency (D point) has been identified for each measurement, where the signal starts to decrease after a trough and a plateau. The D-latency values obtained were used to set the durations of subsequent shape-setting experiments of separate samples (Table 2). The D-latency was in fact reported to mark the achievement of optimal ageing [81].

It is worth mentioning that the method described was originally developed for the optimisation of ageing in Ni-rich NiTi. This is the first report of the application of the same approach to non-Ni-rich NiTi samples. With the present materials it is possible that the limited availability of Ni in the composition could lead to altered precipitation kinetics with some effects on the mechanical behaviour. It was made an initial hypothesis that these alloys could be nonetheless studied using the original unchanged methodology.

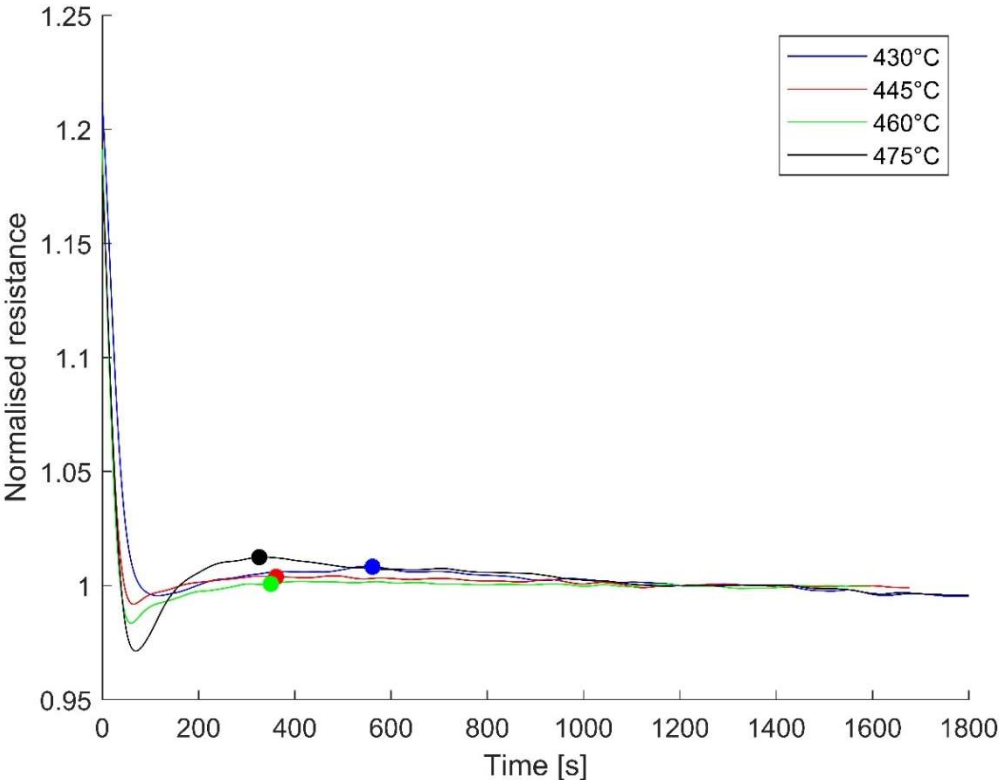


Figure 20 - Electric resistance measurements to determine optimal ageing duration. These measurements refer to samples of the SCu1 alloy aged at different temperatures.

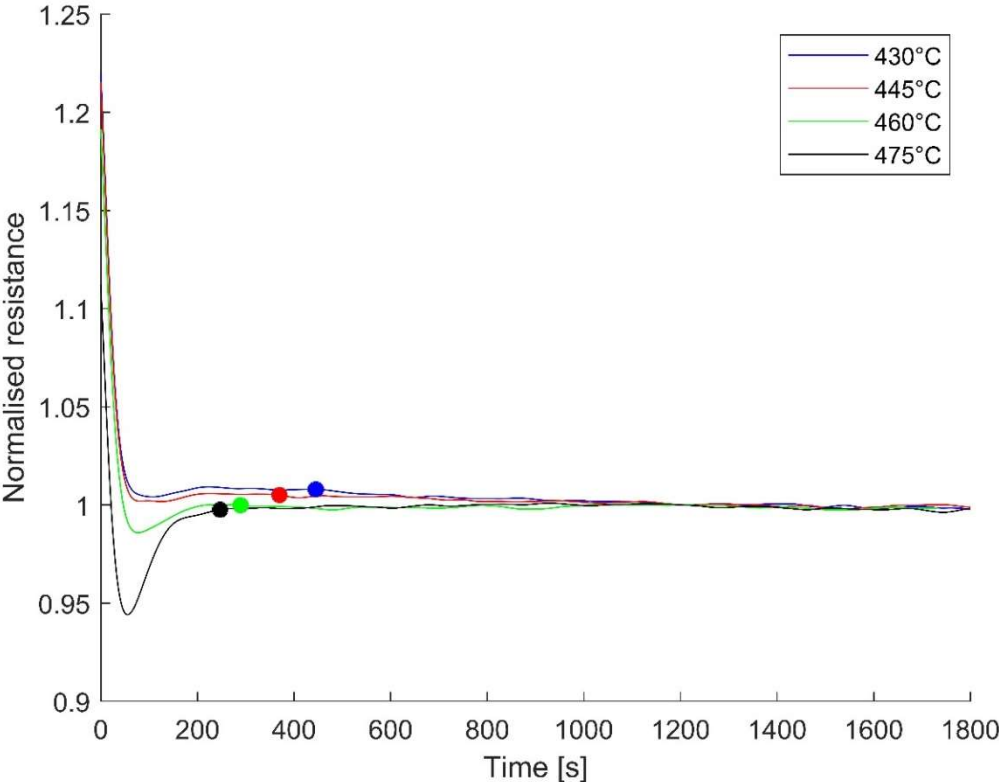


Figure 21 - Electric resistance measurements to determine optimal ageing duration. These measurements refer to samples of the S4 alloy aged at different temperatures.

Table 2 - Durations of subsequent shape-setting experiments of separate samples for the four chosen temperatures, obtained evaluating the D-latency points.

	SCu1	S4
430 °C	561 s	445 s
445 °C	361 s	370 s
460 °C	350 s	261 s
475 °C	326 s	247 s

4.4. Final selection of the SMA material and of the optimal heat treatment

After the different heat treatments were carried out at different temperature, each with a duration determined by the measured D-latency, the samples were characterized by DSC and mechanical measurements. The goal was to observe the effect of the heat treatments on the transition temperatures and mechanical characteristics. To obtain a sufficient transformation of the parent phase into martensite during cooling, the temperature M_f should theoretically be higher than room, but considering that in actuation applications non-zero stresses will be present (raising the transition temperatures), M_f may be acceptable even if very close to or even slightly below ambient temperature. A reason why looking for an M_f not significantly higher than ambient temperature may be appropriate is that, if it were too high, also the other transformation temperatures would be increased, realistically. Such a case, in turn, would not be optimal because, the higher the A_f temperature, the higher will be the energy required for the actuation.

The results of the calorimetric analysis are shown in Figure 22 for the SCu1 samples and in Figure 23 for the S4 ones. The measurements were conducted with a TA Q100 DSC with a temperature ramp of 15° C/min between -20 °C and 100 °C or between -20 °C and 120 °C, depending of the expected A_f .

Considering the SCu1 material the transformation temperatures obtained varying the ageing conditions are all very similar, and the A_s temperatures are all above ambient temperature. The peaks of samples heat treated at 430 °C and 445 °C are quite broad and spread over a wide range of temperatures. It is possible that this characteristic has to do with an incomplete

reduction of the cold-working stresses, or that the SCu1 material undergoes a two-step transformation, which is described for Cu substitutions above 5 %. In this latter case, we should have to assume that the orthorhombic phase transition is very close to the monoclinic transition, so that the two exothermic transformations overlap and give rise to only one peak. Samples heat treated at 460 °C and 475 °C exhibit narrower peaks and M_f temperatures slightly above ambient temperature. For these reasons these two samples seem to be the best candidates, but also the other two have sufficiently good characteristics.

On the other hand, the S4 alloy presents two distinct peaks in the DSC signal since it exhibits a significant rhombohedral phase transition prior to the final transition into the monoclinic martensitic phase, which is especially visible in the cooling branch. If we assumed to exploit mainly the rhombohedral transition for the actuation, it is possible to observe that the transformation temperatures are significantly above ambient temperature in all cases. However, the rhombohedral transformation only provides very limited, albeit very stable, transformation strains. Therefore, in order to exploit also the monoclinic transition, at least partially, it is expected that higher bias stresses will be required. Moreover, it should be observed that the A_f are approximately 30 °C higher than the values obtained for SCu1 samples, implying greater energy requirements for actuation.

Among the S4 samples, the ones thermally treated at higher temperatures are the most promising, since they exhibit the narrower DSC peaks and a smaller overall hysteresis.

In general, SCu1 exhibited more suitable transformation temperatures for room temperature actuation. However, in order to make a more thoroughly-informed choice, mechanical measurements were also carried out on all the samples of both alloys.

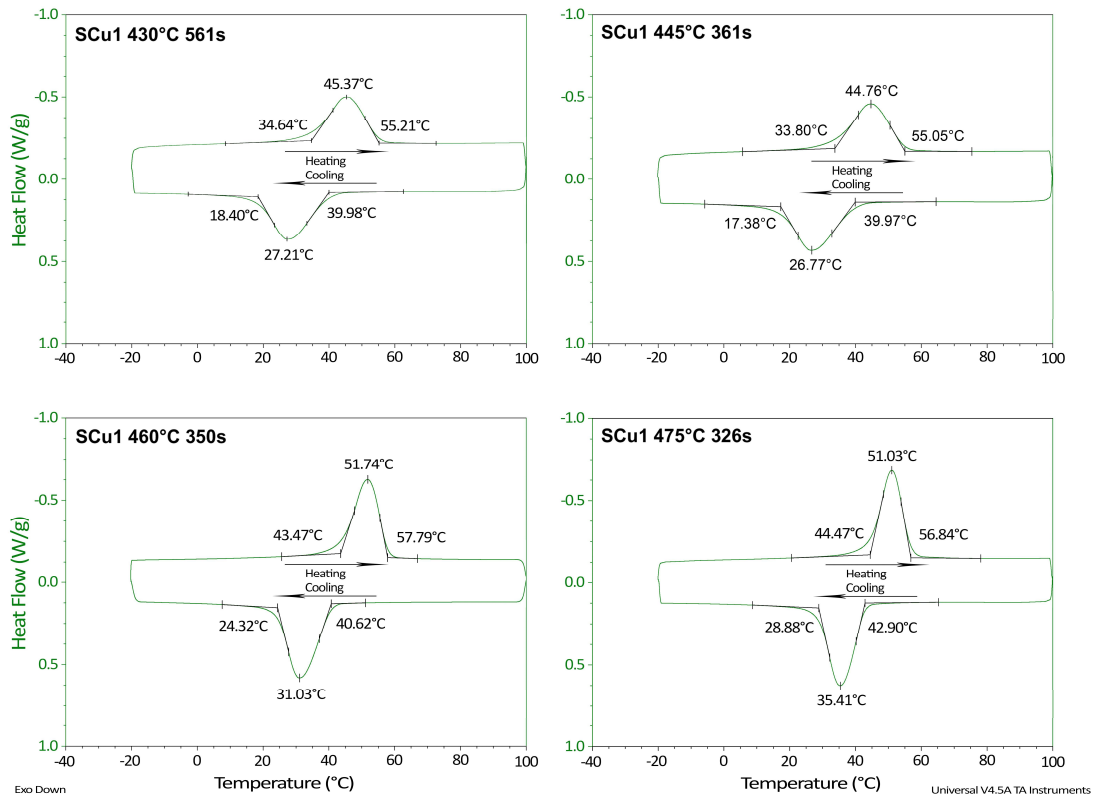


Figure 22 - SCu1 (NiTiCu₆) DSC curves for different heat treatment temperatures at the previous selected durations.

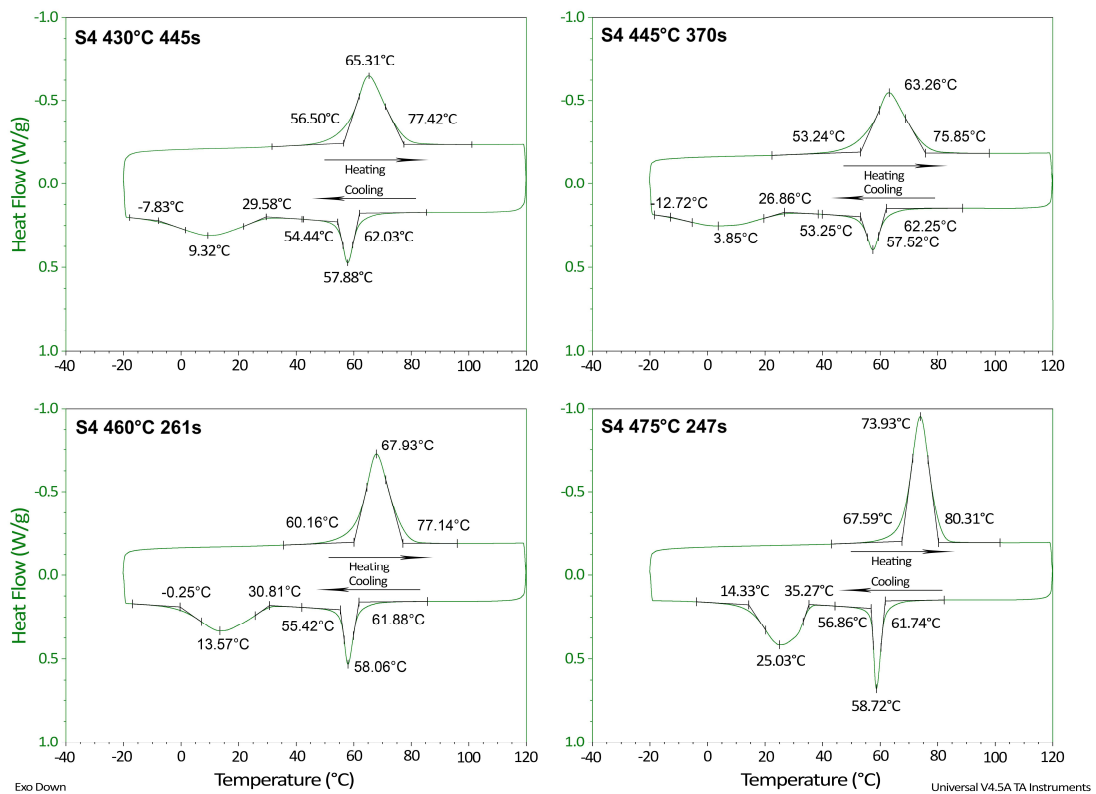


Figure 23 - S4 (NiTi) DSC curves for different heat treatment temperatures at the previous selected durations.

Mechanical tests were carried out with an axial and torsional machine for dynamic-mechanical tests (Instron® ElectroPuls E3000); it is also equipped with a thermal chamber that can heat or cool the sample under study.

Measurements were carried out on S4 (NiTi) and SCu1 (NiTiCu₆) wire samples that were thermally treated as shown in previous section (Table 2).

Initially, every sample was characterised with progressive quasi-static tensile cycles, in which at every loading-unloading cycle, the maximum strain is increased, starting from 1 % and finally reaching 5 %. These tests were conducted at a temperature equal to the sample $A_f + 10$ °C, i.e. 90 °C for the S4 alloy and 66 °C for the SCu1 alloy.

From the pre-stabilisation pseudoelastic behaviour, two thermal treatments of the S4 material had to be discarded, namely 460 °C for 261 seconds and 475 °C for 247 seconds. In fact, it is possible to observe in Figure 24 that upon unloading the residual strain is excessive for both samples. This effect was not completely expected, and is compatible with a poor resistance to plastic flow onset. Since the strain hardening phase was surely effective (42 % reduction produces high hardening in NiTi), the instability has to be dependent on some aspect of the heat treatment. It is possible that the point on the resistance curve that was here identified as the D-latency does not correspond, for a Ni-leaner alloy as this one, to an optimal precipitation of strengthening secondary phases (e.g. Ni₄Ti₃). The treatment duration applied at the higher temperatures (460 °C and 475 °C) was likely more than sufficient to produce abundant recrystallisation, while even longer ageing times would have been required to support effective precipitate growth. A balance of the two mechanisms was possible only for the lower treatment temperatures (especially 430 °C), at which recrystallisation takes longer to occur. A limited synergy between recrystallisation and precipitation was observed also for Ni-rich NiTi in the original paper [81], but for much higher ageing temperatures (above 600 °C).

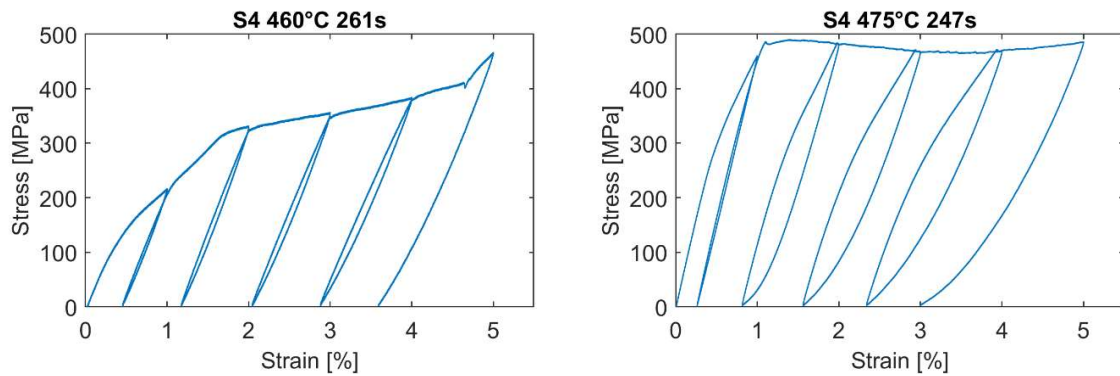


Figure 24 - Progressive quasi-static tensile cycles at high temperature for the two S4 specimens discarded (heat-treated at 460 °C and 475 °C).

The short-listed samples underwent further mechanical tests. In particular, it was interesting to observe the stabilisation of the pseudoelastic behaviour for both materials, and to analyse the characteristics of the stress-strain cycle after the stabilisation has occurred. The stabilisation required 50 tensile cycles up to 3 % strain at $A_f + 10$ °C. The quality of the post-stabilisation characteristics was used as the ultimate parameter to identify the best thermal treatment for the materials. In particular, I looked for good cyclic stability, small hysteresis, as well as a low residual strain.

The post-stabilisation measurements obtained at high temperature ($A_f + 10$ °C) are reported in Figure 25 for the two short-listed S4 samples, and in Figure 26 for all the S4Cu1 samples. These figures reveal the pseudoelastic mechanical behaviour of the samples and it can be seen that especially when increasing the strain, the curves look rather different.

For the S4 material, only the sample heat treated at 430 °C shows good cyclic stability and a low residual strain. In general, for S4Cu1 material, a low residual strain is obtained. The sample that shows the best cyclic stability is the one heat treated at 460 °C.

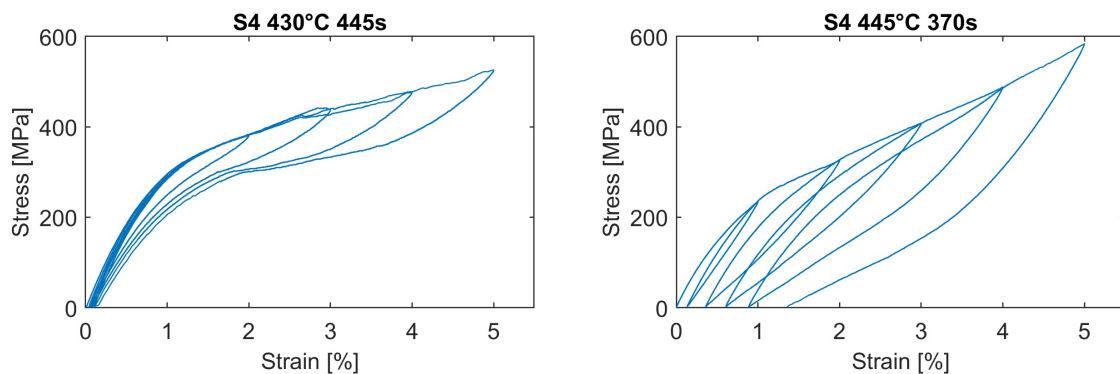


Figure 25 - Results of the progressive quasi-static tensile cycles at high temperature for the two S4 specimens heat-treated at 430 °C and 445 °C.

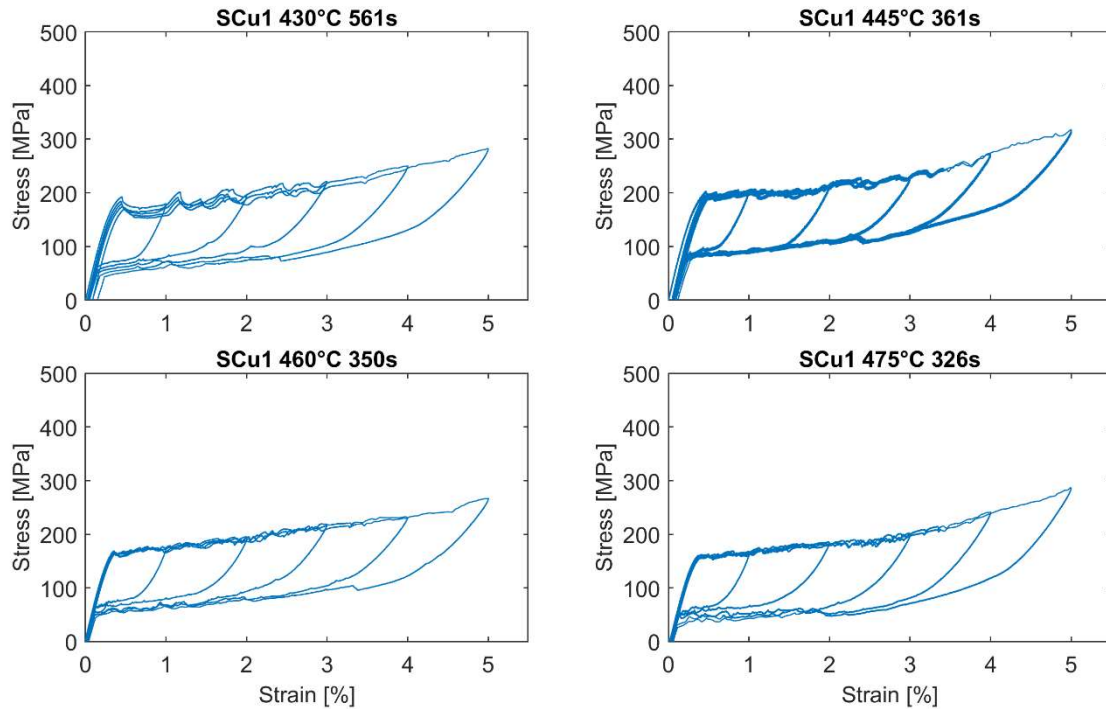


Figure 26 - Results of the progressive quasi-static tensile cycles at high temperature for the four differently heat treated SCu1 specimens.

The post-stabilisation measurements at low temperature (25 °C) are reported Figure 27 and Figure 28. In this case we observe the stresses required to deform the martensite. It is possible to notice a significant difference between the S4 and SCu1 materials in terms of the stress level reached by the curves for the same strains. Among the SCu1, the samples heat treated at 460 °C and 475 °C have lower stress levels. This means that for these samples it is easier to deform the martensite and this could be convenient for the integration of the SMA in a soft matrix and to guarantee large strokes for an actuator.

It is worth mentioning that the curves of Figure 27 and Figure 28 represent relationships between strains and stresses, once any null-stress “self-strain” has been subtracted. This clarification is necessary, because non-negligible two-way shape memory behaviour was noticed in the post-stabilisation SCu1 samples. As a side-effect of the stabilisation cycling, the NiTiCu ternary alloy is indeed prone to develop that feature: upon cooling from the austenitic range, the sheer thermally-driven martensitic transformation (i.e. even under null stress), is sufficient to determine the appearance of a finite strain (as referred to the reference shape-set length of the unstressed austenite). The curves of Figure 27 and Figure 28 were obtained taking the martensitic length as reference and calling that null-strain condition. All the reported strains are therefore related to the application of the load alone and do not include the self-strain produced by the two-way shape memory effect.

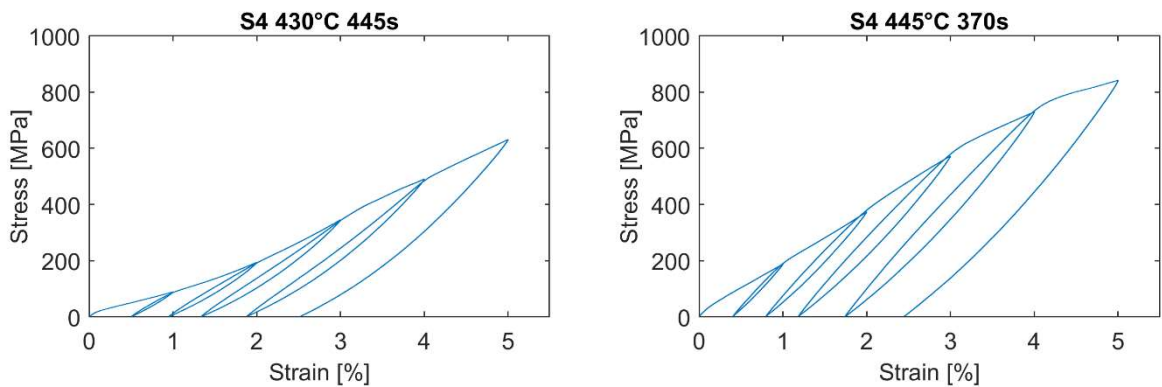


Figure 27 - Results of the progressive quasi-static tensile cycles at low temperature for the two S4 specimens heat-treated at 430°C and 445°C.

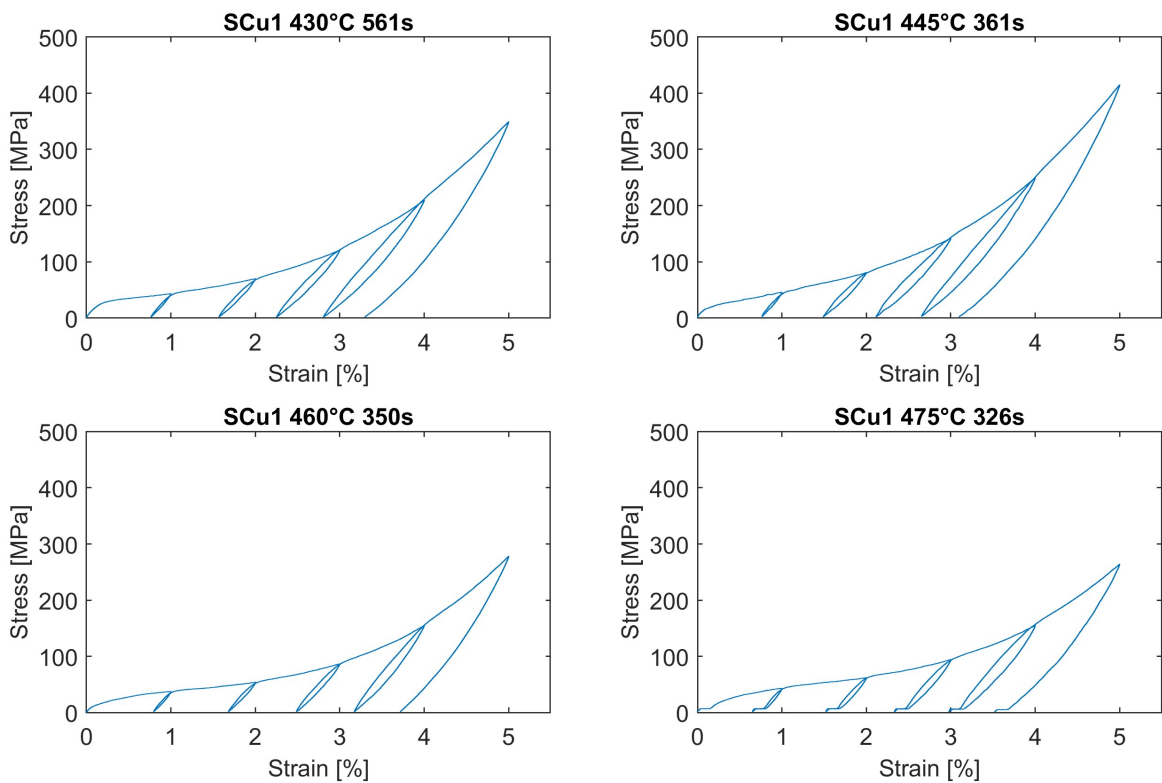


Figure 28 - Results of the progressive quasi-static tensile cycles at low temperature for the four differently heat treated S4Cu1 specimens.

Combining all the observations made about the results of the tests, and especially considering the position and small hysteresis of the transformation temperatures obtained from the calorimetric analysis, and the stable and suitable mechanical behaviours at low and high temperatures, the S4Cu1 alloy heat-treated at 460 °C for 350 seconds was finally selected as the most appropriate material for our current purposes.

4.5. Testing of functional actuation capability and material parameter identification

Strain recovery tests were employed to study the functional range of actuation of the selected wire. Measurements were taken at different constant stresses, i.e. in isotonic conditions, observing the strain variations produced by changes in temperature (Figure 29). For these tests, Instron® ElectroPuls E3000 was utilised. Ascending and descending temperature ramps from 20 °C to 100 °C were applied at 10 °C/min. The test was repeated for different axial loads. The stress was maintained constant at 50, 100, 125, 150, 200 and 300 MPa.

Strain recovery tests are effective in highlighting the functional characteristics of SMA elements under the combined action of temperature and loading, and are an important source of quantitative information about the constitutive parameters of the material in working conditions.

From these measurements I graphically extrapolated the starting and finishing temperatures of the direct and inverse transformations for each load value. In Figure 29, the four critical temperatures can be read as the abscissae of the points taken at the intersection between the tangents (not shown) to the quasi-linear tracts of each curve on either side of the major slope changes. The four critical points related to each measurement are coloured in the same hue as the corresponding curve.

In addition to the actuation temperatures, some interesting information about the mechanical actuation capabilities of the wire can also be extracted with this type of measurement. The most important is the range of usability of the material. In fact, it can be noted that for a stress of 300 MPa the transformation strain is not fully recovered during the heating cycle.

Comparing the results of the strain-recovery tests with the mechanical tests of Figure 28, it can be seen that, for similar values of stress, the strain values at ambient temperature are considerably higher. This occurs because in the strain-recovery measurements the effects of two-way memory are not compensated for, so the presence of the self-strains is accounted for in this description of the functional behaviour of the wire.

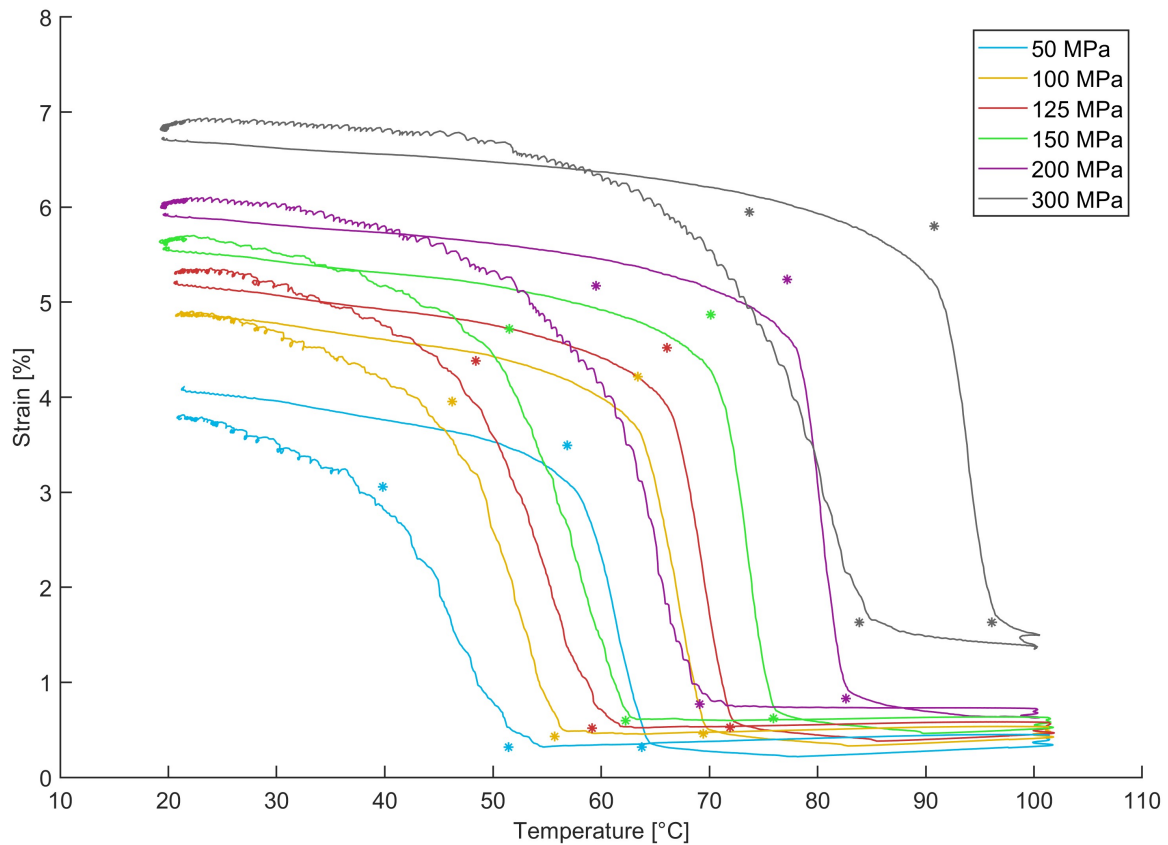


Figure 29 - Strain recovery curves obtained for different isotonic conditions. The abscissae of the points marked by circular dots correspond to the transformation temperatures. The positions of the points were obtained using the method of tangent intersections applied to the curves of the same colour.

From the strain-recovery curves, it is also possible to derive information also about the values of the Clausius-Clapeyron coefficients. The critical temperatures extracted from strain recovery curves, as explained above, are reported in Figure 30 as functions of the applied stress. The slopes of the interpolating linear fits provide the required coefficients. They have been calculated as the inverse of the mean between the slopes of the two lines referred to the critical temperatures of the direct transformation and of the two lines referred to the inverse transformation. They were found equal to $C_A = 7.49 \text{ MPa}/^\circ\text{C}$ (for austenite) and $C_M = 7.43 \text{ MPa}/^\circ\text{C}$ (for martensite). Using the same fitting lines, a second approximation of the transformation temperatures at zero stress can be derived, which is determined from functional rather than calorimetric (DSC) tests. In particular, here we obtained $M_f = 32.1 \text{ }^\circ\text{C}$, $M_s = 43.2 \text{ }^\circ\text{C}$, $A_s = 49.8 \text{ }^\circ\text{C}$, $A_f = 56.6 \text{ }^\circ\text{C}$.

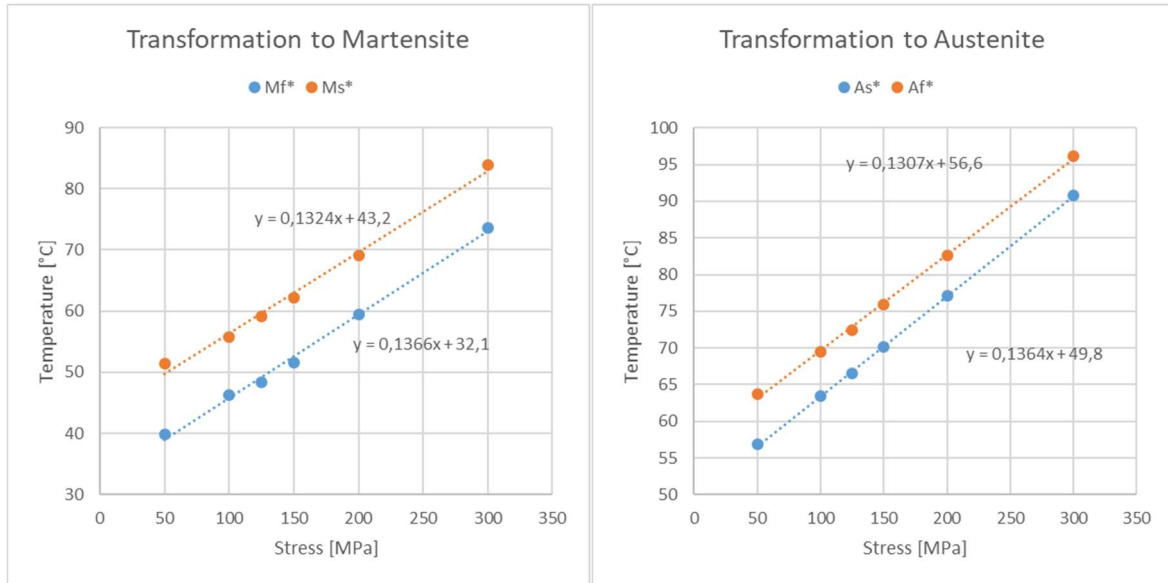


Figure 30 – Dependence of the transformation temperatures on the applied stress. The lines are linear fits of the data, and are accompanied by the corresponding equations.

Additional constitutive parameters required to inform the models of Chapter 6 can be more easily determined from the isothermal tensile measurements in pseudoelastic regime, especially because they are not affected by the effects of two-way memory. The post-stabilisation curve was used to identify the remaining mechanical parameters of the SMA wire through graphical interpolation, as seen schematically in Figure 31. Firstly, we evaluated the transformation strain ϵ_L as the length of the detwinning plateau. A first estimate of this parameter was 4.2 %. Then, we evaluated the (effective) Young’s moduli of austenite and martensite by estimating at the slopes of the linear tracts at low (loading) and high (unloading) stresses respectively. We estimated $D_A = 56$ GPa and $D_M = 10$ GPa.

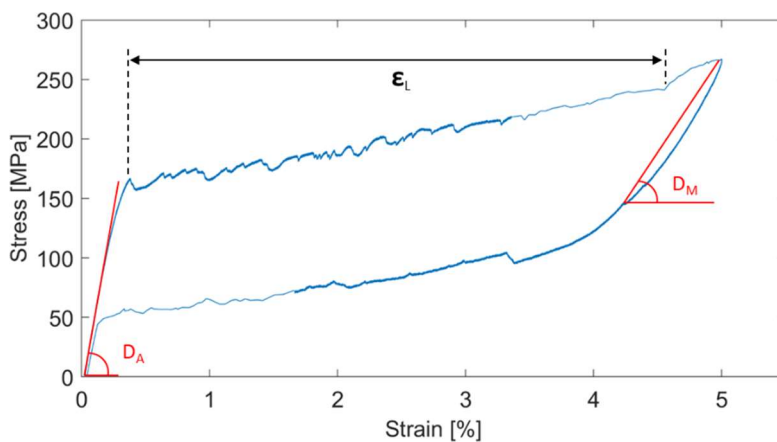


Figure 31 - Parameter estimation from stress/strain graph.

All the values extracted from the experimental tests, reported in Table 3, will be further optimised by simulating the system behaviour using a modified version of Brinson's model (Chapter 6) and fitting the measured set of strain-recovery curves with the simulated ones.

Table 3 – Values of the constitutive parameters extracted from the experimental tests for the chosen NiTiCu wire.

Parameter	Value
M_F	32.1 °C
M_S	43.2 °C
A_S	49.8 °C
A_F	56.6 °C
ε_L	4.2 %
D_A	56 GPa
D_M	10 GPa
C_A	7.49 MPa/°C
C_M	7.43 MPa/°C
L_h	16.18 J/g

4.6. Conclusions

In the light of the results of a multimodal physical and mechanical characterisation of different material samples, the ternary NiTiCu₆ alloy has been finally selected for the current project. The heat treatment was optimised for smallest hysteresis in order to have fast transformation and low energy losses. The wire was stable after 50 tensile cycles. With thermomechanical processing it was also possible to obtain two-way shape memory training, which is expected to have a positive effect on actuation (position reset upon cooling). The mechanical performances met the requirements of sufficient available strain (> 2 %) at 200 MPa. Furthermore, the low level of the martensite detwinning stress is expected to couple well with a possible biasing action of a soft matrix aiding the re-setting of the device position upon cooling.

The identification of the material functional parameters by physical and mechanical characterisation has been carried out completely and forms a basis for the modelling of the SMA wire, which will be carried out in the next chapters of this work.

CHAPTER 5

Matrix modification

In order to optimise soft actuators based on SMA embedded in a polymeric matrix one of the possible strategies, that have been applied here, is the functionalisation of the matrix itself.

Samples of silicone rubber modified with carbon fillers have been produced with the primary objective to obtain improvements in heat transport properties; secondly, the samples produced were characterized to evaluate their mechanical and electrical characteristics.

The functional effects on the performance of the soft actuator produced by the modification of the soft matrix are addressed in Chapter 8 together with an analysis of the thermal interaction between the two materials (SMA and soft matrix).

5.1. Introduction

As shown in Section 1.2, many of the soft actuators described in literature include a polymeric matrix, often embedding the SMA element, whose main functions are creating an interface towards the external world, and providing some level of bias action. Commonly, the matrix will have to allow broad deformations, in order to adapt to the shape changes that the SMA element undergoes, so elastomers such as silicone rubber [14]–[17], [20], polyurethane [82], [83] or 3D printed rubber-like photopolymers [27], [31], are often employed for the purpose.

As explained in Section 1.3, the modification of the matrix is one of the possible methods to optimise the performance of the multimaterial actuators. Only few groups [36] have explored that kind of strategy. Polymeric matrices have very interesting characteristics for interfacing the environment and the objects that the actuator is to act upon. They generally tend to have

medium-to-low stiffnesses and poor thermal and electric conductance, which may be limiting factors for certain applications.

The modification or improvement of those characteristics can be achieved by material engineering techniques, i.e. often by the addition of fillers. In some cases, the fillers will change more than one of those properties, so it is important to find appropriate ranges and types of modifications that suit different applications balancing correctly the property changes.

5.2. Choice of the polymer matrix

Among the polymers commonly used as matrices in soft composites, silicone rubber (polydimethylsiloxane, PDMS) was selected as the most suitable material for the purposes of the present study. Firstly, one of the main advantages of PDMS is the good deformability, which allows its reshaping in a great variety of configurations, and the accommodation of large strains. Furthermore, with a correct manufacturing method, the silicone wets the metal surface well without voids or air bubbles. Therefore, compared to other polymers, it allows for good heat transfer properties at the interface with the SMA material. It has a rather high friction coefficient with respect to most material surfaces, which enables secure grip for grasping and holding objects. When cast, it takes readily the shape of the mould, retaining even fine details. It can be extracted easily from moulds because naturally it does not stick to most metals and plastics. Moreover, silicone rubber is characterised by an excellent self-adhesion capability, both in fresh-on-fresh and fresh-on-cured conditions, which is a crucial feature in view of the production of devices by stepwise moulding-and-assembling. In addition, an important benefit connected to the use of a silicone rubber matrix is the possibility to modify it, e.g. by addition of fillers or additives, to obtain the desired functional properties in the composite material.

The selected silicone rubber was the Ecoflex™, which is available with Shore hardnesses ranging from 00-30 to 10-A. Ecoflex™ rubbers are platinum-catalysed silicones that are versatile and easy to use. In fact, the curing procedure to induce the cross-linking of polymer chains is not complex. Ecoflex™ rubbers are mixed 1A:1B by weight or volume and cured at room temperature with negligible shrinkage. Low viscosity ensures easy mixing and de-

airing. A further advantage of the chosen silicone rubber is its biocompatibility, which allows the development of devices that can come into contact with the human body.

Ecoflex™ with a low Shore hardness of 00-30 was selected for the present application, anticipating that the fillers would have the effect to raise the mechanical properties. An overview of its characteristics is shown in Table 4.

The chemistry of Ecoflex™ curing, being based on Pt-catalysis, is expected to be based on the condensation of vinyl-terminated polysiloxane and Si-H containing polysiloxane, through the hydrosilylation reaction (Figure 32). [84].

Table 4 - Ecoflex™ 00-30 technical sheet.

Parameter	Value
Specific Gravity	1.07 g/cc
Specific Volume	0.935 cm ³ /g
Pot Life	45 minutes
Cure Time	4 hours
Shore Hardness	00-30
Tensile Strength	1.379 MPa
100% Modulus	69 kPa
Elongation @ Break	900 %
Die B Tear Strength	38 pli
Shrinkage	<.001 mm / mm
Mix Ratio By Volume	1A:1B
Mix Ratio By Weight	1A:1B
Colour	Translucent
Useful Temperature (min)	-18 °C
Useful Temperature (max)	232 °C
Mixed Viscosity	3,000 cps

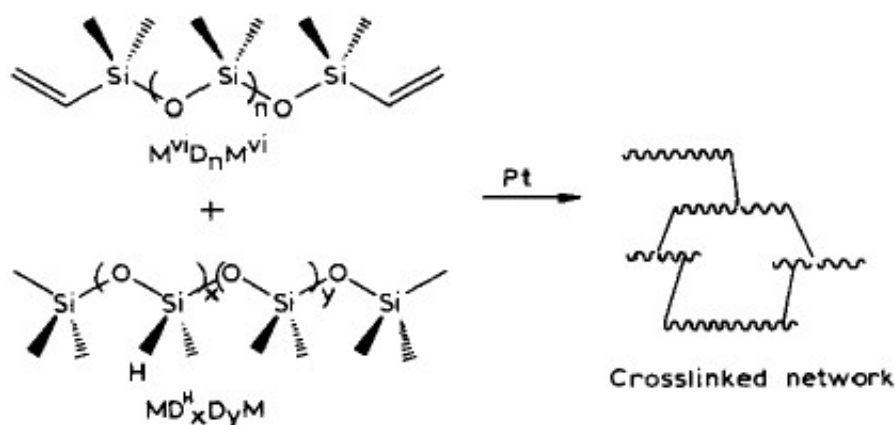


Figure 32 - The cross-linked network is created by the addition of platinum to a mixture composed of a difunctional vinyl-containing polydimethylsiloxane and the multifunctional Si-H containing copolymer of polydimethylsiloxane and methylhydrogen siloxane [84].

Practically, the silicon-hydrogen (Si-H) bond is added in correspondence of the terminal unsaturated carbon-carbon double bond ($H_2C=C$) of the vinyl-terminated polysiloxane. This results in the formation of a silicon-carbon (Si-C) bond. The hydrosilylation reaction can occur only with the addition of a platinum catalyst such as Pt(0) complex containing vinyl-siloxane ligands. Moreover, some inhibitors including maleates and fumarates are usually present to control the Pt-mediated polymer curing reactions but their presence inhibits also the hydrosilylation, and hence crosslinking, at low temperatures. On the other hand, the addition of inhibitors accelerates the reaction at higher temperatures [84].

The fact that Ecoflex™ cross-links in this way was indirectly verified by analysing the base components and the cured rubber. A qualitative analysis by means of infrared vibrational spectroscopy (FT-IR) has been performed on the two components A and B and on a sample cured mixture using a Nicolet Nexus FT-IR spectrometer coupled with a ThermoElectron Continuum IR microscope (Thermo Fisher Scientific, Waltam (MA), USA).

The aim was to identify which component contained Si-H bonds, possibly which one included the carbon-carbon double bonds, and to verify that the peaks related to those moieties show a decreased intensity after the reaction.

The FT-IR spectra (Figure 33) were recorded on samples deposited on aluminium foil in Attenuated Total Reflectance mode (ATR) using a silicon tip single bounce ATR accessory attached to the microscope objective (128 scan, 4 cm^{-1} resolution). The red plot - spectrum of component B – shows weak absorption peak at 2160 cm^{-1} . This absorption corresponds to the characteristic wavenumber of the Si-H bond stretching vibration [85]. The spectrum of the component A does not show a peak at that position, therefore, it is possible to say that

the component B is the only one containing Si-H bonds. The other component could be identified as the base polymer containing the terminal carbon-carbon double bonds. Unfortunately, in component A, the presence of this kind of bond could not be confirmed through FT-IR analysis. In fact, the dipole transitions associated to vibrations localised on the vinyl bonds are usually quite weak, especially the ones related to stretching modes [85], and the number of the vinyl groups is limited since they are in the terminal positions of the polymeric chains.

Looking at the spectrum of the cured mixture (green) it is evident that the Si-H peak is greatly reduced, which is consistent with its involvement in the cross-linking reaction.

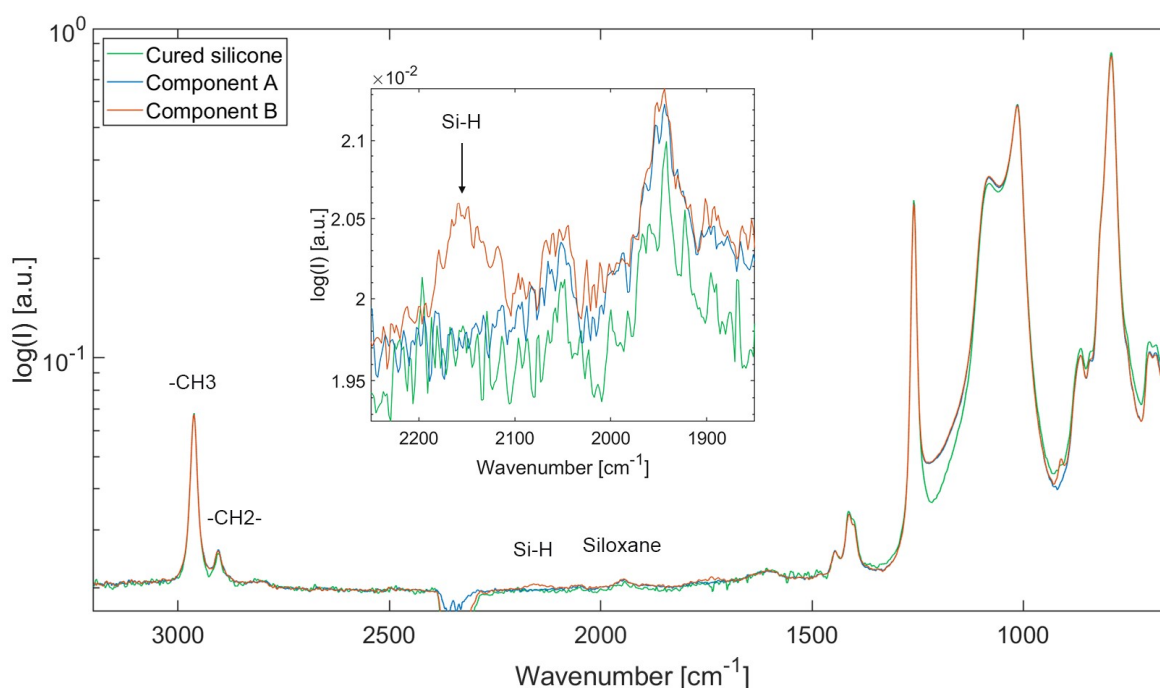


Figure 33 - ATR FT-IR spectra of the two components of Ecoflex™ 00-30 silicone on aluminium foil. In the inset is reported a magnification of a portion of the measure which show a characteristic energy for the Si-H species at 2160 cm^{-1} and its evolution with curing.

With the material thus examined, different samples were produced. The method of casting and moulding are the same as reported in Section 5.4.1. The plain silicone samples were characterised by calorimetry in order to estimate the specific heat (c_p) and thermal conductivity (k); then, their density was assessed through Archimedes' method, and the mechanical behaviour was investigated through tensile stress-strain tests. The results of these characterisations are showed in Section 5.4.2 in comparison with the measurements carried out on the composite (modified matrix) samples.

5.3. Choice of the fillers

The need to functionalise the soft matrix led us to search for the best filler that could provide the desired properties. The main requirement is the optimisation of the soft matrix from the point of view of heat exchanges. Other aspects that may be useful in the optimisation of SMA soft actuators, and which have been investigated, are piezoresistivity and the modulation of the mechanical stiffness of the soft component. In the literature there are various nano- and micro-particles which are inserted into the silicone to obtain a variation of these characteristics. The most widely used are carbon black [86], [87], carbon nanotubes [88]–[92], graphene [93], [94], graphite [95]–[97], silver nanowires [98], [99], alumina [100]–[102] and droplets of Ga-In-based liquid metals [103].

Graphene nanoparticles (GNPs) have been chosen for the present project thanks to their efficacious contribution to the modulation of thermal [104], electrical [105], [106] and mechanical [94], [107] properties, and for their relatively low weight and cost. Their mode of action as fillers and the dependency of their effects on their dimensional and morphological characteristics will be briefly described in the next section.

5.3.1. Selection criteria for GNPs as polymer matrix fillers

Graphene is a two-dimensional (2D) material with a high in-plane thermal conductivity due to covalent sp^2 bonding between carbon atoms, and a low out-of-plane thermal conductivity limited by weak van der Waals coupling [108]. In particular, the thermal conductivity of graphene is attributed to phonons and electrons giving it quasi-metallic properties [104]. Within the graphene sheet, made by a network of condensed aromatic rings, each Carbon atom provides one $2p_z$ electron to the π -orbitals, which are delocalised on the whole 2D crystal and enable efficient conduction of electricity (and heat to some extent). In addition, the ordered lattice of graphene also enables phonon transport, which results in high thermal conductivity. Overall, phonons are thought to play a greater role than electrons in the thermal conductivity of graphene [109].

The presence of size confinement and structural defects in graphene hinders the propagation of phonons by increasing scattering and decreases its thermal conductivity [108], [110]. Several commercial GNPs are available, with different structural characteristics as particles shape, degree of exfoliation – i.e., particles thickness - average particles size and size

distribution. The choice of the most suitable GNPs material is therefore essential to obtain the best characteristics of the composite. Moreover, the tuning of the relative amount of the filler plays a fundamental role in the optimisation of the composite properties.

To help defining the requirements for GNPs and to understand more in depth the influence on GNPs on the elastomer-based composites, a research on the physical mechanisms of polymer-filler interaction has been carried out.

Loading and percolation. The loading of graphene in the matrix exerts a significant effect on the electrical and thermal conductivity of the resulting composites. It is found that there is a critical loading (percolation threshold) of GNPs such that, when the loading exceeds this value, the particles get sufficiently tightly packed that electrons can tunnel through the spaces left among them, and the electrical conductivity of the composite material is improved significantly (Figure 34). The value of the percolation threshold depends on filler type, shape, size, and filler dispersion and distribution in the composite. For example, the use of a spherical conductive filler and smaller in size will lower the percolation threshold [106]. Conversely, there are different opinions as to whether there is a true percolation threshold phenomenon affecting thermal conductivity [108].

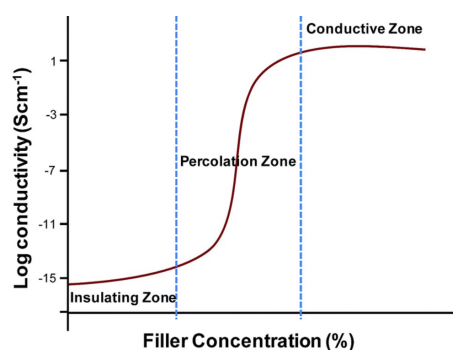


Figure 34 - Electric effect of the loading of conductive fillers reinforced polymers composites. The percolation zone defines the filler loading value at which the composite begins to become electrically conductive [106].

Heat conduction mechanisms mediated by graphene in polymers are complex. In general, graphene has a very high specific surface area. When being added in a polymer, large numbers of interfaces are produced. These interfaces will lead to phonon scattering and introduce ultrahigh interfacial thermal resistance. Therefore, it is difficult for heat to transfer through the graphene/polymer interface. When the loading of the filler is below the percolation threshold, the filler particles cannot connect directly to each other to form a continuous thermal conduction pathway. In this case, the interfacial thermal resistance of graphene and the polymer will be the main factor determining the thermal conductivity of

the composite. However, when the loading is above the percolation threshold, the heat in the composite mainly transfers through the thermal conduction pathway, due to the high thermal conductivity of graphene [108], [111]. Even when the percolation network exists, the improvement in thermal conductivity produced by GNPs is limited by interface resistances between filler particles and between filler and matrix (Kapitza resistance) [112].

Aspect ratio. Not only the loading, but also the shape (e.g. the lateral size and thickness) of the GNPs affects the thermal conductivity of composites. For example, thermal conductivity across a graphene/epoxy interface increases when increasing the number and the size of graphene layers in the GNP. Furthermore, a larger aspect ratio (defined as the lateral size to the thickness ratio) results in an effective improvement in the thermal conductivity and heat dissipation ability of the composite [113]. This same result may be extended to other classes of polymer matrix [114].

Morphology. The morphology of graphene has an influence on the thermal conductivity of composites too. It is possible in fact that graphene gets warped and wrinkled due to external mechanical actions (like energetic sonication), so its shape is deformed. When using graphene nanoplates with more wrinkles as a filler, the composites will exhibit lower thermal conductivity. The reason for this is that the waviness of GNPs significantly affects the intrinsic characteristics of GNPs (such as thermal conductivity, aspect ratio) and the interfacial phonon coupling behaviour between GNPs and polymers [115].

Orientation. Other aspects have been reported to affect electrical, thermal and mechanical characteristics of the composites, such as distribution and orientation of fillers in the matrix materials [116], [117]. In particular, orientation increases graphene composite stiffness especially when the fillers are aligned in the direction of strain. Thermal conductivity is also enhanced by orientation which however creates anisotropy in the material.

Filler/matrix interface. A significant effect on thermal and electrical conductivity and the percolation threshold of the composite is given also by the interface properties between the filler and the polymer [104], [106], so, filler surface modification can be useful. When the loading of the filler is below the percolation threshold, surface modification of the graphene has been proved to be an applicable method to enhance graphene-polymer interface interaction, and an efficient technique to decrease interfacial thermal resistance. In a composite, graphene acts as a highly thermal conductive channel, and the GNP surface modification can facilitate the phonon transfer from the graphene to the polymer and also promote the phonon transfer from the polymer to the graphene [104]. Various filler

functionalisation techniques have been applied to improve their dispersion and optimise the thermal effect they have on the composite [118], [119].

5.3.2. GNP selection and characterisation

Two commercial high-quality GNPs with high aspect ratio (> 625) were purchased from <https://graphene-supermarket.com/>:

- A-12 are GNPs with an average flake thickness greater than 3 nm (between 3-8 graphene monolayers) and a lateral size of 2-8 μm .
- AO-2 GNPs have an average flake thickness of 8 nm (20-30 monolayers) and a lateral size $\sim 5 \mu\text{m}$.

For the characterisation of this two GNPs, Raman spectroscopy and scanning electron microscopy (SEM) have been used.

Raman measurements (Raman spectrometer Labram HR800 equipped with an Olympus BX41 microscope; Peltier cell cooled CCD detector) were recorded with excitation laser wavelength of 632.8 nm and a power at the sample of 0.5 mW. The Raman spectra of the two GNPs samples are shown in Figure 35.

In graphene, the inelastic scattering of the exciting laser photons creates two main peaks in the Raman spectrum designated as the G and 2D bands. A third peak, the D band, may also be apparent in graphene when defects within the carbon lattice are present, or because of size confinement, in the case of GNPs [120]–[124].

The shape and intensity of the 2D band are correlated to graphene layer thickness [125]. The 2D peak in Figure 35 shows the characteristic band splitting of the 2D band going from single layer graphene to multilayer graphene. Also the asymmetric shape of 2D band, reveals the presence of stacking of graphene sheets, confirms the GNPs in the sample are multilayer. The degree of disorder can be estimated from the intensity ratio I_D/I_G that it is directly related to the density of defects. [126], [127] A D' component is often present as a shoulder on the higher wavenumbers side of the G peak. It is associated to vibrations localised on the particles edges: for this reason, it allows to assess the nature of the defects, through the analysis of the $I_D/I_{D'}$ ratio. In fact, it is maximum (~ 13) for defects associated with sp^3 hybridisation, it decreases for vacancy-like defects (~ 7) and reaches a minimum for boundary-like defects in graphite (~ 3.5) [128]. AO-2 GNPs showed a good quality, namely a good integrity of the graphene sheets, as indicated by a low intensity ratio $I_D/I_G = 0.33$.

A comparison of the spectra in Figure 35 also shows the comparatively bad quality of the A-12 sample, for which we found an intensity ratio $I_D/I_G = 1.1$ and broadened peaks also due to disorder. In addition, a broad component in the spectral region between the G and the D bands reveals the presence of abundant very disordered or amorphous phases.

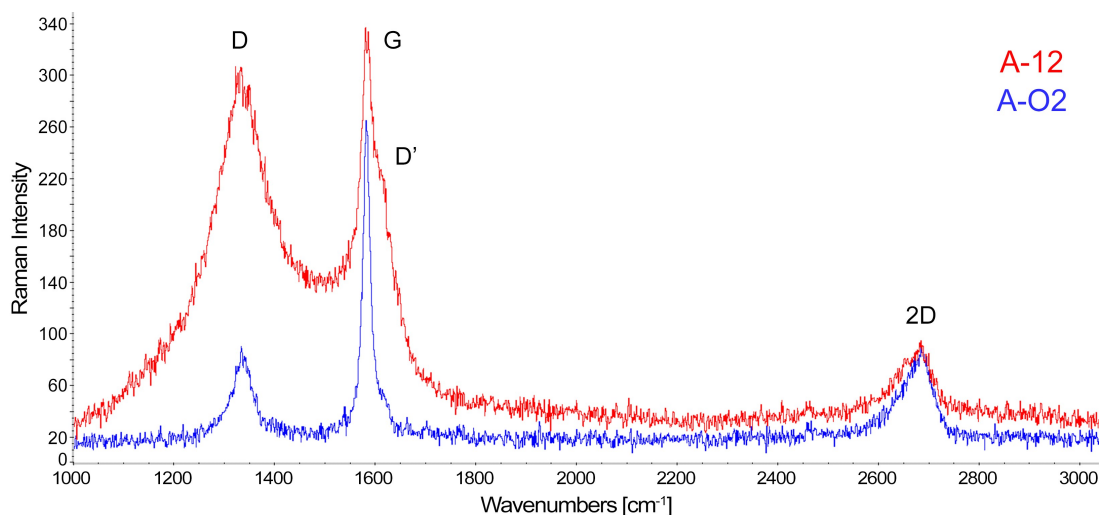


Figure 35 – Raman spectra of A-12 (red) and AO-2 (blue) GNP samples. The shape of I_{2D} peaks confirm they are multilayer GNPs. AO-2 GNPs shows a better quality than A-12 GNPs, as demonstrated by the lower I_D/I_G , a parameter directly related to the density of defects.

To investigate the quality of the two GNPs, SEM images were taken at various magnifications. The images were taken using a SEM Zeiss Leo 1430. Secondary electrons (SE) are very useful for the inspection of the topography of the sample's surface. In Figure 36 it is possible to see images of the sample AO-2 GNPs, as received. The A-12 GNPs sample (Figure 37) looks very different AO-2 GNPs, in fact the images of the as-received sample show the particles crammed in packets. Unlike AO-2 GNPs, which could be analysed as received, this was not possible for A-12 GNPs without any mechanical pre-processing.

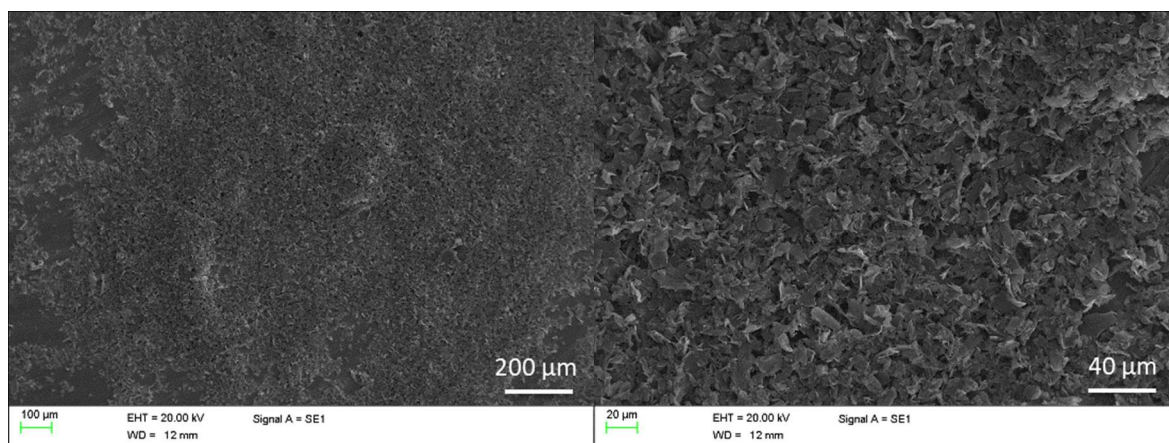


Figure 36 – SEM (SE) images of AO-2 GNPs, as received, taken at various magnifications. The flakes appear generally separated, and their main characteristics can be appreciated.

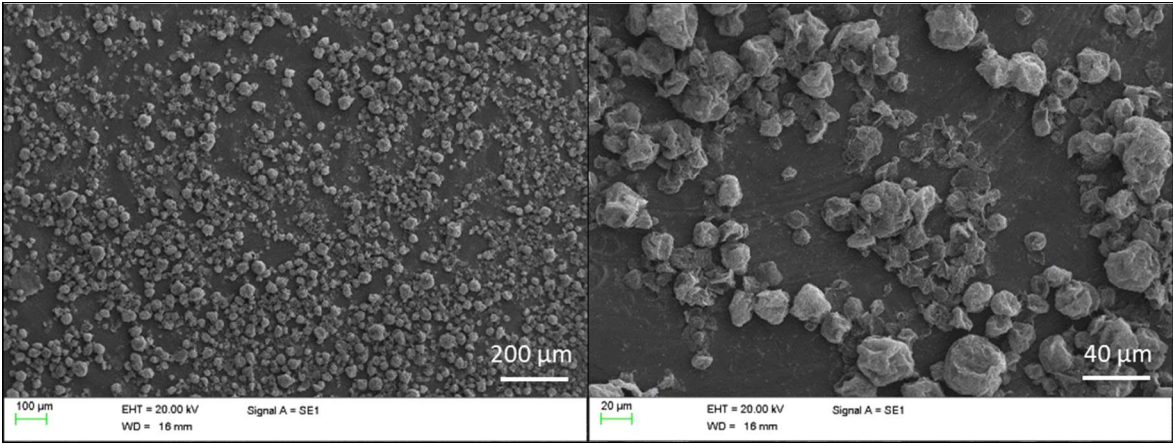


Figure 37 – SEM (SE) images of A-12 GNPs as received taken at various magnifications. The flakes are not clearly distinguishable, because they appear compacted into spherical packets.

In order to separate the flakes, and investigate their characteristics, simple manual stirring and bath sonication in Isopropyl Alcohol (IPA) for different durations have been performed. In Figure 38 it is possible to see that for sonication durations shorter than 60 minutes some packets are still present.

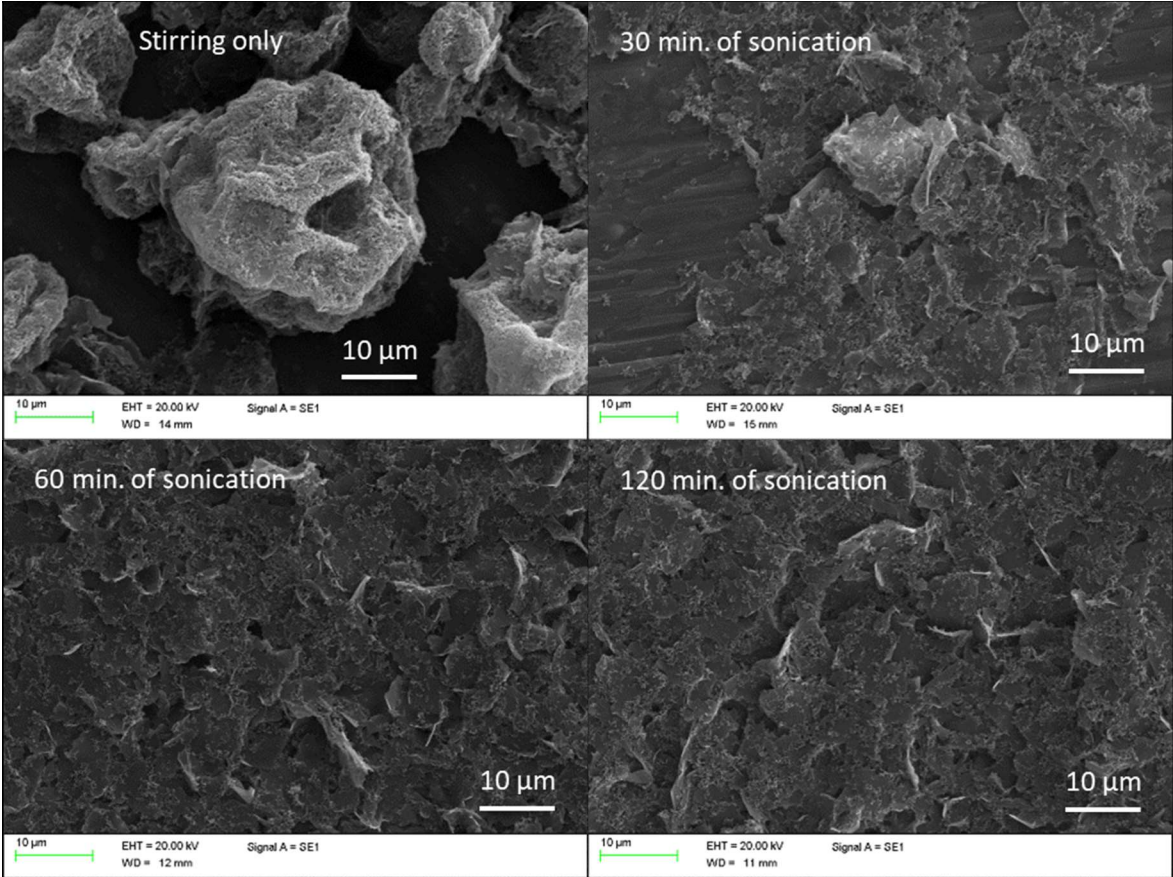


Figure 38 - SEM (SE) images of A-12 GNPs after mechanical processing. Simple manual stirring and bath sonication for different durations have been tried.

As the presence of defects and deformation in GNPs worsens the characteristics of the composites, particularly thermal conductivity, I have established that 60 minutes was the right sonication time needed to separate A-12 graphene particles without damaging (warping) them excessively.

From SEM images at high magnifications (Figure 39 - left) it has been possible to confirm the good quality of AO-2 GNPs and their lateral size compatible with the nominal one.

The image of A-12 GNPs sonicated for 60 minutes shows that also for this sample the lateral size was compatible with the nominal one (Figure 39 - right). It was also possible to observe a large presence of smaller particulate matter, that indicate a lower batch quality and a possible cause of the broadening of peaks in the Raman spectrum.

In light of these observations, AO-2 GNP was finally selected for its higher quality to make the GNP/PDMS composite samples.

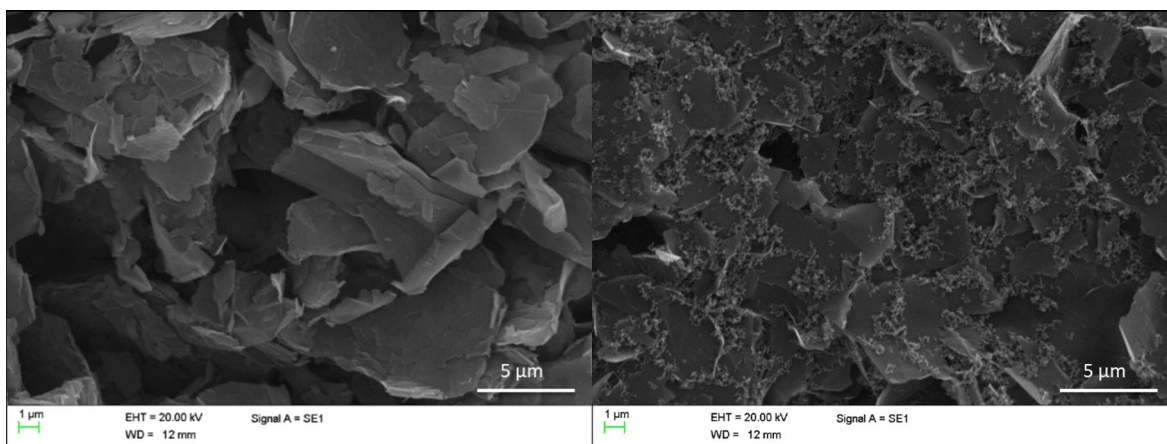


Figure 39 – SEM (SE) images of AO-2 (left) and A-12 (right) GNPs.

5.4. Preparation of the GNP/PDMS composite

Different samples of silicone/AO-2 GNPs composite were made to evaluate what percentage of filler was most suitable to insert in the soft matrix. The volume fraction and distribution of the nanoparticles dispersed inside polymer nanocomposites are known to have a significant impact on the physicochemical properties of the final materials. Particular attention was paid to the choice of the manufacturing process and to the characterisation of the samples. To comprehend and optimise the properties and functionality of the nanocomposites, a thorough understanding of platelet dispersion and organisation in the

polymer matrix was necessary. Indeed, a potential inhomogeneity in the graphene dispersion could lead to anisotropy or inhomogeneity of the thermal and physical response of the composite. To obtain information about GNP dispersion direct observation through electron microscopy (SEM imaging) was chosen as a valuable characterisation technique.

Subsequently, I carried out calorimetric and gravimetric assessments with the aim to investigate thermal diffusivity as an important parameter characterising heat transport, and to evaluate how the amount and dispersion of graphene in the composite can affect its value. Thermal diffusivity measures the ability of a material to conduct thermal energy relative to its ability to store it. Therefore, materials with high diffusivity can transfer heat rapidly. Since thermal diffusivity is calculated as:

$$\alpha = \frac{k}{\rho c_p} \quad 5.1$$

where k is the thermal conductivity [W/(m·K)], c_p is the specific heat capacity [J/(g·K)] and ρ is the mass density [g/cm³], all three parameters had to be estimated.

Moreover, in order to provide a complete description of the physical behaviour of the silicone/GNPs composites, also mechanical and piezoresistive characterisations were carried out.

5.4.1. Preparation of the composite samples: dispersion of GNP in the PDMS matrix

For the creation of polymer nanocomposites, known techniques such as solution blending, melt mixing, and *in-situ* polymerisation are most frequently employed. [107]

Since it was necessary for the current project to make composites moulded in different shapes, the process chosen to produce the filler/polymer mixing was solution blending. In this process, the polymer is first dissolved in an appropriate solvent. After that, the GNPs are dispersed in a solvent that is compatible with the one in which the polymer was previously dissolved, and the two solutions are blended together. During the subsequent simple mixing, shear mixing or ultrasonication, the polymer adsorbs onto the graphene flakes.

The formation of the nanocomposite and the uniform dispersion of the flakes take place during this process. In addition, the final properties are highly sensitive to the presence of

any residual solvent which could plasticise the matrix with a tendency to stay at the surface. It was therefore crucial to ensure that the solvent completely evaporates. [107]

The exact procedure applied here to prepare the composite samples is shown in Figure 40. The first step was to create the dispersion of GNPs in isopropyl alcohol (IPA). The chosen GNPs/IPA weight ratio was 1:20 and the time of bath sonication was 60 min. After that, we mixed the dispersion of GNPs with component B of the silicone and stirred them until IPA evaporation. Particular attention has been paid to verify that IPA had completely evaporated before adding the suspension to part A of the silicone and starting the cross-linking. A fundamental step for the success of the sample creation was the cooling of the compound to 25 °C before adding the component A, because a high temperature of the composition would speed up cross-linking too much, thus decreasing the pot life.

The final mixture composed by GNPs and the two components of silicone rubber was stirred manually for 2 minutes. This operation was carried out slowly and carefully to prevent the formation of air bubbles inside the material that could affect its physical and mechanical properties. Subsequently, the compound was cast in a mould creating a thin continuous thread of mixture to promote the breaking of eventual air bubbles. The samples produced were left to rest for one day to allow the completion of the curing reaction before starting any kind of test.

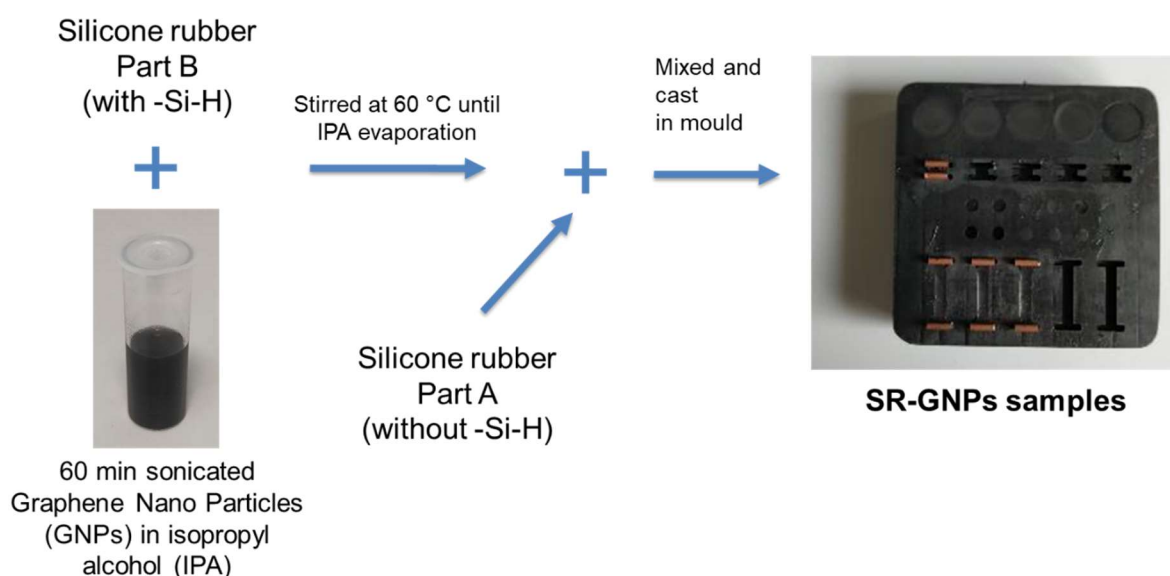


Figure 40 - Preparation procedure of SR-GNPs samples.

Samples were made with four different concentrations of graphene (2 wt%, 3 wt%, 5 wt%, 10 wt%). For concentrations between 2 wt% and 5 wt% it was possible to make the samples

in all desired shapes (Figure 41). As regards the composites with 10 wt%, only the three smallest samples were produced. The reason was that the curing time in this case was significantly reduced and also the composite was too viscous to be properly poured into the mould of the biggest one.

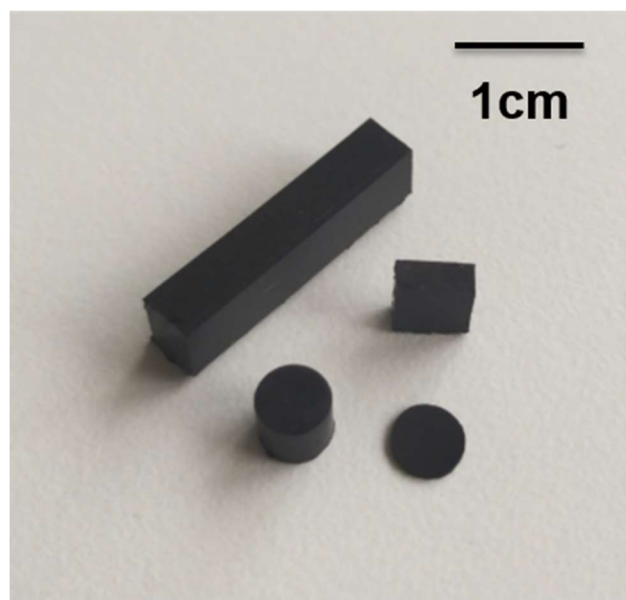


Figure 41 - Samples of composite made in various shapes. (round for thermal characterisations, rectangular for piezoelectric and mechanical characterisations).

5.4.2. Characterisation of the modified silicone samples

In order to obtain information about graphene distribution in the cured silicone rubber, SEM microscopy was chosen as a suitable technique for the investigation of the filler dispersion. To evaluate the effect of the amount and dispersion of graphene on the thermal diffusivity of the composites, the thermal properties (specific heat and thermal conductivity) and the density were investigated experimentally.

Finally, to complete the composites characterisation, some mechanical measurements and piezoresitivity evaluations were carried out.

5.4.2.1. Scanning electron microscopy (SEM)

The composite samples were frozen by immersion in liquid nitrogen and then broken. In this way, it was possible to observe clearly the arrangement of the GNPs particles on the fracture surface. To enhance visualisation of their surface features, samples were gold sputtered.

Figure 42 shows SEM images of four composite samples produced with different graphene concentrations. The images were taken in flat areas to improve focussing.

Upon a generally dark background, some bright areas can be observed and they reveal how graphene sheets are distributed throughout the polymer matrix. Indeed, the secondary electron yield is enhanced where the graphene is located, creating a contrast between the graphene network and the polymer matrix due to the different capacities for charge transport of the conductive graphene and the insulating polymer matrix. In all four samples, the particles appear to be well dispersed throughout the thickness of the sample, both in the centre and towards the edges.

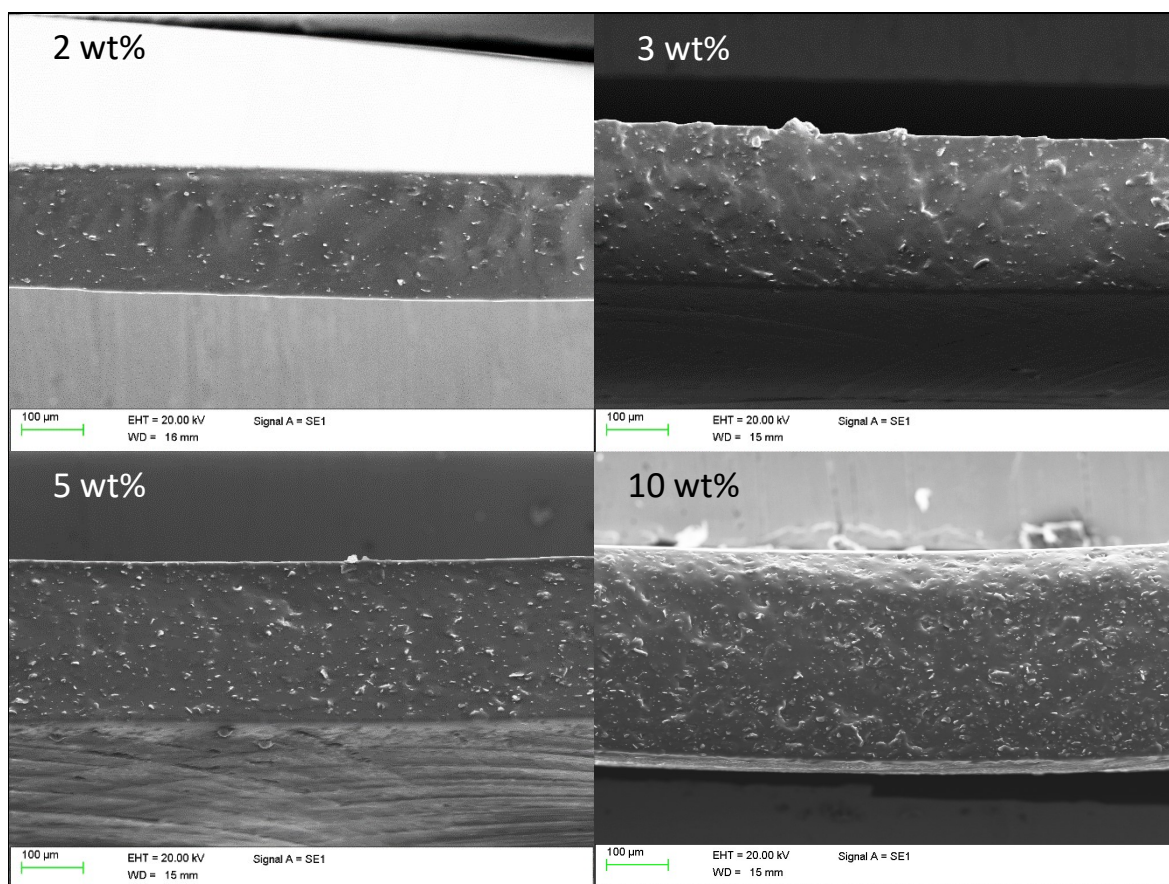


Figure 42 – SEM images (400x magnification, secondary electrons signal) of four composite samples produced with different AO-2 GNPs concentrations.

Images at higher magnification are reported in Figure 43 and provide more information about local features of the dispersion and about the distances between graphene particles. The homogeneity is overall good. At low graphene concentrations, the dispersion appears to be slightly less homogeneous, but this may be due to some particles being located just below the fracture surface. However, as the concentration of graphene increases, the particles are

closer to one another and appear more frequently near the surface, so the apparent homogeneity of dispersion increases. Moreover, it is important to observe that, in all the samples, there is no agglomeration of the particles, which is essential for the performance of the composite to be optimised. Considering concentrations up to 5 wt%, even if the apparent 2D distances among the graphene particles are quite variable, it seems the particles do not come into contact. Therefore, the effect of some inhomogeneity in the dispersion of graphene should not have a significant impact on the composite properties: a critical improvement in conductivity is expected when the particles are almost touching. Only at the concentration of 10 wt% the graphene particles seem to come into contact creating percolation paths.

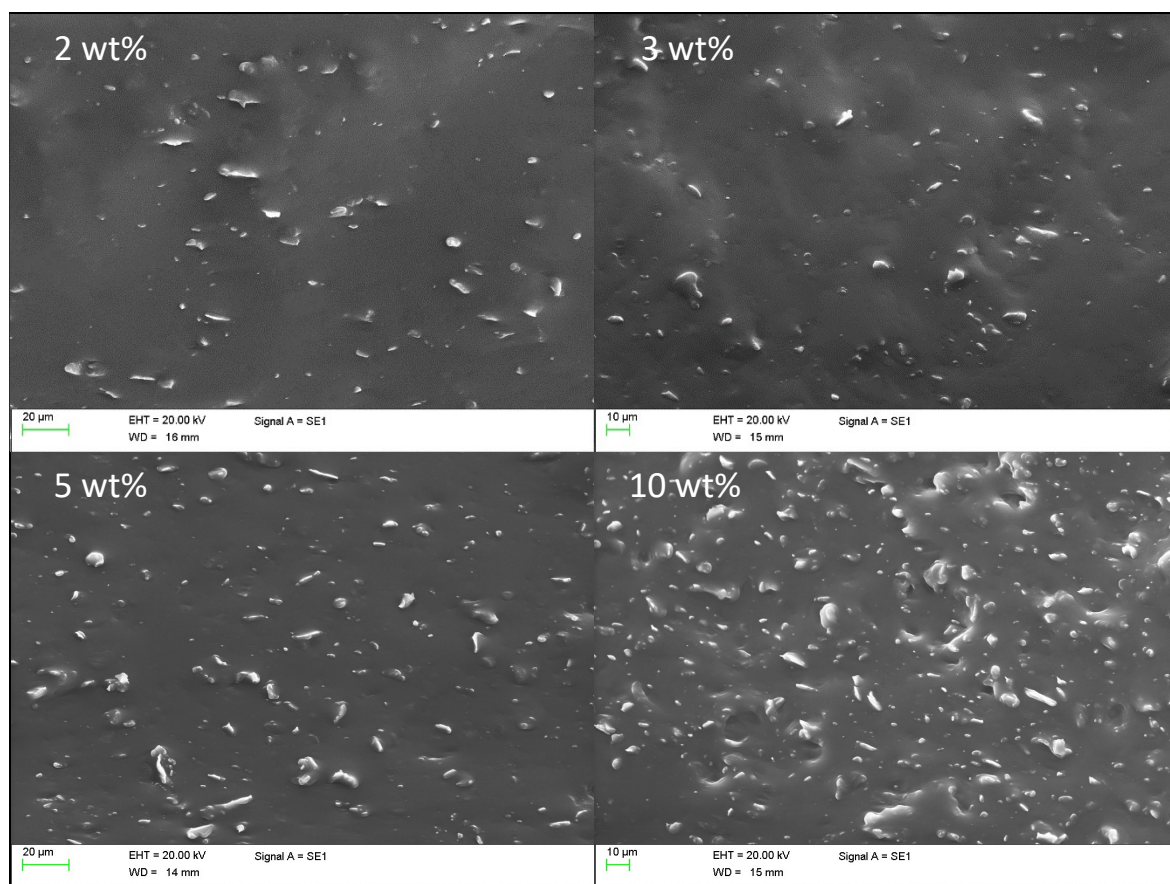


Figure 43 - SEM images (1500x magnifications, secondary electrons signal) of four composite samples produced with different AO-2 GNPs concentrations.

Moreover, this observation of the cross sections of the samples allowed to verify the absence of air bubbles confirming the reliability of the chosen production process despite not having performed a degassing procedure on the material before curing.

5.4.2.2. Thermal properties

To characterise the thermal properties of the modified silicone rubber, two methods have been taken into account. The first one (based on ASTM E 1952) uses a Modulated DSC to detect thermal conductivities in the range: 0.1-1 W/mK. The second method, also using DSC, is based on the study of the sample response to a temperature step in the frequency domain and is nominally employable to estimate thermal conductivities in the range: 0.1-2 W/mK [129].

The complex algorithm for the calibration and signal processing of the measured data required for the second method has been fully developed and some preliminary measurements were acquired. Finally, the method was not used because the preliminary measurements showed that, at least with our set-up, silicone rubber properties could not be estimated accurately. The study of this procedure and the development of the algorithm could be useful in future to characterise samples with higher thermal conductivities.

Instead, the first method was used for the current study: it has the advantage of being easier to use and it was chosen since the expected conductivity values of the samples fall well within its validity range. Preliminary tests confirmed that estimates obtained with this method were in good agreement with the expected range for silicone rubbers.

Thermal measurements were performed on cylindrical samples (see Figure 41) with a diameter of 4.75 mm and thicknesses of 0.2 mm and 4 mm.

The modulated DSC measurements were conducted at 40 °C in a DSC Q25 (TA Instruments LTD). The temperature was modulated with an amplitude of 0.5 °C and a time period of 80 s for 25 minutes, in order to achieve a stable heat flow signal. Some reference measurements with the same parameters were performed on known polymers (Polystyrene and PMMA) and showed good results (Specific Heat error < 15 %, Thermal Conductivity error < 25 %). For each graphene concentration, 5 samples were measured twice and the results for the c_p and k are reported in Figure 44 and Figure 45, respectively.

It is possible to notice a sharper increase in k is registered with increasing graphene content up to 10 wt%. In fact, with this graphene content, an 11.2 % decrease in the specific heat capacity and a 156 % increase in the thermal conductivity were obtained with respect to plain silicone rubber. This means that k is predicted to give a more significant contribution to the thermal diffusivity changes, with respect to c_p .

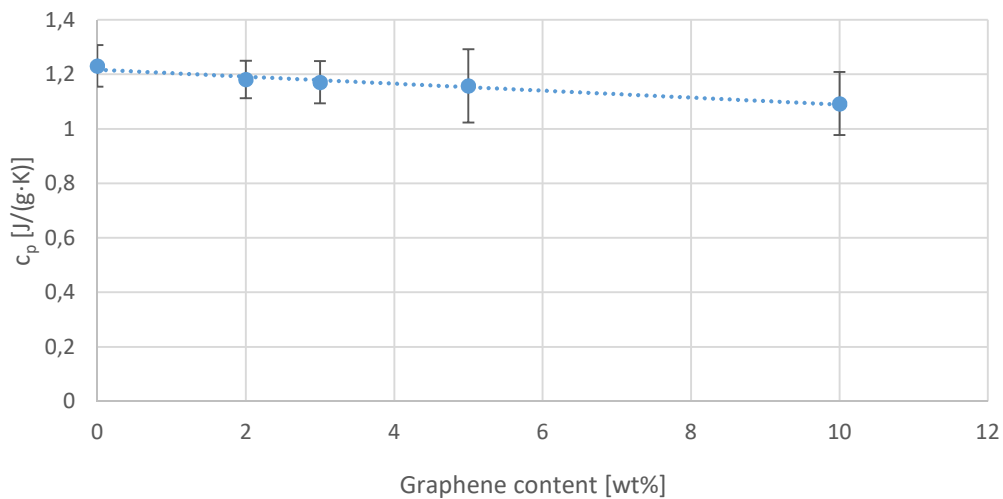


Figure 44 - Specific heat capacity (dots with whiskers showing standard deviation in the repeated measures). A linear interpolant was plotted to guide the eye.

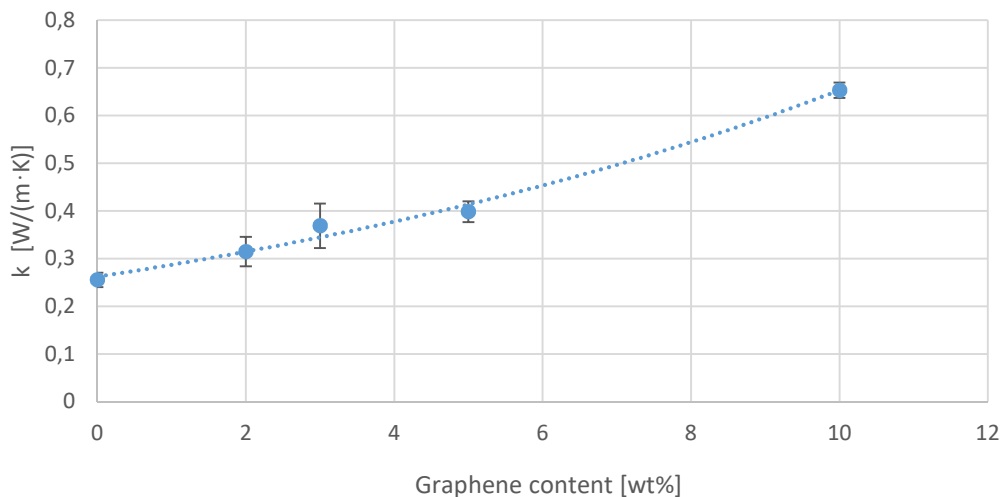


Figure 45 - Thermal conductivity (dots with whiskers showing standard deviation in the repeated measures). The dotted line is the second degree interpolant, to guide the eye.

Density measurements were carried out through Archimedes' method (Gibertini E50S/2, Figure 46). For each graphene concentration, measurements were repeated 10 times. In Figure 47 it can be seen that the density slightly increases as the amount of graphene increases. A 3.4 % increase in the density was measured for the sample with 10 wt% of graphene.

From the obtained thermal conductivity, specific heat capacity, and density, the estimated thermal diffusivities for the plain and modified silicone rubbers, are as reported in Table 5.

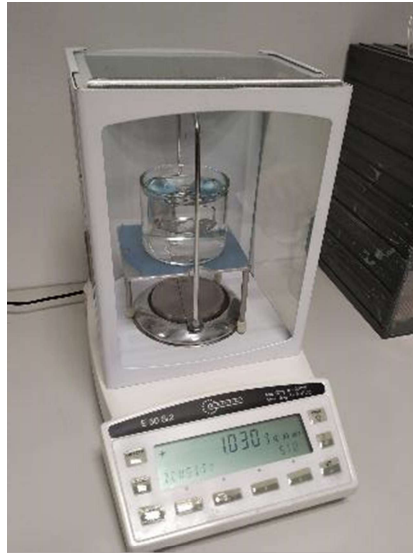


Figure 46 - Instrumentation for the measurement of the mass density through Archimedes' method.

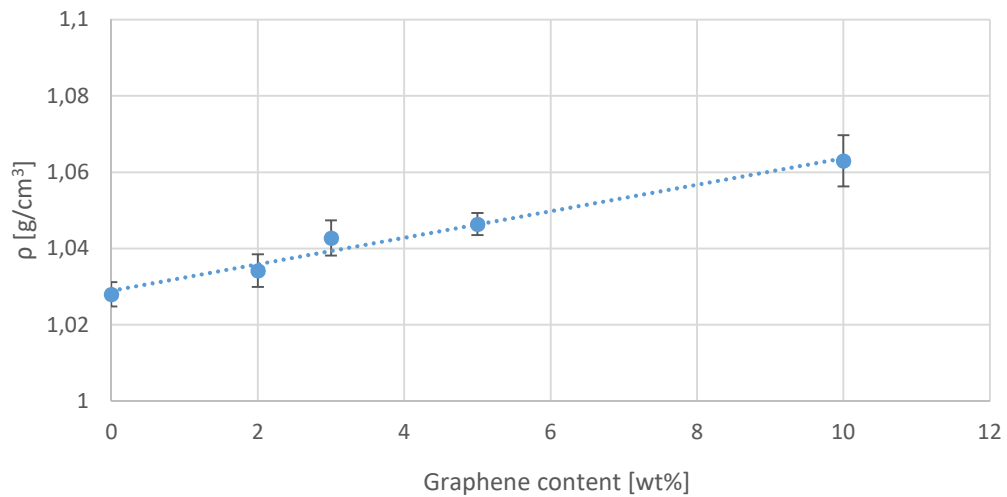


Figure 47 - Density measurements (dots with whiskers showing standard deviation in the repeated measures). A linear interpolant was plotted to guide the eye.

Table 5 – Mean values of measured thermal conductivity k , specific heat capacity c_p , and density ρ . Thermal diffusivities α were estimated using equation 5.1.

		k [W/(m·K)]	c_p [J/(g·K)]	ρ [g/cm ³]	α [mm ² /s]
Graphene content [wt%]	0	0.256	1.231	1.028	0.20
	2	0.315	1.181	1.034	0.26
	3	0.369	1.171	1.043	0.30
	5	0.399	1.158	1.046	0.33
	10	0.653	1.093	1.063	0.56

5.4.2.3. Mechanical characterisation

The mechanical characterisation of the produced composite samples was conducted by means of a dynamic mechanical analyser (DMA) (Q800, TA Instruments) equipped with a 17 N load cell and a tensile test clamps. The geometry of the samples is shown above in Figure 41 (section 5.4.1). Prismatic 5 (width) x 4 (thickness) mm bars with a gauge length of 8 mm were used. This size was preferred to thin sheets because we thought that it would represent better the bulk material quality obtainable by the moulding process. In order to avoid edge effects, the ends were held by tightening the clamps against a 3.5 mm thick steel reference that prevented excessive localised shear strains. The tensile stress-strain measurements were carried out at room temperature with a strain rate of 10 %/min up to a strain of 100 %, and the results are shown in Figure 48. It is possible to notice that the slope of the curve for the plain silicone rubber is lower than those of the composite samples and reaches the maximum stress of 0.063 MPa for 100 % strain. This value also corresponds to that declared by the manufacturer. Moreover, the slope of the composites curves increases with increasing graphene content (Table 6). The maximum stress reached by the sample with 5 wt% graphene concentration is 0.125 MPa.

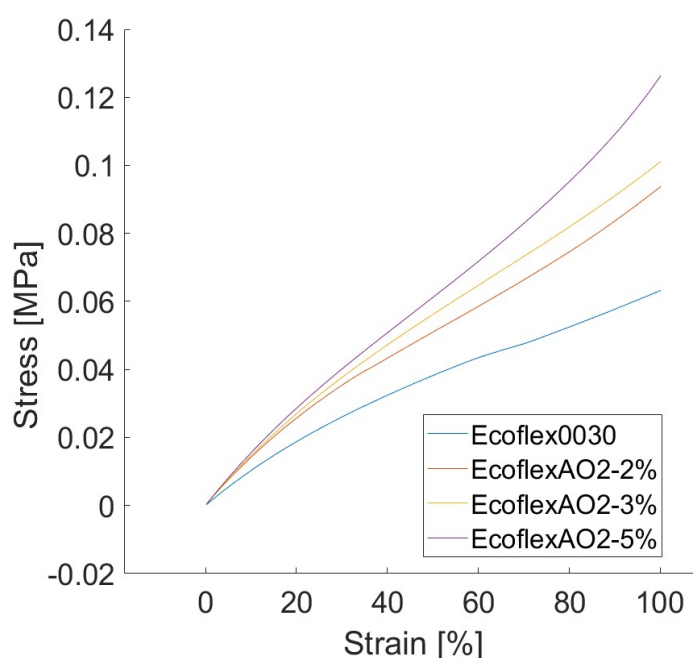


Figure 48 - Stress-strain curves. The sample with 10 wt% GNP concentration was not characterised as it was not possible to make it properly with the chosen production method.

Table 6 - Numerical data extracted from mechanical curves. Young's modulus was calculated as the initial slope at null strains.

		Young's modulus [MPa]	Stress at 100 % [MPa]
Graphene content [wt%]	0	0.115	0.063
	2	0.157	0.094
	3	0.160	0.101
	5	0.168	0.125

5.4.2.4. **Electrical properties and piezoresistivity**

Electrical measurements were performed on rectangular samples (see Figure 41) with a face size of 4x5 mm and a thickness of 2.3 mm.

Using Keithley 2450 Source Meter it was possible to verify that none of the samples analysed was electrically conductive. The resistance value was in fact out of range and with this I can estimate that the conductivity was greater than $10^7 \Omega \cdot m$.

In addition, piezoresistivity measurements were carried out at room temperature by means of Instron Electropuls E3000 testing machine equipped with a 3 kN load cell of and the compression plates. An additional 200 N load cell was inserted mechanically in series with the device to obtain a measurement with a better signal-to-noise ratio. A compression ramp has been applied at the speed of 50 %/min up to 50 %. The simultaneous measurement of the electrical resistance of the sample was obtained by inserting a fixed resistance of 2 M Ω in series with the sample. A constant voltage of 9 V was then applied (AimTTi CPX400DP power supply) and the voltage was measured over the fixed resistor with a data logger (16-bit Data Acquisition system (DAQ)).

The electrical contact to the sample was made by means of two silver discs, electrically insulated with double-sided tape from the mechanical measurement system. A photo of the measurement system can be seen in Figure 49.

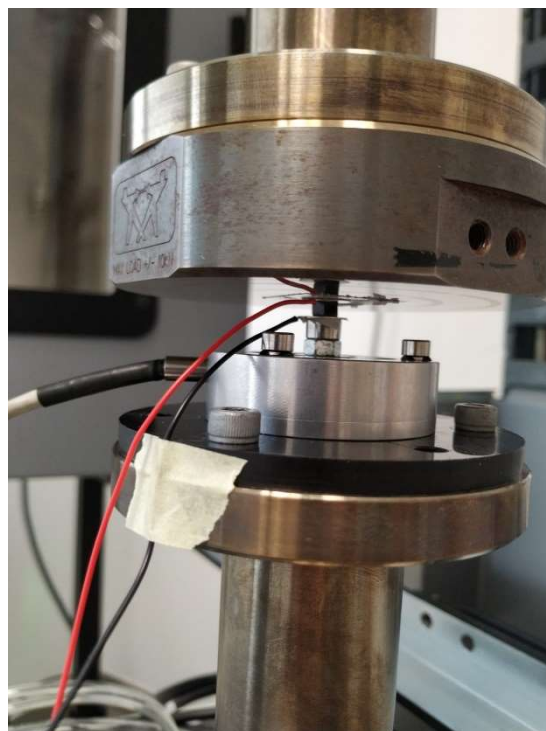


Figure 49 – Set-up for the measurement of the piezoresistivity of the samples.

The only sample that gave a signal under the pressure exerted is the one with a percentage of GNPs equal to 10 wt% (Figure 50). The piezoresistive response is non-linear and has a hysteresis between loading and unloading. Furthermore, the resistance could only be measured for pressures greater than 2 N.

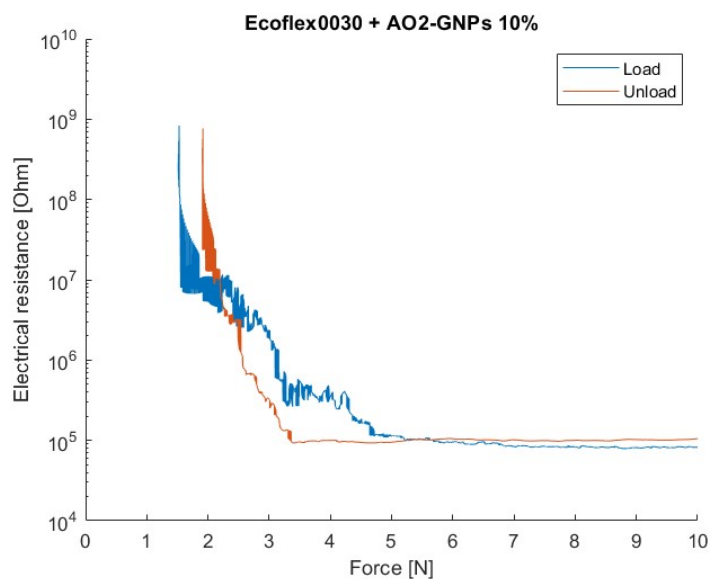


Figure 50 - Piezoresistivity curve of 10 wt% AO-2 GNPs composite. Variation of the resistance with the variation of the pressure exerted on the sample.

5.5. Conclusions

Through SEM imaging, a good dispersion of the AO-2 GNPs in the PDMS matrix was observed in all the samples investigated.

The thermal effects produced with the higher-quality large-aspect-ratio GNPs selected are marked. Loading fractions of 5 wt% and above were able to produce a significant increase in thermal conductance, a mild increase in mass density, and a decrease in specific heat capacity. Consequently, thermal diffusivity can be increased as desired in a range of interest for the current project.

Despite the rather high percentages of graphene employed, the observed effect on electrical conductivity was extremely low, probably due to the comparatively large size of the selected GNPs (in fact, for a given weight fraction of fillers, the interparticle distance is lower the finer is the dispersion, i.e. the smaller the particle size). This expected result can be traced back to the minimal creation of percolation paths, which is consistent with the interparticle spacings seen in the SEM images. That the electrical conductivity of the matrix remains low can be an advantage in the construction of devices where this component is required to provide some insulation between the SMA elements (that are traversed by an electric current), and the outside world. With a GNP fraction of 10 wt%, piezoresistive behaviour was observed for large applied stressed. This effect could be useful for the creation of matrix-embedded pressure sensors (e.g. for actuator control purposes) in localised regions of the interface with the environment, but this functionalisation will not be attempted in the present project.

Finally, the modification of the PDMS with the employed GNPs causes moderate increases in the mechanical properties, which could be exploited in designing the actuator, in order to increase the inherent bias-spring action on the SMA element, which could be deployed by the matrix itself.

CHAPTER 6

Numerical models of the multimaterial actuator

Tackling the optimisation of SMA-based soft actuators, it is essential to be able to simulate the influence of material properties and morphology on their thermomechanical behaviour. This can be done through suitable mathematical models able to describe the main physical characteristics of the system. In Section 6.1 we shall define a very simple multimaterial soft-actuator as a case study, on which all the simulations will be carried out, in order to make the results as easy to comprehend and generalise as possible.

The present chapter includes simulations at two different dimensionalities, which are focussed on diverse aspects of the multimaterial design and overall actuation problem.

One-dimensional (1-D) Finite Element (FEM) simulations were carried out using the COMSOL Multiphysics 5.5 software, in order to investigate the characteristics and optimisation of the materials, and the effects of intermaterial interfacing and sizing. This strategy was chosen because it enabled the implementation of an accurate and complete model with sufficient detail on field variables such as temperature distribution in the matrix. Additionally, a lumped parameter (0-D) model of the actuator was implemented to test automatic control strategies specialised for the multimaterial-based design. The corresponding simulations were run with in Simulink (Mathworks Inc.). This choice was made because the advanced control algorithm we developed requires a simple – but equally reliable – model that can be run in real time. For the SMA material, an *ad-hoc* modified version of Brinson’s model [64] was developed. The parameters of the SMA wire, obtained from material characterisation in Section 4.5, have been optimised to find a best fit between the simulated model and the experimental measurements. The behaviour of the PDMS matrix was taken into account in a simplified manner in the 0-D model, under appropriate assumptions on heat transfer conditions through the matrix.

By the end of the chapter, it will be clear that the two simulation methods are consistent and mutually verifiable. Hence they will be considered usable to make further considerations about the design of SMA/PDMS actuators and the related control.

6.1. Definition of the reference actuator for the present study

The actuator we based on for all the simulations in this thesis work is as a linear actuator composed by a SMA wire enveloped in a silicone rubber sheath in direct contact with the wire; the actuator is surrounded by air (Figure 51). The SMA wire is 10 cm long and has a diameter of 0.65 mm (selected in section 4.1). The soft matrix is cylindrical with a thickness t_M , composed of a homogeneous low-modulus elastomeric material. The interface between the two materials has a thermal contact resistance R_c . The heating of the SMA wire takes place by Joule's effect, i.e. in response to the passage of the electric current generated by an electric voltage source V_{In} applied between the wire's ends. Heat exchange with the air occurs by natural convection, with a coefficient h_0 whose value falls within a range of 5–35 W/(m²·K). These values are reachable with different orientations of the system or different air speeds. A constant stress σ_0 (typically 200 MPa) is applied to the wire, and the wire strain ε is a calculated output. The average temperatures of the wire and silicone sheath are dubbed T_1 and T_2 , respectively.

The deliberate choice to employ a straight wire as our reference actuator is motivated by the objective of this study, i.e. to provide generalisable contributions to the optimisation of SMA-based soft actuators. While the sheathed wire element can of course be viewed as a specific type of actuator, it is simple enough and free from geometrical complexities (other than the presence of a second material), that it can also be regarded as the most suitable case study to give general indications on the optimisation of a multimaterial system. Furthermore, with the right approximations, the actuator we have chosen can allow easy extension to 1-D modelling, and, as will be shown in the last chapter, is sufficiently informative to generate guidelines for the design of systems of a rather more complicated morphology.

As will be described in the next sections, the complete mathematical description of the proposed model comprises several sub-systems of equations, including constitutive relations for the SMA wire, evaluation of Joule's effect for an SMA conductor, and the heat transfer through the multimaterial.

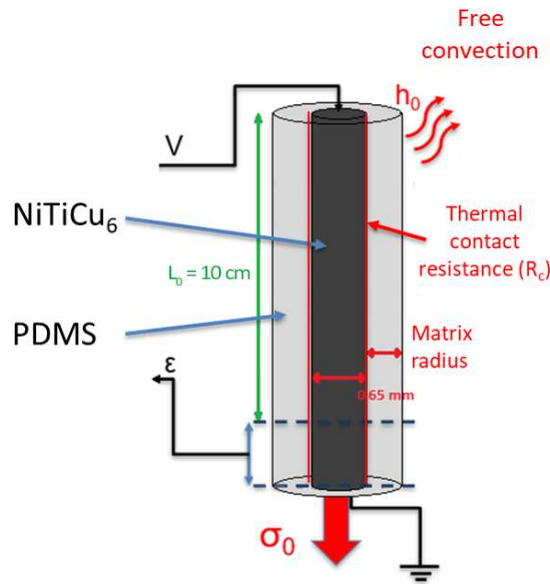


Figure 51 – Our target actuator. A linear SMA wire actuated by joule effect, surrounded by a silicone rubber in direct contact with the wire.

6.2. Constitutive modelling the SMA wire

In order to build a multimaterial model for our actuator, we chose to start from Brinson's model [64] since it is the most complete among the 0-D phenomenological models of SMA we reviewed. Furthermore, it is widely used, with many examples of its application to refer to in literature.

The constitutive law of Brinson's model is reported in Section 3.2.3.

For the sake of our modelling, we shall use:

$$\varepsilon = \frac{1}{D(\xi)} [\sigma - \sigma_i + D(\xi_i)\varepsilon_i - \Omega(\xi)\xi_S + \Omega(\xi_i)\xi_{S_i} - \theta(T_1 - T_{1_i})] \quad 6.1$$

instead of eq. 3.8. Here, the wire strain ε is the dependent variable; σ is the stress applied on the wire, D is the total elastic modulus, which is a linear combination of the elastic moduli of austenite and martensite, respectively D_A and D_M , proportionally to the total martensitic fraction ξ ; Ω is the stress/transformation coefficient and ε_L is the maximum transformation strain, and finally θ is the thermoelasticity modulus. The subscript i indicates the initial value of a variable. The subscript S refers to the stress-induced part of the martensitic fraction (which directly impacts on the transformation strain).

Part of the dependence on temperature and stress is dealt with by additional evolutionary relations of ξ . Brinson defined some laws to calculate the martensitic fraction during the evolution of the phase transformation: she did this by describing the transitions from and to different zones of the $\sigma - T$ plane, in which the system is austenitic, self-accommodated-martensitic, detwinned-martensitic, or some combination of these possibilities. The phase transition rules are presented in the next section, where we shall list them alongside new rules we have added specially for this work. The original versions can be found for comparison in Section 3.2.3.

Then, the length of the wire can be calculated as:

$$L = L_0(1 + \varepsilon) \quad 6.2$$

where L_0 is the initial wire length.

6.2.1. Modified Brinson model for the SMA

In order to describe fully the behaviour of our selected wire actuator, Brinson's model had to be completed with some further equations, which account for some observed but unmodelled effects. The changes we have made to the laws relating the martensitic fraction to the stress applied and the temperature of the wire, following Brinson, are described in the next sections. Briefly, we have made changes to the subdivision of the phase transformation zones originally devised by Brinson; we implemented specific algorithms with the aim to obtain the correct description of the phenomenology of partial and discontinuous transformations; and we introduced new equations in order to describe two-way shape memory.

After, we have also added some relationships describing the electrical response, as it is relevant for our chosen heating method, i.e. by Joule's effect.

6.2.1.1. *New transformation subzones*

The subdivision into new transformation zones was found necessary because the original model had a single level of conditional controls for each transformation zone. This could be a problem if the model equations were to be used in an implementation of a control system that makes use of the state-space representation. This issue can be solved by breaking down the transformation conditions into individual equations for each zone. Therefore, the

proposed and implemented solution relies on subdividing the original zone (III) into different subzones. The new zone 3 is where the conversion to twinned martensite takes place, below the critical stress σ_s^{cr} . The martensite detwinning takes place in the new zone 4, at temperatures below M_f . In the new zone 5, both effects can occur, depending on the zone-traversing path. This area of the state diagram is the most problematic: if taken as a single domain, specific transformations occurring here cannot be handled correctly. Our modified scheme introduces nested controls involving two independent conditions on the differentials of T_1 and σ (\dot{T}_1 and $\dot{\sigma}$, respectively). Practically, we divided zone 5 into 3 subzones (5', 5'' and 5''') according to different combinations of conditions on the signs of \dot{T}_1 and $\dot{\sigma}$. This means that the underlying domain is always the same as the whole zone 5, what changes among subzones is the direction of the traversing paths. In subzone 5''', conversion to twinned martensite takes place, in the same way as for zone 3 and with the same transformation equations. Likewise, the transformation described by subzone 5'' is equivalent to zone 4. Subzone 5' is active if the transformation path develops with simultaneous increases in the stress and decreases in the temperature, leading to martensite detwinning and, at the same time, also to a variation in the amount of twinned martensite. The original zones (I) and (II) did not need to be changed (nor did the corresponding transformation conditions), and were just renamed zone 1 and zone 2 for consistency. Figure 52 schematically shows the changes we have made to the original subdivision of the phase transformation zones by Brinson (Figure 16). The summary of the modified SMA model equations governing the martensitic fraction evolution for each new zone is reported in Section 6.2.1.4.

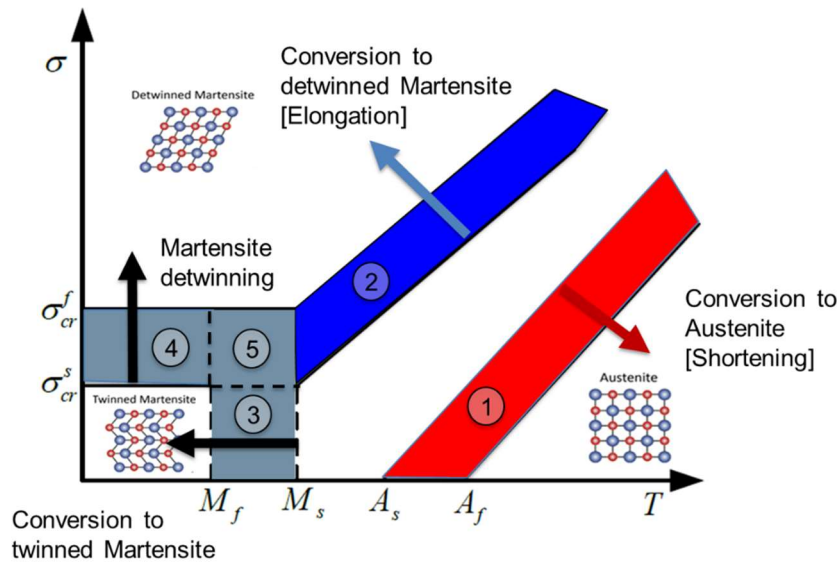


Figure 52 - Plane σ - T in which the new subdivision of the transformation zones is highlighted. The arrows schematically show the directions of the transformations.

6.2.1.2. Partial cycles and discontinuous transformations

A correct treatment of partial or discontinuous cycles of transformation is required when using the numerical model to simulate the SMA wire for the design of closed-loop control. In the Brinson kinetic laws, the transformations are dependent on the martensite fraction ζ_i that is present at the beginning of the transformation itself. Taking this memory term into consideration (as well as the other variables identified with the subscript i), small cycles are intrinsically modelled [130]. To achieve this, we introduced the provision that the system updates the starting value of T_{li} , σ_i , ζ_{Si} , ζ_{Ti} and ε_i , at the beginning of each transformation, and includes those variables in the equations in place of fixed starting points. Furthermore, it should be noted that the transformation equations give an indication of the ζ value as a function of the current temperature and stress values, but that this does not necessarily coincide with the amount of martensite that is actually present in the material, considering history. Since the transformations are one-way in each transformation zone, the new ζ value given by the formulas can be taken as effective only if it is higher than the one of the previous timestep, in the case of the direct martensitic transformation; otherwise it must be lower than the one in the previous timestep, for the inverse transformation. Only taking this effect into account discontinuous transformations can be fully described. The present actual ζ value was defined as ζ_{act} , and the relationships that establish whether it should be updated to the new ζ calculated by the use of the equations described so far, are listed in Section 6.2.1.4.

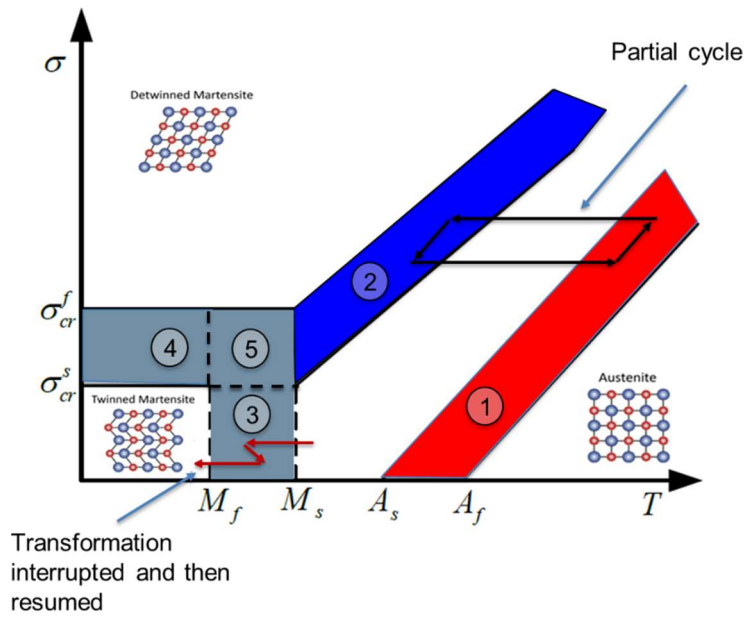


Figure 53 - Examples of transformation cycles in the σ - T plane. A partial cycle (black arrows) is characterised by alternating incomplete transformations. A transformation is discontinuous if it is interrupted and resumed without an inverse transformation is taking place (red arrows).

6.2.1.3. Two-way shape memory (TWSME)

One other important modification we deemed necessary was the explicit introduction of the TWSME in the equations. Due to repeated thermomechanical actuation during the stabilisation process, our NiTiCu₆ wire developed this effect. Hence, when the martensitic transformation occurs at low stresses, we observe the formation of a non-negligible fraction of single-variant martensite ζ_S . This is not typical of an untrained SMA as the one modelled by Brinson.

To model this effect, we imposed that some of the twinned martensite be directly transformed into detwinned martensite, independent of stress (i.e. even for null stress). The self-transforming fraction can be calculated by the use of proportionality constant χ , which we called the TWSME retransformation coefficient, and which for our wire has been estimated equal to 0.8. Therefore, we first calculate actual martensitic fractions ζ_{Sact} and ζ_{Tact} using the original equations without TWSME, then we account for the stress-induced martensitic fraction created by the TSWME with equations 6.25 and 6.26.

6.2.1.4. Summary of the modified SMA model equations

The modified laws that account for the effects presented above have been added to the relationships developed by Brinson. The final complete list of the equations governing the martensitic fraction evolution for each zone is as follows:

- Zone 1 - Conversion to Austenite:

if $\left[\left(A_s < T_1 - \frac{\sigma}{C_A} < A_f \right) \right]$ then

$$\xi = \frac{\xi_i}{2} \left\{ \cos \left[a_A \left(T_1 - T_{1i} - \frac{\sigma}{C_A} \right) \right] + 1 \right\} \quad 6.3$$

$$\xi_S = \frac{\xi_{S_i}}{\xi_i} \xi \quad 6.4$$

$$\xi_T = \frac{\xi_{T_i}}{\xi_i} \xi \quad 6.5$$

- Zone 2 - Conversion to detwinned Martensite:

if $[(T_1 > M_s) \wedge (\sigma_S^{cr} < \sigma - C_M(T_1 - M_s) < \sigma_F^{cr})]$ then

$$\xi_S = \frac{1 + \xi_{S_i}}{2} + \frac{1 - \xi_{S_i}}{2} \cos \{ a_M [\sigma - \sigma_F^{cr} - C_M(T_1 - M_s)] \} \quad 6.6$$

$$\xi_T = \frac{\xi_{T_i}}{1 - \xi_{S_i}} (1 - \xi_S) \quad 6.7$$

- Zone 3 - Conversion to twinned Martensite:

if $[(M_s < T_1 < M_f) \wedge (\sigma < \sigma_S^{cr})]$ then

$$\xi_S = \xi_{S_i} \quad 6.8$$

$$\xi_T = \frac{(1 - \xi_{S_i}) + \xi_{T_i}}{2} + \frac{(1 - \xi_{S_i}) - \xi_{T_i}}{2} \cos [a_{TM}(T_1 - M_f)] \quad 6.9$$

- Zone 4 - Martensite detwinning:

if $[(T_1 < M_f) \wedge (\sigma_S^{cr} < \sigma < \sigma_F^{cr})]$ then

$$\xi_S = \frac{1 + \xi_{S_i}}{2} + \frac{1 - \xi_{S_i}}{2} \cos [a_X(\sigma - \sigma_F^{cr})] \quad 6.10$$

$$\xi_T = \frac{\xi_{T_i}}{1 - \xi_{S_i}} (1 - \xi_S) \quad 6.11$$

- Zone 5 - Martensite detwinning and conversion to twinned Martensite. This zone is peculiar since the equations depend also on the combination of the temperature and stress derivatives:

if $[(M_s < T_1 < M_f) \wedge (\sigma_s^{cr} < \sigma < \sigma_F^{cr})]$ then

- Zone 5' - cooling and loading:

if $[(\dot{T}_1 < 0) \wedge (\dot{\sigma} > 0)]$ then

$$\xi_S = \frac{1 + \xi_{S_i}}{2} + \frac{1 - \xi_{S_i}}{2} \cos[a_\Sigma(\sigma - \sigma_F^{cr})] \quad 6.12$$

$$\xi_T = \frac{(1 - \xi_S) + \xi_{T_i}}{2} + \frac{(1 - \xi_S) - \xi_{T_i}}{2} \cos[a_{TM}(T_1 - M_f)] \quad 6.13$$

- Zone 5'' - heating and loading:

if $[(\dot{T}_1 \geq 0) \wedge (\dot{\sigma} > 0)]$ then

$$\xi_S = \frac{1 + \xi_{S_i}}{2} + \frac{1 - \xi_{S_i}}{2} \cos[a_\Sigma(\sigma - \sigma_F^{cr})] \quad 6.14$$

$$\xi_T = \frac{\xi_{T_i}}{1 - \xi_{S_i}} (1 - \xi_S) \quad 6.15$$

- Zone 5''' - cooling and unloading:

if $[(\dot{T}_1 < 0) \wedge (\dot{\sigma} \leq 0)]$ then

$$\xi_S = \xi_{S_i} \quad 6.16$$

$$\xi_T = \frac{(1 - \xi_{S_i}) + \xi_{T_i}}{2} + \frac{(1 - \xi_{S_i}) - \xi_{T_i}}{2} \cos[a_{TM}(T_1 - M_f)] \quad 6.17$$

The shorthand parameters appearing in the equations are:

$$a_A = \frac{\pi}{A_F - T_{1i} + \frac{\sigma_i}{C_A}} \quad 6.18$$

$$a_M = \frac{\pi}{\sigma_i - \sigma_{cr}^f - C_M(T_{1i} - M_s)} \quad 6.19$$

$$a_{TM} = \frac{\pi}{T_{1i} - M_f} \quad 6.20$$

$$a_\Sigma = \frac{\pi}{\sigma_i - \sigma_{cr}^f} \quad 6.21$$

Then, ξ_S and ξ_T values are used to update the present values ξ_{Sact} and ξ_{Tact} if and only if:

$$\text{in zone 1} \quad \rightarrow \quad (1 - \xi_S - \xi_T) > (1 - \xi_{Sact} - \xi_{Tact}) \quad 6.22$$

$$\text{in zones 2, 4, 5', 5''} \quad \rightarrow \quad \xi_S > \xi_{Sact} \quad 6.23$$

$$\text{in zones 3, 5''' } \quad \rightarrow \quad \xi_T > \xi_{Tact} \quad 6.24$$

Finally, with the following equations we calculate the actual martensitic fractions accounting for the stress-induced martensitic fraction created by the TSWME:

$$\xi_{Sact}^{TSWME} = \xi_{Sact} + \chi \cdot \xi_{Tact} \quad 6.25$$

$$\xi_{Tact}^{TSWME} = (1 - \chi) \cdot \xi_{Tact} \quad 6.26$$

6.2.2. Tuning of the constitutive SMA model parameters

In order to assess the model behaviour against functional measurements obtained from the real wire, we used the stress-recovery curves discussed in Section 4.5 as ground truth.

The modified SMA wire model was firstly implemented in Simulink without the Joule's heating part (the complete implementation is reported in Section 6.4.4). The input to the system was directly the wire temperature T_l , as was the case in the experimental tests. We ran preliminary simulations to assess the correct functioning of the numerical implementation, and in view to optimise further the constitutive SMA parameters.

Simulations of complete heating and cooling cycles have been carried out. Ramps on the wire mean temperature T_l were imposed at different constant stresses, allowing the wire to cycle between 20 °C and 100 °C.

To improve stress-recovery curve fitting, we executed many transformation cycles, tuning the model parameters one at a time to approximate better the real wire behaviour. The parameters have been firstly chosen to optimise the strain levels at low and high temperatures. Since the experimental measurements are very noisy during the cooling phase, it was then decided to fit the curves in the best possible way during the heating phase.

In Figure 54 we can see the comparison between our final simulated curves (dashed), and the measured behaviour of the real wire (continuous).

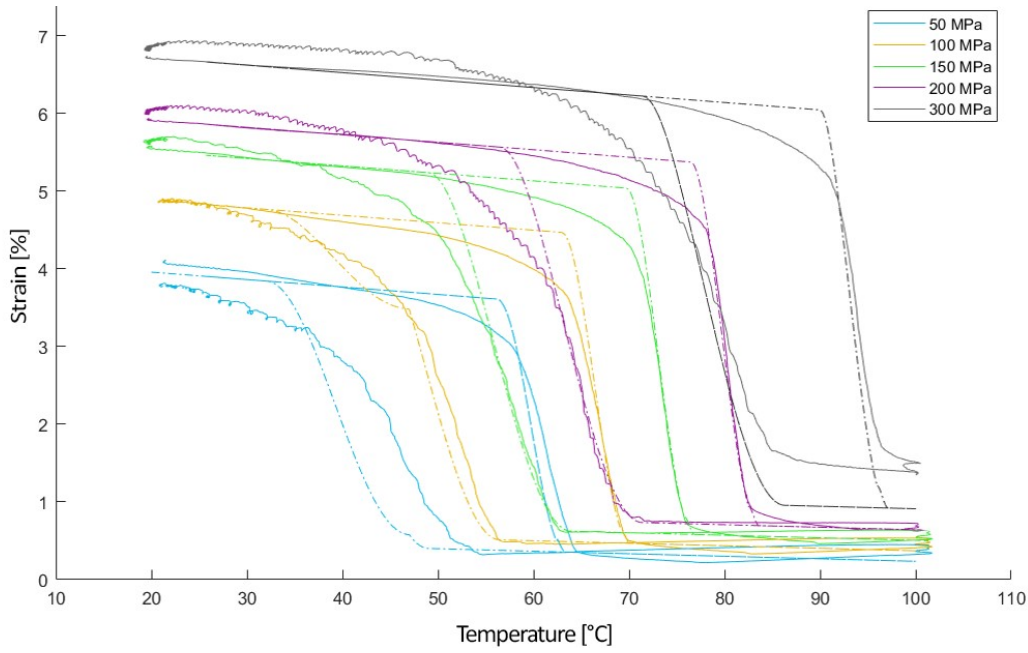


Figure 54 - Comparison between measured (continuous curves) and simulated (dashed curves) strain-recovery curves.

The best accordance between the simulated and real behaviour can be observed for medium stress curves (from 100 to 200 MPa). For the 50 MPa curve, a larger difference can be noticed at low temperatures during the cooling phase. For the 300 MPa curve a discrepancy is present at high temperatures, where the real wire shows unrecovered strains of 1.5 % and our model predicts an unrecovered strain of 1 %. Furthermore, in all curves there are some differences at the end of the martensitic transformation and at the beginning of the austenitic one, due to the possible presence of some orthorhombic phase.

The final best-fit values of the constitutive model parameters for our chosen NiTiCu₆ wire are listed in Table 7 (Section 6.5).

6.3. Modelling of Joule's effect in the SMA wire

In our model, the power input that enables heating of the SMA wire is provided by Joule's effect. In particular, the electric power injected can be calculated as:

$$P_{In} = \frac{V_{In}^2}{R_{el}} \quad 6.27$$

where the wire resistance is a function of the martensite fraction:

$$R_{el} = \frac{L_0(1 + \varepsilon(\xi))}{A_0(1 - \nu_{NiTi}\varepsilon(\xi))^2} [\rho_A + \xi(\rho_M - \rho_A)] \quad 6.28$$

In this equation, that takes into account the wire deformation and the resistivity change between the cubic and monoclinic crystals, L_0 is the initial wire length, A_0 is the initial wire area and ν_{NiTi} is the Poisson's ratio, while ρ_A and ρ_M are the electrical resistivities of austenite and martensite, respectively. Of the total incoming power, the share used to carry out mechanical work – $\sigma \dot{\epsilon}$ by unit volume – is negligible (SMA actuation efficiency is of the order of 3% [9]), while the part transmitted as heat through the PDMS sheath (i.e. eventually dissipated) is discussed in detail in Section 6.4. The remaining share of power, used to sustain the phase change in the SMA, can be expressed as follows:

$$P_{Lh} = m_l L_h \dot{\xi} \quad 6.29$$

where m_l is the mass of the wire and L_h is the latent heat (specific transformation enthalpy) term.

Table 8 lists the SMA parameters, taken from literature [131], we used in the Joule's heating equations. In relation to the kinetics of Joule's effect in the 0-D model, the wire heating is considered instantaneous, i.e. without delay relative to the electric power input ($T = T_l$, average wire temperature). In fact, the mechanical response of SMAs under a rapid heating impulse has been experimentally studied in [132] and a characteristic response time of some tens of microseconds has been identified, between the heating impulse and the SMA wire response ($d = 0.2$ mm). The modelling of thermal transfer will be discussed in the case of 0-D and 1-D multimaterial in Section 6.4.3, where the parameters characterising the thermal diffusivity of SMA are reported in Table 9 (Section 6.5).

6.4. Modelling of the multimaterial interaction in the SMA/PDMS actuator

After the development of the SMA wire model we move on to consider the interaction between the wire and the soft matrix. This section describes the assumptions and model equations that we added to the SMA constitutive relations, in order to describe the effects of the matrix, particularly from the thermal point of view.

6.4.1. Mechanical interaction

The interface between the two materials is considered tight and stable. The mechanical contribution of the soft matrix on the overall stiffness is neglected with respect to the external applied force due to its low stiffness and small thickness.

6.4.2. Thermal interactions and material properties

The wire was chosen much longer than its diameter, so heat transfer through the two ends of the wire can be ignored. The two end faces have therefore been considered adiabatic. The heat transfer occurs completely through the soft matrix. The PDMS layer is placed between the wire and the surrounding air, strongly conditioning its thermal behaviour. The thermophysical properties characterising the two materials are listed in Table 9 and Table 10 (Section 6.5). The SMA parameters were taken from literature [131], while the reference parameters of the polymer matrix are those measured, as explained in Section 5.4.2, for plain Ecoflex™ 00-30.

The thermal contact resistance of the interface between the wire and the matrix has been modelled as an equivalent thin resistive layer.

Its value was estimated after an analysis of the literature. Models have been presented to represent the thermal contact resistance in polymer-metal junctions, but only in the case of rough materials as in [133].

In [134], the thermal contact resistance at the metal-elastomer interface was measured experimentally on flat samples, and it has been found that it changes slightly with the pressure exerted on the samples and the incoming heat flux.

In order to obtain a reliable result experimentally, it is necessary to be able to measure the temperature gradient in the silicone matrix once it is fully operational. For thin SMA wires as in our case, the heat flux levels at the interface between the two materials reported in [134] are obtained with energy values injected into the SMA wire such that they raise its temperature by tens of °C over a period of a second. The difficulty in measuring the thermal resistance in our case therefore lies in the fact that the equilibrium condition is at very high temperatures (beyond the range of use).

Although we expect the heat flux at the interface to be higher during activation and then to stabilise during wire cooling, we have chosen to use a constant value of R_c which is approximately equal to the mean value measured in [134]. This is because we expect to have heat fluxes of a value similar to those reported (i.e. of the order of few kW/m²), and because the variability of the contact resistance with the flux is relatively small. Then, for simulations involving automatic control, we assumed R_c equal to $1.5 \cdot 10^{-3}$ (K·m²)/W. Finally, a parametric study of the influence of thermal contact resistance R_c variability on the performance of SMA-based soft robots will be presented in Chapter 8.

6.4.3. Different implementations of multimaterial heat transfer for the 0-D and 1-D simulations

The 0-D and 1-D models of the actuator will be used to study different effects.

Lumped parameter modelling is chosen for its low computational requirements to mimic the wire during the designing and testing of an automatic controller. To study the closed-loop control of the multimaterial actuator, the algorithm implemented in Simulink needs simplified equations not only for the wire, but also for its interaction with the matrix. For this reason, we have developed a lumped parameter model to describe the heat transfer between the two materials. The use of the average temperature of the soft matrix instead of the temperature distribution is a valid simplification under the condition that the Biot number $Bi = \frac{hL}{k} \ll 1$, where L is a characteristic length (for a cylinder it is equal to half the radius), h is the convective coefficient of exchange with air, and k is the thermal conductivity of the matrix. In order to verify this condition, and be able to work with average temperatures, a constant thickness of the matrix equal to 1 mm was chosen for the lumped parameter model implementation.

Considering instead the finite element simulations, the 1-D model can better explain the interplay of different factors, such as the matrix sheath thickness, the value of interface contact resistance, and the variations in matrix thermal diffusivity as produced by PDMS modification with GNPs. Since the thickness r_M of the soft matrix has to be varied during this type of study of the matrix functionalisation, the numerical analyses carried out in COMSOL exploited the use of a distributed parameter thermal model, where not the average temperature, but the temperature distribution along the matrix radius is evaluated at every timestep.

Given the high thermal diffusivity of the SMA material compared to that of the polymer matrix, we assumed the wire to be isothermal. Therefore, in both implementations, the lumped parameter equations describing the transformation kinetics of the SMA (cf. Section 6.2.1) have as input the mean temperature of the wire T_1 .

6.4.4. Lumped parameter implementation of the SMA/Matrix heat transfer

According to the lumped methodology, each of the two materials can be described with a single thermal capacity having a unique temperature. The two main state variables of the thermal model are T_1 , the wire temperature, and T_2 , the silicone average temperature. The

lumped system can be described as an equivalent electric circuit composed by two thermal resistances and the two capacitances properly connected. The lumped parameter network model of the multimaterial actuator is depicted in Figure 55. Our model is similar to the one presented by F. Scarpa and M. De Rosa about the heat conduction in insulated electric wires [135]. The differences are in the addition of the latent heat of transformation and the thermal contact resistance between SMA and PDMS. The latent heat term, which depends on the derivative of the martensitic fraction (cf. equation 6.29) is negative when the SMA is transforming into austenite and the energy is absorbed, and positive when the phase is changing into martensite (exothermic process). The thermal resistance between the wire and the matrix is R_{t1} , while R_{t2} is the thermal resistance between the matrix and the surrounding air.

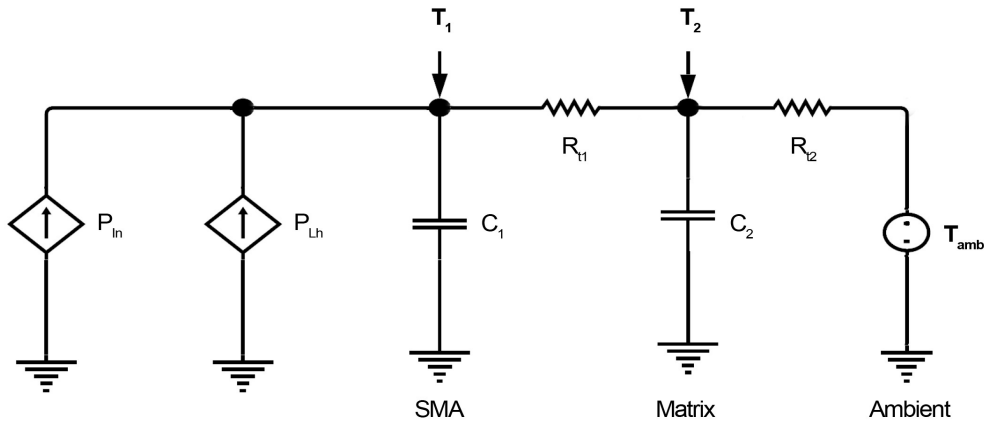


Figure 55 - Lumped parameter network model of the target multimaterial actuator. P_{in} is the heat generated by Joule's effect, P_{Lh} is the latent heat absorbed or released during phase transformations, C_1 and C_2 are the wire and matrix heat capacities, while R_{t1} , and R_{t2} are the heat transfer resistances at the interfaces between wire and matrix, and between matrix and air. Finally, T_1 , T_2 and T_{amb} are the average temperatures of the wire matrix, and surrounding environment.

The equivalent lumped parameter heat transfer equations are:

$$m_1 c_1 \dot{T}_1 = \frac{V_{In}^2}{R_{el}} + m_1 L_h \dot{\xi} - \frac{T_1 - T_2}{R_{t1}} \quad 6.30$$

$$m_2 c_2 \dot{T}_2 = \frac{T_1 - T_2}{R_{t1}} - \frac{T_2 - T_{amb}}{R_{t2}} \quad 6.31$$

where m_1 and m_2 are the masses of the wire and matrix, c_1 and c_2 are their respective specific heat capacities.

The equations of the two thermal resistance are:

$$R_{t1} = \frac{1}{L} \left(\frac{R_c}{2\pi r_1} + \frac{\ln \frac{r_h}{r_1}}{2\pi k_{PDMS}} \right) \quad 6.32$$

$$R_{t2} = \frac{1}{L} \left(\frac{\ln \frac{r_2}{r_h}}{2\pi k_{PDMS}} + \frac{1}{2\pi r_2 h} \right) \quad 6.33$$

where L is the length of the actuator, R_c is the interface thermal contact resistance between the SMA and the PDMS, k_{PDMS} is the thermal conductivity of the silicone rubber and h is the convective heat transfer coefficient.

The characteristic radii of the device are:

- r_1 , the radius of the SMA wire;
- r_2 , the sum of the SMA wire radius r_1 and the matrix thickness t_M ;
- r_h , the sum of the SMA wire radius r_1 and the half of the matrix thickness t_M ;

The wire temperature T_1 , as is evident, is determined by the input power and the interplay of different dissipation terms, including in particular the matrix characteristics, and the wire phase transformation. Now, as the SMA model shows, the phase transformation is itself primarily dependent on T_1 and \dot{T}_1 , so it is clear that the constitutive model of the wire and the heat transfer model are tightly coupled and form a complex non-linear system of equations.

The implementation in Simulink sees the equations of the lumped parameter thermal model interact with the other equations of the SMA wire model. T_1 and T_2 are obtained by numerically integrating equations 6.30 and 6.31. Then, the current zone of the σ - T plane is obtained using the current information on the stress, the wire temperature T_1 and their derivatives.

SMA model equations from Section 6.2.1.4 are implemented to compute the current ζ_S and ζ_T . Each equation, contained in a specific subsystem, is enabled by the respective zone boolean signal. The initial values of the system variables at the beginning of the new zone (the variables with subscript i) are updated to the value of that variable at the previous time instant, and are kept constant until the next zone commutation. The variables which need their value to be stored are T_1 , σ , ζ_S , ζ_T and ε .

Finally, the constitutive model equations block computes the strain ε according to equation 6.1. For the computation of the electric resistance, the thermal resistances and the latent heat of transformation term, ε , ξ_S and ξ_T are necessary. In order to avoid algebraic loop errors, the value of the three variables calculated at the previous cycle are used instead of the current ones. Furthermore, the derivative of ξ is low-pass filtered at 5 Hz to avoid instability. All the simulations are executed with a time step t_s of 0.005 s.

Schematically, the computational iteration loop can be represented as follows:

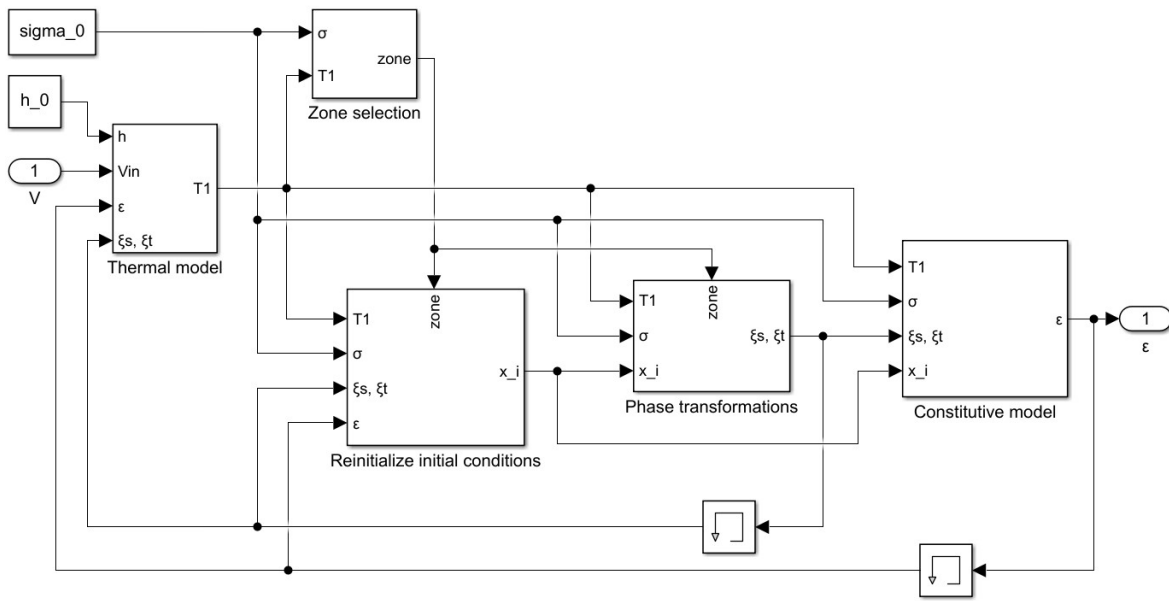


Figure 56 – Schematic of the SMA wire lumped parameter implementation in Simulink.

6.4.5. Distributed parameter implementation of the SMA/Matrix heat transfer

The distributed parameter implementation of the heat transfer model is based on the use of the 1-D axisymmetric representation of the actuator in COMSOL multiphysics.

The temperature distribution in the matrix is considered to be a function of the radial coordinate, and of time, and is obtained by integrating the one-dimensional version of the heat equation (in cylindrical coordinates):

$$0 < r < r_1 \quad \delta_{NiTi} c_1 \frac{\partial T_{NiTi}}{\partial t} = \frac{\left(\frac{V_{In}}{L_0(1+\varepsilon)} \right)^2}{\rho_A + \xi(\rho_M - \rho_A)} + \delta_{NiTi} L_h \frac{\partial \xi}{\partial t} + \frac{1}{r} \frac{\partial}{\partial r} \left(k'_{NiTi} r \frac{\partial T_{NiTi}}{\partial r} \right) \quad 6.34$$

$$r_1 < r < r_2 \quad \delta_{Si} c_2 \frac{\partial T_{PDMS}}{\partial t} = \frac{1}{r} \frac{\partial}{\partial r} \left(k'_{PDMS} r \frac{\partial T_{PDMS}}{\partial r} \right) \quad 6.35$$

where t is the time, r is the radial coordinate, r_1 and r_2 are the characteristic radii of the device, ε is the wire strain, k' is the equivalent thermal conductivity, δ is the density, c is the specific heat and L_h is the latent heat term. The length of the actuator was taken into account in order to calculate the equivalent volumetric power density. Furthermore, since the two equations describe the system only along the radial coordinate, to take into account the elongation of the wire, the equivalent thermal parameters are calculated as follows:

$$k'_{PDMS} = k_{PDMS}(1 + \varepsilon) \quad 6.36$$

$$k'_{NiTi} = [k_{NiTi-Austenite} + \xi(k_{NiTi-Martensite} - k_{NiTi-Austenite})](1 + \varepsilon) \quad 6.37$$

$$h' = h(1 + \varepsilon) \quad 6.38$$

$$R'_c = R_c/(1 + \varepsilon) \quad 6.39$$

Equations 6.34 and 6.35 are coupled with the initial condition:

$$[t = 0; 0 \leq r \leq r_2] \rightarrow T_{PDMS}(r) = T_{NiTi}(r) = T_{amb} \quad 6.40$$

and the following boundary conditions:

$$[t \geq 0; r = 0] \rightarrow \left. \frac{\partial T_{NiTi}}{\partial r} \right|_{r=0} = 0 \quad 6.41$$

$$[t \geq 0; r = r_1] \rightarrow \begin{aligned} T_{NiTi}(r_1) &= T_{PDMS}(r_1) + R'_c k'_{PDMS} \left. \frac{\partial T_{PDMS}}{\partial r} \right|_{r=r_1}; \\ k'_{SMA} \left. \frac{\partial T_{NiTi}}{\partial r} \right|_{r=r_1} &= k'_{PDMS} \left. \frac{\partial T_{PDMS}}{\partial r} \right|_{r=r_1} \end{aligned} \quad 6.42$$

$$[t \geq 0; r = r_2] \rightarrow -k'_{PDMS} \left. \frac{\partial T_{PDMS}}{\partial r} \right|_{r=r_2} = h'[T_{PDMS}(r_2) - T_{amb}] \quad 6.43$$

In this case, the system combining the SMA constitutive model, Joule's heating, and the heat exchange equations is still tightly coupled. The practical implementation is further complicated by the multiscale nature of the system (0-D for the wire model, 1-D for the heat transfer problem in the matrix). The solution is obtained by running the thermal distributed parameter problem in COMSOL, coupled with LiveLink™ for MATLAB. The computational iteration scheme is similar to the one presented for the lumped parameter implementation. Also in this implementation the simulation time step t_s was 0.005 s.

In this case, to reduce the 1-D heat transfer problem to the 0-D one needed by the SMA model, the wire mean temperature T_l was calculated by the use of the average operator in COMSOL. The management of transformation zones and initial state value update was possible thanks to the use of COMSOL discrete states and implicit events.

6.5. Materials tabulated parameters

Table 7 - Optimised values of the constitutive model parameters for the chosen NiTiCu₆ wire.

Parameter	Value
M_f	32.1 °C
M_s	47 °C
A_s	49.4 °C
A_f	56.6 °C
ε_L	3.953 %
D_A	37 GPa
D_M	12.5 GPa
σ_S^{cr}	36.7 MPa
σ_F^{cr}	136.7 MPa
C_A	7.4 MPa/°C
C_M	6.7 MPa/°C
Θ	1.2 MPa/°C
L_h	16.18 J/g

Table 8 - Tabulated parameters used to model Joule's effect in SMA [131].

Parameter	Value
ρ_A	1 $\mu\Omega\cdot m$
ρ_M	0.8 $\mu\Omega\cdot m$
ν_{NiTi}	0.33

Table 9 – Tabulated parameters used to describe thermal diffusivity in SMA [131].

Parameter	Value
ρ_{NiTi}	6.45 g/cm ³
c_1	0.8368 J/(g·K)
$k_{NiTi-Austenite}$	18 W/(m·K)
$k_{NiTi-Martensite}$	8.6 W/(m·K)

Table 10 – Measured parameters used to describe the thermal diffusivity of the plain polymer matrix (Ecoflex™ 00-30).

Parameter	Value
ρ_{PDMS}	1.028 g/cm ³
c_2	1.22 J/(g·K)
k_{PDMS}	0.28 W/(m·K)

6.6. Basic testing and comparison of the model implementations

6.6.1. Cross-validation of the numerical models

In order to test the lumped parameter model accuracy, I compared it to the distributed parameter one which represents our better truth model.

I verified the complete operating cycle by applying a voltage pulse of different values to the SMA at room temperature, letting it cycle between 100 % Austenite and back to 100 % Martensite. I stopped the simulations when the wire was cooled down to M_F . I used a constant stress $\sigma_0 = 200$ MPa in all these simulations.

In addition to the need to compare the two models, the basic tests were used to choose the best supply voltage to use in subsequent simulations. Besides increasing the speed of actuation, high heating rates provide lower energy consumption and better performance in SMA [136]. In SMA-based soft robots, high current pulses with short time periods limit heat dissipation [30]. It is equally true that this value cannot be too high, so as to prevent overheating and thermal fatigue, therefore the maximum heating rate at which the NiTi wires can be heated safely must be estimated. In fact, the heating rate can have a negative effect on the structural and functional fatigue of shape memory wires undergoing thermomechanical cycling [137].

In the five figures shown below, it is possible to see the trends of the simulated temperatures and the differences between the results of the two models, as V_{in} and the convection coefficient h vary. In the temperature graphs, the Simulink results are in blue while the temperatures simulated in COMSOL are in red. The mean temperature of the SMA wire T_1 is represented with the solid line while the mean temperature of the soft matrix T_2 is the dashed line. The dotted line highlights the M_f value at which the simulation is interrupted.

The graphs showing the trend of the error e over time use the solid line for the difference between the two T_1 and the dashed line for the difference between the T_2 .

The first value of the voltage impulse chosen was equal to 0.5 V (Figure 57). The time required to reach the target temperature is greater than 50 s, and increases with the increase in the convection coefficient h . For h equal to 35 W/(m²·K), the target temperature is not even reached. The maximum heating rate value is approximately 5.3 °C/s with an h value of 5 W/(m²·K).

With a voltage of 0.75 V the variability of the actuation time is lower (22–27 s) and the maximum heating rate value is approximately 11.9 °C/s (Figure 58).

The time necessary to reach the target temperature with a voltage of 1 V is approximately 10 s, almost constant as the coefficient h varies, as is the maximum heating rate equal to approximately 21.1 °C/s (Figure 59).

With voltages higher than 1 V, the effect of convection on the temperature trend, during the heating pulse begins to be negligible. With V_{in} equal to 2 V and 3 V, actuation times of 1.22 s and 0.47 s are obtained respectively, and the maximum heating rates are equal to 84.4 °C/s and 189.9 °C/s (Figure 60 and Figure 61). In these cases, h affects only the cooling rate.

Since the maximum heating rate value obtained with V_{in} equal to 3V is already very high, I have not performed tests at higher voltage values.

A comparison between the two models was then carried out. The maximum value of the error on the SMA wire mean temperature T_1 , calculated as the maximum of the absolute value of the difference between the two simulated temperatures, is shown in Table 11. The highest value is equal to 2.878 °C. While at low power supply voltage it varies with the value of h , at high power supplies it is constant and equal to 2.083 °C ($V_{in} = 2$ V) and 1.907 °C ($V_{in} = 3$ V).

The mean value of the error on T_1 , calculated as the average of the absolute value of the difference between the two simulated temperatures, is shown in Table 12. This error is higher at higher voltages, but always lower than 1 °C.

Table 13 shows the average value of the error on the soft matrix mean temperature T_2 . In all the simulations carried out, it also remained below 1 °C.

Table 11 – Maximum value in °C of the error on T_1 between lumped and distributed parameter implementation.

		$h [W/(m^2 \cdot K)]$		
		5	15	35
$V_{In} [V]$	0.5	2.158	3.818	0.247
	0.75	2.235	1.731	0.638
	1	2.878	2.545	1.747
	2	2.083	2.083	2.083
	3	1.907	1.907	1.907

Table 12 - Mean value in °C of the error on T_1 between lumped and distributed parameter implementation.

		$h [W/(m^2 \cdot K)]$		
		5	15	35
$V_{In} [V]$	0.5	0.182	0.338	0.092
	0.75	0.237	0.265	0.195
	1	0.418	0.515	0.586
	2	0.485	0.620	0.841
	3	0.448	0.569	0.760

Table 13 - Mean value in °C of the error on T_2 between lumped and distributed parameter implementation.

		$h [W/(m^2 \cdot K)]$		
		5	15	35
$V_{In} [V]$	0.5	0.576	0.513	0.880
	0.75	0.402	0.269	0.585
	1	0.581	0.561	0.481
	2	0.736	0.792	0.887
	3	0.761	0.799	0.873

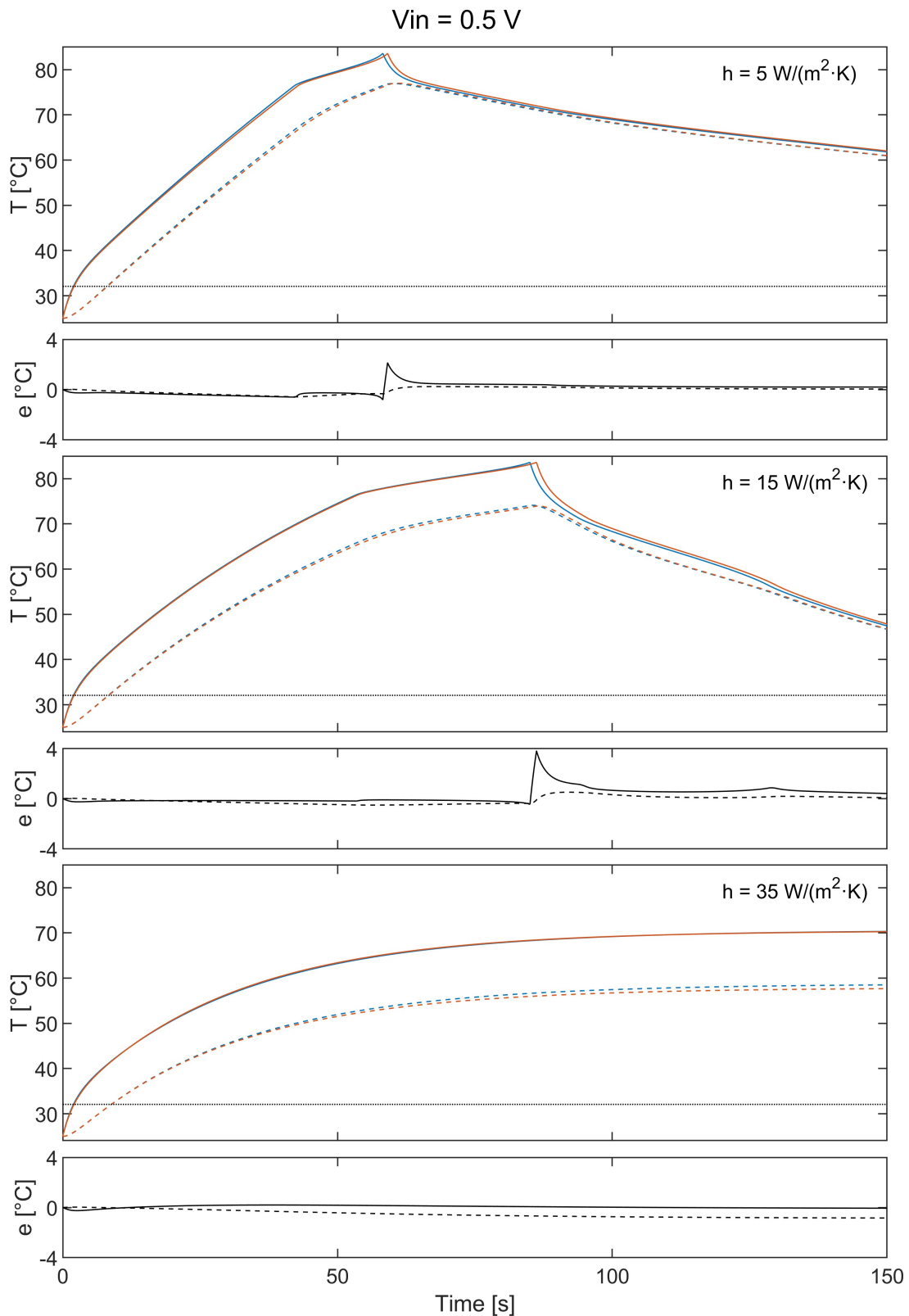


Figure 57 - Comparison of the temperatures simulated in COMSOL (red) and Simulink (blue) with a voltage pulse of 0.5 V for three convection coefficients. In addition to the temperature trend, the differences between the two implementations are shown, with the solid line for T_1 and the dashed line for T_2 . All the simulations are interrupted when M_f temperature is reached (dotted line).

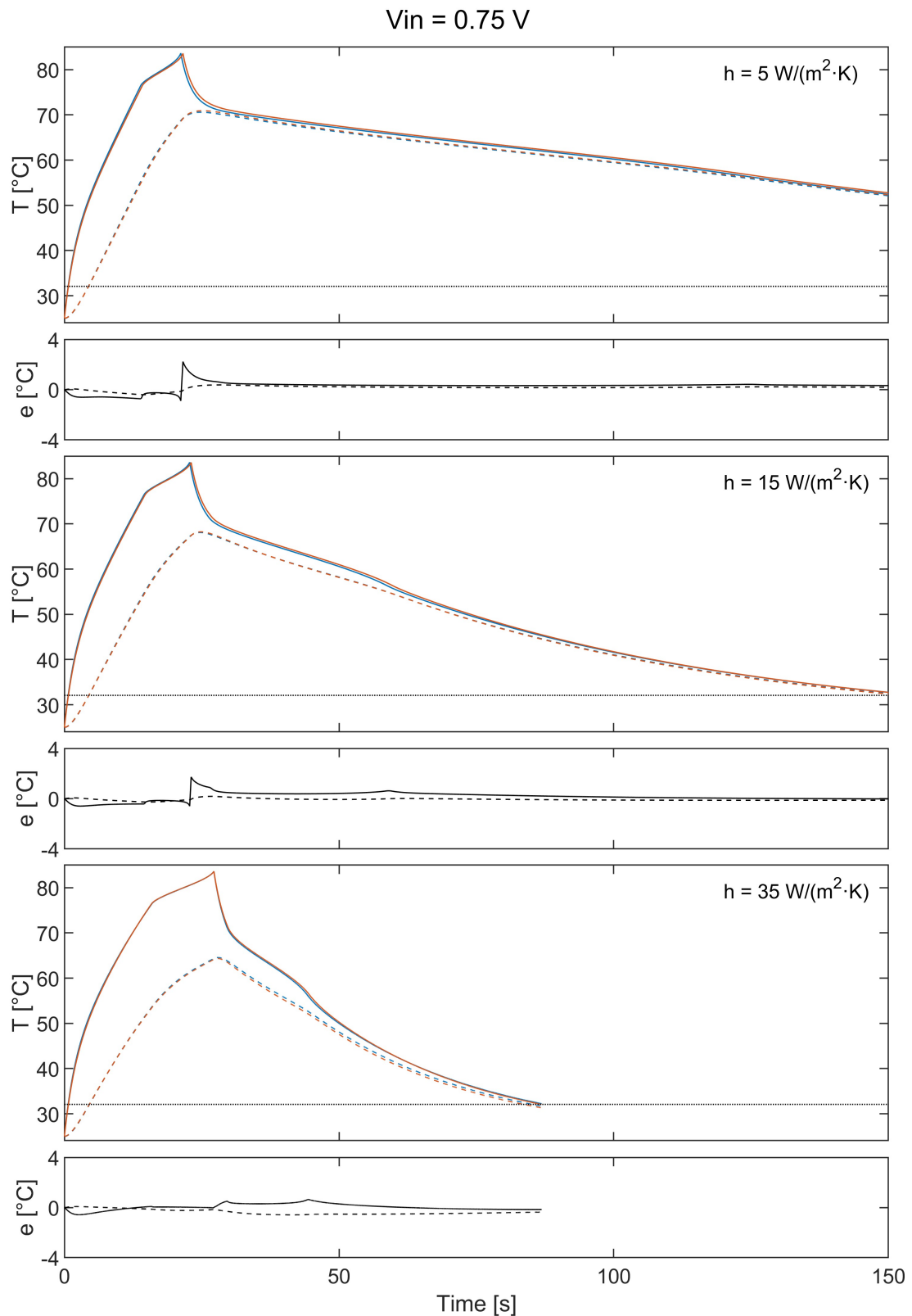


Figure 58 - Comparison of the temperatures simulated in COMSOL (red) and Simulink (blue) with a voltage pulse of 0.75 V for three convection coefficients. In addition to the temperature trend, the differences between the two implementations are shown, with the solid line for T_1 and the dashed line for T_2 . All the simulations are interrupted when M_f temperature is reached (dotted line).

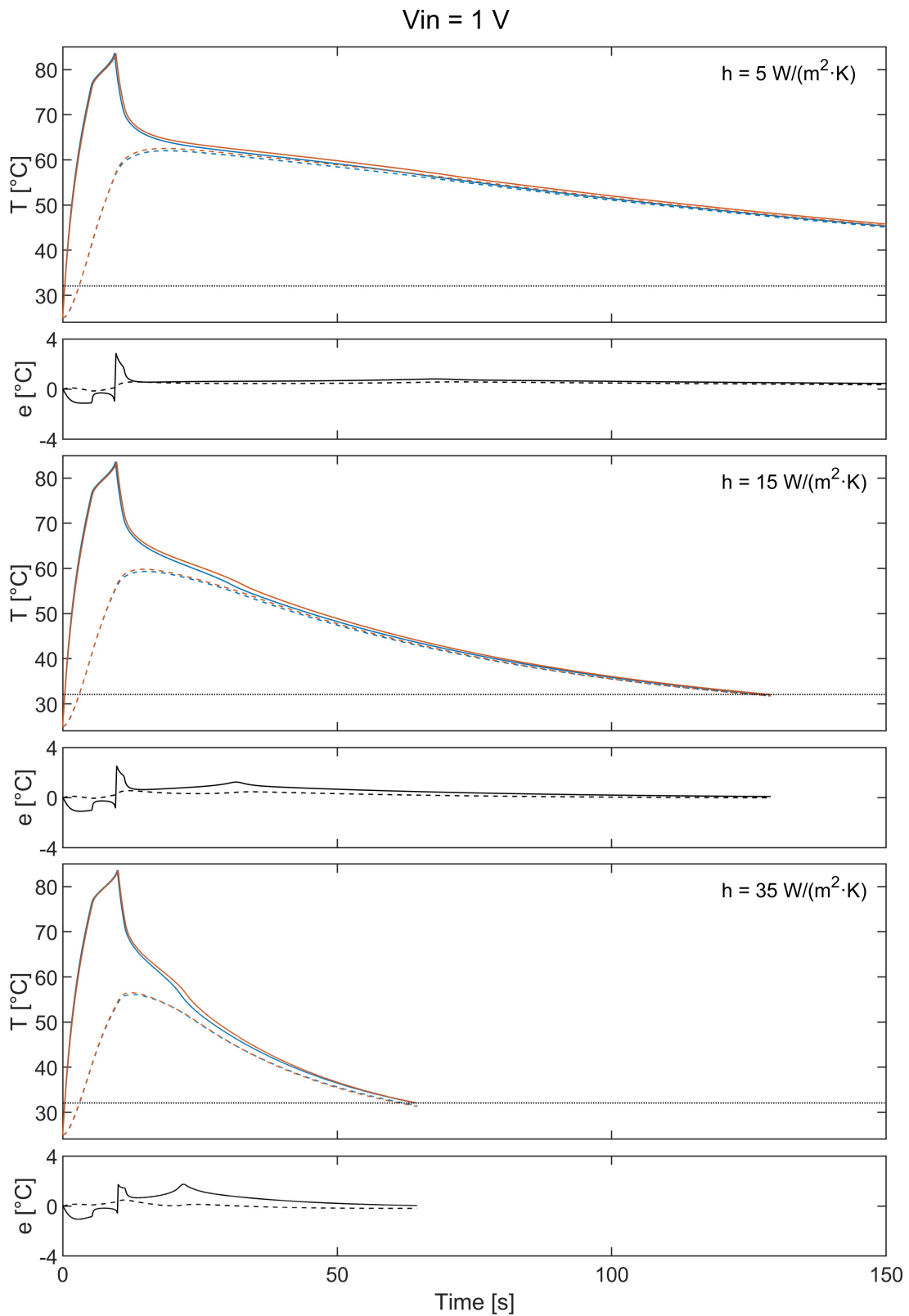


Figure 59 - Comparison of the temperatures simulated in COMSOL (red) and Simulink (blue) with a voltage pulse of 1 V for three convection coefficients. In addition to the temperature trend, the differences between the two implementations are shown, with the solid line for T_1 and the dashed line for T_2 . All the simulations are interrupted when M_f temperature is reached (dotted line).

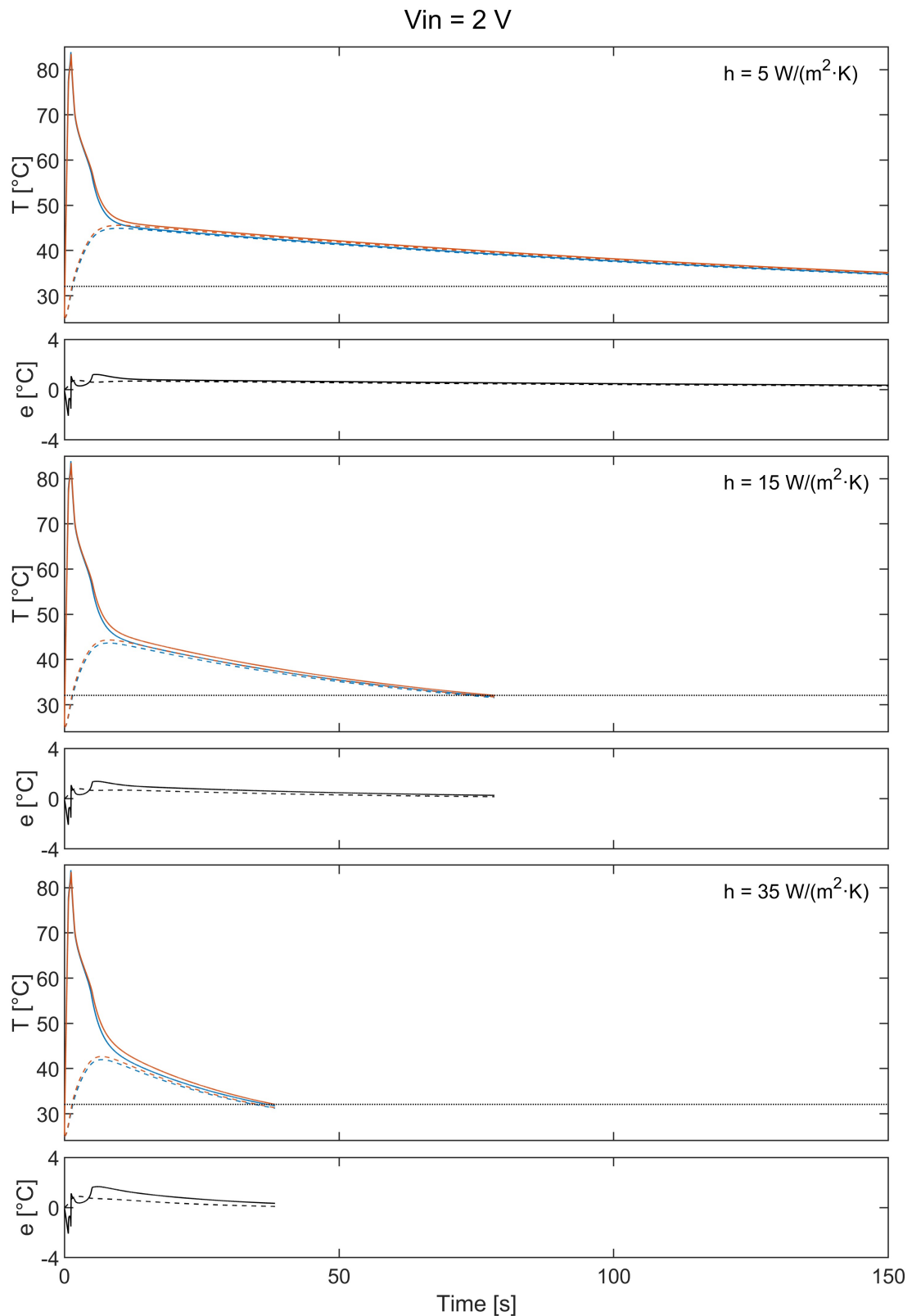


Figure 60 - Comparison of the temperatures simulated in COMSOL (red) and Simulink (blue) with a voltage pulse of 2 V for three convection coefficients. In addition to the temperature trend, the differences between the two implementations are shown, with the solid line for T_1 and the dashed line for T_2 . All the simulations are interrupted when M_f temperature is reached (dotted line).

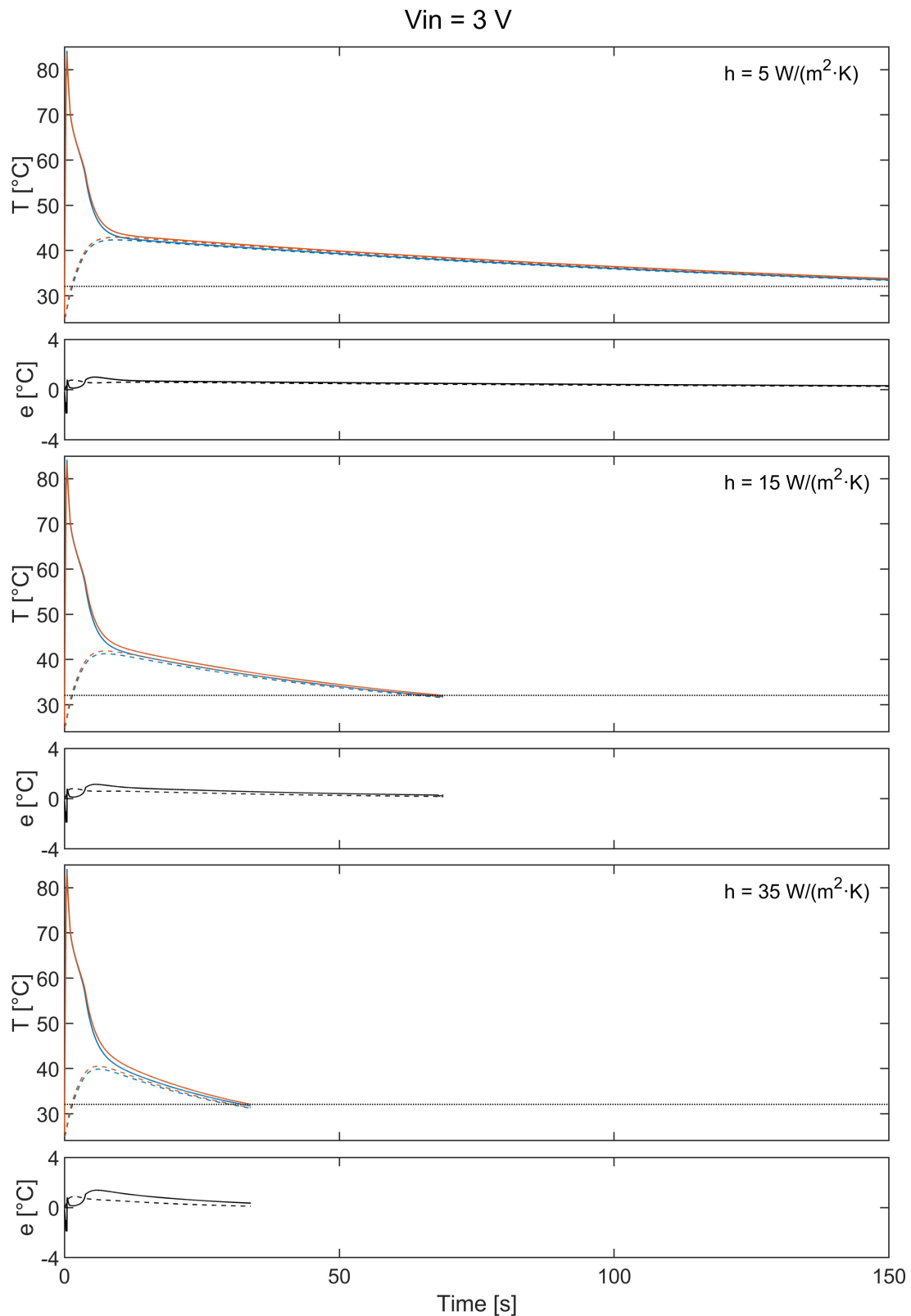


Figure 61 - Comparison of the temperatures simulated in COMSOL (red) and Simulink (blue) with a voltage pulse of 3 V for three convection coefficients. In addition to the temperature trend, the differences between the two implementations are shown, with the solid line for T_1 and the dashed line for T_2 . All the simulations are interrupted when M_f temperature is reached (dotted line).

Finally, in the light of the observations derived from the simulations of this Chapter we can select a maximum voltage value to be used for the simulations of the next Chapters. For V_{in} equal to 1 V, the actuation time is too long (10 s). The voltage pulses with which the best performances in terms of actuation speed are obtained are, as expected, the two highest values used (2 V and 3 V). Given the average resistance of the SMA wire under analysis, they correspond to approximately 6 A and 9 A respectively.

In both cases the errors of the lumped parameters model proved to be sufficiently small. Since the actuation time in these two cases is very similar with respect to pulses at lower voltages, and also very short with respect to the cooling times, these aspects cannot be conclusive. As fatigue life is generally shortened by the repeated application of high supply powers, a conservative approach would lead us to take 2 V as upper limit for voltage [137]. Considering the system controllability for different heating rates, we can observe the following. Multiplying the values of the maximum estimated heating rates by the simulation timestep duration t_s (equal to 0.005 s), the maximum temperature variation T_l in one timestep can be calculated. With a voltage pulse of 2 V it corresponds to 0.422 °C/iteration and for 3 V it is equal to 0.95 °C/iteration.

Since this last value seems too high to obtain good control error rejection, we confirm 2 V as the maximum input voltage limit for the simulations conducted in the next chapters.

6.6.2. Considerations about the experimental validation of the models

Although we took in serious consideration the opportunity to develop an experimental set-up to compare the results of the simulations with the behaviour of a physical system, we realised that in the absence of a good a-priori estimate of the thermal contact resistance R_c and with high measurement uncertainties on the wire and silicone rubber temperatures (difficult positioning of the thermocouples in extremely small material thicknesses), the optimisation of the experiment would be too complex to fit in the general plan of the thesis. Since the comparison with experiments is an important step, we think a possible way to conduct the physical tests in future would be to look carefully to a sizing of the sheathed wire that allows small enough thermocouples to be fixed with due accuracy. By conducting experiments on this system with different energy supply conditions, we could try to ascertain the model predictions while at the same time fitting the simulations to the measurements in order to determine an a-posteriori estimate of the thermal contact resistance R_c .

6.7. Conclusions

An actuator made up of a straight SMA wire enveloped in a PDMS sheath has been defined as our reference scenario, with the aim to study a specific case, free from morphological complexity, that could give general – and conceivably robust – indications on the optimisation of a multimaterial system.

The overall model is composed of several sub-systems of equations, including relations describing the constitutive SMA wire behaviour, Joule's effect for an SMA conductor, and the heat transfer through the multimaterial interface and the matrix. The first results obtained refer to the modification of Brinson's model for SMA, in order to include important effects such as partial cycles and two-way shape memory. After the parameter optimisation process, test runs show that the behaviour of the simulated wire is similar to the real one, as experimentally verifiable by comparison with functionally-relevant isotonic strain-recovery curves. A good accordance between the simulated and real behaviour can be observed especially for intermediate stress values (from 100 to 200 MPa), which are coherent with the expected working conditions. At the two extreme values of imposed stress the model is less accurate. Correspondingly, the simulations and the design optimisation of the next chapters will be carried out for applied loads values of 100-200 MPa. Furthermore, the model has the best accuracy for strains lower than 3 %. For the feedback-control simulations, this operative range will be most suitably employed.

Two models of the multimaterial actuator have been successfully implemented. They differ essentially in the treatment of heat transfer. A higher-dimensional one (1-D) will be used for multiphysics simulations, and a simplified (0-D), faster-to-compute, but equally robust one, will be employed for running automatic control simulations, which can potentially be executed in real time. The two implementations are based on the same SMA phenomenological model and were compared to verify that their overall predictions in basic case scenarios were consistent. In complete operating cycles, employing voltage pulses of different values, and with a constant stress of 200 MPa applied to the SMA wire, a maximum difference on T_l of 2.878 °C is obtained between the two model predictions, while the mean difference is always lower than 1 °C. The positive results of such comparison is a strong suggestion that further findings obtained on different aspects of the actuator functions in the next chapters will remain coherent whatever version of the model is employed.

CHAPTER 7

Advanced control strategy for the multimaterial actuator

In the light of the results obtained and observations made in the previous chapters, it has become clear that a general actuator based on an SMA element and a modified matrix is not only complex as a consequence of the variety of materials involved, but also and foremost due to the number of mostly nonlinear and highly intertwined physical processes occurring during actuation. Regarding automatic control as a fundamental aspect in material performance optimisation opens the way to exploiting control techniques not just to work our complex actuator in a desired manner, but also to regulate the energy flow among its components. An advanced controller has thus been developed with the specific aim to improve the performance of the multimaterial system. Not only did we consider the optimisation of control variable tracking, but also that of energy saving, an aspect that is often ignored for a bare SMA wire.

In order to overcome the limitations of a linear controller, the proposed control scheme consists of a variable proportional-integral (PI) action, whose structure and gains change based on continuously updated estimates of the current SMA working zone and system state variables. The functioning of the estimation algorithm will be briefly explained in Section 7.1, while the complete treatment of its implementation is reported in an M.Sc. thesis that I co-supervised [138]. The variable PI controller has been further developed with respect to that preliminary version. Its characteristics and the upgrades are presented in Section 7.2.

The designed control scheme was used to drive the simulated actuator developed in Chapter 6, instead of a real one. This has the double purpose of speeding up the design and choice of the controller characteristics, as well as allowing a better understanding of the effect of the matrix on an embedded SMA wire.

A comparison of the variable PI controller performance against a standard PI controller will be presented in Section 7.3.1. The tests were carried out in different actuation scenarios: tracking square-wave strain reference signals of various intensities, with a constant stress applied to the wire and three constant values of the convection coefficient h . In Section 7.3.2, the same simulations will be presented for a functionalised-matrix actuator, with the aim of assessing the joint effect of matrix modification and the advanced automatic control.

7.1. State variable estimation of a soft SMA-based actuator

In order to develop an advanced non-linear controller, it was necessary to implement an estimator to be incorporated into the control loop which evaluates the various zones of operation of the multimaterial actuator.

The main information that we wanted to obtain were some of the state variables of the system that cannot be measured directly, and consequently the evaluation of the instantaneous positioning in the σ - T diagram so as to estimate the current transformation zone.

Through state-space representation, it was possible to make use of an Extended Kalman filter, an algorithm that employs a plant model, alongside a series of measurements observed over time, including statistical noise and other inaccuracies, to produce estimates of unknown variables.

In our implementation, the plant model is the same model of the actuator of Chapter 6, whose state vector x includes the following variables:

- T_1 SMA wire average temperature;
- T_2 Matrix average temperature;
- ζ_S Stress induced Martensite fraction;
- ζ_T Thermal induced Martensite fraction;
- ε Wire strain;
- R_{el} SMA wire electrical resistance.
- σ Wire stress;
- h Convection coefficient

where the stress σ and convection h are external parameters modelled as constant.

The output variable y , which is also the measured variable, is the SMA wire strain ε .

The discrete-time Extended Kalman Filter (EKF) model of the system, which we employed, assumes that the state transition and measurement are affected by additive noise. In our case, it takes the form:

$$x_k = f(x_{k-1}, u_k) + w_k \quad 7.1$$

$$y_k = h(x_k) + v_k \quad 7.2$$

where x_k and x_{k-1} are the state vector at the current and previous time instant, u_k is the current input to the system (electric voltage), y_k is the system output (strain) and w_k and v_k are the process and measurement noises, assumed to be white and gaussian with constant covariances Q and R , respectively. With the ‘Extended’ version of the Kalman Filter, the state transition function f and the measurement function h are not required to be linear functions of the state but may instead be generic nonlinear differentiable functions.

For the implementation of our state observer we used the Extended Kalman Filter (EKF) block present in Simulink library, which linearises the functions f and h about an estimate of the current mean and covariance through appropriate Jacobian matrices.

Since the system, in addition to being non-linear, is also a function of the SMA working zone, it was necessary to develop a logic algorithm to select the correct set of state transition equations for the SMA, which change in a discontinuous way every time the estimated operating zone changes. Furthermore, this algorithm deals with the reset of the memory variables (see Section 6.2.1) also necessary for the EKF to manage the partial cycles.

In order to select the current zone, this logic block checks the conditions defined in Section 6.2.1.4 using the estimated values of the wire temperature T_l and stress σ , as well as their derivatives. A low-pass filter ($F_{LP} = 50$ Hz) was used to reject noise and random fluctuation on the two estimated input variables, which could otherwise create a flickering of their computed derivatives, and therefore an instability in the classification of the transformation zones. Since after a change of the equations the EKF needs some iterations to stabilise its functioning and the correctness of the estimation, to further reduce the instability of the zone selection, we introduced another logic block that holds the current zone for up to 0.1 s after every commutation.

It is possible to view the connections of the estimator to other blocks in Figure 65, which shows the complete scheme of the implemented controller.

The Simulink EKF block needs many parameters and inputs. In particular, the input vector of the system u_k composed by the present value of the actuator control voltage V ; the latest

wire strain measurement ε ; and the current estimated SMA zone of transformation from the logic block. The memory variables are reset within the block itself.

Furthermore, the EKF is connected to a MATLAB function, which contains the set of state transition functions f that can be selected according to the operating zone [138].

The output transformation function h is linear with gain equal to one since the system output variable ε is also a state variable.

The process and measurement covariance matrices Q and R , as well as the initial values of the state vector x_0 and process covariance Q_0 were set in a suitable way to obtain a robust interplay between modelling and measurement in producing good estimates: covariances express the balance of how much modelling and measurement can be trusted for each variable [138].

7.1.1. Discussion on the EKF performance

The estimator implementation has been tested using, as reference, the simulated multimaterial actuator, which allows exploiting a complete knowledge of all the state variables.

The state was estimated driving the actuator under both open loop control (full cycles with the maximum voltage) and closed loop control between 1 and 3 % of strain, exploring SMA behaviour in partial cycles.

The system was characterised using ideal model parameter, adding a measurement noise on the simulated strain to mimic a more realistic condition. Tests were conducted in different fixed stress and convection conditions, using correct or incorrect initial estimates of these parameters.

The first tests confirmed the goodness of the EKF formulation and helped us verify its performance with correct initial conditions. They demonstrated that the system can return a good estimate under all operating conditions, showing that the biggest estimation errors are found in correspondence of the zone commutations. This occurs to larger extents when there is an error in the estimate of the time instant, in which the change in the transformation zone occurs. The main causes were estimation errors on T_l and σ , because they directly condition the choice of the transformation zone, and the presence of the filter on the zone selection block, because it introduces a slight delay in detection. Despite that, the system has proved

to be robust to errors in estimation of variables and zones, and with good reactivity in correcting them.

The estimation of the h coefficient saw an average error kept below 1 %, with some spikes of intensity up to 77 %, but corrected within a few seconds. The mean error on σ remained below 0.3 MPa, with a maximum of 1.1 MPa. Temperature estimation was also very good; the largest discrepancies on T_1 and T_2 were equal to 1.2 °C, mainly during the cooling phase. In the second set of trials, we tested the ability of the system to correct for imprecise initial values of stress and convection coefficient, leaving the EKF free to tune their estimate. In fact, unlike the other state variables, which follow a known, albeit nonlinear, dynamic equation, the stress σ and convection coefficient h are external variables that can be subject to disturbances or could be inaccurately estimated or measured.

An example showing the output of the estimator compared with the ‘true’ values calculated by the simulated actuator can be seen in Figure 62, for σ and h , and Figure 63 for the other state variables. The EKF was set up, this time, with incorrect initial condition on σ_0 (180 MPa instead of 200 MPa) and h_0 (30 W/(m²·K) instead of 15 W/(m²·K)). The strain reference was a square waveform with 2 % of amplitude (between 1 and 3 % of strain), with an initial delay of 120 s, an activation time of 36 s and a period of 120 s.

This simulation is an example of how the system is able to correct easily large estimation errors of these two variables. The system adjusts most of the error estimation on h during the first transformation into austenite (zone 1). Some errors are present above all at the beginning of the martensitic transformation (zone 2), and tend to decrease as the simulation progresses.

The error on σ starts to be corrected from the first instant of the simulation, even before the transformation takes place. When the initial value is wrongly set smaller than the real one, as in this example, the EKF takes more time to converge to the correct value, but the convergence is then stable. In other tests, we found that when the initial value of σ was larger than the real one, the stress estimate converged more rapidly to the correct value, only to depart from it soon afterwards and accumulate a slight drift. It is therefore better to underestimate the initial stress, in order to reduce the estimation error. The time needed to obtain a sufficiently reduced error is equal to the initial delay we used, approximately 120 s. The estimation of convective heat transfer coefficient h has a higher variability than the other states variables, however its influence on their estimation has proved to be very limited.

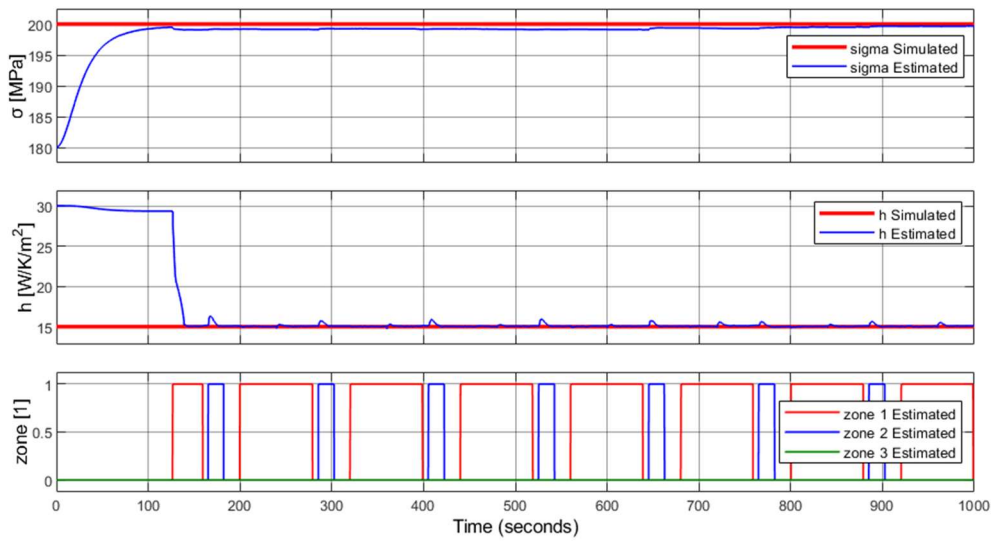


Figure 62 - Time evolution of σ and h values, which shows how the EKF acts to correct their estimations with respect to the incorrect initial condition: $h_{of} = h_0 + 15 \text{ W/m}^2\text{K}$ and $\sigma_{of} = \sigma_0 - 20 \text{ MPa}$ [138].

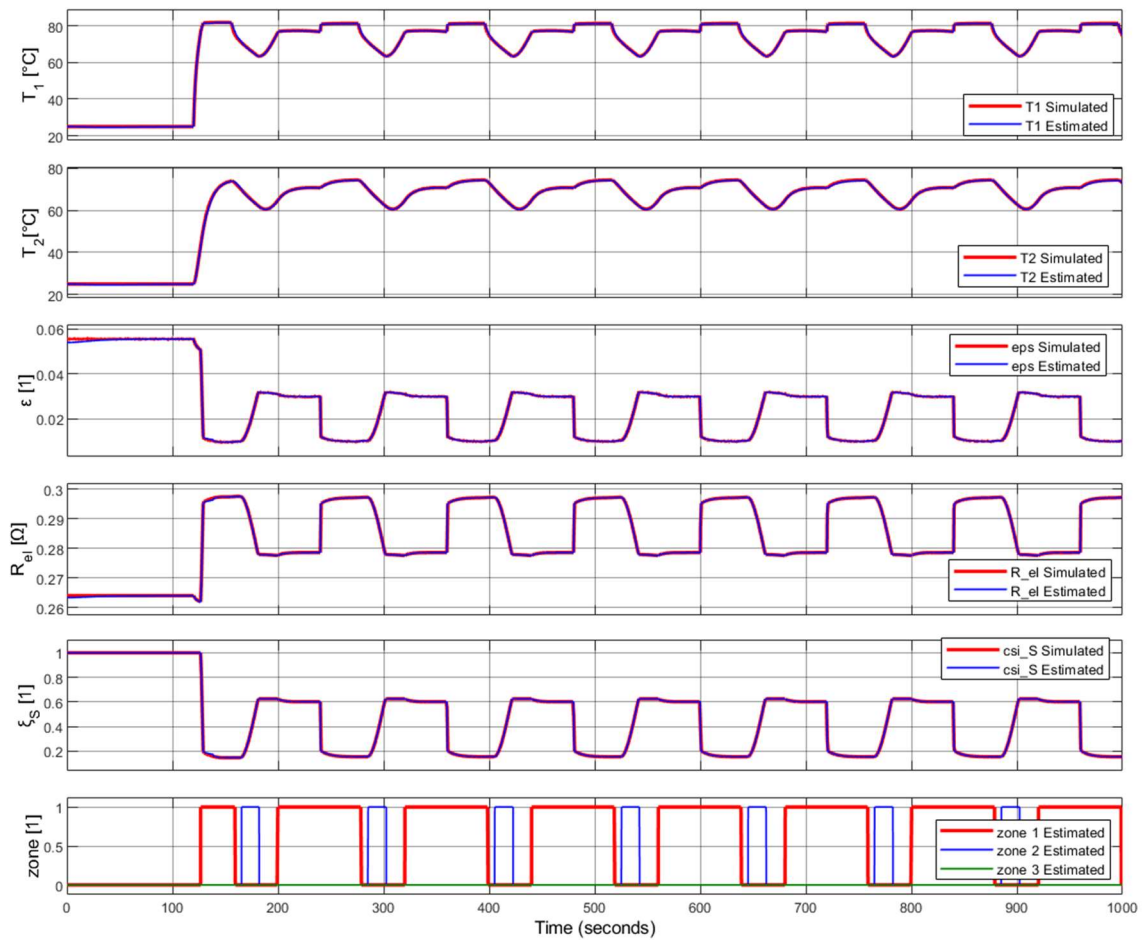


Figure 63 - Comparison between the simulated and estimated state variables of the multimaterial actuator driven by a standard PI controller. The 2 % square wave strain reference, not shown on graph, has an initial delay of 120 s, an activation time of 40 s and a period of 120 s. The EKF is set with incorrect initial condition: $h_{of} = h_0 + 15 \text{ W/m}^2\text{K}$ and $\sigma_{of} = \sigma_0 - 20 \text{ MPa}$ [138].

In Figure 64 it is possible to see an enlarged plot of T_I , together with a calculation of the error with respect to the simulated actuator signal, and the estimated transformation zones. In this case, the greatest error on T_I , equal to almost 1.7 °C, occurs at the end of Zone 1 (transformation into austenite). The zone is extended with respect to the correct instant of time in which it should have ended (156 s). Following the increase in the T_I error, the zone management resumes correctly, and the estimate is brought back to a more correct value.

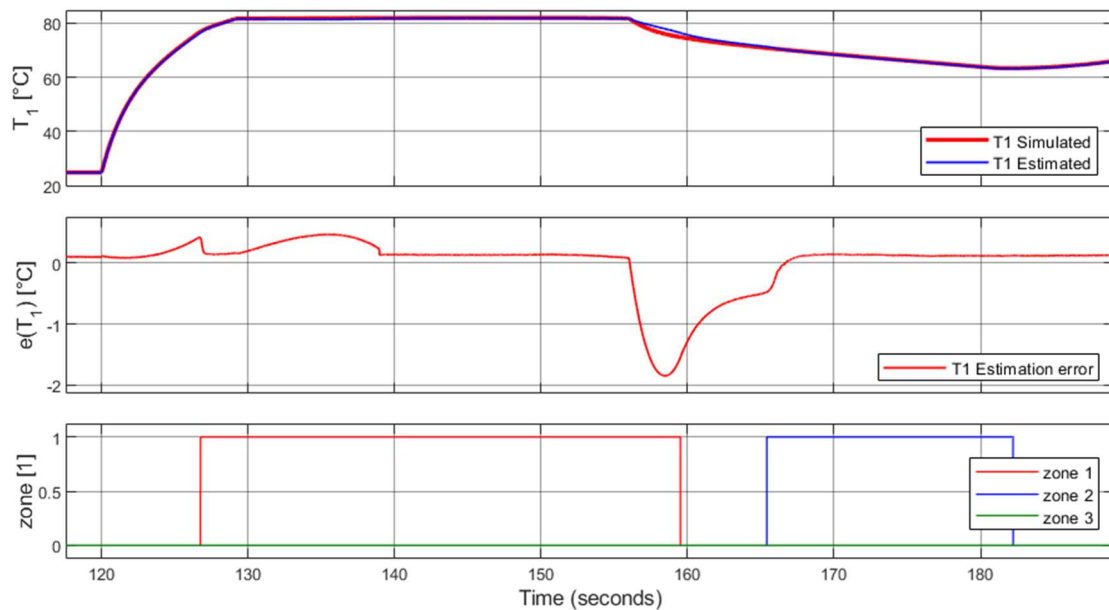


Figure 64 - Magnification of the T_I temperature during the first actuation. The graph shows how the algorithm was wrong in estimating the austenite transformation zone 1, and how this leads to an error in the estimation of T_I which, however, is corrected as soon as zone management resumes correctly. The EKF is set with incorrect initial condition: $h_{of} = h_0 + 15 \text{ W/m}^2\text{K}$ and $\sigma_{of} = \sigma_0 - 20 \text{ MPa}$ [138].

Other simulations showed what happens when the estimated zone is prematurely interrupted: the EKF increases the estimation errors on T_I and σ , which in turn are quickly corrected by the system by re-entering the correct transformation zone. The estimation errors are thus contained and reduced.

In all the tests that have been carried out, the errors evaluated after the initial transient phase have remained low, in a similar way to the tests carried out with correct initial conditions of σ and h . The estimation of the h coefficient saw an average error kept again below 1 %, with a much smaller maximum error, equal to 8.8 %. The mean error on σ was up to 2.1 MPa, with a maximum of 4 MPa. This led to slightly higher errors on T_I , with a maximum value of 2 °C, which however we consider low.

To obtain good results, the initial delay must be respected. It is fundamental to allow a sufficient correction of the error on the initial state σ_0 , and avoid grossly incorrect estimation of the other state variables.

In general, the system has shown to be stable and robust, to be able to react to estimate variations, and, above all as regards temperatures and stress, to return consistent values with reduced errors, which means that the changes in operating zones can be identified correctly.

7.2. Concept of a variable PID controller based on state variables estimation

A closed-loop control scheme is necessary to regulate the thermal evolution of the SMA, not only with the aim to follow a reference strain path, but also to be able to increase the heating rate of the electrically driven SMA by passing larger currents through it, while limiting the risk to overheat and damage the actuator.

In a control system, the difference between the measured variable and the reference value, the so-called error signal, is used to determine the best value of the controller's output variable, which in our case is the supply voltage of the SMA wire.

A well-designed controller should make the SMA achieve the reference strain precisely and as fast as possible, also producing a limited overshoot. Because in our case the cooling process only depends on air convection, an oscillatory response should also be avoided because it could be suppressed effectively only having active cooling available.

In a Proportional-Integral-Derivative (PID) controller, the output response can be adjusted in relation to the following three factors:

- the value of the error signal (proportional action);
- the past values of the error signal (integral action);
- how fast the error signal varies (derivative action).

The general concept of the proposed controller is based on the use of the Extended Kalman Filter (EKF) and the zone selection algorithm developed in [138] to modulate the gains of the three actions, thus practically obtaining a model-based switch (variable) PID controller.

A controller based on the PID concept was chosen as the forward block due to its robustness and ease of implementation. Furthermore, the development of a variable controller gave us the possibility to customise its characteristics in the best possible way in relation to the working conditions of the actuator, and in particular to adapt to the zone-conditional and hysteretic behaviour of the SMA element. The control action is thus continuously adjusted to the changing SMA response. The connection diagram of the blocks that compose the control system is shown in the Figure 65, together with the simulated actuator that is controlled.

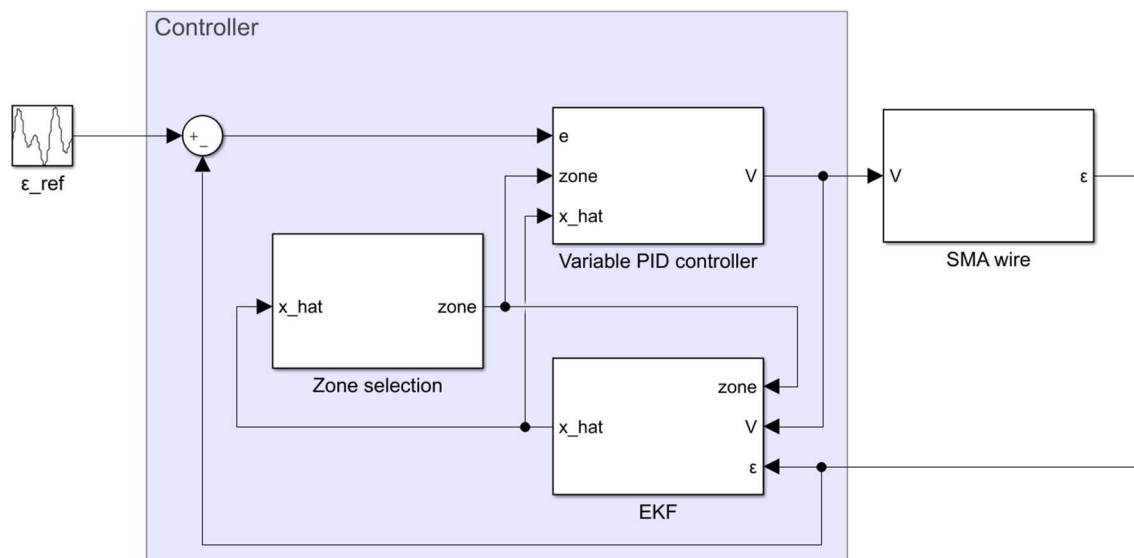


Figure 65 – Schematic of the proposed controller acting on a simulated SMA-based multimaterial actuator. The variable PID block acts on the SMA wire with a control action dependent on the current strain error by some coefficients which change depending on the estimation of the control zone and the state variables. The inner loop composed by the Extended Kalman Filter (EKF) and zone selection block produces an estimate of the unmeasured state variables of the multimaterial actuator using as information the control voltage (V) and its output measurement (ϵ).

7.2.1. Range of operation and test protocol

The operational strain and stress values have been chosen to fit the best accuracy of the simulated model of the multimaterial actuator. As seen in Chapter 6, the best operating strain range is below 3 %, and the optimal stress is for intermediate values (100-200 MPa). These values also reflect possible real working conditions.

In the literature we find many recurring waveforms used to check the controller performance of SMA systems, but the most widely used ones are sine and square waves. We decided to focus on this latter mode of operation, therefore both the reference system and the advanced controller presented in the next sections have been designed to work best with stepped strain reference waveforms.

The timings of the reference waveform were based on the basic tests presented in Section 6.6. For the maximum V_{in} we had (2 V) and the actuation time was 1.22 s in open-loop conditions, which can be considered a minimum time to reach A_f^* temperature at 200 MPa, so here we set the activation time to 2 s, to allow for observation of controller action. The off part of the cycle, on the other hand, was chosen so as to obtain complete deactivation, at least in the first extension cycle. It has been graphically estimated from Figure 60 that a time of 18 seconds was sufficient to complete the martensitic transformation, which leads to an overall waveform period of 20 s.

To summarise, we have tested the proposed controller tracking a square strain reference of two different amplitudes within the selected range. The smallest is 0.2 % (from 1 to 1.2 % of strain) and the largest is 2 % (from 1 to 3 % of strain).

Then, with the intention of testing the highest needed working temperatures, we selected for all tests the same constant stress value of 200 MPa.

To explore the full range of intensities representing free convection in air, the control systems was tested with three different h coefficients: 5, 15 and 35 W/(m²·K).

The same values were used to set up the estimator, which was then used with ideal model parameters and correct initial conditions.

7.2.2. Configuration of a standard PI controller

Before developing the advanced controller, we designed a standard controller based on PID architecture, to verify the performance obtainable with a non-variable controller, equally optimised for the step-wise control of the multimaterial actuator.

Because the control action is unidirectional and involves the heating of the SMA wire only, some decisions have been made on the implementation of both controllers.

Furthermore, since our system is heated via Joule effect, a negative voltage would have the same effect as a positive one. The output is then saturated between 0 V and the maximum operating voltage V_{SAT} , which is set at 2 V.

In order to avoid the accumulation of negative or excessively large errors also the integral part of the action was limited, in a range 0–0.6 V chosen during the tests. Moreover, in view to improve the reactivity of the control action, we have decided to reset the integral of the error at each change of the reference.

Since in our case the system to be controlled is non-linear and time varying, automatic calibration methods of the controllers have not been used, but rather the coefficients have been adjusted iteratively.

After carrying out some tests, we decided not to use the derivative component since its contribution was irrelevant in our operating range. So, effectively it was set up as a PI controller (derivative gain $K_D = 0$).

The proportional and integral gains that show the best compromise between reduced overshoots and low steady state error were $K_P = -2000$ and $K_I = -40$, respectively.

7.2.3. Development of the non-linear variable PI controller

The general concept of the variable PID controller that we implemented has been introduced in Section 7.2, above. It exploits information on the state variables (made available by the use of the EKF) and on the error on the output variable, to adjust the gains of the control actions. In other words, while the standard PID (really a PI) presented in Section 7.2.2 has constant gains, in the variable PI presented here, the same K_P and K_I change in relation to the operating zone.

In particular, we identified some peculiar working conditions, in which a change in the gains could be beneficial.

During the heating action it may be useful to implement a fast control, which however could be slowed down quickly in order to stop the action once the reference strain is almost reached, so as to limit any overshoot. Once the target position has been reached, following the shortening of the SMA wire, it may not be necessary for the system to be very reactive, as only the larger errors have to be corrected, therefore its action ought to be moderate. In this case, exploiting the thermal hysteresis of the SMA material, it is possible to maintain position at the lowest temperature above the start of the martensitic phase transition, which may be crucial to save energy.

At a change of reference, if the actuation direction is elongation (cooling), there is no control action until the target position is reached. Then, the control system must turn as reactive as possible to avoid overstretching, which should eventually be compensated with an inverse transformation and therefore a significant increase in temperature.

Finally, we expect that in some of these zones of operation, the controller action could be modulated to make it more or less intense in relation to the entity of some state variables (e.g. variations in the temperature of the matrix).

A first implementation of this idea was developed in [138], where we obtained an improvement in the efficiency during position holding and in the reactivity at the start of cooling. Compared to that preliminary version, the control action has been now further improved especially during the later stages of cooling. Furthermore, the gains of the controller zones have been optimised in order to be able to exploit a greater range of electrical control voltages, thus improving the performance of the system also during heating.

Implementation of operating subzones for special control purposes

The tests on EKF discussed in Section 7.1.1 highlighted that, in spite of an overall satisfying performance, under certain circumstances, zone estimation can be affected by errors in identifying the correct instants of transformation start or end. In order to tackle this specific problem, the controller zones are determined in a more complex way than was done for the simulated SMA model.

In fact, the mere knowledge of the operating zones of the SMA wire was found insufficient to differentiate the command action in the ways described in the previous Section. Hence, the controller zones ($Zone_c$), where different control approaches can be applied, are more finely discriminated than the model zones ($Zone$) presented in Section 6.2.1. Such controller zones are set according to the logical conditions shown in Table 14. In particular, it is possible to note how the original zones of martensitic transformations have been grouped into one, and that the model zone accounting for absence of transformation ($Zone\ 0$) has been divided into two controller zones according to whether the actuator is to be heated or cooled. In the definition of the controller zones, the strain error e was used instead of T_l to prevent possible problems induced by fluctuations in the estimate of this temperature.

In addition to the described rearrangement of the operating zones, a further subdivision of some of the zones has been made, in order to allow the controller to handle special situations, e.g. the proximity to the target position (strain). Such special controller zones are set and reset using an SR Flip-flop logic (Table 15) according to precise combinations of the variables describing the working conditions.

Summing up, the conditional equations necessary to define all the controller zones make use of: The $Zone_C$ variable identifying the controller zone itself, the strain reference, the error e , and some information about the state of the actuator estimated by the EKF: in particular, the model Zone and the value of ξ .

Table 14 - Controller zones enabled by logical conditions only.

$Zone_C$	Description	Conditions
F_H	Free heating	$(e < 0) \wedge (Zone = 0) \wedge (Zone_C \neq 'A_H, M_H, A_{100}')$
F_C	Free cooling	$(e \geq 0) \wedge (Zone = 0) \wedge (Zone_C \neq 'A_H, M_H, A_{100}')$
A	Transformation to austenite	$(Zone = 1) \wedge (Zone_C \neq 'A_H, M_H, A_{100}')$
M	Transformation to martensite	$(Zone = 2 \div 5) \wedge (Zone_C \neq 'A_H, M_H')$

Note: Some of the symbols are defined in Table 15.

Table 15 - Controller zones managed using a set-reset (SR) Flip-flop logic.

$Zone_C$	Description	Conditions	
		Set	Reset
A_H	Austenite holding	$e > K_H$ \wedge $Zone_C = 'A'$	reference change \vee $Zone = 2 \div 5$
M_H	Martensite holding	$e \leq 0$ \wedge $Zone = 2 \div 5$	reference change \vee $Zone = 1$
A_{100}	Austenite 100 %	$\xi < 10^{-6}$	$Zone_C = 'M'$

Note: K_H is a threshold that sets the activation range of zone A_H . In this work it has been set to 0. Some more symbols are defined in Table 14.

To complement the controller zone structure, the saturation and reset logics of the integral part, which were introduced for the standard PI in Section 7.2.2, have been applied equally

for this advanced controller: also in this case the derivative action was not used ($K_D = 0$). The controller is therefore a variable PI.

Table 16 shows the chosen controller gains and special controller actions that characterise the behaviour of the variable PI in each controller zone. As can be appreciated, in order to exploit as much as possible the available information on the state of the system, some additional variables estimated by the EKF are used to modulate the control action, i.e. the stress σ , the mean wire temperature T_1 , and the average matrix temperature T_2 . In some cases, they have been used to modulate the parameters of the controller, while in the A_H zone a direct control of the output voltage V has been implemented. The convective heat transfer coefficient h was not used, as its estimate variability was deemed too large.

Table 16 - List of parameters and command actions set for each operating zone of the controller.

Zonec	K_P	K_I	Direct action on V
F _H	-4000	-40	
A	-6000	-300	
A _H	-500	0	$K_{TC} \cdot \left(\frac{1}{T_1 - (M_s^* + T_{AH})} \right)$
A ₁₀₀	$-250/\sigma$	0	
F _C	-4000	-40	
M	-4000	-40	
M _H	$-200 \cdot (90 - T_2)$	-80	

Note: For a definition of K_{TC} , M_s^* and T_{AH} see text below.

The direct control action on the voltage V , as defined in Table 16, is inversely proportional to the difference between the temperature T_1 and the target temperature, by means of a gain K_{TC} (set to 0.5). The target temperature was defined as the sum of T_{AH} , a safety coefficient that in this work is set to 2 °C, and M_s^* , the temperature limit of the nearest martensite transformation zone calculated as:

$$\text{if } \sigma > \sigma_s^{cr} \quad \text{then} \quad M_s^* = M_s + (\sigma - \sigma_{cr}^s)/C_M \quad 7.3$$

$$\text{if } \sigma \leq \sigma_s^{cr} \quad \text{then} \quad M_s^* = M_s \quad 7.4$$

The rationale is that, in order to hold the position reached during heating, the temperature can be allowed to decrease naturally (saving energy) only until before the martensitic transformation sets on. Just before that point, the controller should react rapidly to prevent losing position.

7.3. Results and discussion

In the following sections, I present results on the performance of the variable PI controller, first as compared to the standard PI, and then as used to drive two actuators with different matrix characteristics.

In all the tests a transient is visible, during which the performance varies. In fact, it will be noted that with each repetition of the actuation cycle the temperature T_2 of the soft matrix increases, until a stable condition is reached. For this reason, I have always shown the first three cycles. All simulations start from an initial strain equal to 5.5 %, which has not been displayed in order to be able to zoom in on the working range. In addition to the trend of the strain over time, a magnification of the strain error was presented. The temperatures of the two materials are also shown, as well as the trend of the electric power supplied by the two controllers to the simulated multimaterial actuator.

7.3.1. Comparison of the variable and standard PI controllers, driving the actuator with a non-modified matrix

The graphs presented in this section show the performance of the standard and variable controllers subjected to different strain reference amplitudes.

Let us first analyse the cooling steps. From the tests carried out with a low value of the convection coefficient ($h = 5 \text{ W}/(\text{m}^2 \cdot \text{K})$), it is immediately possible to notice the great variability in the times required for the extension of the actuator. This effect, already mentioned above, is mainly due to the increase in the temperature T_2 of the matrix over time (Figure 66). In particular, the first cycle is very different from the subsequent ones, during which the evolution of the matrix temperature gradually takes place and plateaus.

Analysing the behaviour of the variable PI controller in this operating segment, the improvements compared to the standard PI controller are marked, but not sufficient to make the actuator reach the higher target strain in repeated cycles.

For smaller amplitudes of the strain reference change (Figure 67), the tracking occurs in a much more effective way. Despite the limited convection, T_2 stays low enough not to condition the performance excessively, even in subsequent stretching cycles.

In this working condition the improvements introduced with the variable PI controller are high, especially obtaining faster transitions in the cooling phase.

As convection increases (Figure 68 through Figure 71), there is a general improvement in performance in the cooling phase, as expected. Even under these conditions, the variable PI controller optimises the actuation times during the extension phase, obtaining improvements compared to the standard PI controller in a range of 40-60 % of the duration of cooling. It can be seen that this improvement can be traced back to two effects: less start-up delay and greater temperature gradient.

The active temperature control, implemented in the A_H zone, allows the controller to keep the heated SMA wire at a lower temperature (just higher than $M_s^* + T_{AH}$) without compromising the position holding, and to make the system more reactive at the start of the following elongation (cooling). Furthermore, the corresponding opportunity to supply globally less energy allows the average temperature of the matrix T_2 to be maintained at a lower value, increasing the cooling rate.

Having analysed the cooling step, we can now consider the heating phases: in these segments of the cycle, no particular differences between the two systems are noted, so the variable PI performs similarly to the standard version.

Finally, we shall turn our attention to the precision in maintaining the reference strains. When looking at the conservation of the shortened configuration after heating (1 % of strain), it can be observed that the static errors generated by the variable PI at the end of activation are always lower than the standard PI controller. On the other hand, the variable PI introduces spikes that the standard one does not produce. As the magnitude of the spikes is however very small compared to the static error, their presence seems acceptable. To conclude, during the maintenance of the elongated configuration (i.e. at the end of cooling), the improvement introduced by the variable PI is remarkable. The overshoots are especially very small compared to the ones produced by the standard PI.

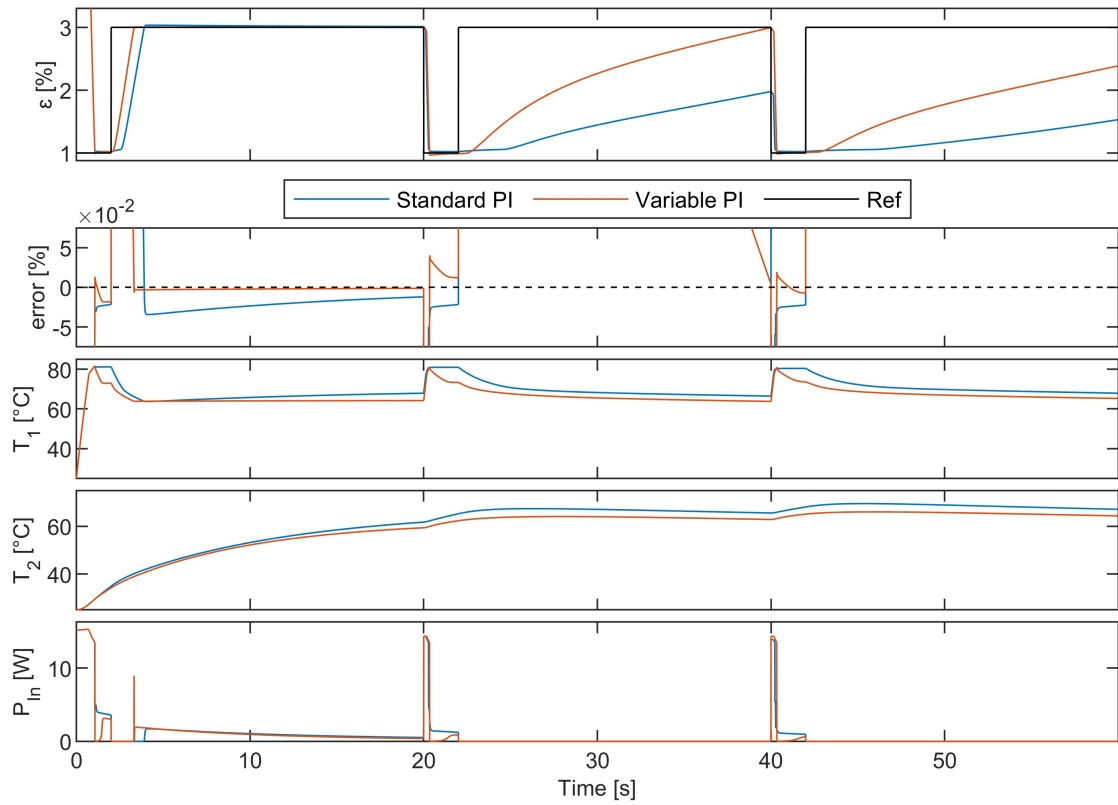


Figure 66 - Performance comparison of the two controllers with a 2 % amplitude square reference (1-3 %) and $h = 5 \text{ W}/(\text{m}^2 \cdot \text{K})$.

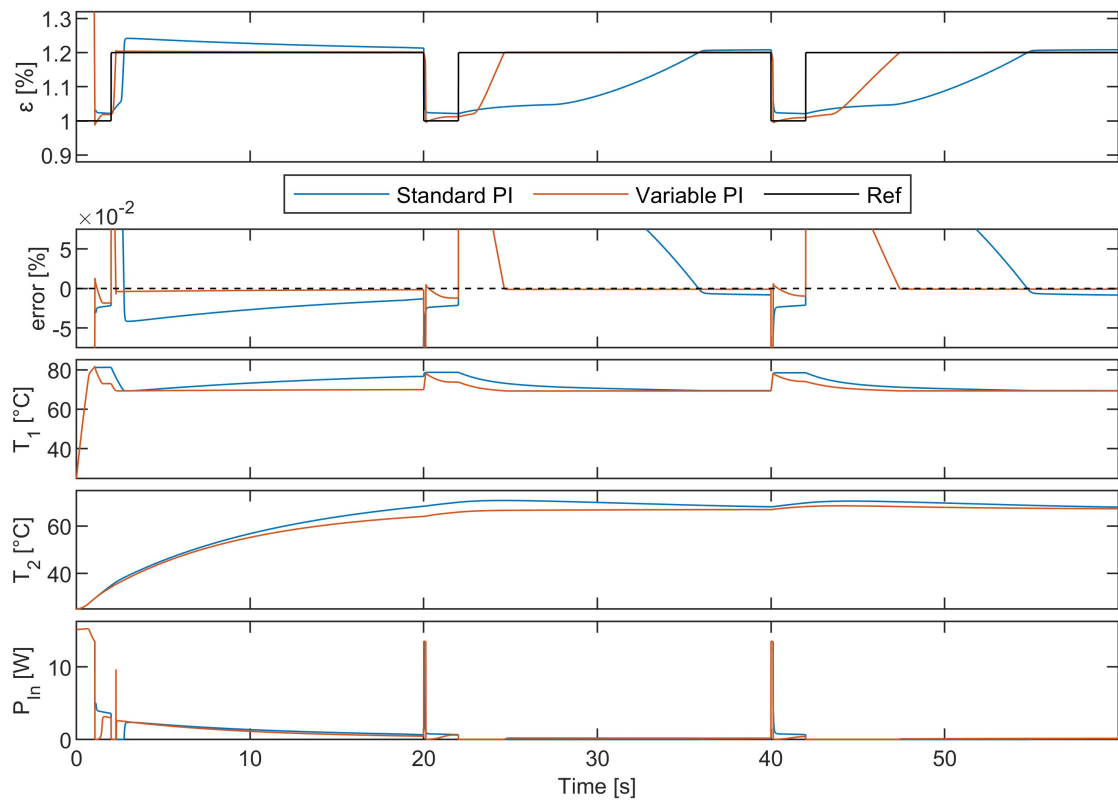


Figure 67 - Performance comparison of the two controllers with a 0.2 % amplitude square reference (1-1.2 %) and $h = 5 \text{ W}/(\text{m}^2 \cdot \text{K})$.

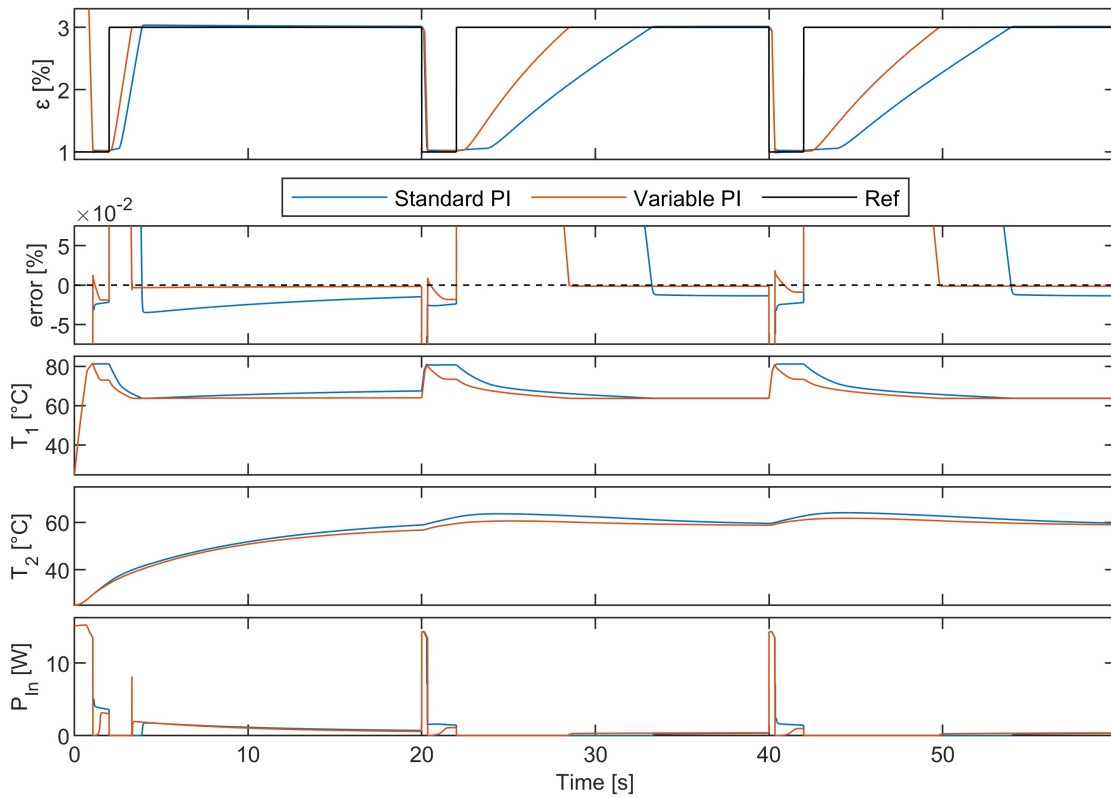


Figure 68 - Performance comparison of the two controllers with a 2 % amplitude square reference (1-3 %) and $h = 15 \text{ W}/(\text{m}^2 \cdot \text{K})$.

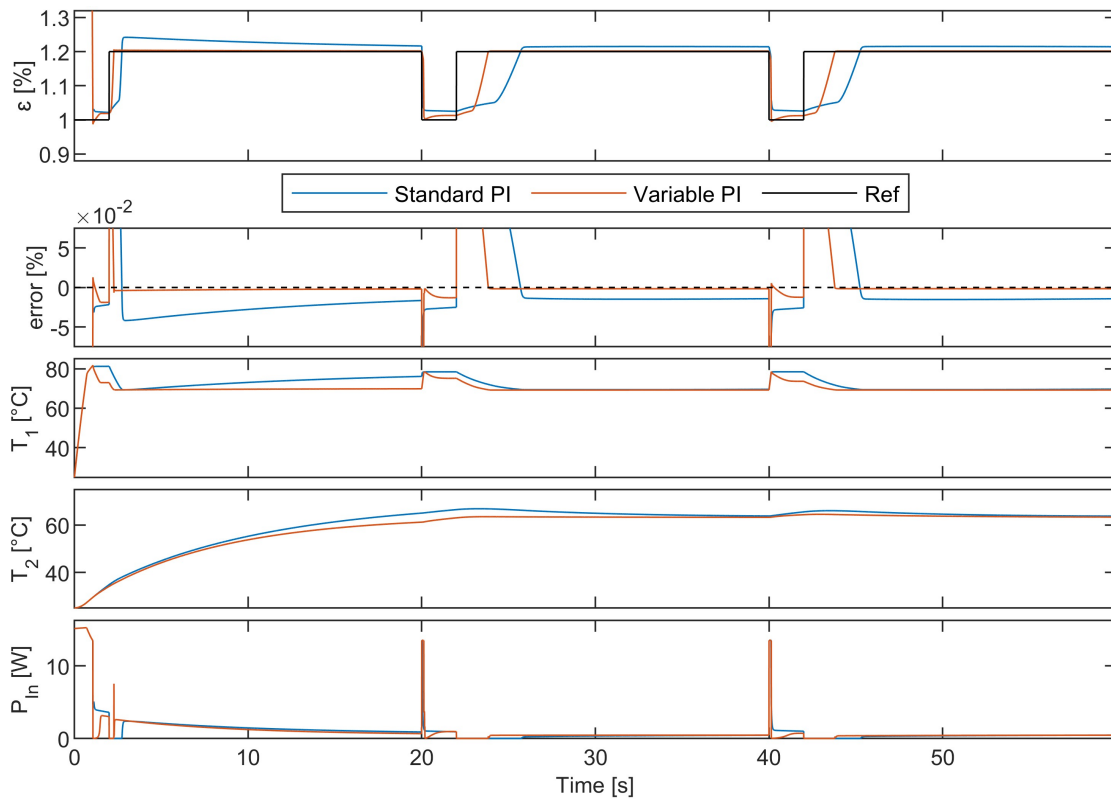


Figure 69 - Performance comparison of the two controllers with a 0.2 % amplitude square reference (1-1.2 %) and $h = 15 \text{ W}/(\text{m}^2 \cdot \text{K})$.

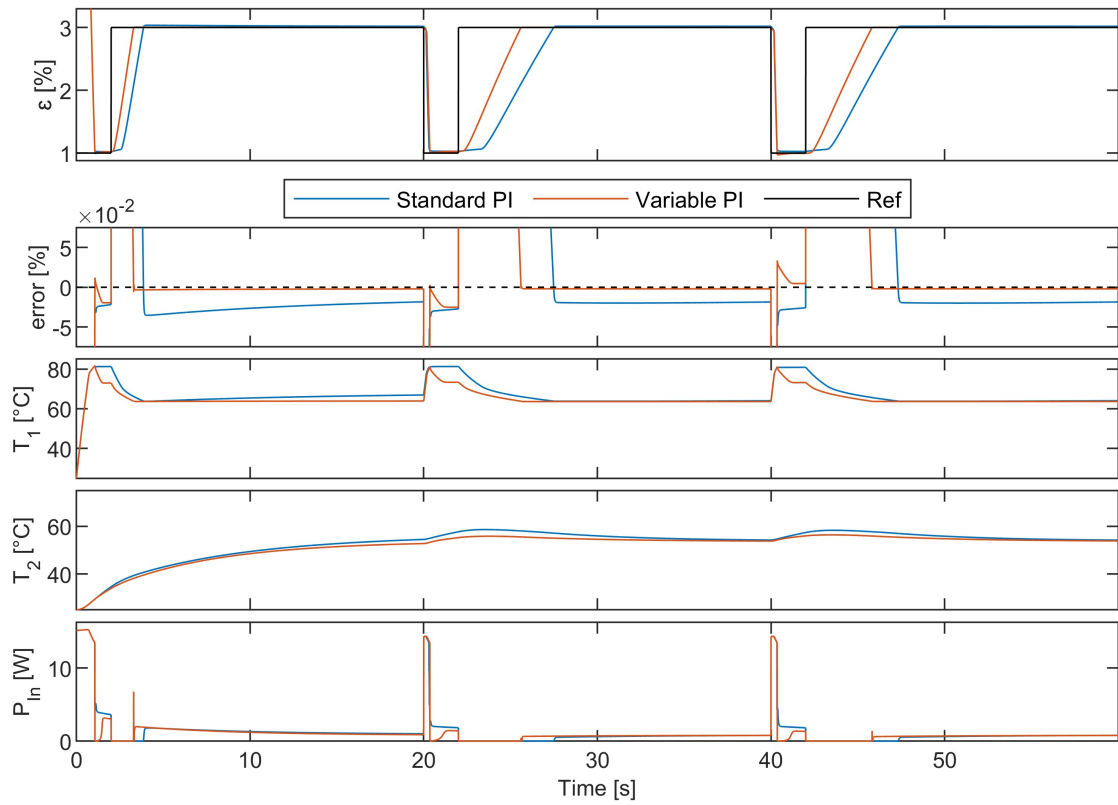


Figure 70 - Performance comparison of the two controllers with a 2 % amplitude square reference (1-3 %) and $h = 35 \text{ W}/(\text{m}^2 \cdot \text{K})$.

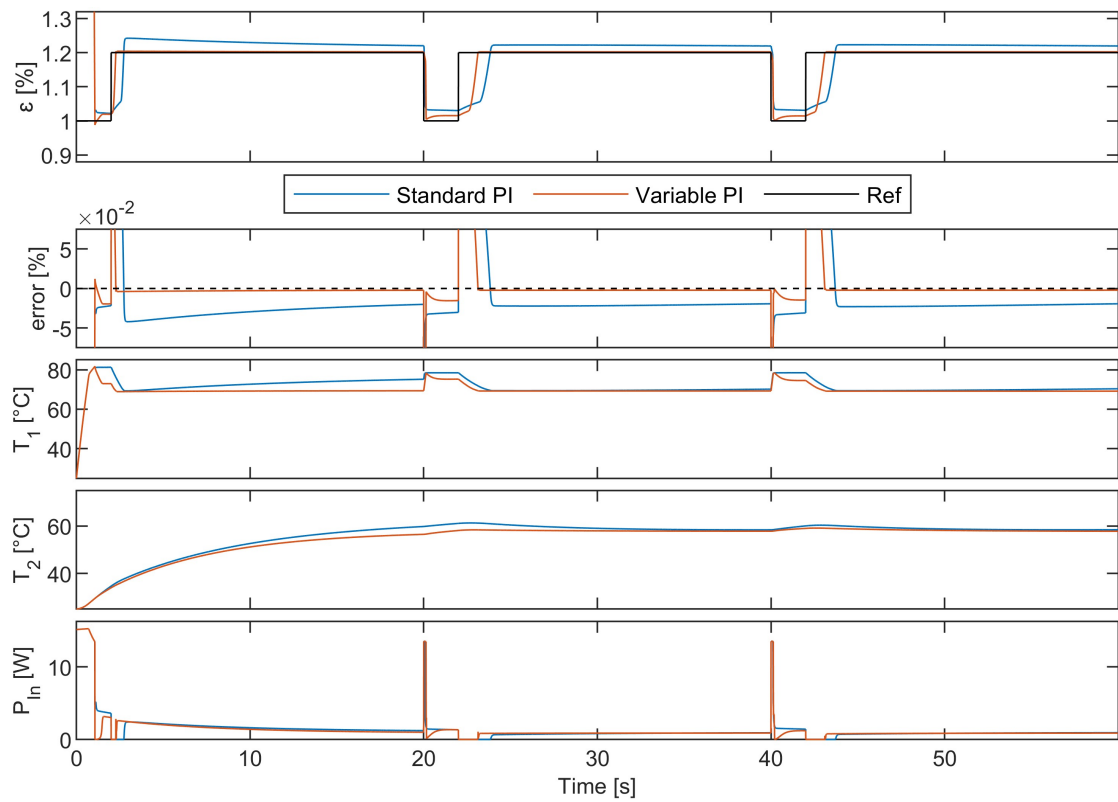


Figure 71 - Performance comparison of the two controllers with a 0.2 % amplitude square reference (1-1.2 %) and $h = 35 \text{ W}/(\text{m}^2 \cdot \text{K})$.

7.3.2. Effect of the matrix modification in conjunction with the variable PI controller

The simulations with the largest strain steps (1-3 %) were performed by setting the thermal conductivity of the matrix to a higher value. This was done with the aim of verifying whether the modification of the matrix, in conjunction with an optimised control, could serve to obtain faster actuations. The chosen value of conductivity is equal to $0.65 \text{ W}/(\text{m}\cdot\text{K})$, which is the maximum obtained experimentally (Chapter 5).

Also in this case the behaviour during the first cycle is independent of the coefficient h . The effect of the matrix modification leads to an improvement in the actuation time by 19 %.

In the subsequent cycles, the behaviour is different, especially in the cooling phase of the SMA wire and therefore in the elongation phase. With a low value of the convection coefficient ($h = 5 \text{ W}/(\text{m}^2\cdot\text{K})$, Figure 72) the more conductive matrix leads to a deterioration in performance. With a medium value of the convection coefficient ($h = 15 \text{ W}/(\text{m}^2\cdot\text{K})$, Figure 73) there is still a deterioration but of lesser intensity. With a high value of the convection coefficient ($h = 35 \text{ W}/(\text{m}^2\cdot\text{K})$, Figure 74) the matrix allows to obtain an improvement, albeit quite small ($< 6.8 \%$).

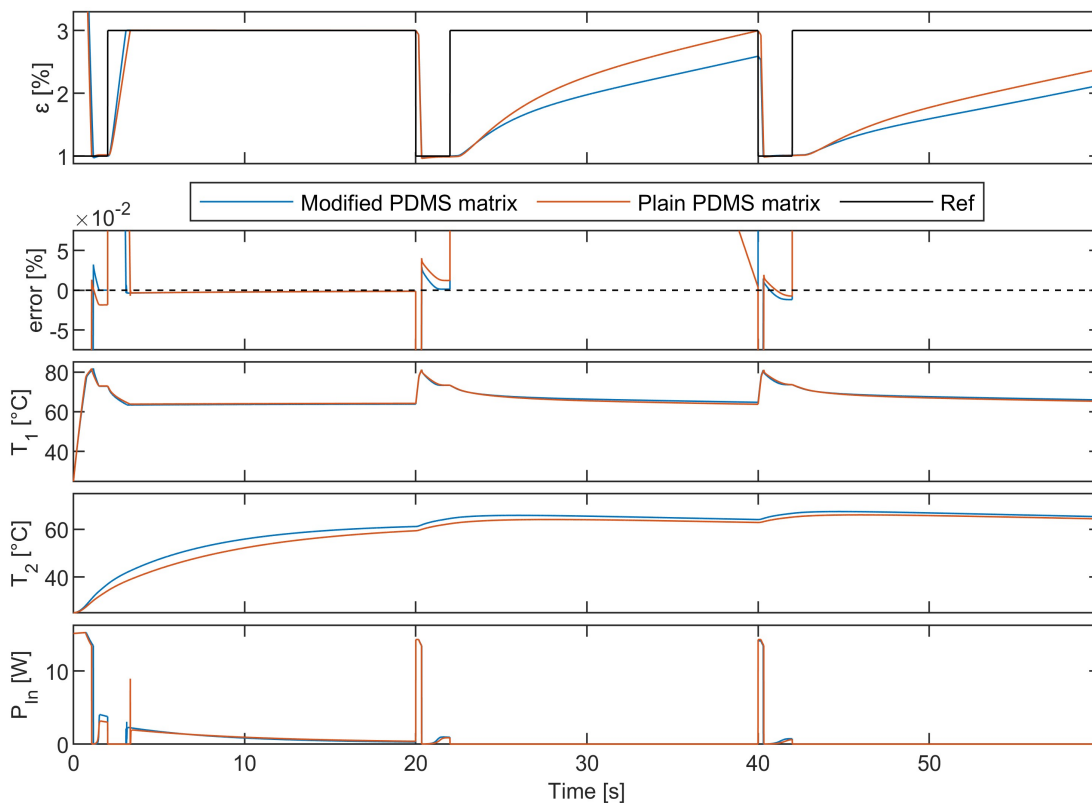


Figure 72 - Study of the increase in the conductivity of the soft matrix combined with the use of the variable PI controller with a 2% amplitude square reference (1-3 %) and $h = 5 \text{ W}/(\text{m}^2\cdot\text{K})$.

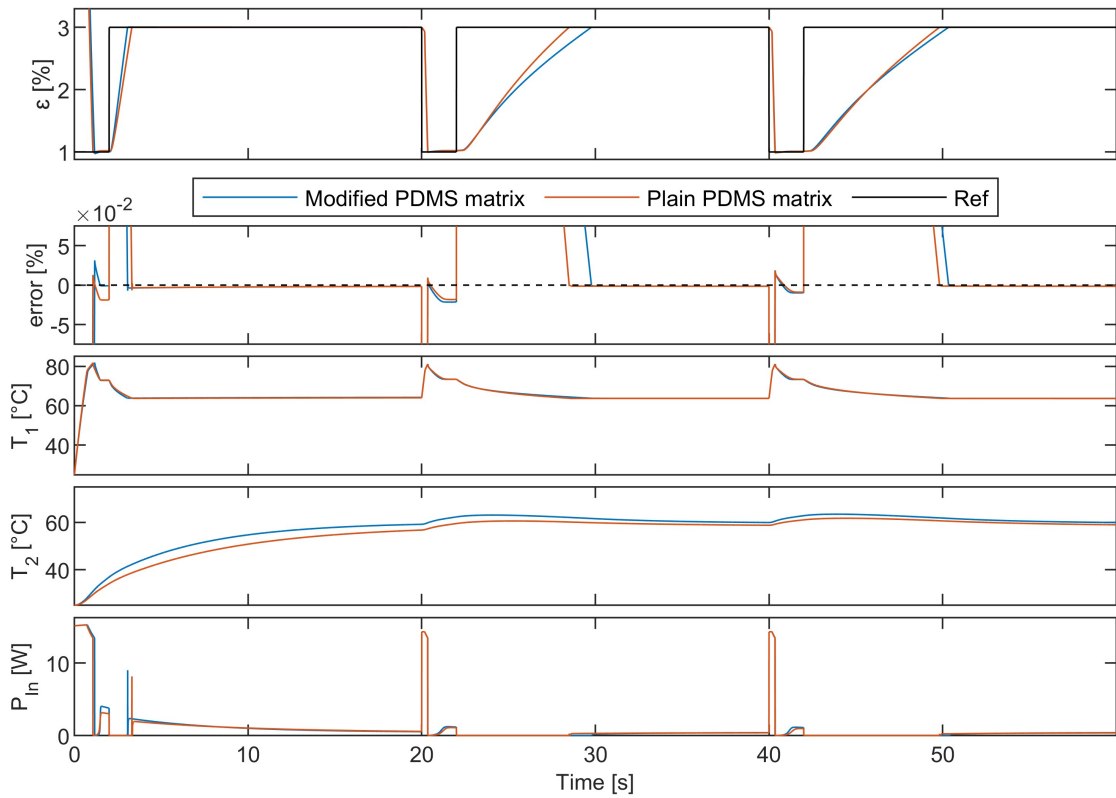


Figure 73 - Study of the increase in the conductivity of the soft matrix combined with the use of the variable PI controller with a 2% amplitude square reference (1-3 %) and $h = 15 \text{ W}/(\text{m}^2 \cdot \text{K})$

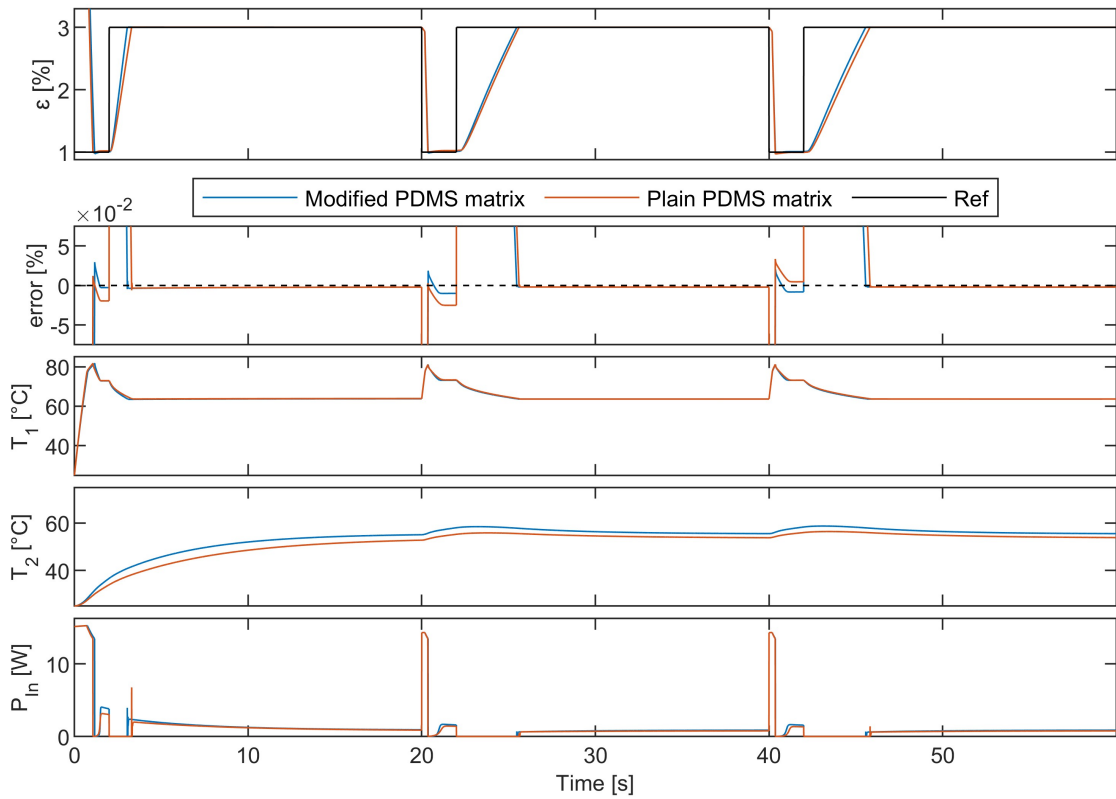


Figure 74 - Study of the increase in the conductivity of the soft matrix combined with the use of the variable PI controller with a 2% amplitude square reference (1-3 %) and $h = 35 \text{ W}/(\text{m}^2 \cdot \text{K})$

This behaviour can be explained by noticing that, if the heat extraction by convection is not effective enough, a larger matrix conductivity favours the heat transfer between the wire and the matrix itself. A hotter matrix decreases the temperature gradient, which is the driving potential for a fast SMA cooling.

7.4. Towards the application of the advanced control with a real system

In the preceding sections I have shown that a model-rooted estimator-informed switch PI controller can provide interesting opportunities for the optimisation of an SMA-based multimaterial soft actuator. The tests have been conducted exploiting a digital mock-up of the physical actuator.

A fundamental future step on the way to the practical application of the proposed controller is a further optimisation of the estimator, carried out by verifying its behaviour with a real SMA wire. So far, it is possible to draw conclusions based on the analysis of the Extended Kalman Filter sensitivity to uncertainties, which was performed through a digital twin, i.e. using the simulated system: this analysis can be of invaluable help in the configuration of the filter, and to set-up its use with a real actuator.

In the complete system, the filter is certainly the part having to cope most crucially with uncertainties concerning the properties of the multimaterial device. In fact, the model-rooted information is not used directly in the formulation of command actions, but indirectly via the EKF. It is worth focussing some attention on at least two possible cases that may require additional optimisation.

Real case scenarios in which position holding must be optimised against uncertainties

The variable that most affects the behaviour of the variable PI controller, as implemented in this thesis work, is the estimated temperature of the wire T_I .

It is used to carry out a temperature control in parallel to the action based on the strain error, specifically in the position holding phase following a shortening of the SMA wire. This action is direct and very sensitive to estimation errors. A possible remedy, depending on how different the behaviour of the model is found to be compared to the real wire, is to adjust (increase) the value of the T_{AH} parameter, which defines the maximum difference between the estimated T_I and the reference temperature to be maintained. By this method, even if at

the expense of the controller performance, it is possible to reduce the sensitivity to the uncertainties of the model and increase the overall reliability.

Real case scenarios with perturbations involving external mechanical or thermal loads

Based on specific needs and the field of application, it will be necessary to evaluate whether to study and eventually optimise the response of the system to other disturbances such as those affecting σ and h . Those are the two variables that are most prone to unexpected variations in certain working environments. The tests carried out on the Extended Kalman Filter have shown that it is possible to correctly estimate the two aforementioned variables even if they are initially unknown, so, if necessary, the estimator filter can be inherently useful for developing disturbance rejection methods.

I believe that the presence of the soft matrix is of fundamental importance for this purpose, as it filters out the high-frequency components of external disturbances and allows the estimator to have time to evaluate the actual variations in the h coefficient. This may work even to compensate for changes in the environmental temperature, which also affects convection.

Another interesting observation is that the stress estimation error is corrected well but with a limited frequency band. In fields where the stress is not constant, but can be modelled with a functional relationship involving the measured strain (e.g. a linear spring), I expect that the performance of the estimator can be even better than that obtained in this work.

7.5. Conclusions

A variable PI controller was developed and tested in different scenarios, as applied on a digital twin of the multimaterial actuator, based on the SMA wire model. Its nonlinear implementation has shown superior performance over a standard non-variable controller. The control action was adjusted according to the current strain error by some coefficients, which change depending on the estimated controller zone, as well as the estimation of the mean SMA wire temperature T_1 , and the temperature T_2 , which is able to provide information about the energy stored in silicone rubber and strongly affects predictions about the cooling behaviour. The EKF filter used to estimate the state variables showed high performance,

with reduced errors calculated against the model variables. In particular, the mean temperature of the SMA wire T_I was estimated with an error of less than 2 °C.

The filter formulation is very versatile and will allow for further development if needed, and if additional information on specific real actuators are available to complement the model equations and covariance matrices. The possibility of measuring other state variables in addition to or in place of the strain could be evaluated. In fact, measuring more variables can improve the effectiveness of the estimator (e.g. applied force or electrical resistance of the SMA wire). Alternatively, the strain can be replaced with electrical resistance to obtain a self-sensing control system. I expect the system to maintain the same performance given the good linearity between the two variables [139].

Although the work developed requires further tests to bring the application to a real system, the simulations carried out have given fundamental indications on which directions to follow in order to optimise the control of multimaterial actuators based on SMA. Optimised control strategies to reduce energy waste and keep the matrix cooler are absolutely necessary to make these systems performant.

To pursue this goal, focussing specifically on the aspects concerning the material properties, some simulations have been carried out by exploring the effects of raising the thermal conductivity of the matrix, as I proposed to do in Chapter 5. Comparing the effects obtained with respect to an unmodified matrix, in the example case with a thickness of the soft material of 1 mm, it showed worsening in sequential operation, especially for low values of h . Changing the matrix may help for one-shot applications, but it doesn't seem like the right way to proceed for applications where repeated actuations are needed.

This result, contrary to what we would have expected, certainly needs further study. In the next Chapters I shall add an important aspect, which has been disregarded so far: size and morphology. I shall study in particular what happens with larger thicknesses of the soft matrix.

CHAPTER 8

Numerical analysis: functionalisation and system dimensioning

The preliminary investigations on the effect of the increased thermal conductivity of the soft matrix posed several questions on the impact of its functionalisation and its sizing on the general performance of the device.

In this Chapter, a set of simulations are presented, aimed to characterise particular aspects of the actuator's behaviour, with respect to the variation of some parameters that I considered fundamental, and of greater incidence. The objective was not to select the best parameters for a particular application, but to study how materials interact to evaluate the preferential directions to follow in the design of these actuators to obtain improved performance.

Since the lumped parameter model used in the previous chapter is reliable only for small thicknesses of the matrix, the distributed parameter model has been implemented to study the effect of PDMS radii greater than 1 mm (see Chapter 6).

Coupling COMSOL with LiveLink™ for MATLAB allowed me to use the one-dimensional (1-D) actuator implementation in order to run a parametric study with the aim to investigate how the interplay of the size, the properties of the intermaterial interface and the characteristics of the soft material affect the performance of a multimaterial actuator.

Since LiveLink™ does not allow to directly interface Simulink with COMSOL to use the already implemented control algorithm, which includes the estimator, I decided to implement a simplified SMA wire heating pattern that could mimic a control action.

A constant stress σ equal to 200 MPa was used, for similarity with the previous chapter.

The results that will be presented address the use of the multimaterial actuator both in single cycles and in repeated actuations.

8.1. Test procedure

By means of the simulations used to test the controller in the previous Chapter, it was noted that the behaviour of the SMA wire is greatly influenced by PDMS sheath temperature T_2 , and therefore by the energy stored by the soft matrix. In particular, the first cycle was very different from the subsequent ones, which varied following a transient, as the trend of T_2 gradually stabilised. In this Chapter, I wish to emulate a similar simulated test strategy, but, to facilitate the discussion, I distinguish two borderline cases, and analyse them through the study of single actuations. In one case, the system is initially cold as for a first cycle, and its starting temperature is equal to the room temperature T_{amb} (25 °C), while in the other case, the system is entirely “hot” at the start of the cycle, to simulate a late actuation cycle. In this way we were able to investigate the influence of the actuator parameters on the system performance in case of one-shot activations, as well as sequential activations. In fact, we can hypothesise, based on the results of Chapter 7, that in conditions of repeated cycles maintaining the strain at the end of SMA cooling, the temperature of the entire system gradually settles and plateaus. Under such conditions, despite not explicitly running multiple cycles, I consider equally indicative the information that can be obtained by simulating single actuation cycles with the actuator initially stable at a meaningful pre-set temperature. The chosen control routine imposes an input voltage, which allows to obtain an average temperature pattern of the SMA wire similar to the one obtained through the variable PI controller in the previous chapter.

The routine is divided into various steps. During the activation step, a constant voltage equal to V_{SAT} (2 V) is imposed, to complete the transformation into austenite by heating the SMA wire from temperature T_0 to A_f^* (Figure 75). Having considered as case of interest the one in which the wire is subjected to a constant stress σ of 200 MPa, this temperature is always equal to 83.6 °C for our wire. In the second step, the goal is to hold the position for a pre-set time t_H (Figure 76). A closed-loop control of the mean temperature of the SMA wire, identical to the one implemented with the variable PI controller of Chapter 7, is adopted here too to keep it above a reference value equal to $M_s^* + T_{AH}$ (71.5 + 2 °C). Once the selected time has elapsed, the control voltage is set to zero and the SMA wire is allowed to cool down (Figure 77). In this step, the third in the sequence, the martensitic transformation takes place and ends when the mean temperature of the SMA wire reaches M_f^* (56.5 °C @ 200 MPa).

For the tests in which the initial system temperature T_0 is equal to M_f^* , the cycle ends here. For the simulations that analyse the behaviour of the system starting from a T_0 equal to T_{amb} (25 °C), additional time is given to the wire to cool down (Figure 78). This fourth step is meant to be used to check how long it takes for the mean temperature of the SMA wire to drop down to a lower temperature. The M_f temperature was chosen arbitrarily, but it was considered interesting because it is both higher than T_{amb} , and also much lower than M_f^* .

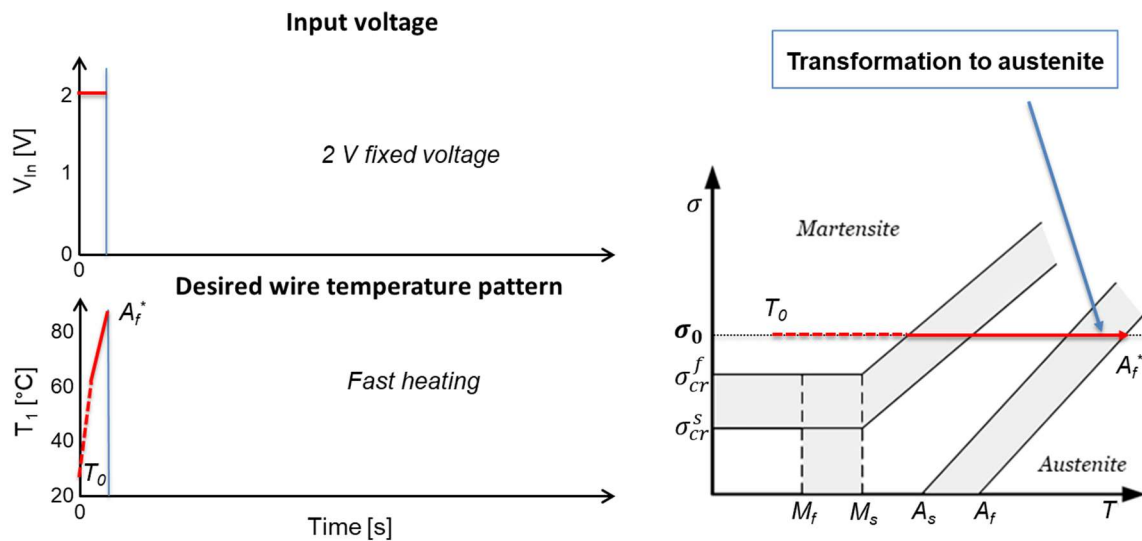


Figure 75 – Step 1, activation. A constant electric voltage equal to 2 V is used to heat the SMA wire by joule effect. The step ends when the complete transformation into austenite has taken place.

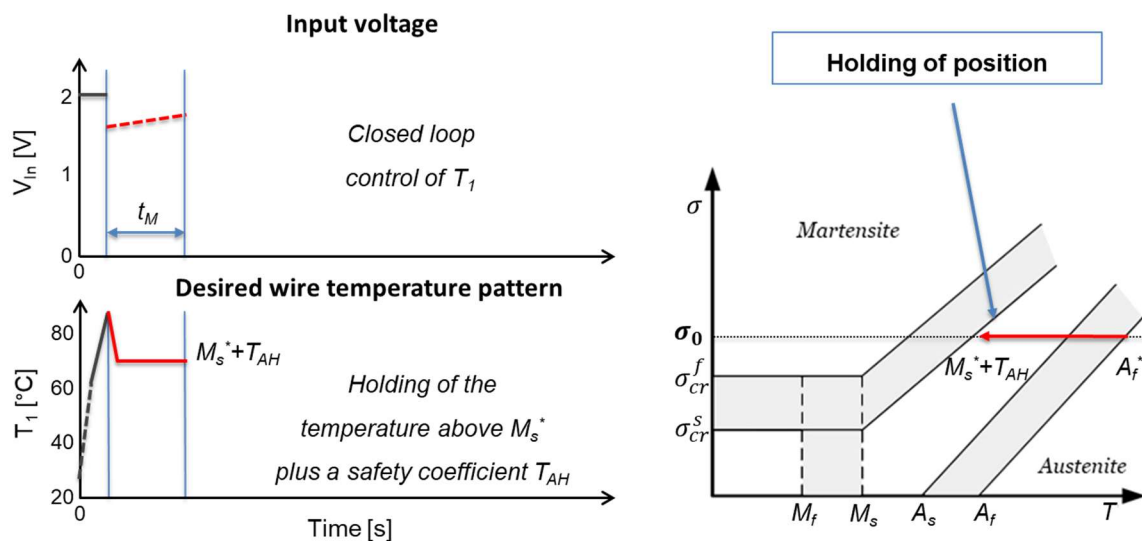


Figure 76 – Step 2, holding. A closed-loop control of T_1 is implemented to supply to the SMA the energy necessary to keep the wire sufficiently hot to avoid the martensitic transformation. The mean temperature T_1 of the SMA is maintained above a threshold for a predetermined time t_H .

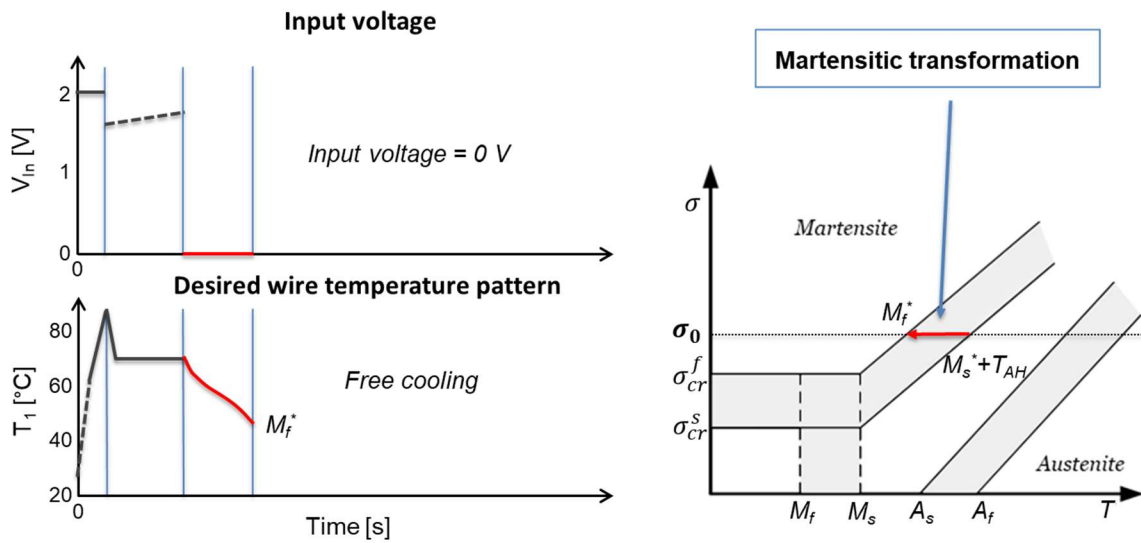


Figure 77 – Step 3, deactivation. Once the temperature holding is finished, the SMA wire is free to cool down. The step ends once the martensitic transformation is completed.

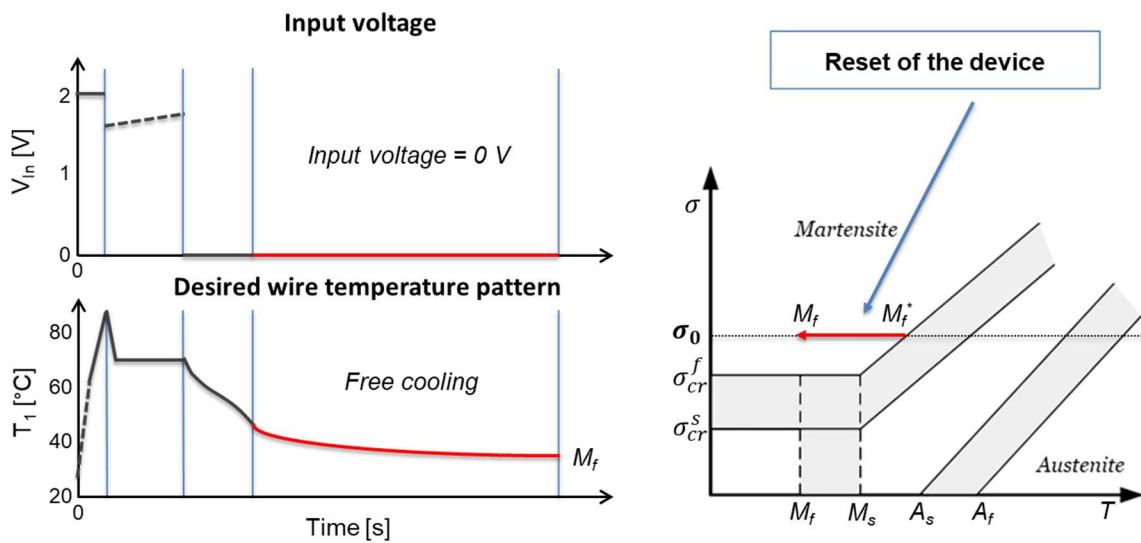


Figure 78 – Step 4, reset. Once the austenitic transformation is complete, additional time is given to the wire to cool down to a reference temperature.

8.2. Physical parameters expected to affect performance

The simulations will address several aspects of interest for performance, whose related parameters in the model are detailed next.

The first aspect we were interested in looking into is how the behaviour of the entire device is affected by modifications in the thermal properties of the soft matrix. Values of thermal

conductivity k_{PDMS} have been selected in a range that varies between the standard value for a silicone rubber, to a fairly high value obtained from the literature: 0.2, 0.4, 0.6, 0.8, 1.0, 1.2 and 1.4 W/(m·K). Higher values than the ones obtained in this work were also used, in order to study a broader range of matrix modification opportunities.

Another variable that I considered interesting, as it certainly affects the behaviour of the device from a thermal point of view, is the thermal contact resistance R_c between wire and matrix. In the previous Chapter, its value was assumed to be constant and equal to 1.5 (K·m²)/W (Section 6.4.2). In this work, direct characterisation or modification of the thermal interface between the two materials could not be carried out. Exactly for this reason, the influence of the thermal contact resistance was a fundamental aspect on which to focus the parametric study. In this way we could obtain useful information on its influence both in the range of values similar to the one I have hypothesised most correct, and for values that differ more. In particular, the most realistic values for an elastomer-to-metal interface fall within a range of $1-3 \cdot 10^{-3}$ (K·m²)/W [134]. Values down to two orders of magnitude smaller have been chosen to analyse the usefulness of a possible modification of the interface to reduce its thermal contact resistance and thus improve heat exchange. Conversely, values of at least an order of magnitude higher were chosen to evaluate modifications with the opposite purpose, and, at the same time, to investigate what is expected when the worsening of the thermal contact should occur spontaneously, e.g. due to device wear.

The chosen values are all combinations of factors {1,2,4,7} multiplied by magnitude orders { $10^{-5}, 10^{-4}, 10^{-3}, 10^{-2}$ }.

Convection, as in the previous chapter, remains of particular interest; accordingly, the same values of the h parameter were used: 5, 15 and 35 W/(m²·K).

All the simulations were repeated for three different values of the holding time t_H defined in the previous section. The chosen values are: 0, 6 and 10 s.

Finally, in order to explore actuator sizes compatible with the examples common in the literature, three different thicknesses of the matrix were selected: 2, 4 and 15 mm.

The simulation of single actuation cycles, rather than longer and more complex studies, allowed for the exploration of more combinations of parameters. With the ones chosen, combining their values differently, a total of 6048 simulations were run.

8.3. Results and discussion

The most interesting of the processed data, which will be presented, include the energy necessary to activate and keep the SMA wire heated, the temperatures in some characteristic instants, and the times of execution of the various actions especially during the cooling phases.

Some 3D surface plots will be presented to allow the simultaneous evaluation of the influence of two particular parameters on a third one.

Some of these graphs have been sectioned in correspondence with two R_c values which delimit the more realistic range of thermal contact resistance for our application. The chosen area of interest falls within $1-4 \cdot 10^{-3}$ (K·m²)/W. The 2D graphs resulting from the sectioning show the results in correspondence of these two R_c values as curves, to allow a better quantitative appreciation of the trends.

8.3.1. Complete actuation cycle starting with the system stabilised at $T_0 = 25$ °C

8.3.1.1. Activation

The first thing that has been evaluated is the electric energy required to activate the SMA wire, for all three matrix thicknesses of interest. The results for the smallest thickness among those chosen ($t_M = 2$ mm) is shown in Figure 79. Figure 80 shows the results for an actuator with a thickness t_M equal to 4 mm, while Figure 81 relates to the maximum thickness t_M of 15 mm. The effect of the convection coefficient h on the trend of the three figures is particularly small. In fact, all the results have been calculated and plotted for three different values of h , and while in some situations that we will see later it will be possible to distinguish three very different trends, in this case the three graphs are practically coincident. By analysing the shapes of the surfaces we can identify the dependence of the required input energy with respect to variations of the parameters in the test range. For all the three thicknesses of the matrix, and for all three values of h tested, the minimum energy value is equal to 14.24 J on the entire edge of the surface corresponding to the maximum value of thermal contact resistance ($R_c = 7 \cdot 10^{-2}$ (K·m²)/W). Being equal on the whole edge, the energy trend is therefore independent of the value of the thermal conductivity of the matrix k_{PDMS} . This occurs because at this R_c value the heat transfer between the two materials is very low. In fact, the amount of energy supplied, which is used to transform SMA into

austenite is equal to 3.46 J, while the heat supplied to raise its temperature to 83.6 °C is equal to 10.49 J. As the thermal contact resistance R_c decreases, more energy is exchanged between the two materials; as a consequence, the electrical energy to be injected increases.

Furthermore, for intermediate values of R_c , such as those identified with the two coloured curves in the 3D and corresponding 2D graphs, an increase in energy is required even for an increase in k_{PDMS} . Here, the effects caused by these two parameters start to interact. The lower the R_c , the greater the influence of k_{PDMS} on the energy absorption. We can therefore deduce that a lower R_c (better thermal transfer at the interface between the SMA wire and the elastomeric matrix) combined with an increase in the heat transfer capacity of the elastomeric matrix, means that much of the injected energy of the system is transferred to the matrix itself instead of being used to heat and actuate the SMA wire.

While in correspondence with the two lines which delimit the range of contact thermal resistance of interest the dependence on k_{PDMS} is limited, for R_c values lower than $1 \cdot 10^{-3}$ (K·m²)/W it becomes extremely high, significantly reducing energy efficiency. Furthermore, in this region of the surface, the energy also varies with the thickness of the elastomeric matrix. A larger thickness (and therefore a greater volume of the elastomeric matrix) leads to the matrix ability to store (subtract) more energy.

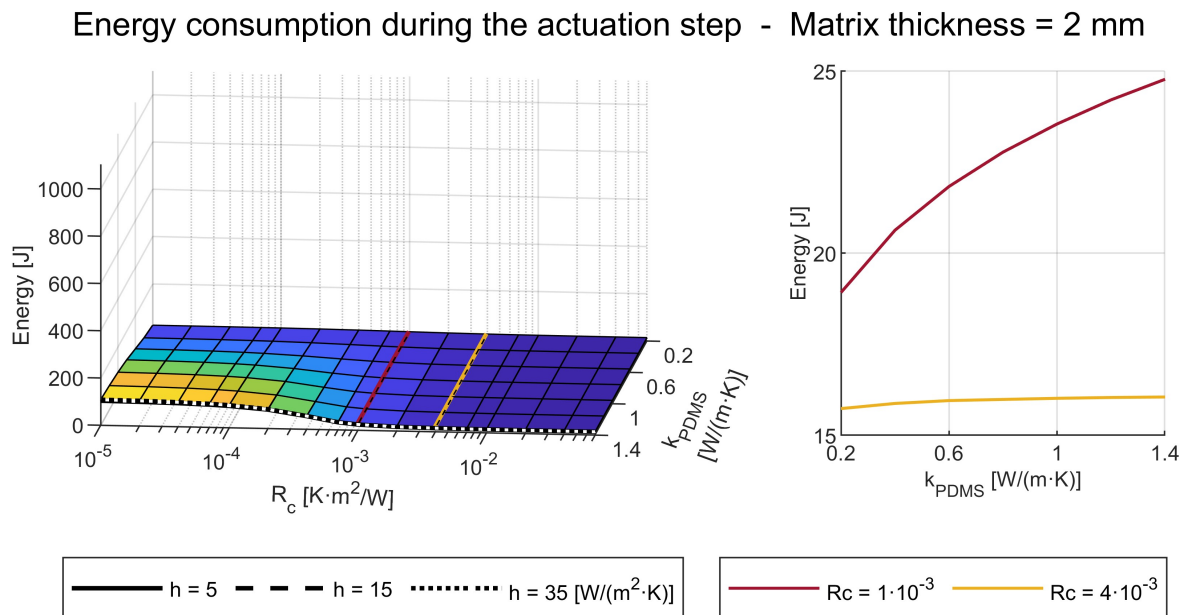


Figure 79 - 3D surfaces representing the energy consumption calculated for three values of the convection coefficient h (left). The variability given by h is less than 5 %, so the surfaces are almost indistinguishable. The energy values calculated for the two R_c values that delimit the normality range, represented by the yellow and red coloured lines, are reported in a 2D graph (right).

Energy consumption during the actuation step - Matrix thickness = 4 mm

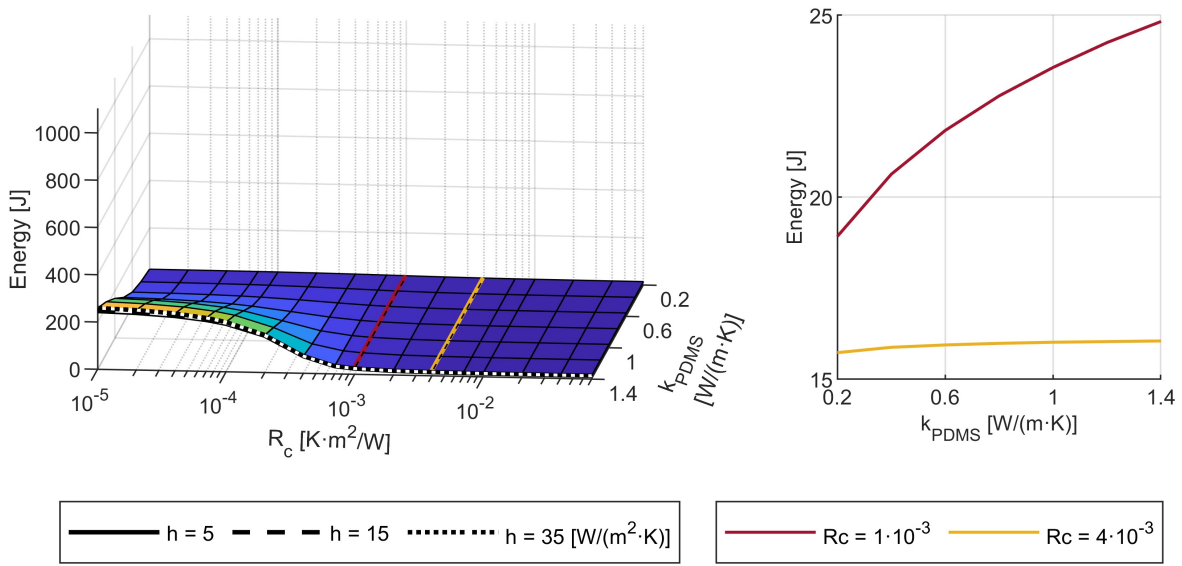


Figure 80 - 3D surfaces representing the energy consumption calculated for three values of the convection coefficient h (left). The variability given by h is less than 5 %, so the surfaces are almost indistinguishable. The energy values calculated for the two R_c values that delimit the normality range, represented by the yellow and red coloured lines, are reported in a 2D graph (right).

Energy consumption during the actuation step - Matrix thickness = 15 mm

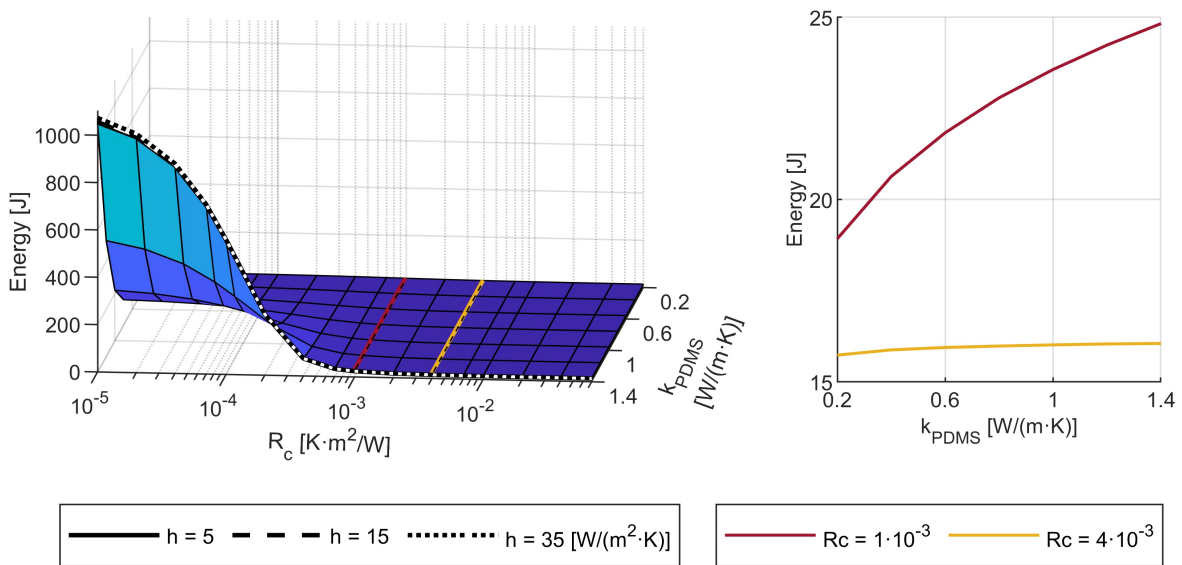


Figure 81 - 3D surfaces representing the energy consumption calculated for three values of the convection coefficient h (left). The variability given by h is less than 5 %, so the surfaces are almost indistinguishable. The energy values calculated for the two R_c values that delimit the normality range, represented by the yellow and red coloured lines, are reported in a 2D graph (right).

The time needed to complete the actuation step is shown in Figure 82 ($t_M = 2$ mm), Figure 83 ($t_M = 4$ mm) and Figure 84 ($t_M = 15$ mm). The trends are qualitatively very similar to those just presented for the injected energy. Since the electric control voltage is constant

during this step of the test cycle, the energy is strongly connected to the time taken to complete the actuation of the SMA wire, the resistivity changes due to phase transformation having a more limited impact.

Time to complete the transformation to austenite - Matrix thickness = 2 mm

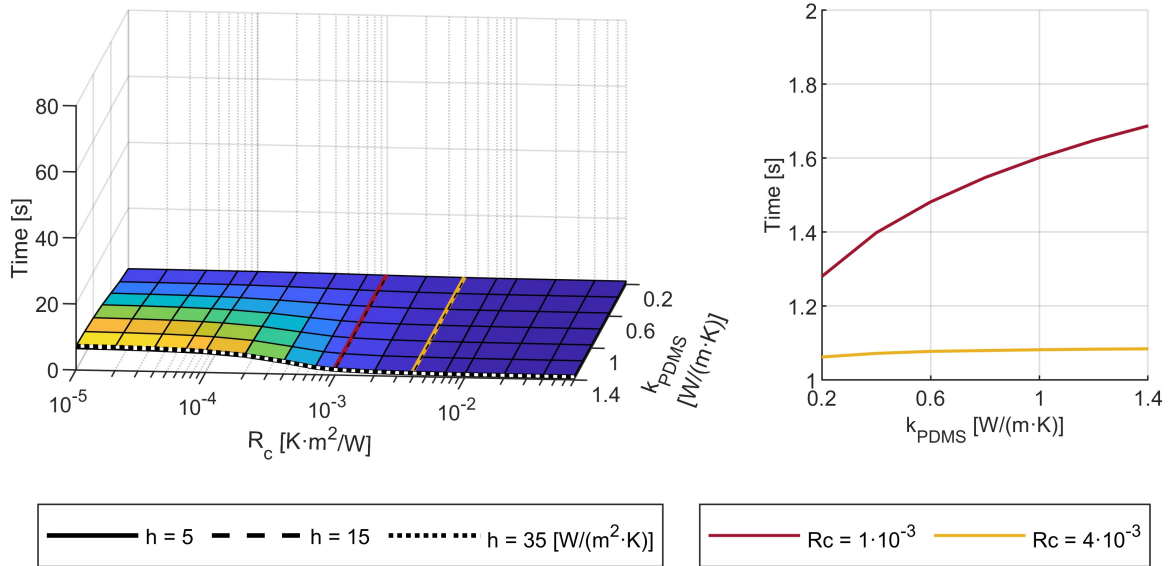


Figure 82 - 3D surfaces representing the time needed to complete the first step (left). Also in this case the results are almost independent of the coefficient h , and the trends are almost identical to those shown for the energy consumption. The time values calculated for the two R_c values that delimit the normality range are slightly dependent on the thermal conductivity k_{PDMS} (right).

Time to complete the transformation to austenite - Matrix thickness = 4 mm

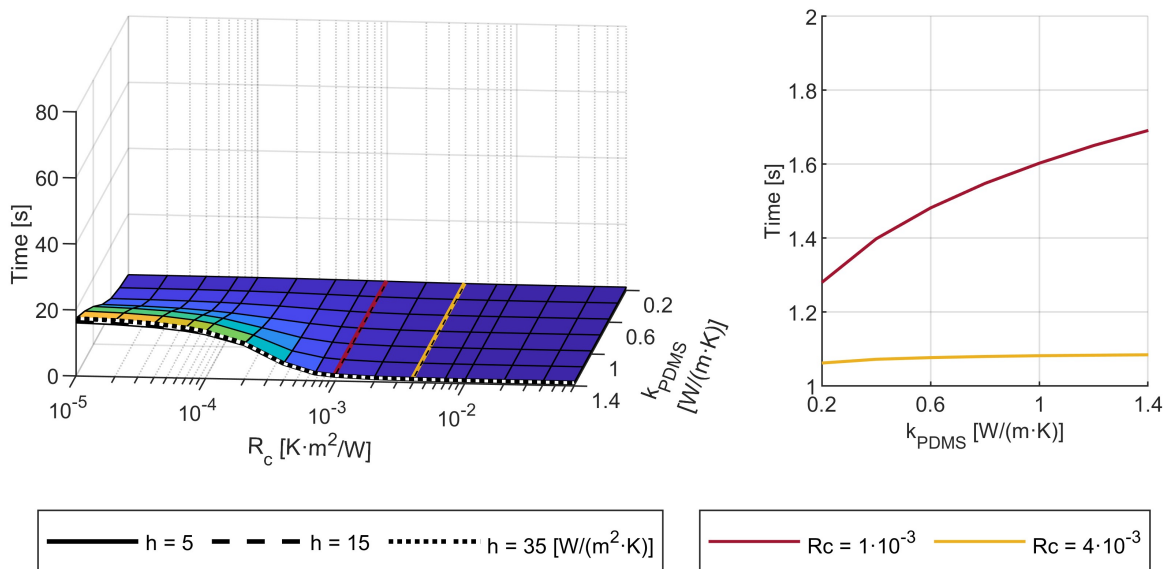


Figure 83 - 3D surfaces representing the time needed to complete the first step (left). Also in this case the results are almost independent of the coefficient h , and the trends are almost identical to those shown for the energy consumption. The time values calculated for the two R_c values that delimit the normality range are slightly dependent on the thermal conductivity k_{PDMS} (right).

Time to complete the transformation to austenite - Matrix thickness = 15 mm

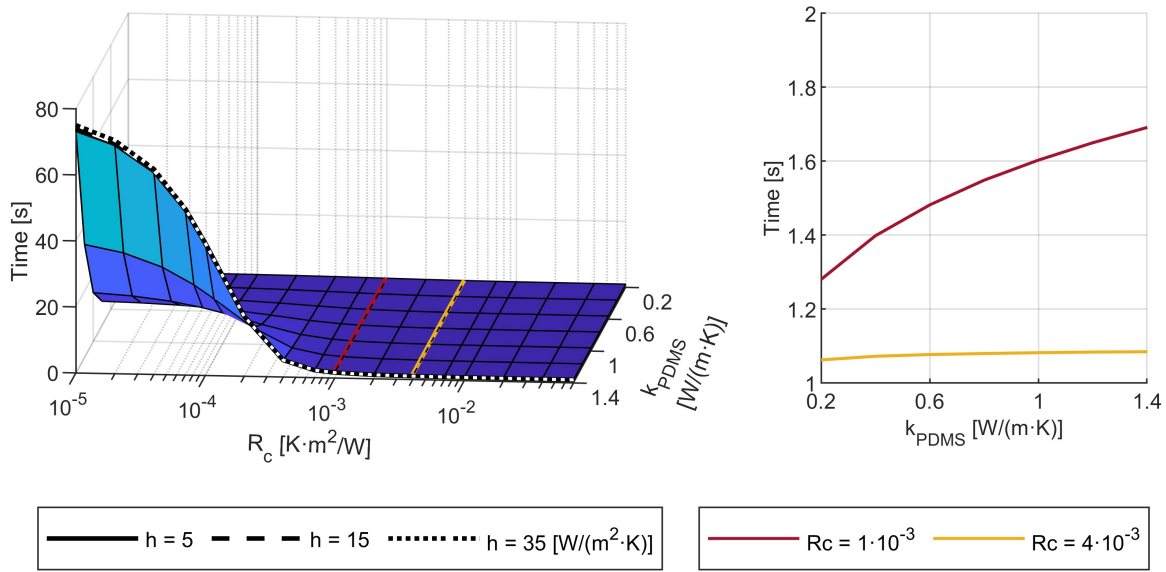


Figure 84 - 3D surfaces representing the time needed to complete the first step (left). Also in this case the results are almost independent of the coefficient h , and the trends are almost identical to those shown for the energy consumption. The time values calculated for the two R_c values that delimit the normality range are slightly dependent on the thermal conductivity k_{PDMS} (right).

In order to quantify the effect that the amount of energy transferred through the elastomer-SMA interface has on the matrix, its average temperature T_2 at the final instant of this actuation cycle was evaluated. The results are presented in Figure 85 ($t_M = 2$ mm), Figure 86 ($t_M = 4$ mm) and Figure 87 ($t_M = 15$ mm).

For all the thicknesses of the matrix taken into consideration, a considerable degree of heating can be noted especially in correspondence of low values of R_c and high values of k_{PDMS} . The trend of the surfaces is similar to the previous figures, therefore a greater energy injected into the wire has the consequence of heating the soft matrix more.

Although for low values of t_M the energy supplied was lower, the smaller volume of the soft matrix causes the overheating to be greater compared to higher thicknesses of the matrix.

The effect of the convection coefficient h on T_2 is almost null for all the cases considered here. In fact, also in the case of the matrix temperature it is difficult to distinguish in the graphs the three curves plotted for the three different values of h , which are almost superimposed. This may mean that most of the energy supplied in this first section of the test cycle, and which is not used by the SMA material during the transformation into austenite, is retained by the soft matrix.

T_2 at the end of actuation step - Matrix thickness = 2 mm

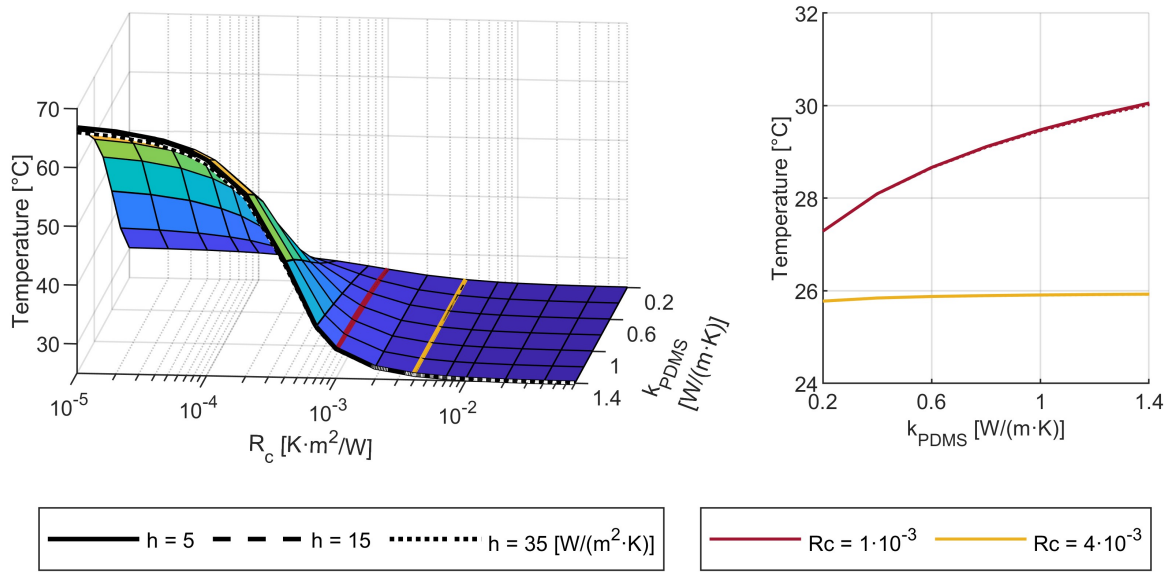


Figure 85 - 3D surfaces representing the mean temperature of the matrix T_2 at the end of the first step (left). For some values of R_c and k_{PDMS} , the T_2 can reach high values. In the normal range delimited by the two coloured lines, the overheating of the matrix is limited and poorly dependent on k_{PDMS} (right).

T_2 at the end of actuation step - Matrix thickness = 4 mm

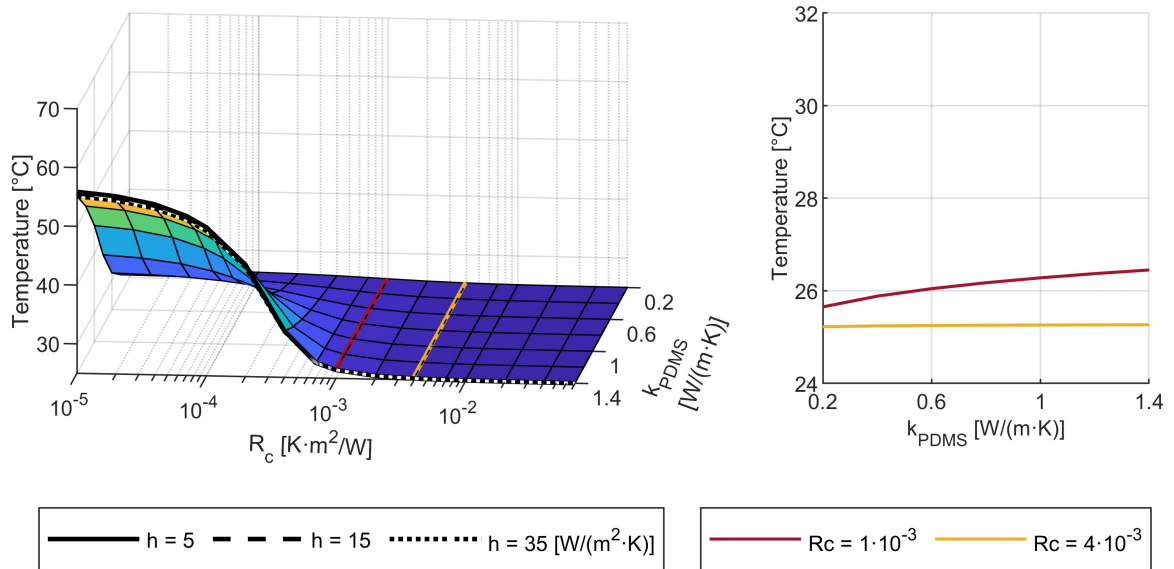


Figure 86 - 3D surfaces representing the mean temperature of the matrix T_2 at the end of the first step (left). For some values of R_c and k_{PDMS} , the T_2 can reach high values. In the normal range delimited by the two coloured lines, the overheating of the matrix is limited and poorly dependent on k_{PDMS} (right).

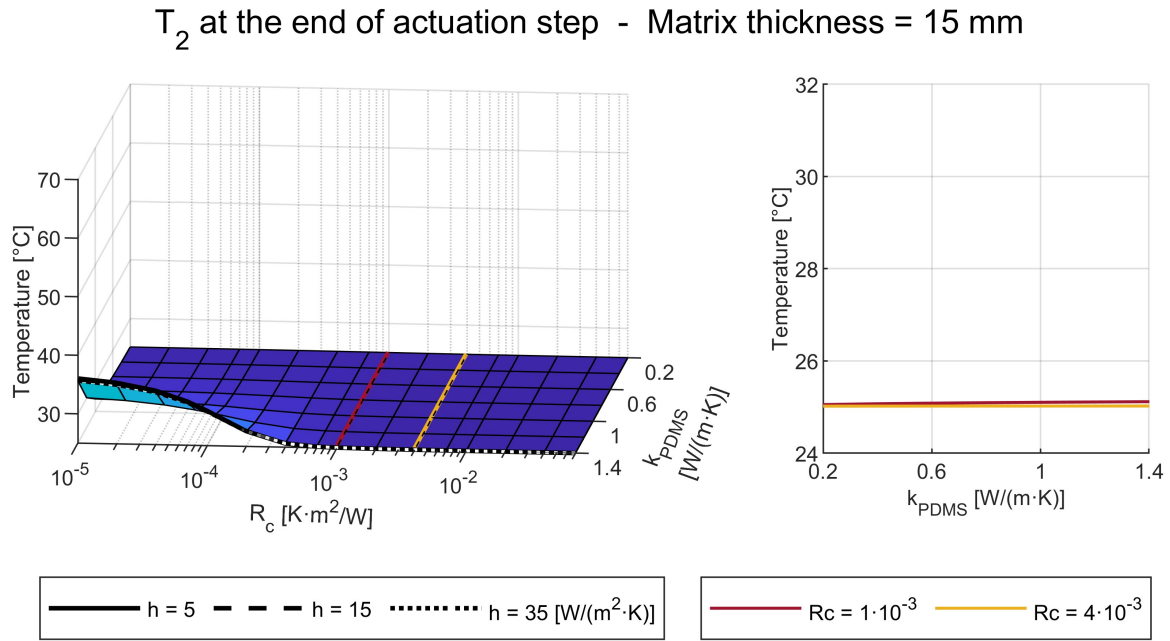


Figure 87 - 3D surfaces representing the mean temperature of the matrix T_2 at the end of the first step (left). In this case, unlike to the smaller thicknesses of the matrix, the T_2 always maintains contained values. In the normal range delimited by the two coloured lines, the overheating of the matrix is null (right).

The increase of k_{PDMS} leads to an overheating of the matrix only for low values of R_c . Furthermore, the threshold of R_c at which this effect occurs decreases with increases in thickness t_M . It can in fact be noted that the trends of T_2 in correspondence with R_c equal to $1 \cdot 10^{-3}$ ($K \cdot m^2/W$) (red lines) changes in relation to the thickness of the elastomeric matrix. Anyway, in the most realistic range of contact resistances, the average temperature of the matrix remains lower than $30 \text{ }^\circ\text{C}$ even in correspondence with the highest k_{PDMS} value.

8.3.1.2. Holding

After having completed the actuation step by means of the transformation of the SMA material into austenite, the new objective value of temperature T_I is just above $M_s^* + T_{AH}$ ($71.5 + 2 \text{ }^\circ\text{C}$) to be maintained for a predetermined time t_H . The energy necessary to keep the wire sufficiently hot to avoid the martensitic transformation is thus supplied. The surfaces showing the trend of the energy injected into the SMA wire in this step, as the parameters vary, are shown in Figure 88 ($t_M = 2 \text{ mm}$), Figure 89 ($t_M = 4 \text{ mm}$) and Figure 90 ($t_M = 15 \text{ mm}$).

The first thing that can be noticed is that the energy supplied increases with the value of the holding time. For the selected t_H values, the energy is always lower than the one required to actuate the SMA wire.

As in the previous step, the increase in the thermal contact resistance between the two materials has a drastic effect on the injected energy. While overall the trend is non-monotonic, for the mid-higher end of the explored R_c range, energy consumption decreases the more R_c increases. The minimum values are about 0.6 J with $t_H = 6$ s and 1.2 J with $t_H = 10$ s.

Considering mixed effects of two parameters, even in this case, an isolated decrease in R_c (with baseline k_{PDMS}) or an isolated increase in k_{PDMS} (with baseline R_c) leads to an increase in the energy required for the holding step. However, there is a substantial difference when low values of R_c and high values of k_{PDMS} are present simultaneously, as this causes the injected energy to decrease. This occurs, above all in correspondence with low values of the thickness, because the matrix it is already overheated following the activation step of the SMA wire (as we have seen in the previous section), which hinders further heat transfer. In the holding step, the effect of the convection coefficient h starts to show itself, and is greater as the thickness of the matrix decreases (Figure 88 - left). A greater value of h corresponds to a greater energy required.

Regarding the average matrix temperature, since during the holding step the SMA wire is kept at a temperature higher than 73.5 °C, T_2 at the end of this step is further increased. Especially for low R_c values and high k_{PDMS} values, this additional heating leads to final temperatures above the M_f^* value of 56.5 °C, which may impact negatively on the cooling performance (see next section 8.3.1.3).

Considering in particular the R_c range of interest (between the red and yellow lines), compared to the actuation step, the increase in k_{PDMS} corresponds to an even greater increase in energy consumption. This effect is also magnified as the holding time t_H increases. Here, the influence of h is slightly present for a matrix thickness t_M of 2 mm, and with t_H of 10 s (Figure 88 - bottom right).

Energy consumption during the holding step - Matrix thickness = 2 mm

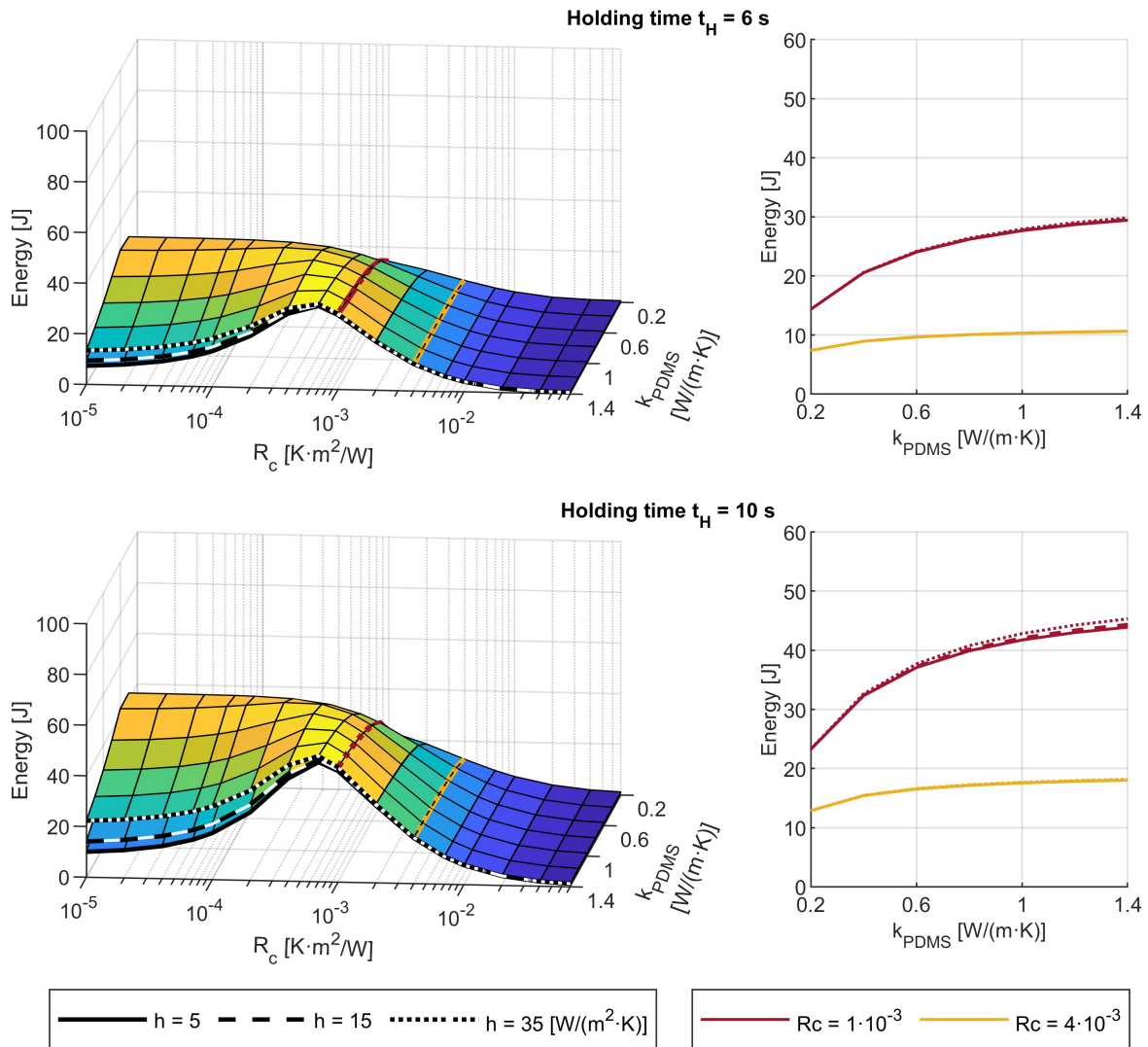


Figure 88 - Energy consumption calculated for two different values of the holding time. The 3D surfaces show that the dependence on the coefficient h occurs only in some regions (left). In correspondence with the R_c value highlighted by the red lines, the increase in the energy supplied as the thermal conductivity of the matrix k_{PDMS} increases is considerable (right).

Energy consumption during the holding step - Matrix thickness = 4 mm

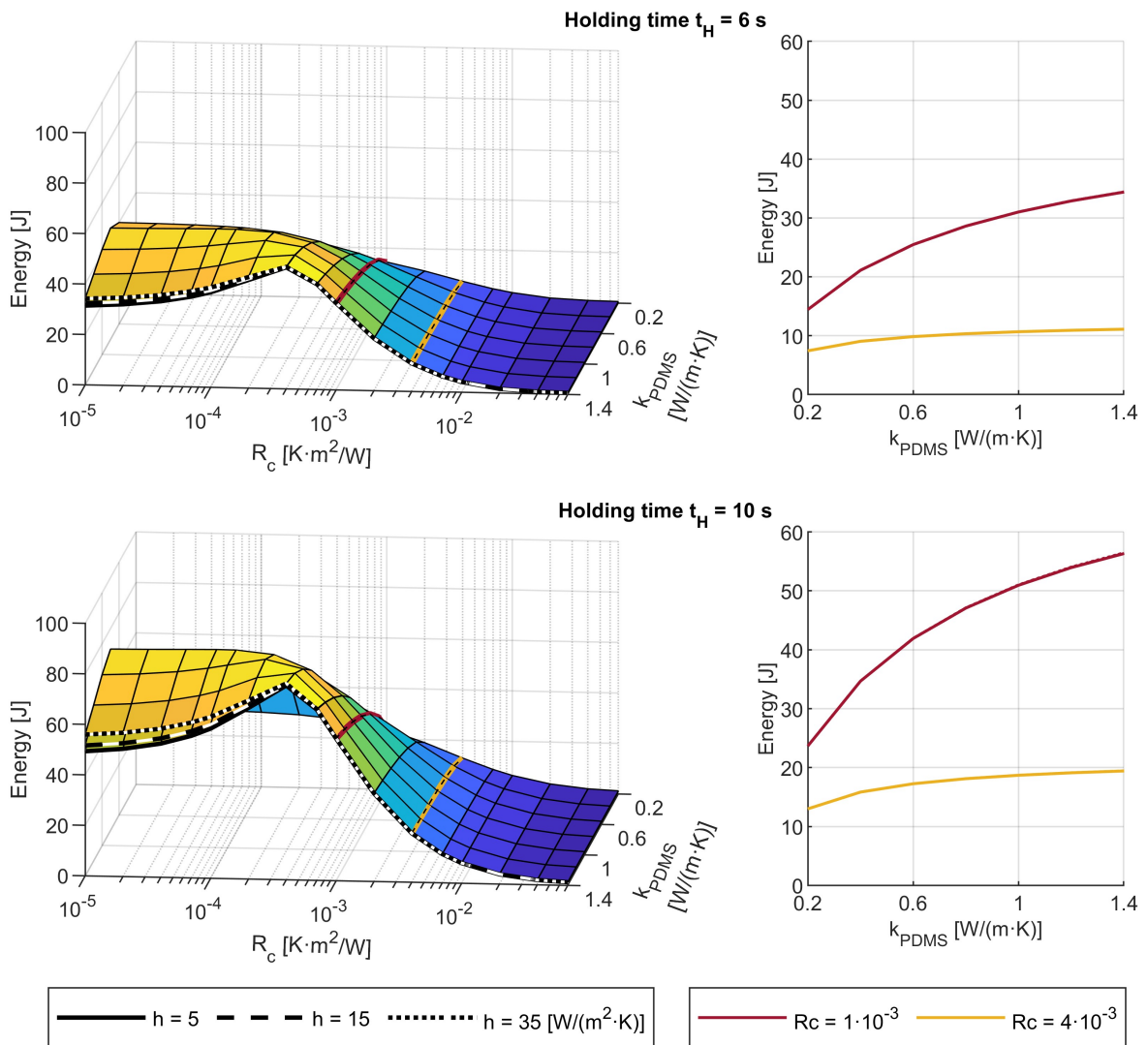


Figure 89 - Energy consumption calculated for two different values of the holding time. The 3D surfaces show that the dependence on the coefficient h occurs only in some regions (left). In correspondence with the R_c value highlighted by the red lines, the increase in the energy supplied as the thermal conductivity of the matrix k_{PDMS} increases is considerable (right).

Energy consumption during the holding step - Matrix thickness = 15 mm

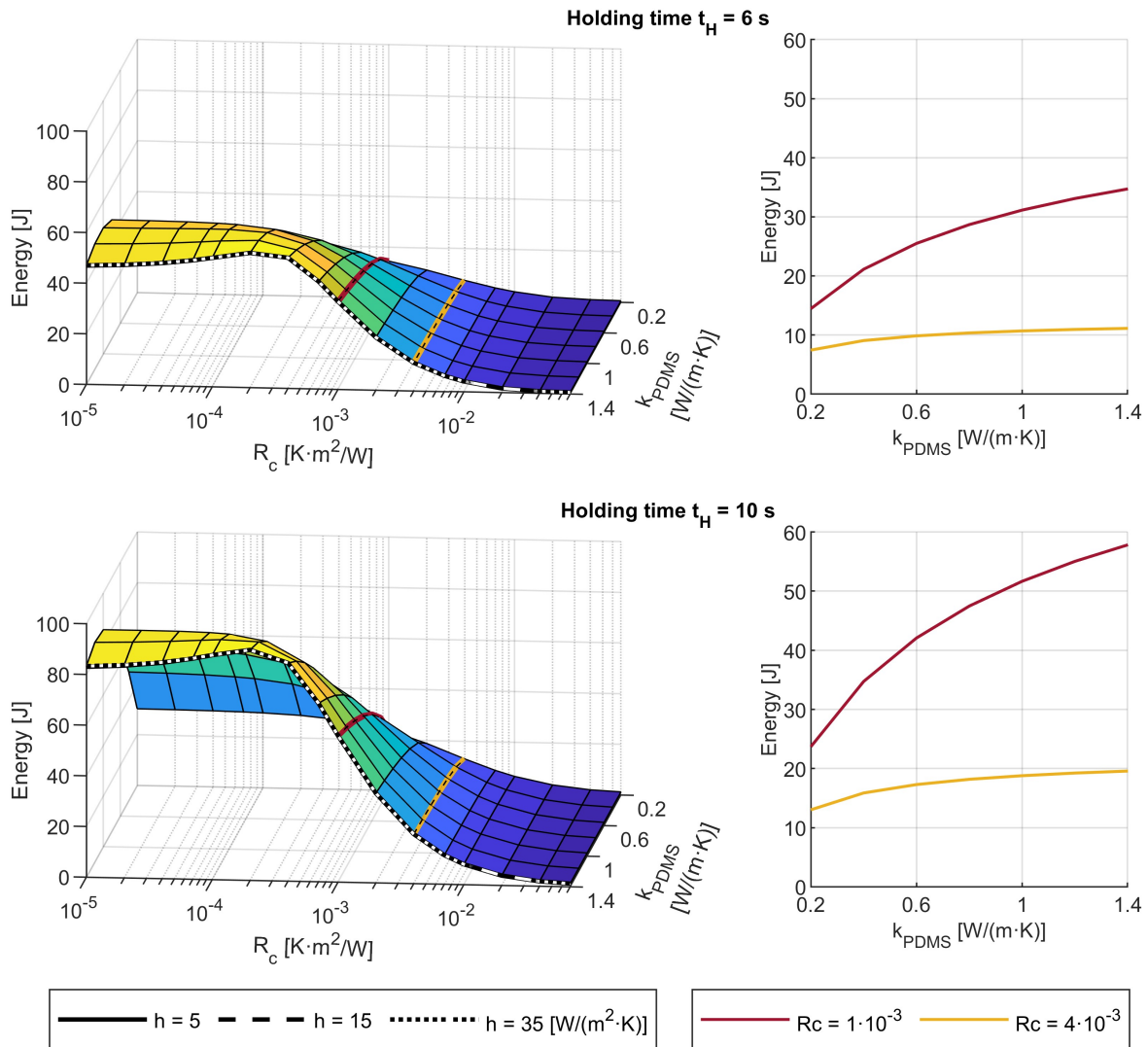


Figure 90 - Energy consumption calculated for two different values of the holding time. The 3D surfaces show that the dependence on the coefficient h occurs only in some regions (left). In correspondence with the R_c value highlighted by the red lines, the increase in the energy supplied as the thermal conductivity of the matrix k_{PDMS} increases is considerable (right).

8.3.1.3. Deactivation

Once the temperature holding is finished, the SMA wire is free to cool down. The time required to complete the martensitic transformation is the next important performance index, and one which is an important determinant of the applicability of SMA actuators, as has been already mentioned several times in previous chapters. It is strongly dependent on various aspects. The first is the overheating of the matrix, and involves all those cases in which the matrix temperature was raised to a value higher than the M_f^* value of 56.5 °C through the activation and holding steps. It occurs for low R_c values and high k_{PDMS} values, severely

lengthening cooling duration in the cases of low thicknesses of the soft matrix (Figure 91 and Figure 92), while causing no performance loss for a thickness of 15 mm (Figure 93). Differently from the previous steps, the influence of the convection coefficient h to counteract the effect of matrix overheating is considerable. With t_M equal to 2 mm, in particular, the duration of the transformation can go from more than 100 s ($h = 5 \text{ W}/(\text{m}^2 \cdot \text{K})$) to about 20 s ($h = 35 \text{ W}/(\text{m}^2 \cdot \text{K})$).

The values of the mean temperature of the matrix T_2 at the end of this step are shown in Figure 94 ($t_M = 2 \text{ mm}$), Figure 95 ($t_M = 4 \text{ mm}$) and Figure 96 ($t_M = 15 \text{ mm}$).

The second case worth analysing is related to the occurrence of contact resistances in the upper range of R_c , which, while in the previous steps favoured heating efficiency, in this one significantly increase the cooling duration. In correspondence with the maximum value of R_c tested, the transformation time reaches the value of almost 50 s, which can be reduced by about 3 s by increasing the k_{PDMS} . As can be seen in the figures, the effects of the contact resistance are invariable with the thickness of the matrix and with the convection coefficient h . The reason for this can be attributed to the fact that a high thermal contact resistance limits the transfer of energy present in the SMA material towards the elastomeric matrix, almost independently of the thermal exchanges present beyond the interface itself. On the other side, since the temperature of the SMA wire in the holding step always stabilises at the same value, the influence of t_H is quite limited.

As R_c increases, a rather moderate decrease in performance results, compared to the impact of overheating which conditions the martensitic transformation duration drastically. As can be seen in Figure 91, the duration can still increase considerably with small variations in the R_c and k_{PDMS} parameters; their evaluation and careful choice can therefore be fundamental especially for small values of matrix thickness.

The best performances are found in the intermediate values of R_c , within the two coloured lines. Here, the increase of k_{PDMS} can lead to a decrease in martensitic transformation time, with improvements that reach 50 %. For high holding durations, the overheating of the matrix can undermine the positive effect of the k_{PDMS} modification. In particular, it is possible to see how this occurs with a matrix thickness of 2 mm and a low value of h (Figure 91, $t_H = 10 \text{ s}$, red line). With small thicknesses of the matrix, if higher t_H values are needed, especially for R_c values of the order of $10^{-3} \text{ (K} \cdot \text{m}^2)/\text{W}$, a k_{PDMS} of medium-low values in the tested range may be preferable. With a thicknesses t_M of 4 mm (Figure 92), the effect of matrix overheating is less accentuated and occurs at lower R_c values.

Martensitic transformation time - Matrix thickness = 2 mm

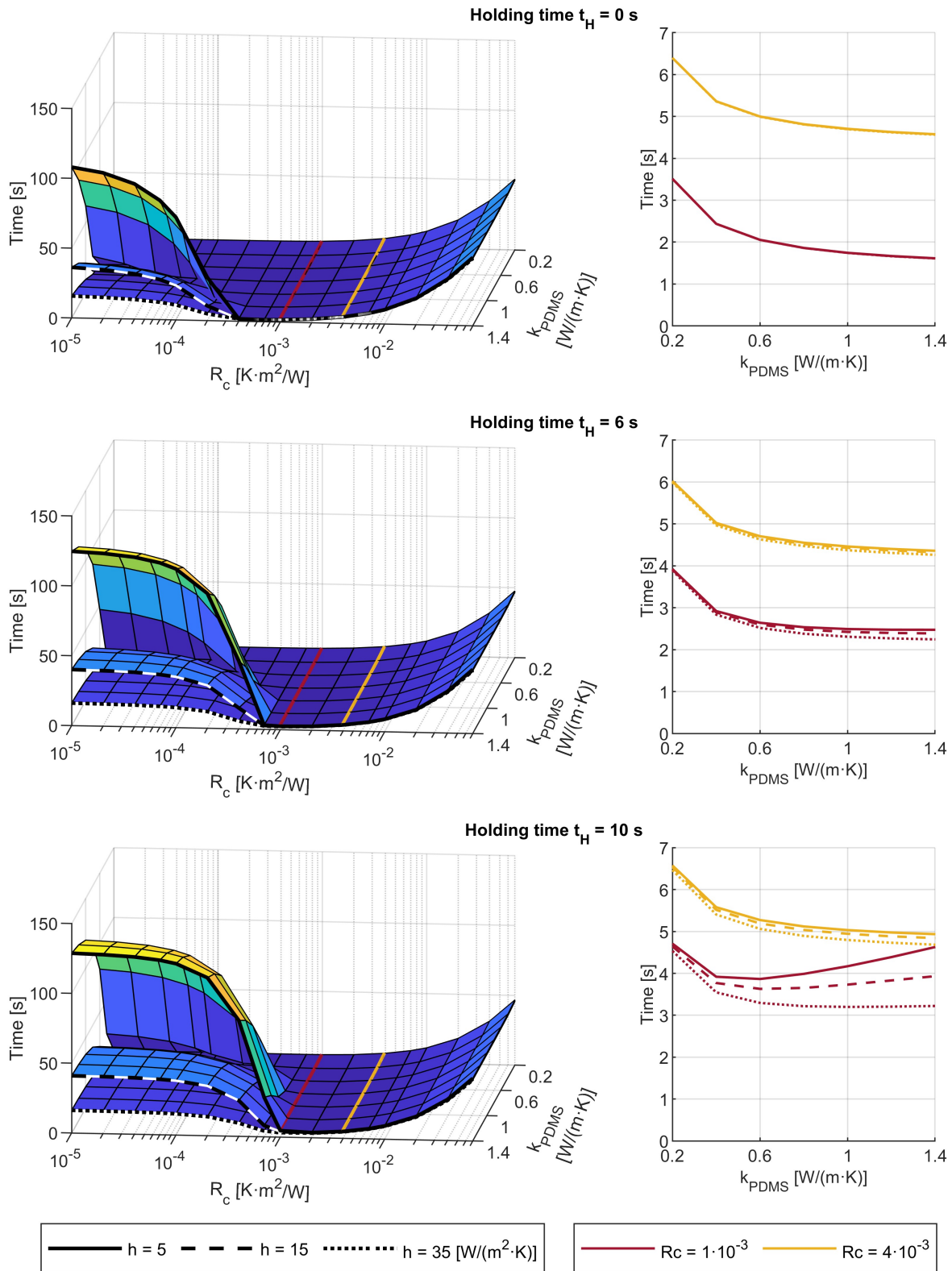


Figure 91 - 3D surfaces representing the time needed to complete the martensitic transformation after an holding step with a duration t_H (left). A greater convection coefficient h speed up the transformation in regions where overheating of the elastomeric matrix was present. Where overheating has not occurred, increasing k_{PDMS} can speed up the transformation (right).

Martensitic transformation time - Matrix thickness = 4 mm

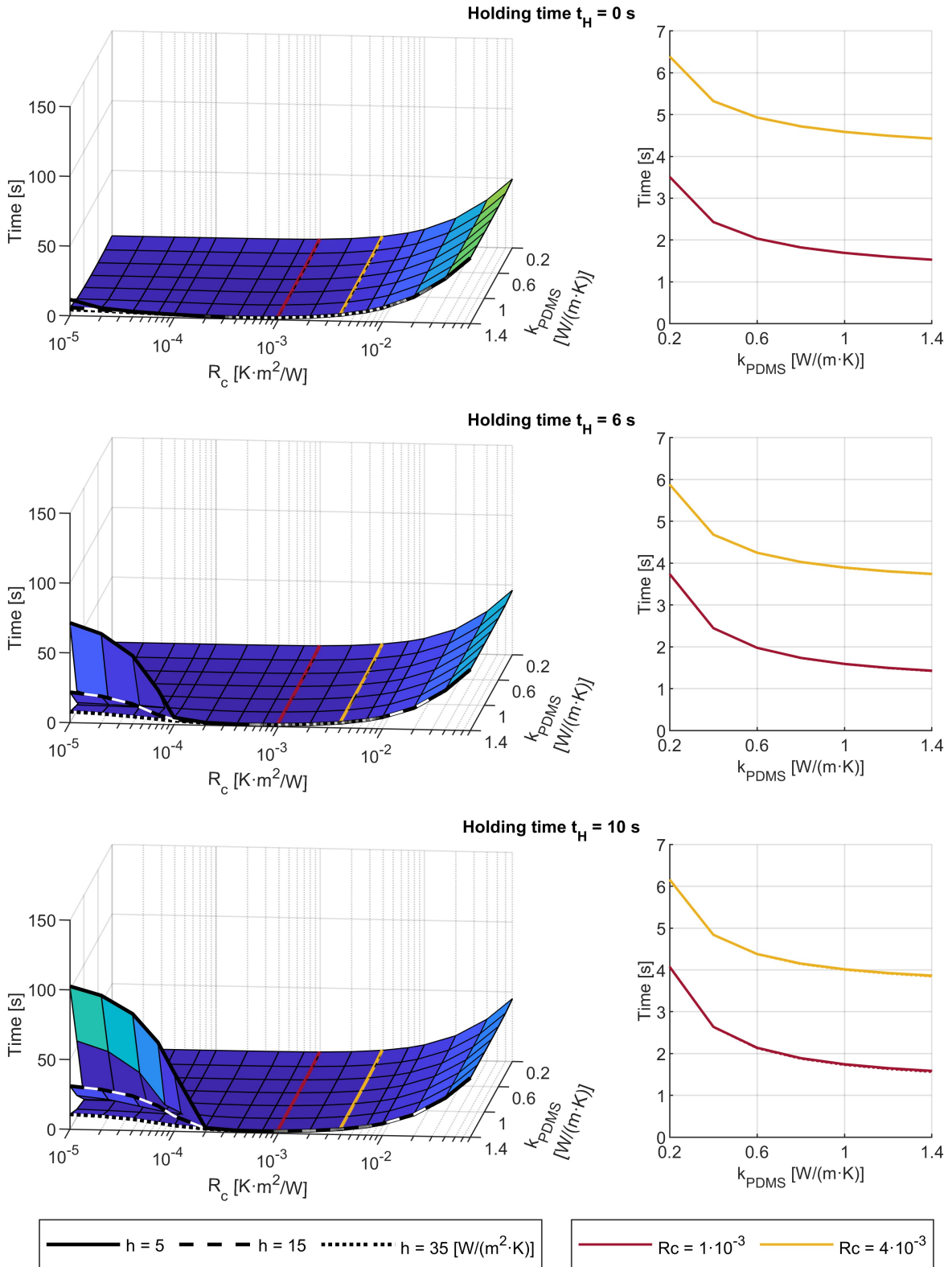


Figure 92 - 3D surfaces representing the time needed to complete the martensitic transformation after an holding step with a duration t_H (left). A greater convection coefficient h speed up the transformation in regions where overheating of the elastomeric matrix was present. Where overheating has not occurred, increasing k_{PDMS} can speed up the transformation (right).

Martensitic transformation time - Matrix thickness = 15 mm

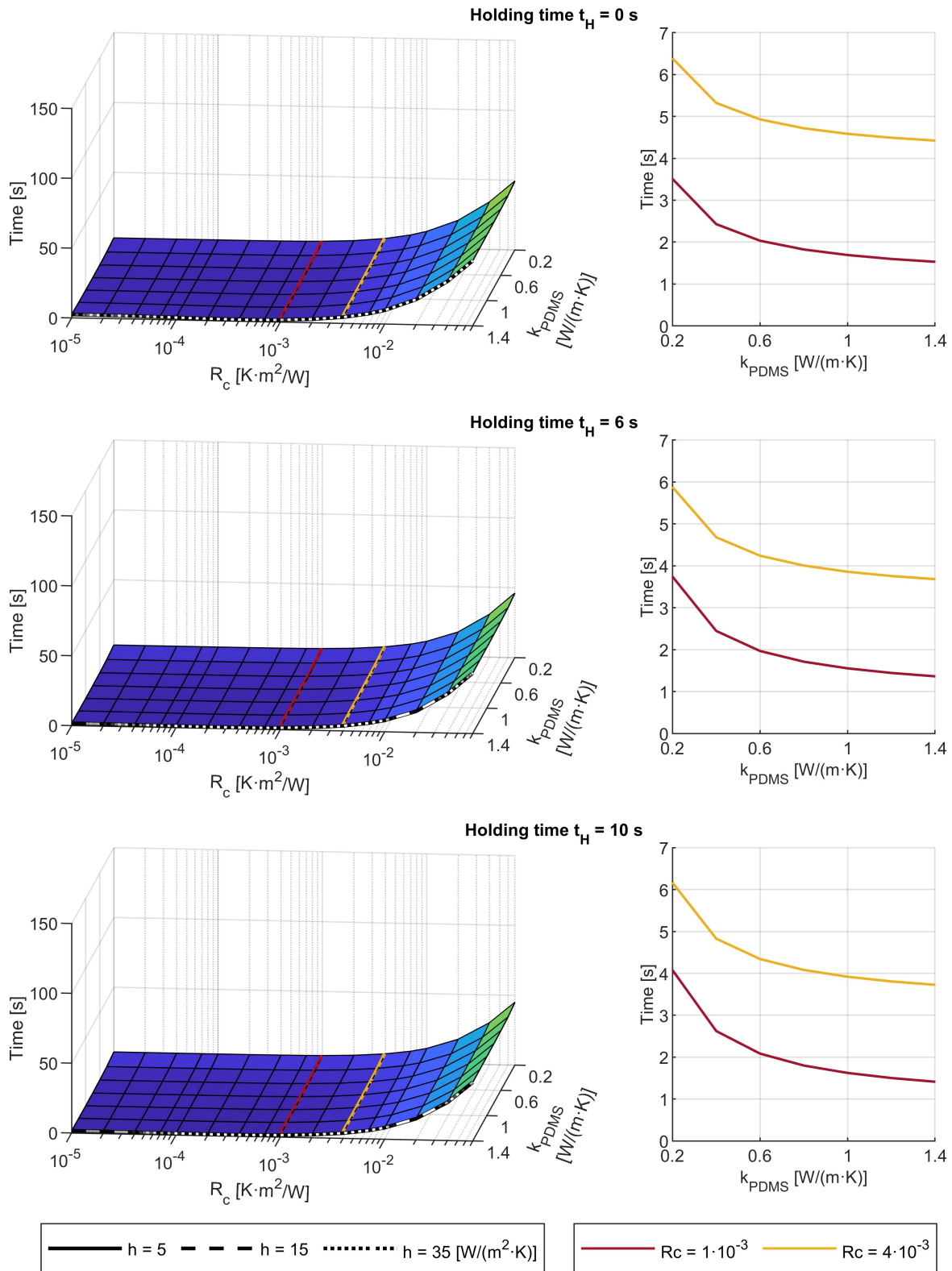


Figure 93 - 3D surfaces representing the time needed to complete the martensitic transformation after an holding step with a duration t_H (left). A greater convection coefficient h speed up the transformation in regions where overheating of the elastomeric matrix was present. Where overheating has not occurred, increasing k_{PDMS} can speed up the transformation (right).

T_2 at the end of martensitic transformation - Matrix thickness = 2 mm

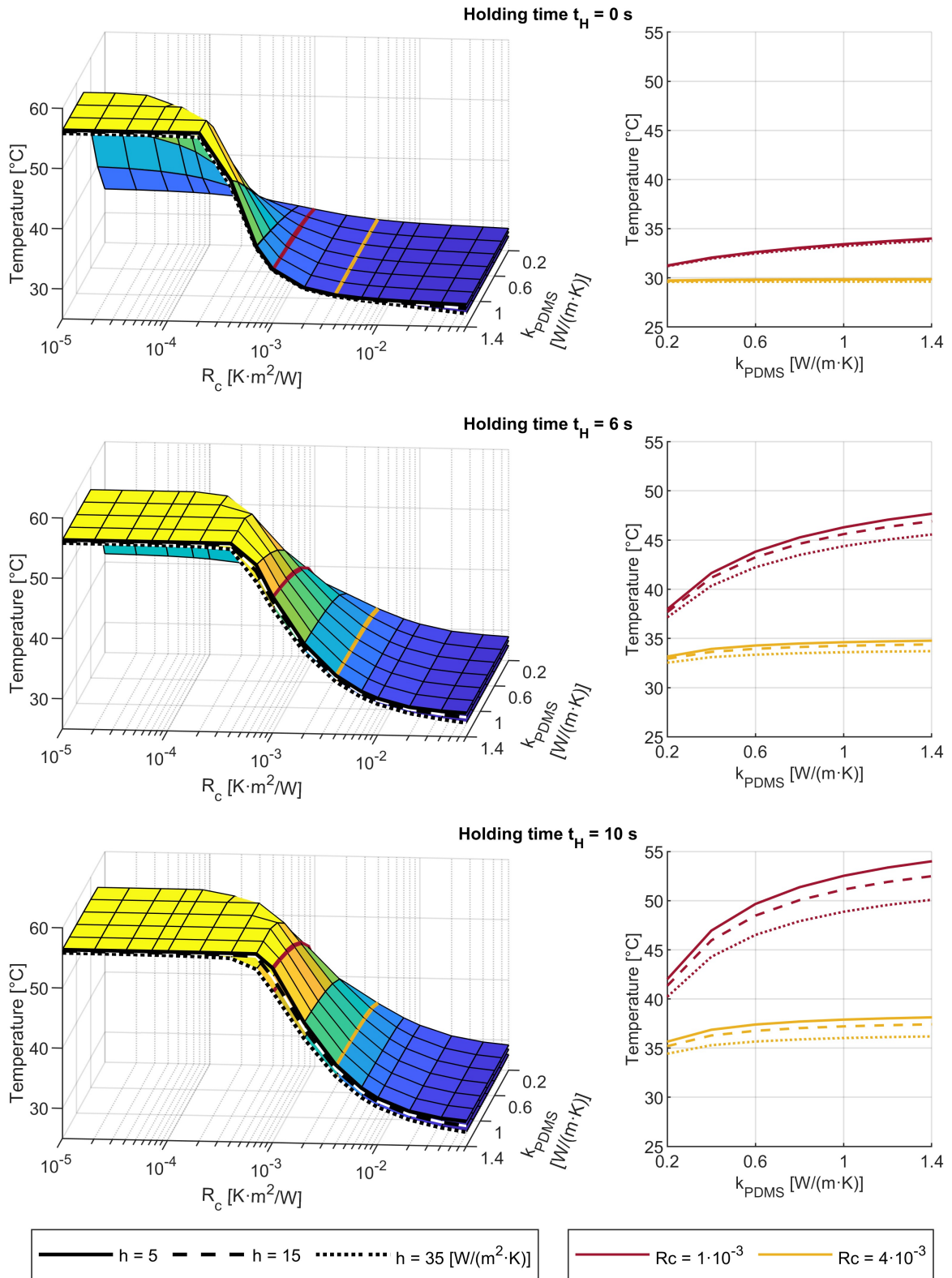


Figure 94 - 3D surfaces representing the mean temperature of the matrix T_2 at the end of the holding step (left). Small thicknesses of the matrix are subject to high heating even in the region delimited by the two coloured lines. Increasing k_{PDMS} causes more heating (right).

T_2 at the end of martensitic transformation - Matrix thickness = 4 mm

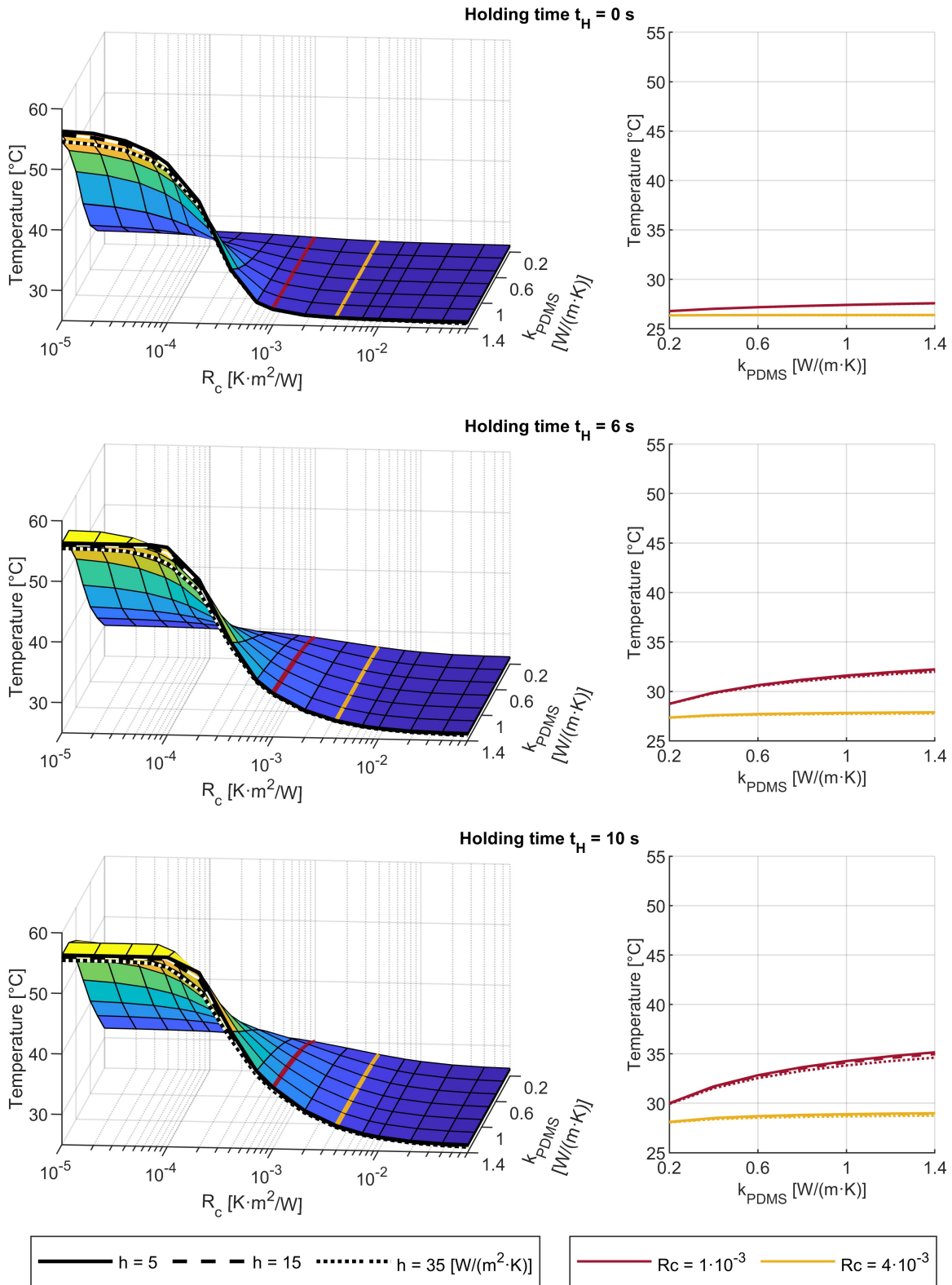


Figure 95 - 3D surfaces representing the mean temperature of the matrix T_2 at the end of the holding step (left). Medium thicknesses of the matrix are less subject to high heating in the region delimited by the two coloured lines (right).

T_2 at the end of martensitic transformation - Matrix thickness = 15 mm

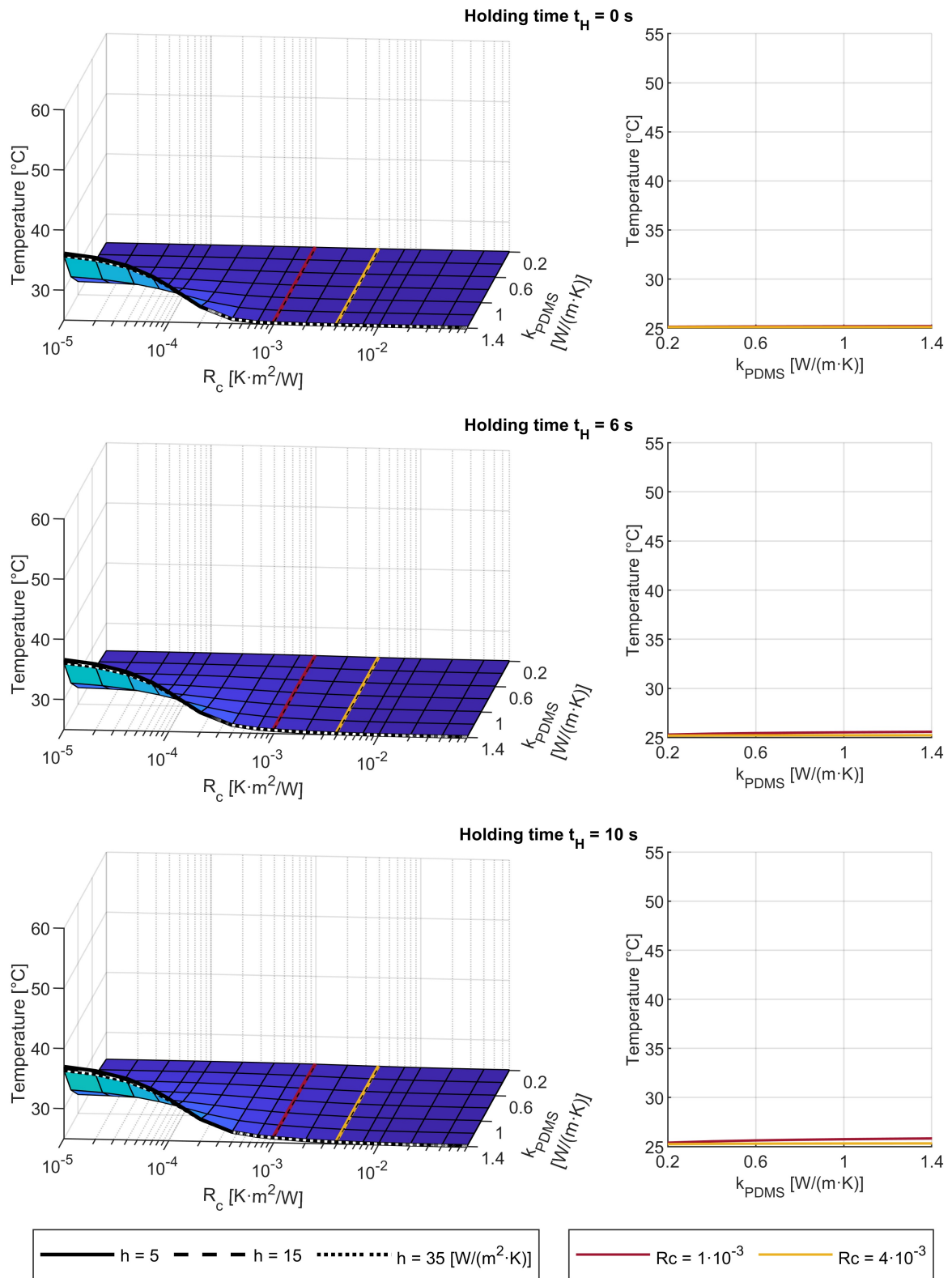


Figure 96 - 3D surfaces representing the mean temperature of the matrix T_2 at the end of the holding step (left). Large thicknesses of the matrix allow to avoid the heating of the matrix in the range of thermal contact resistance R_c delimited by the two coloured lines (right).

8.3.1.4. **Reset**

In this step we analyse the behaviour of the device in a situation similar to the previous one. Here the objective is to verify how long it takes for the SMA wire to pass from an average temperature T_1 equal to M_f^* (56.5 °C) to a temperature equal to M_f (32.1 °C).

As the martensitic transformation is already completed, the cooling is directly linked to the energy stored by the SMA wire and the soft matrix. Indeed, a certain similarity of the results presented in this section can be noted with the graphs of the temperatures T_2 evaluated at the end of the previous step. For those combinations of k_{PDMS} and R_c where the overheating occurred, convection plays a crucial role in the dissipation of the heat stored in the device. Higher values of the coefficient h produce a clear reduction of the cooling times.

From the graphs it is possible to notice how an increase in the thickness of the matrix negatively affects this aspect. For a thickness of the matrix equal to 2 mm the maximum cooling times are shorter than for the higher thicknesses, with the same values of the coefficient h .

In the graphs presented, it can be seen how, also during this step, the higher R_c values introduce a slowdown in cooling, effectively limiting the heat exchange between the SMA wire and the matrix. This can be stated since the T_2 at the end of the previous step was minimum for the maximum value of R_c used ($7 \cdot 10^{-2}$ (K·m²)/W).

For low convection values, the worst performances are found in the scenarios, for which overheating occurred (low R_c). Instead, the limitation introduced by high R_c values is predominant for high h values, since a good convection is able to dispose better of excessive heat in the matrix but cannot affect the wire temperature if it is decoupled from the matrix's. Between these two effects lie the best conditions. The minimum is localised in medium-high values of R_c , which are highly dependent on the thickness of the matrix, and on the holding time used. Only in these areas, where the overheating of the matrix has not occurred, the increase in the thermal conductivity of the matrix k_{PDMS} has the effect of reducing the cooling time. The performances obtainable in this case are very similar as the thickness of the matrix varies.

Within the range delimited by the two coloured lines, good performances can only be obtained with high thicknesses of the matrix (> 4 mm), or with small thicknesses together with reduced holding times t_H .

Reset time - Matrix thickness = 2 mm

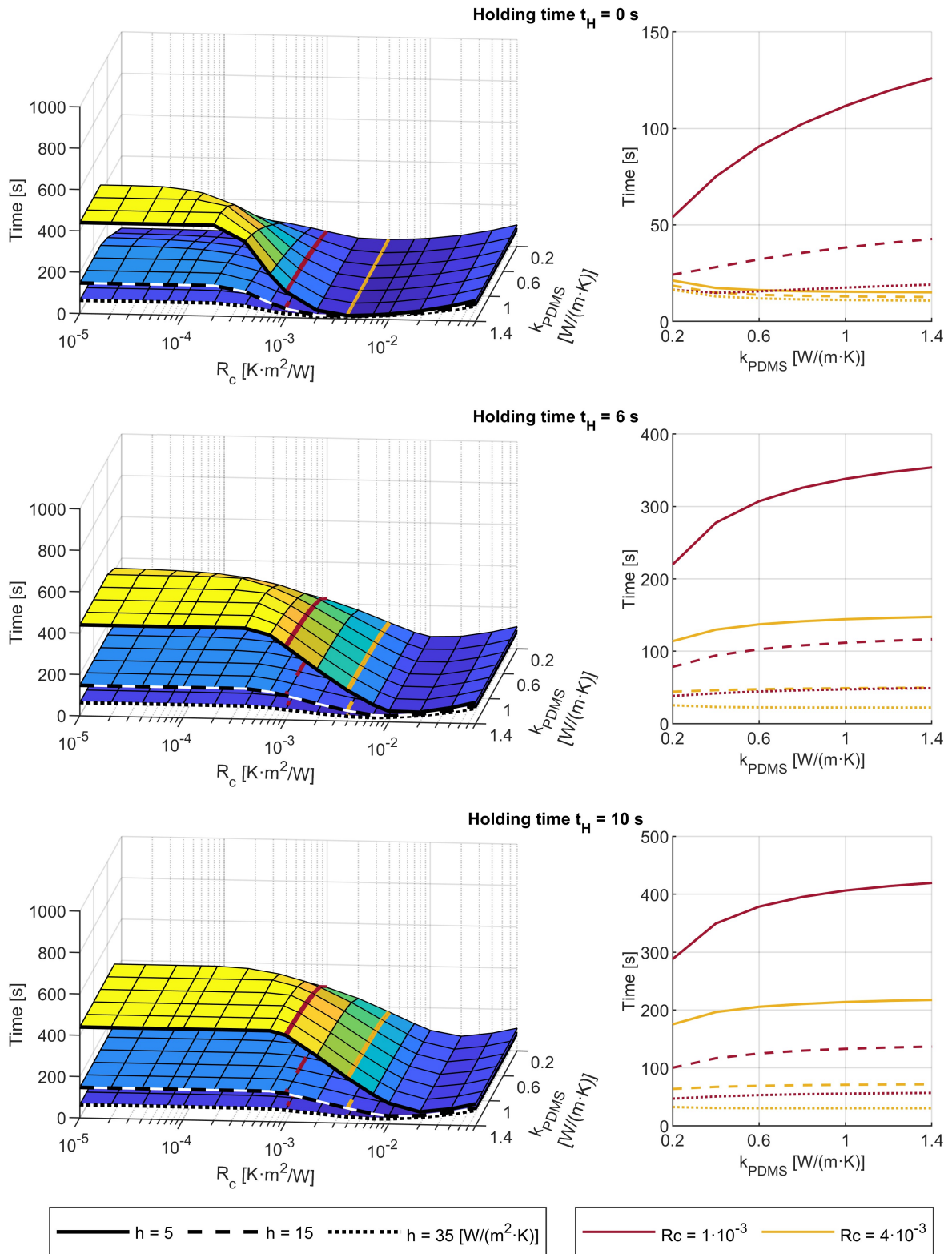


Figure 97 - 3D surfaces representing the time needed to cool down the SMA wire to M_f temperature (left). A greater convection coefficient h speed up the cooling of the system in regions where overheating of the elastomeric matrix was present. If convection is low, it is inadvisable to make the matrix more conductive if this leads to overheating of the matrix (right).

Reset time - Matrix thickness = 4 mm

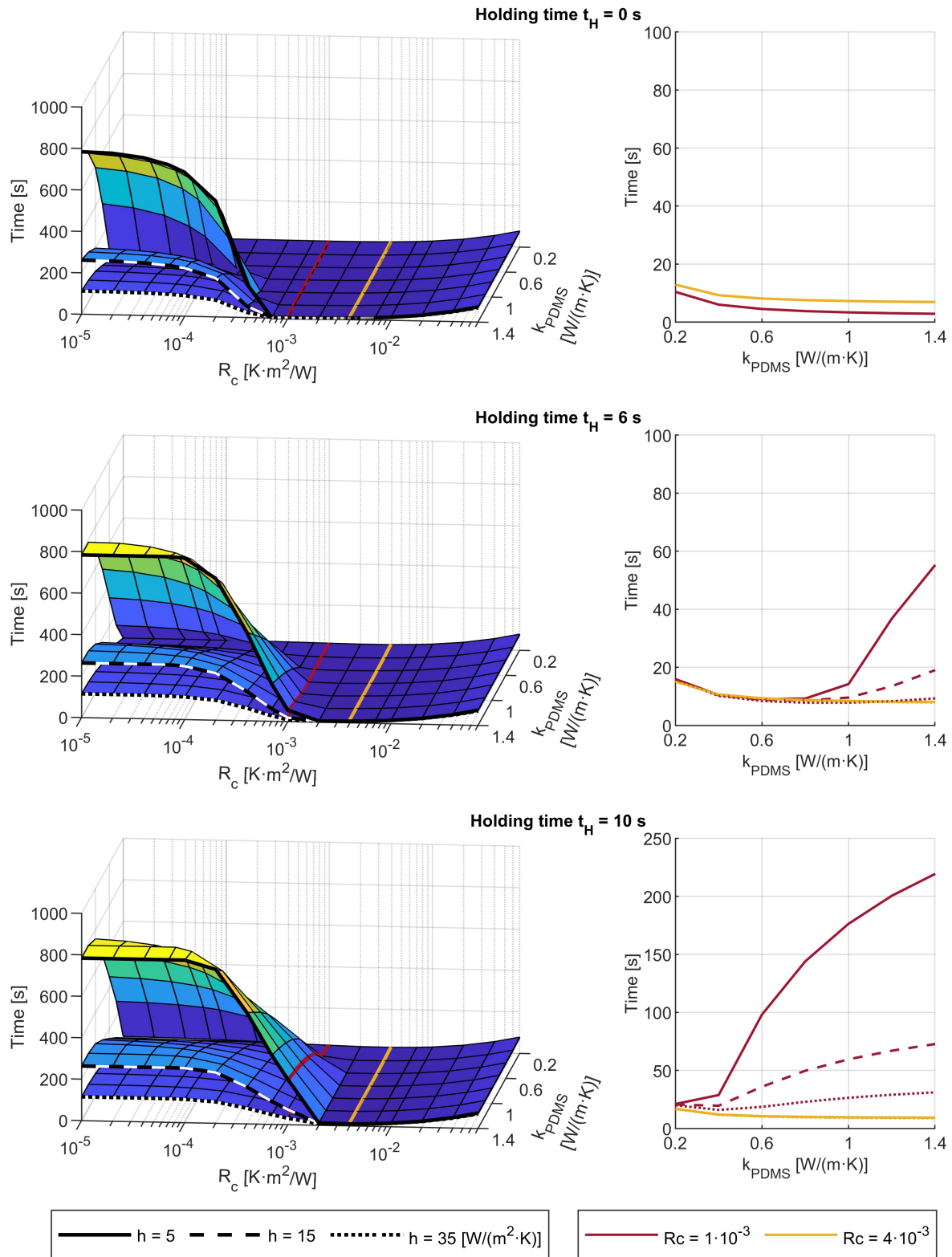


Figure 98 - 3D surfaces representing the time needed to cool down the SMA wire to M_f temperature (left). A greater convection coefficient h speed up the cooling of the system in regions where overheating of the elastomeric matrix was present. If convection is low, it is inadvisable to make the matrix more conductive if this leads to overheating of the matrix (right).

Reset time - Matrix thickness = 15 mm

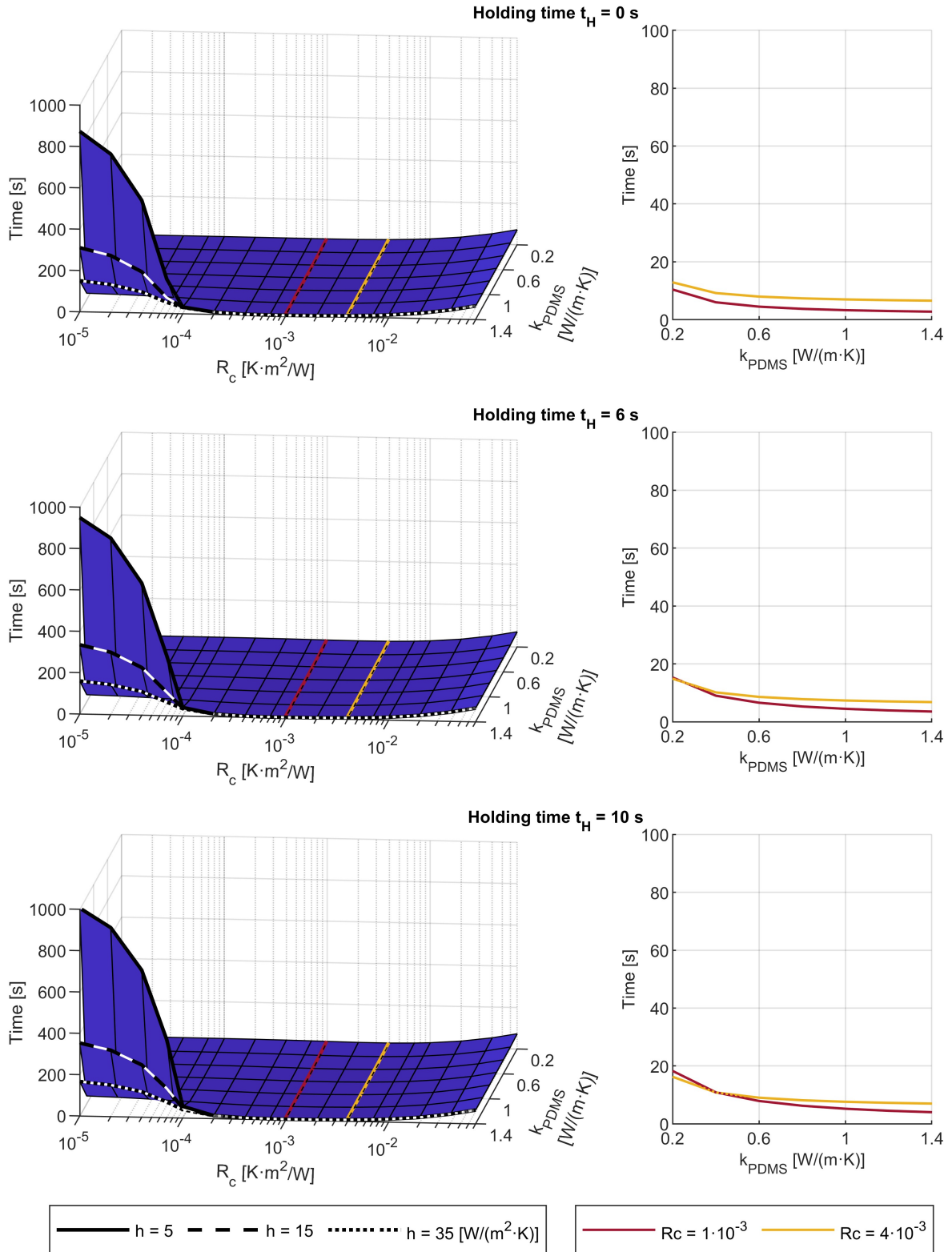


Figure 99 - 3D surfaces representing the time needed to cool down the SMA wire to M_f temperature (left). Large thicknesses of the matrix allow to take advantage of the optimisation introduced by the increase of k_{PDMS} as they are more immune to overheating. This can reduce cooling times by more than 50 % (right).

8.3.2. Complete actuation cycle starting with the system stabilised at $T_0 = 56\text{ }^\circ\text{C}$

8.3.2.1. Activation

The electric energy supplied to obtain a complete transformation, besides being invariant with respect to the convection coefficient h , as was the case for the type of cycle described in Section 8.3.1.1, in the present test situation is also invariant with respect to the thickness of the matrix: Figure 100, Figure 101 and Figure 102 are practically identical.

The lower the R_c value, the greater the influence of k_{PDMS} and therefore the increase in energy required to complete the actuation step. At high R_c values the effect of the k_{PDMS} modification is minimal.

Compared to the test situation for which the initial temperature T_0 is equal to $25\text{ }^\circ\text{C}$, the electrical energy required to complete the transformation into austenite is much lower. This happens of course since the matrix is already "hot" it drains less energy even for low R_c values.

Energy consumption during the actuation step - Matrix thickness = 2 mm

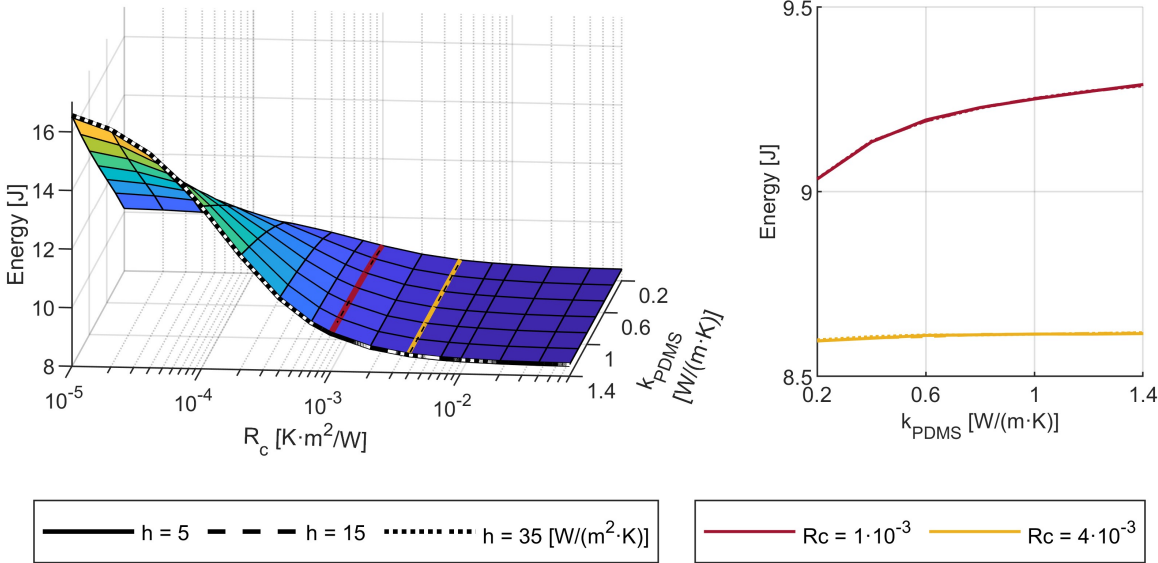


Figure 100 - 3D surfaces representing the energy consumption calculated for three values of the convection coefficient h (left). The variability given by h is less than 1 %, so the surfaces are indistinguishable. The energy values calculated for the two R_c values that delimit the normality range, represented by the yellow and red coloured lines, are reported in a 2D graph (right).

Energy consumption during the actuation step - Matrix thickness = 4 mm

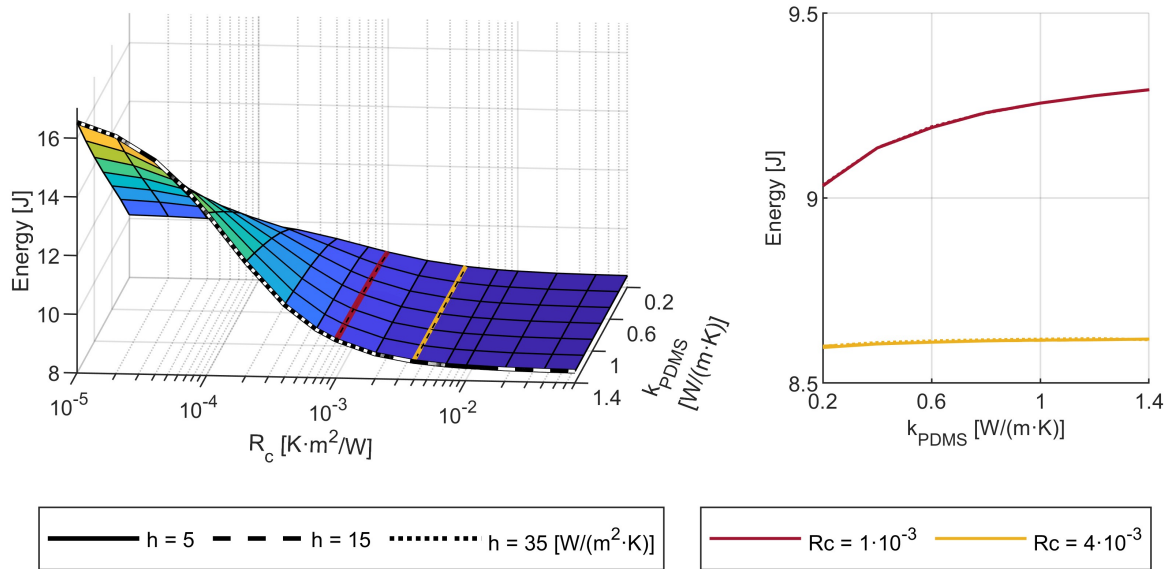


Figure 101 - 3D surfaces representing the energy consumption calculated for three values of the convection coefficient h (left). The variability given by h is less than 1 %, so the surfaces are indistinguishable. The energy values calculated for the two R_c values that delimit the normality range, represented by the yellow and red coloured lines, are reported in a 2D graph (right).

Energy consumption during the actuation step - Matrix thickness = 15 mm

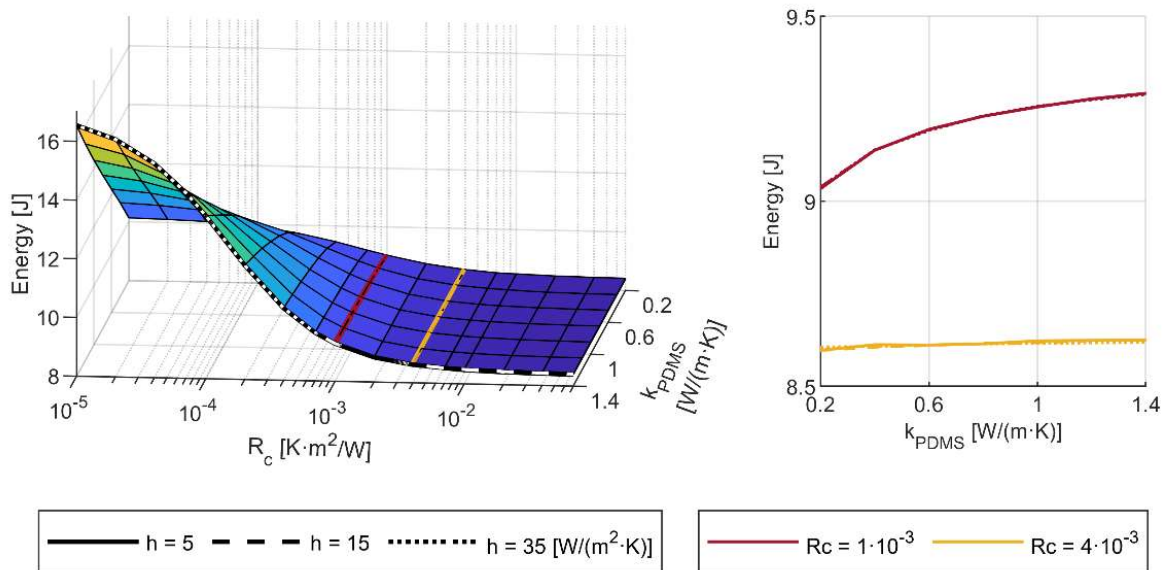


Figure 102 - 3D surfaces representing the energy consumption calculated for three values of the convection coefficient h (left). The variability given by h is less than 1 %, so the surfaces are indistinguishable. The energy values calculated for the two R_c values that delimit the normality range, represented by the yellow and red coloured lines, are reported in a 2D graph (right).

Like the energy, also the time needed to complete the actuation is decreased, with a minimum value of about 0.25 s for R_c equal to $7 \cdot 10^{-2}$ (K·m²)/W, and a maximum of 0.5 s in correspondence with the minimum value of R_c and the maximum of k_{PDMS} tested.

The average values of the temperature of the matrix T_2 at the final instant of this actuation cycle are shown in Figure 103 ($t_M = 2$ mm), Figure 104 ($t_M = 4$ mm) and Figure 105 ($t_M = 15$ mm). Again in this test case, the average temperature of the T_2 matrix is affected by its thickness. Since the energy supplied to the system does not vary with the matrix thickness, smaller structures are more likely to overheat. The convection coefficient h has only a slight influence on the value of the temperature T_2 , which is constant throughout the domain for which the surfaces are represented. Its effect increases if the thickness of the matrix is reduced, up to a value of some tenths of °C.

The maximum increase in T_2 is equal to 4 °C for a matrix thickness of 2 mm. In the range of R_c delimited by the coloured lines, the temperature T_2 has a very limited increase.

T_2 at the end of actuation step - Matrix thickness = 2 mm

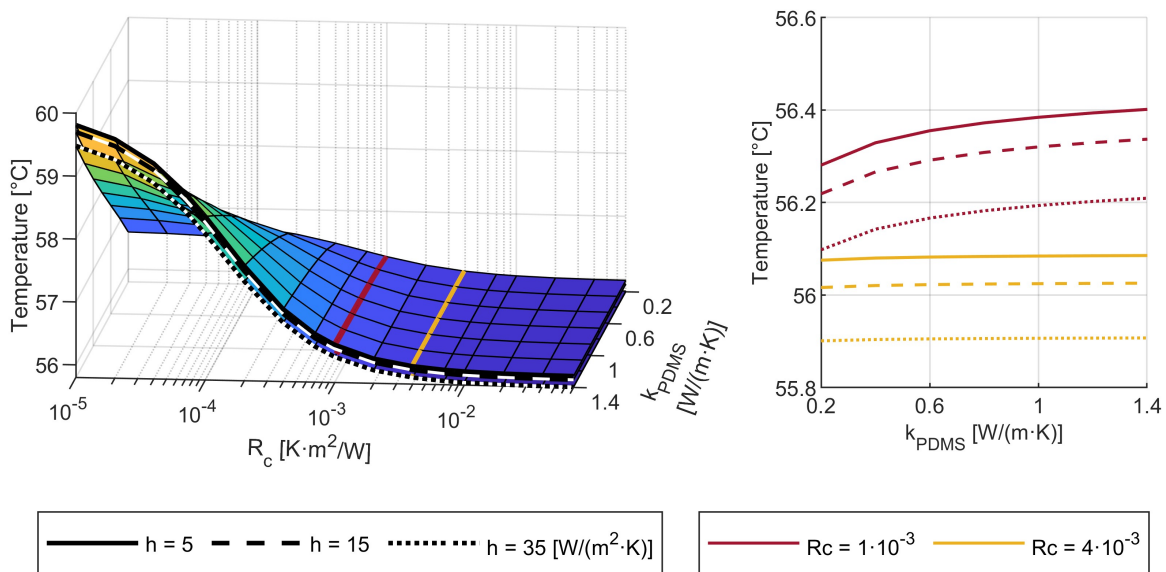


Figure 103 - 3D surfaces representing the mean temperature of the matrix T_2 at the end of the actuation step (left). For some values of R_c and k_{PDMS} , the T_2 can reach higher values compared to those obtained with larger matrix thicknesses. In the normal range delimited by the two coloured lines, the overheating of the matrix is limited and poorly dependent on k_{PDMS} (right).

T_2 at the end of actuation step - Matrix thickness = 4 mm

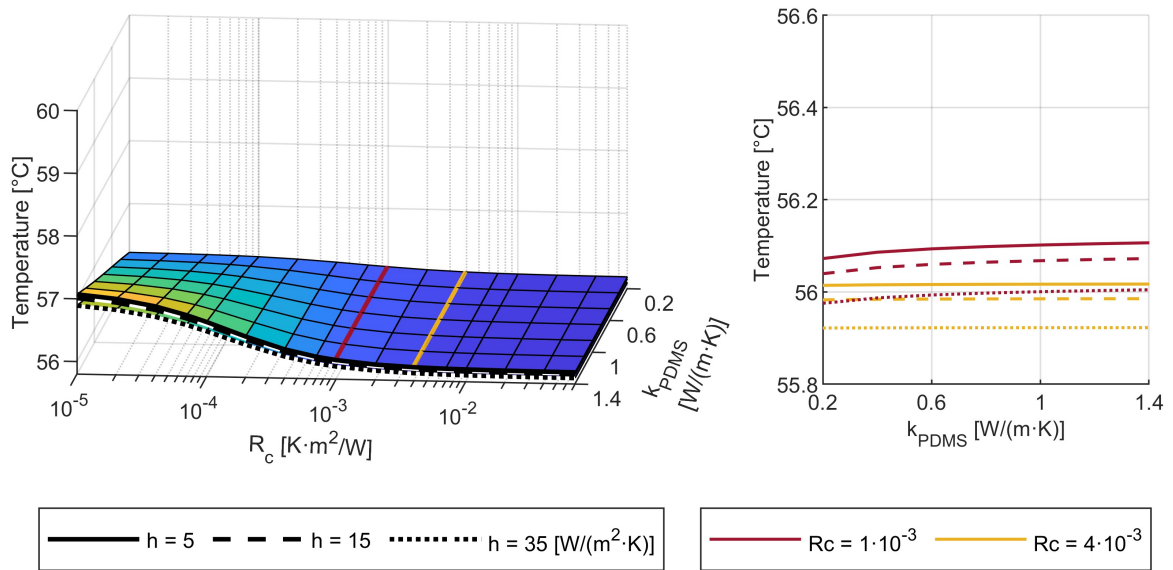


Figure 104 - 3D surfaces representing the mean temperature of the matrix T_2 at the end of the actuation step (left). The variations of T_2 are very limited. In the normal range delimited by the two coloured lines, the overheating of the matrix is limited and poorly dependent on k_{PDMS} (right).

T_2 at the end of actuation step - Matrix thickness = 15 mm

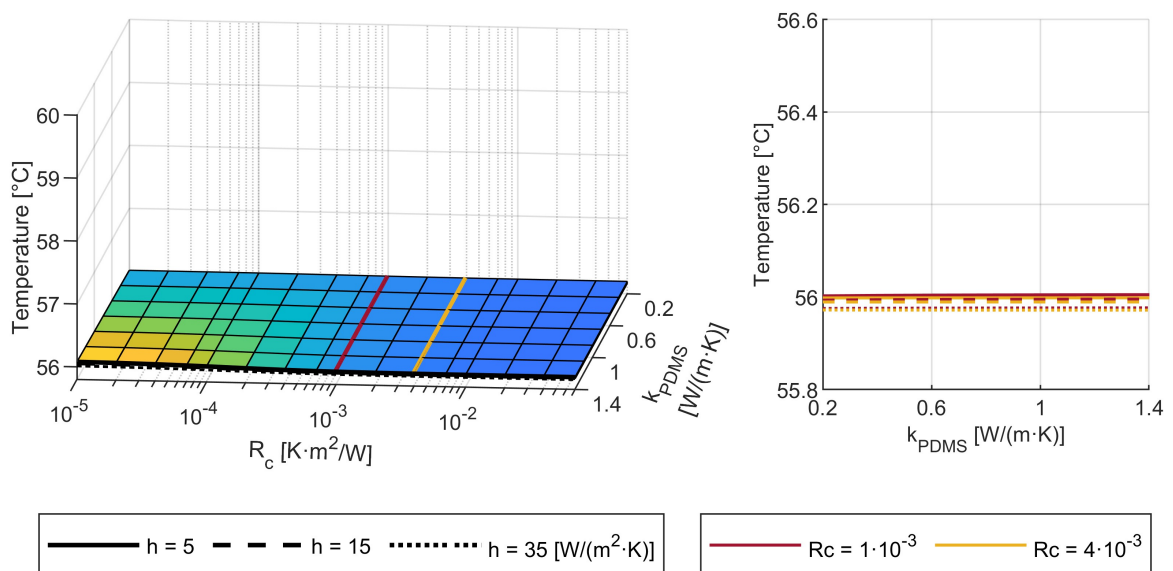


Figure 105 - 3D surfaces representing the mean temperature of the matrix T_2 at the end of the actuation step (left). In this case, unlike to the smaller thicknesses of the matrix, the T_2 has very limited variations. In the normal range delimited by the two coloured lines, the temperature is constant as k_{PDMS} varies (right).

8.3.2.2. Holding

The surfaces showing the trend of the energy injected into the SMA wire in this step, as the parameters vary, are shown in Figure 106 ($t_M = 2$ mm), Figure 107 ($t_M = 4$ mm) and Figure 108 ($t_M = 15$ mm).

The effect of convection is noticeable as the holding time increases and the thickness of the matrix decreases. The electric energy required for the holding step may in some cases be higher than the one required in the previous actuation step.

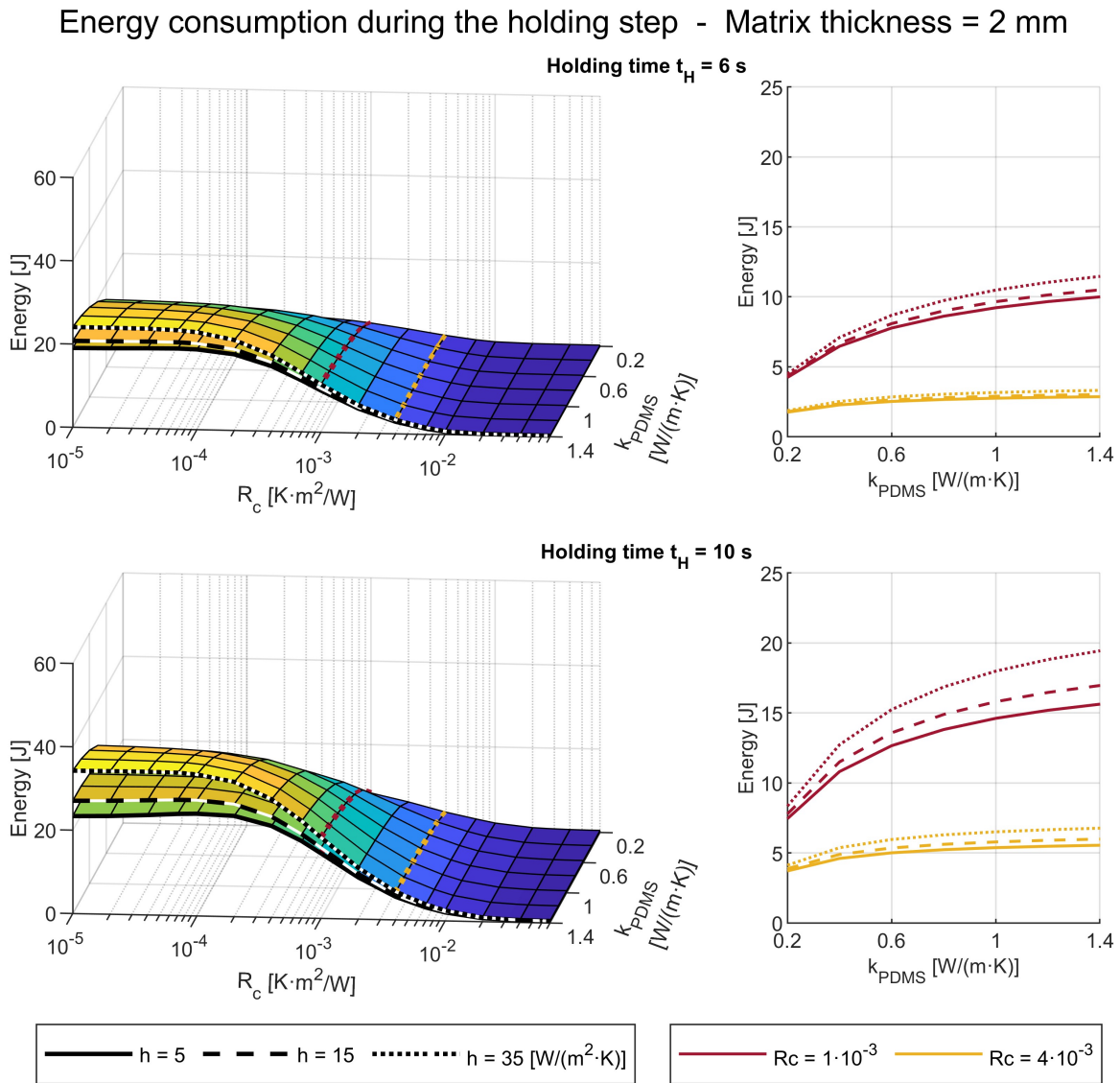


Figure 106 - Energy consumption calculated for two different values of the holding time. The 3D surfaces show that the dependence on the coefficient h occurs only in some regions (left). In correspondence with the R_c value highlighted by the red lines, the increase in the energy supplied as the thermal conductivity of the matrix k_{PDMS} increases is considerable (right).

Energy consumption during the holding step - Matrix thickness = 4 mm

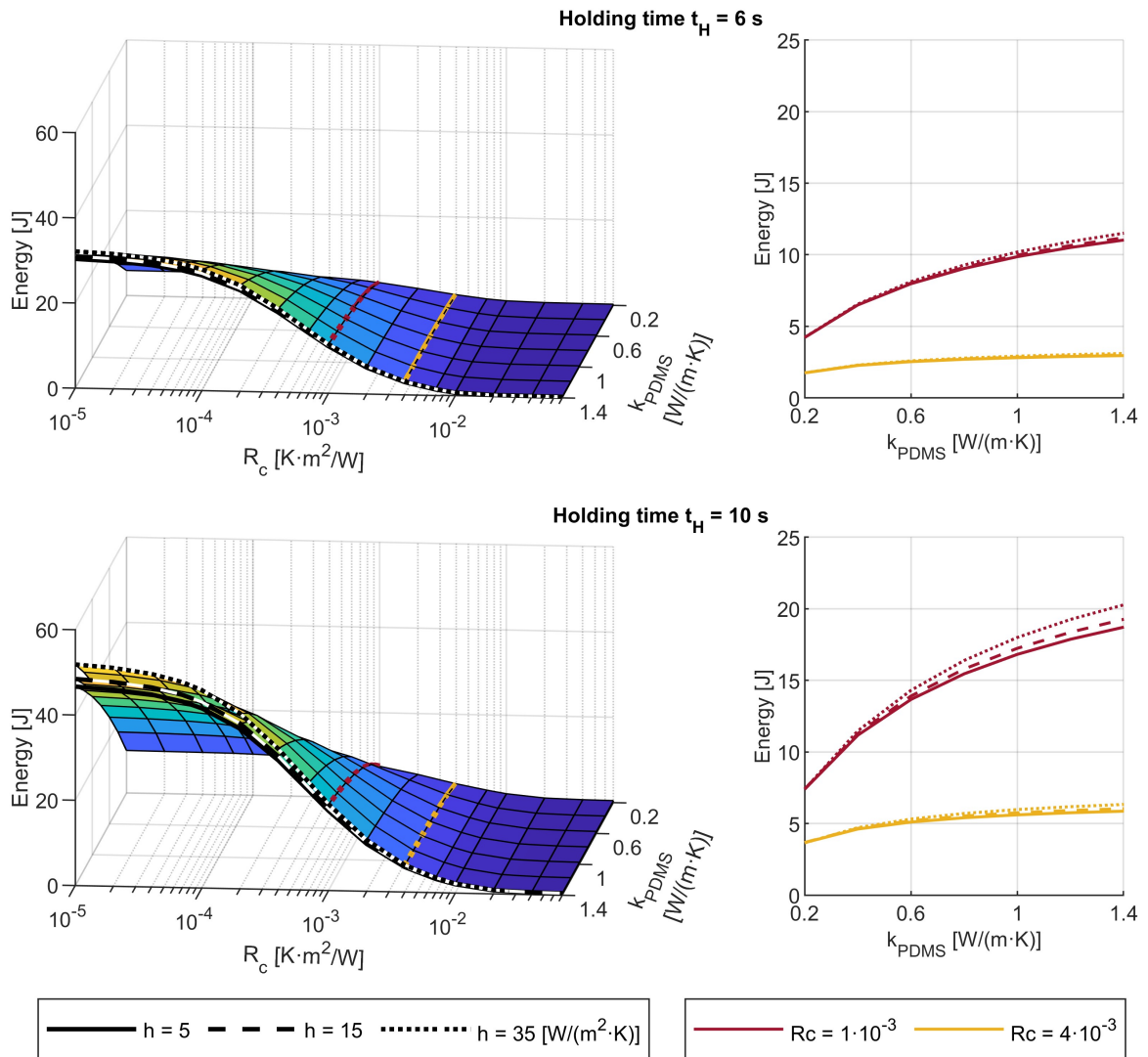


Figure 107 - Energy consumption calculated for two different values of the holding time. The 3D surfaces show that the dependence on the coefficient h occurs only in some regions (left). In correspondence with the R_c value highlighted by the red lines, the increase in the energy supplied as the thermal conductivity of the matrix k_{PDMS} increases is considerable (right).

Energy consumption during the holding step - Matrix thickness = 15 mm

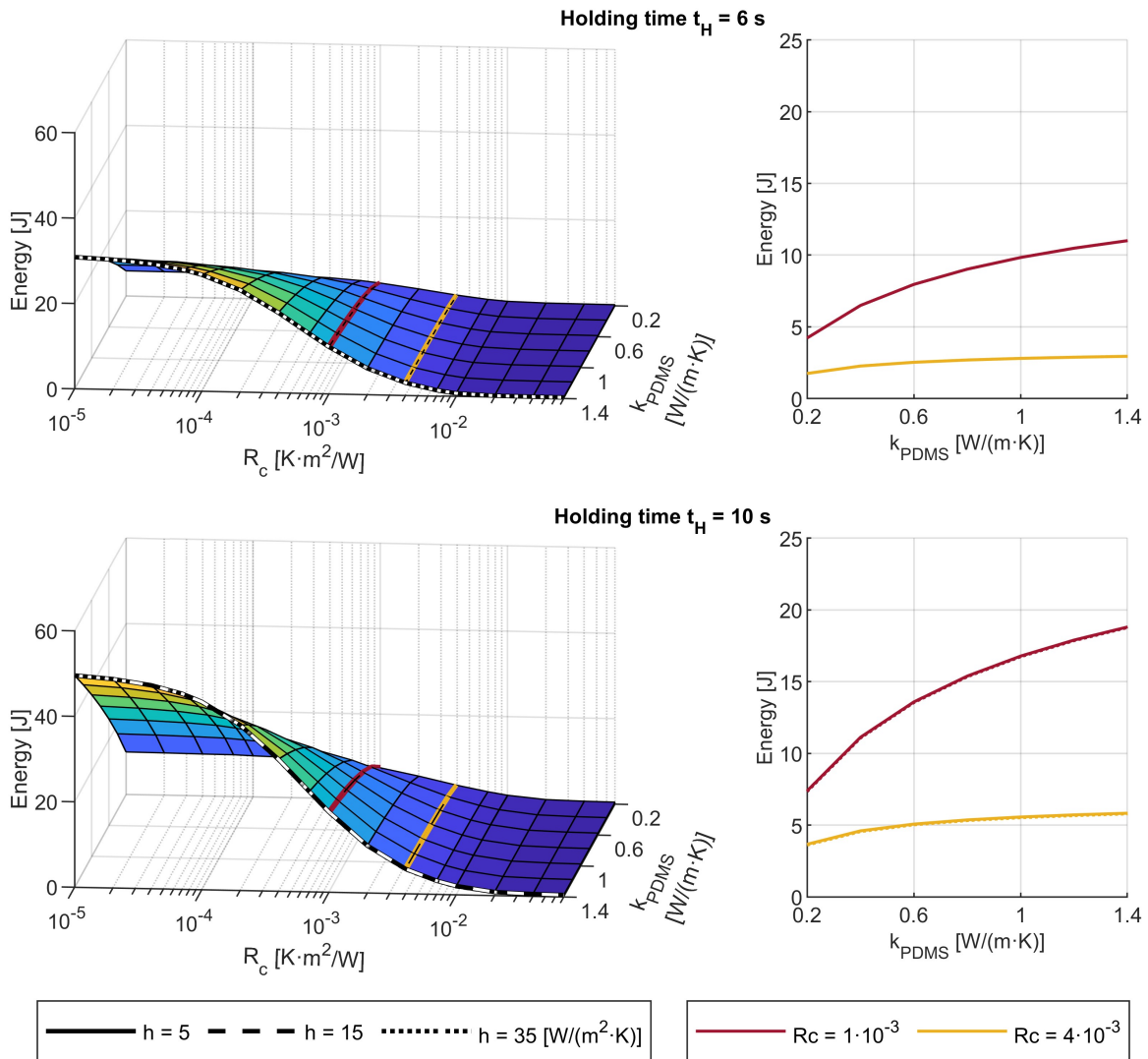


Figure 108 - Energy consumption calculated for two different values of the holding time. The 3D surfaces show that there is not a dependence on the coefficient h (left). In correspondence with the R_c value highlighted by the red lines, the increase in the energy supplied as the thermal conductivity of the matrix k_{PDMS} increases is considerable (right).

8.3.2.3. Deactivation

With a thickness of the matrix of 2 mm, the martensitic transformation time is highly dependent on the value of the coefficient h (Figure 109). Optimising the convection in this case is crucial to obtain a fast cooling. As the holding time increases, the minimum of the surface that identifies the best performances is located at increasing R_c . For the times t_H tested, the R_c value identified by the yellow line always allows good cooling times to be obtained.

Martensitic transformation time - Matrix thickness = 2 mm

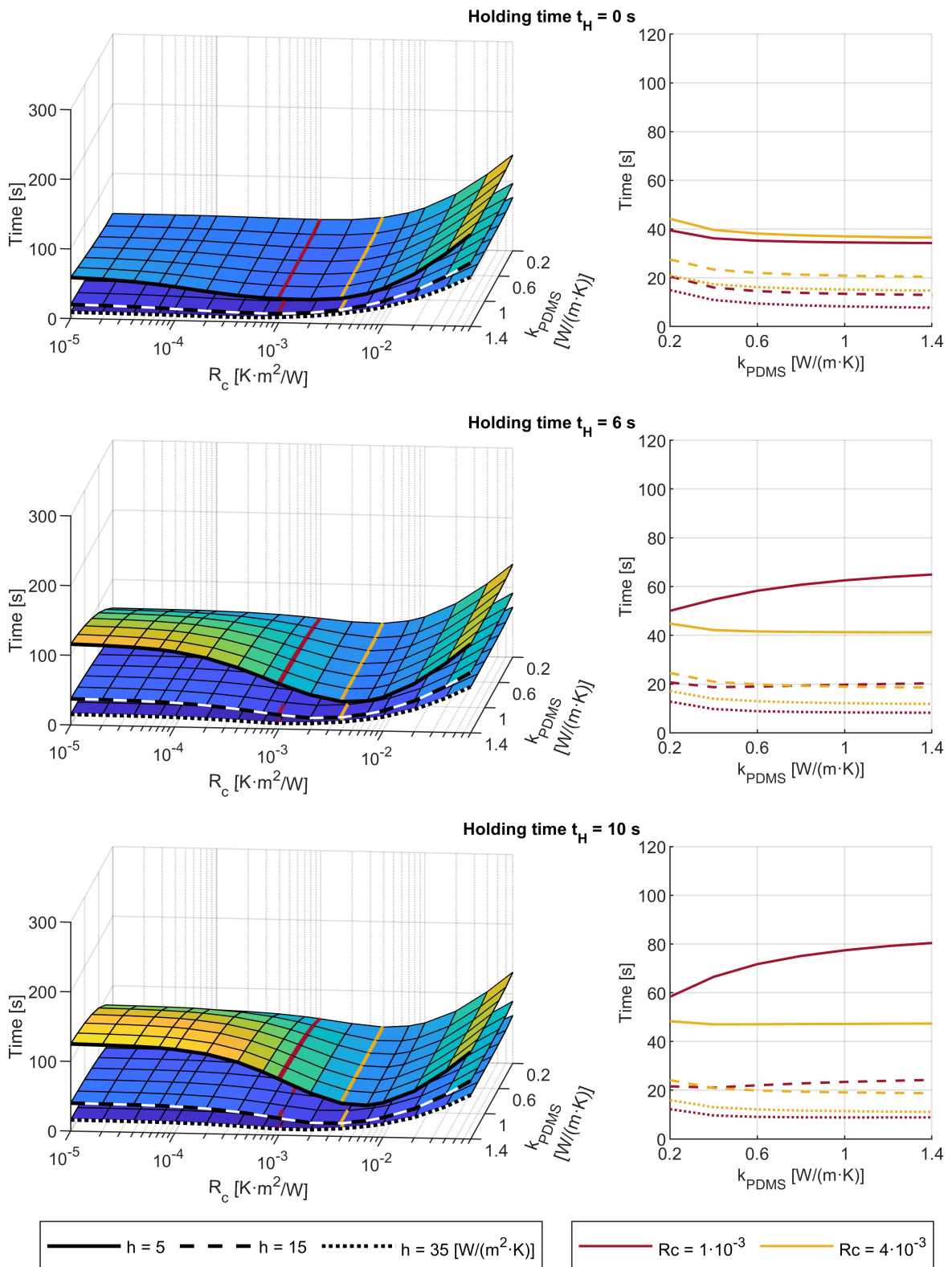


Figure 109 - 3D surfaces representing the time needed to complete the martensitic transformation after an holding step with a duration t_H (left). Optimised convection through high values of the coefficient h is decisive in achieving fast cooling. Where overheating has not occurred, increasing k_{PDMS} can speed up the transformation (right).

Martensitic transformation time - Matrix thickness = 4 mm

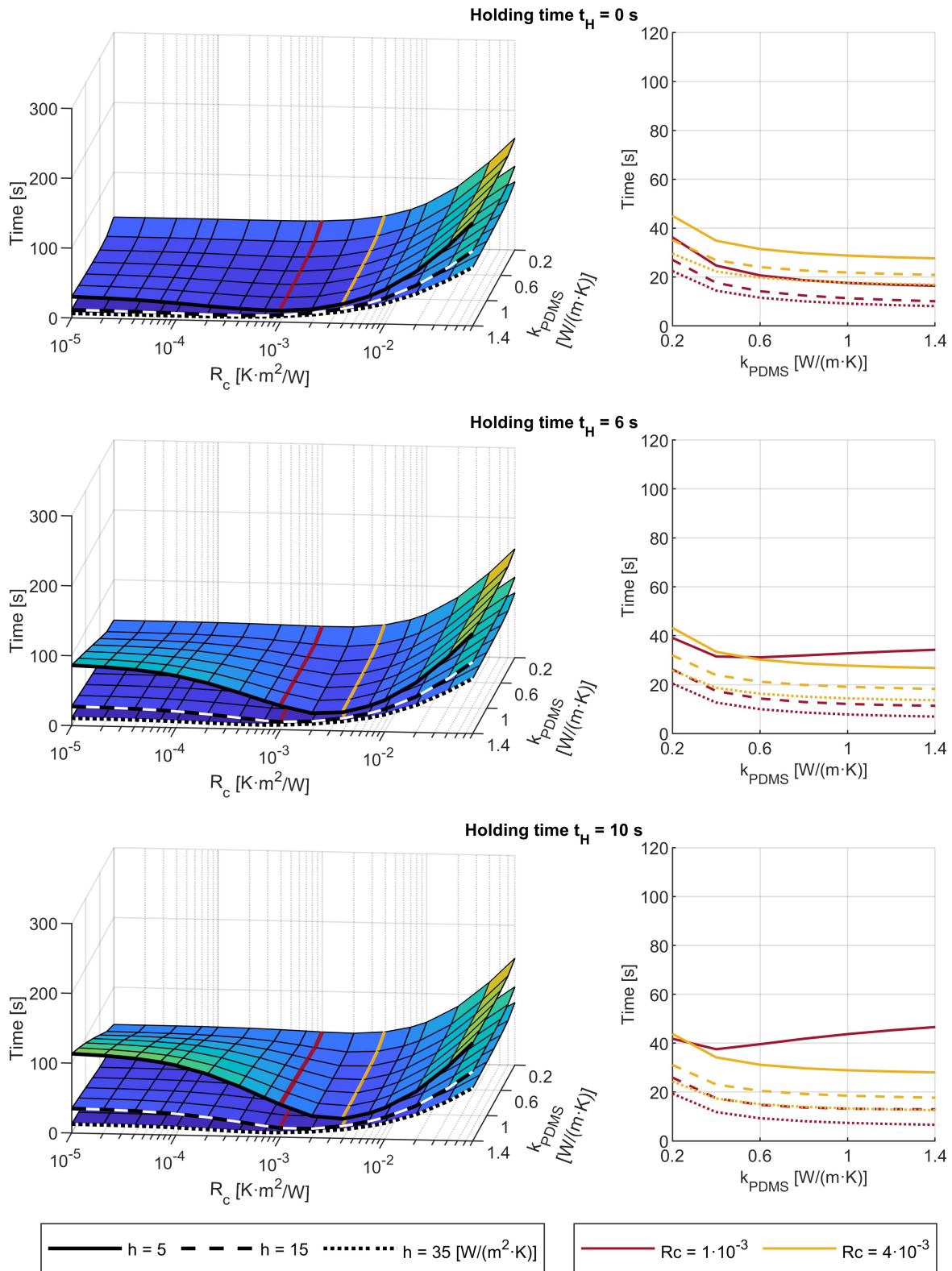


Figure 110 - 3D surfaces representing the time needed to complete the martensitic transformation after an holding step with a duration t_H (left). Optimised convection through high values of the coefficient h is decisive in achieving fast cooling. Where overheating has not occurred, increasing k_{PDMS} can speed up the transformation (right).

Martensitic transformation time - Matrix thickness = 15 mm

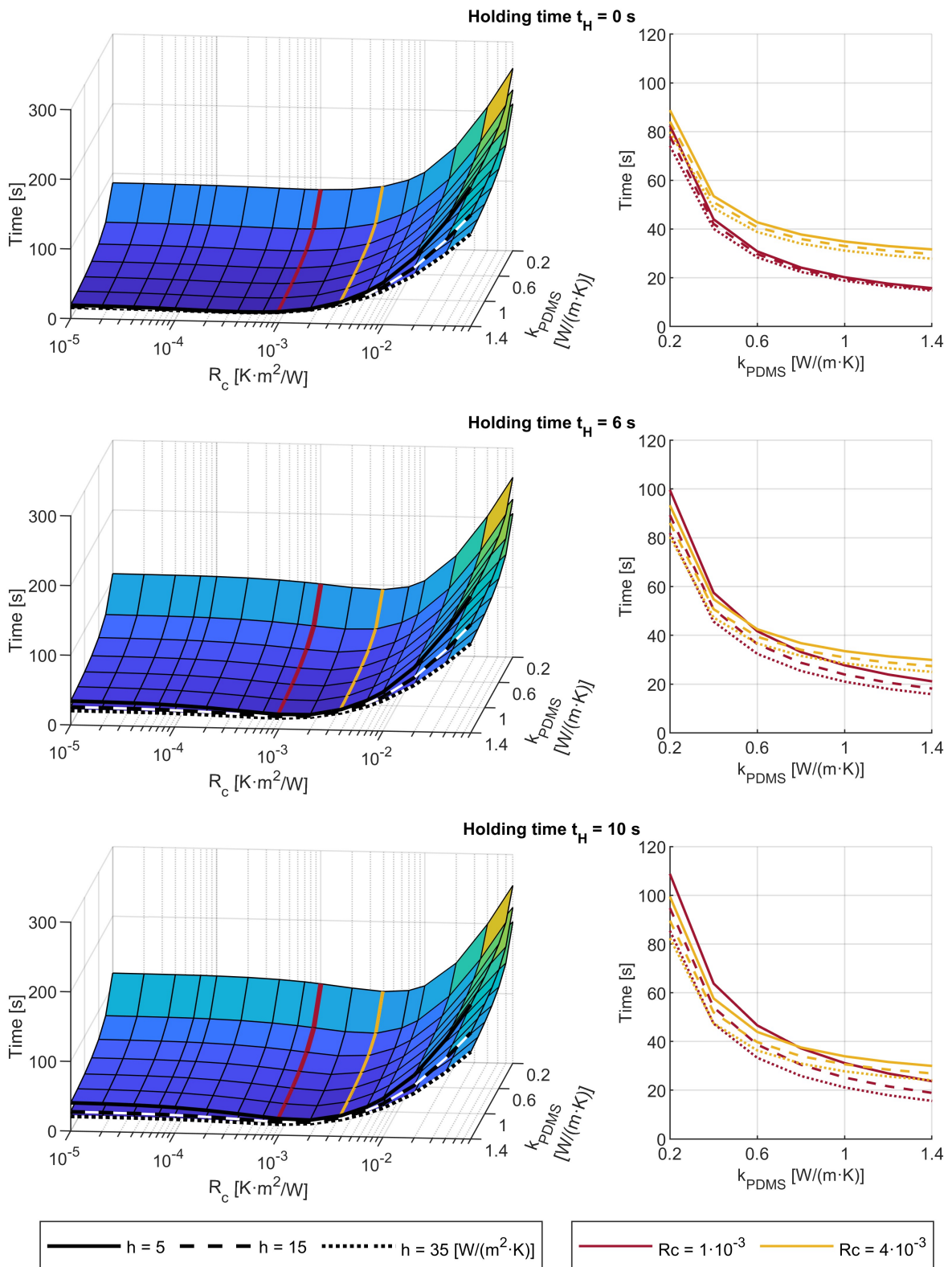


Figure 111 - 3D surfaces representing the time needed to complete the martensitic transformation after an holding step with a duration t_H (left). Optimised convection through high values of the coefficient h is decisive in achieving fast cooling. Where overheating has not occurred, increasing k_{PDMS} can speed up the transformation (right).

With a thickness of 4 mm (Figure 110), a good performance is obtained throughout the range identified by the two coloured lines.

As the thickness of the matrix increases, the influence of the coefficient h decreases.

With a thickness of 15 mm (Figure 111), at low k_{PDMS} conductivity values, very high martensitic transformation times are obtained compared to smaller thicknesses. In this case, to obtain good cooling performance it is necessary to apply a strong thermal modification of the matrix by greatly increasing the k_{PDMS} .

8.4. Possible expansions of the parametric study

Since this thesis work has been specifically focused on an SMA wire with a diameter of 0.65 mm, it will be interesting to evaluate in a future work how the wire size influences the obtained results. The study can be extended using the SMA wire size as a parameter.

8.5. Conclusions

A multiparametric study was carried out to investigate how the behaviour of a multimaterial actuator changes upon variation of some of its design characteristics and also with changes in operating conditions.

Modifying the matrix to increase thermal conductivity can help reduce cooling times, with the drawback of degrading energy efficiency. It is very important to verify that this does not lead to overheating of the matrix, otherwise the improvement obtained will be lost.

The search for a better thermal interface between the two materials does not seem to be the right way forward to optimise these devices. It is in fact not recommended to implement methods to reduce the thermal contact resistance R_c , especially if the elastomeric material has been modified to obtain a greater thermal conductivity.

For one-shot activations, especially if long holding times are needed, matrices of at least 4 mm of thickness are recommended. The greater the thickness, the lower the risk of overheating the matrix. In this range, increasing the matrix thermal conductivity moderately can provide additional benefits.

For consecutive activations, which lead the matrix to increase its temperature and stabilise on an average warm temperature, there are various observations that can be made regarding

the sizing of the actuator. Small thicknesses perform well only if convection is optimised, otherwise the probability of overheating the matrix is high.

Thicknesses of the order of 4 mm make it possible to obtain the best balance between deactivation speed and risk of overheating. For holding times greater than 10 s it is counterproductive to increase the conductivity of the matrix too much, while moderate upgrading can be beneficial.

Large thicknesses are not recommended, unless very long holding times are required ($t_H > 10$ s), and only if it is possible to carry out a strong thermal modification of the matrix ($k_{PDMS} > 1$ W/(m·K)).

CHAPTER 9

Proof-of concept actuator: The Orca gripper

The development of the proof of concept was carried out with the aim of verifying the feasibility and evaluating the effectiveness of the thermal functionalisation of the soft matrix. A device such as the gripper was chosen to verify the applicability of the indications obtained via the study of a simple cylindrical soft actuator to a more complex system with a specific function, and the robustness of our whole performance optimisation scheme.

Weaving together all the pieces of information gathered through physical and simulated experiments, a dimensioning of the concept actuator was attempted. According to the models, the PDMS thickness around the wire had to be in the range of a few millimetres and a graphene content of around 5 wt% (AO-2 GNPs) can provide the required moderate increase in thermal conductivity. The selected NiTiCu₆ ternary alloy was used due to its small hysteresis. The SMA wire has been heat-treated to obtain the same characteristics as the optimised one in Chapter 4.

Two versions of the actuator have been produced: one in plain PDMS and one with the graphene-modified matrix. The two devices have been tested performing a one-shot activation, using a high current to activate the wire with the aim of inducing less heating in the PDMS. The holding phase has been implemented with the use of a closed loop control, in order to minimise the use of electric energy. Finally, a comparison of the two devices was carried out using the same actuation pattern.

9.1. General concept of the gripper and dimensioning

The concept of the device is based on a curved SMA wire that can bend and extend during grasping and releasing, and a surrounding PDMS matrix that envelops it, providing an

interface with the outside world and a stable grip with the grasped objects. Upon heating by Joule's effect, the wire curvature increases causing the jaws of the gripper to close; as the current is switched off, the wire cools down and the jaws reopen under the bias action of the matrix (hyper)elastic spring-back. The dimensioning and detailed design of the gripper were developed starting from the wire. The SMA wire thickness was set to 0.65 mm diameter (the same chosen in Section 4.1), which was estimated to be a reasonable size to generate adequate force and hold objects in the centimetre size range. The basic shape of the SMA spring in an uncoiled (open-jawed) configuration was drawn with a central arch and straight ends, which would be roughly perpendicular to the direction of the gripping force when the actuator is holding an object 10mm thick. This open spring configuration will correspond to a reference closed shape in the form of a noose (see Shape setting of the SMA element, below). The drawing of the actuator and a diagram of the action performed by the SMA spring are shown in Figure 112. The outline of the soft matrix, in which the wire was to be incorporated, was chosen based on the open-jawed shape of the SMA spring. The matrix was designed with open holes in order to provide a balanced stiffness, so the wire is allowed to bend enough during heating and to get extended back during cooling. Also, the open areas favour heat exchanges between the matrix and the air. The matrix thickness around the SMA wire was kept in the range of a few millimetres, according to the optimised design principles developed in the previous chapters.

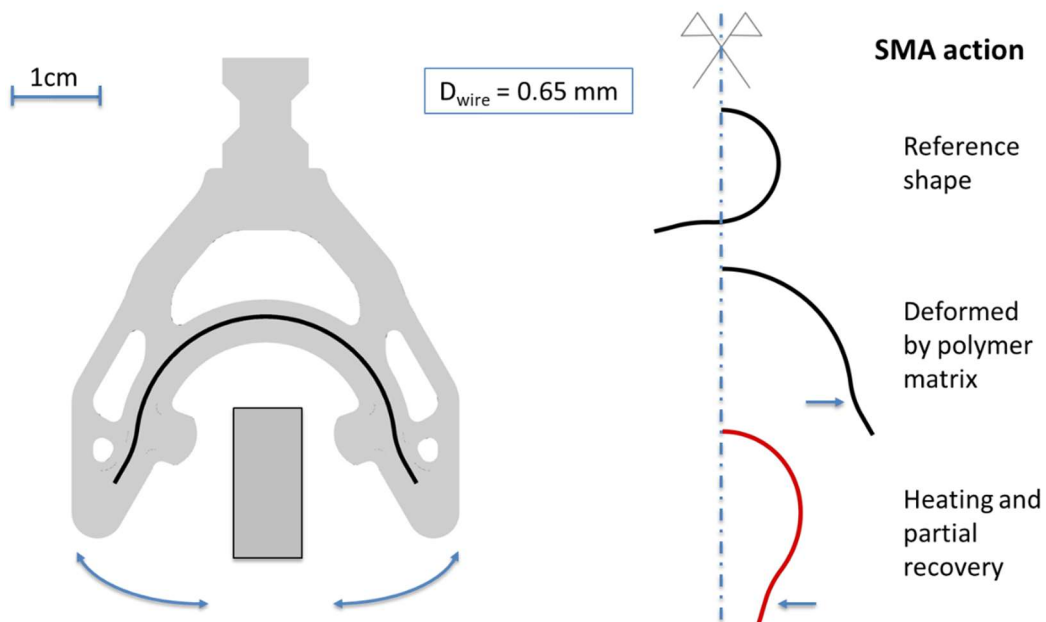


Figure 112 - Drawing of the actuator (left) and the diagram of the action performed by the SMA spring (right). The outline of the soft matrix, in which the wire was to be incorporated, was chosen based on the open-jawed shape of the SMA spring.

The PDMS characteristics change in different zones of the matrix volume. While most of the volume is taken up by Ecoflex™ 00-30 (modified with 5 wt% AO-2 GPNs, as explained in Chapter 5), the extremities of the gripper jaws are fabricated with plain white PDMS of higher Shore hardness (Rhodorsil RTV 3527 – Shore A-28). This choice was made because, whereas the matrix surrounding the wire and making up the body of the gripper serves functions such as heat transfer and bias spring action, the sturdier extremities are meant to hold the wire in place, protect the electric connections, and sustain the gripping force exerted on the grasped objects. The common chemical nature of the two matrices allow them to get attached to one another during step-wise moulding (see below).

The diagram describing the parts of which the device is composed is shown in Figure 113. Besides the elements already mentioned, the figure shows the position and course of the electric wire used to provide the power supply. The chosen diameter of that copper wire is 0.4 mm, i.e. thin enough as not to condition excessively the mechanical behaviour of the device. Furthermore, since the resistivity of copper is about 50 times lower than that of NiTiCu, the current density is still low enough that the length of copper wire (ca. twice the length of the SMA element) will dissipate only about 9.5 % of the total power, while the rest is available to foster actuation. The copper wire diameter was not chosen even smaller, also in order to minimise the probability that it may cut the PDMS matrix.

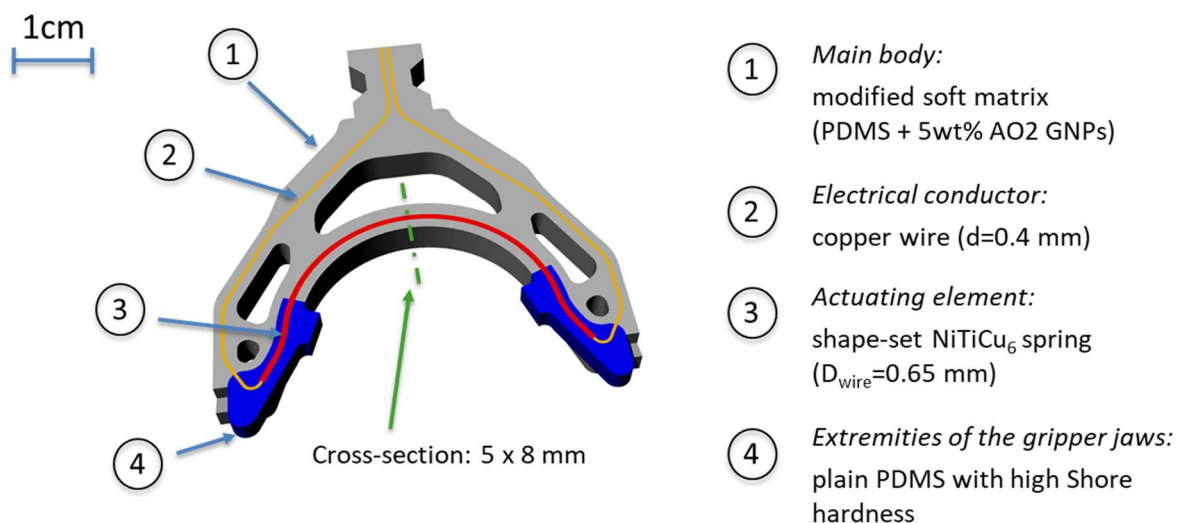


Figure 113 - Mid plane section of the actuator, showing its parts, and providing some information on the most important design choices.

9.2. Actuator fabrication

The actuator was initially made in a non-functionalised version, i.e. with a plain PDMS matrix. The baseline feasibility of the production process was thus evaluated. That device was characterised and used as a reference. A second functionalised device was then produced following the same procedure, but employing PDMS + 5 wt% GNPs, in order to assess the efficacy of matrix modification in improving the performance.

The next sections describe the operations carried out to create the two actuators, from the shape setting of the NiTiCu wire and the characterisation of the SMA element, to the production of the devices by stepwise moulding-and-assembling.

9.2.1. Shape setting of the SMA element

In order to fabricate the actuator, the SMA spring was to be shape-set in a closed (noose-like) position, then deformed before being inserted into the device. For the forming of the springs in the closed noose-shaped configuration, a suitable jig to hold the wire during the heat treatment had to be produced. This was done by first determining an appropriate reference shape for the spring, and then designing the corresponding jig.

9.2.1.1. Determination of the closed spring shape

In order to decide on the shape that the closed spring should have, structural simulations were carried out using the COMSOL Multiphysics software. The approach was heuristic and intended to find a shape compatible with the designed open-jawed configuration via a *reasonable* displacement history, and to evaluate the order of magnitude of the corresponding strains. A 3D model of a half spring was created in the open-jawed configuration exploiting symmetry to abate computational cost. The material properties were set through the Lagoudas SMA model available in COMSOL, using suitable parameters to represent the alloy characteristics in the fully martensitic range (room temperature, below M_f – cf. Chapter 6). A force was imposed on the free end of the spring, constantly directed perpendicular to the tail in order to limit axial compression along the wire. This force gradually changed the wire curvature towards more rounded shapes producing a reasonable displacement course for the bending spring (Figure 114). Along the displacement history a suitable closed-jawed shape was chosen observing the maximum absolute first principal

strains induced in the spring, which should be limited to no higher than a few percent (3 % max), in order not to compromise fatigue life. In the closed shape thus defined, the wire tails cross far away from the functional (stressed) region of the spring, which is desirable because unwanted torsional effects causing asymmetries during actuation should thus be minimised.

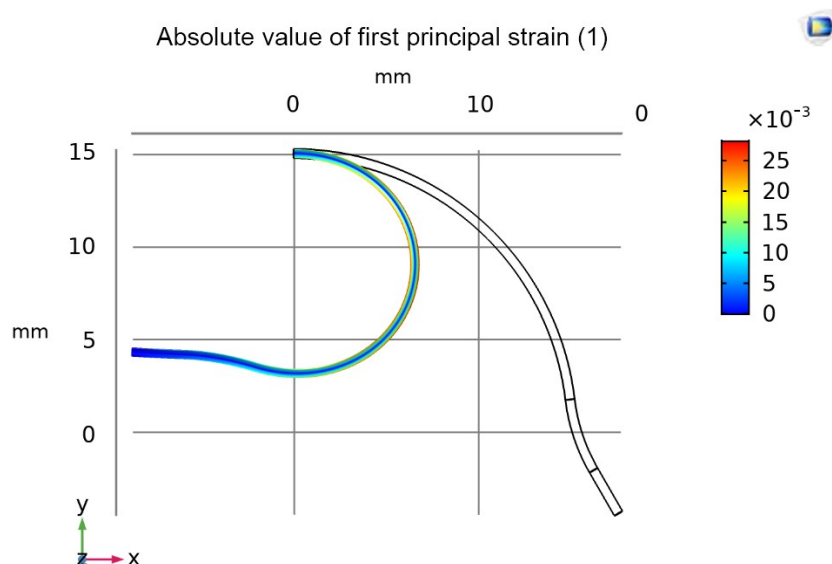


Figure 114 - Result of the structural simulation used to identify the closed shape of the spring for the construction of the jig.

9.2.1.2. Construction of the jig and shape-setting procedure

The jig was designed with a flat steel plate and a turned brass disc with an undercut to constrain the wire on the plate surface. Bolts and washers were placed at suitable positions to model the tails and hold the spring fixed. The jig, which is shown in Figure 115, was employed to impart the desired noose shape to the SMA springs.

They were heat-treated at 460 °C and quenched in water. In order to compensate for the thermal inertia of the jig, the optimised ageing duration of Chapter 4 was increased by 20 %. A DSC analysis confirmed that the transformation temperatures of the spring were the same as for the optimised wire. Calorimetric analyses were conducted with a TA DSC25 with a temperature ramp of 10 °C/min.

After heat treatment, the tails of the spring were cut to the desired length according to the design. In Figure 116 it is possible to observe one of the springs produced.



Figure 115 - Jig used for heat treatment of SMA spring. The wire loops around the brass disc and the tails are formed and held fixed by bolts and washers.

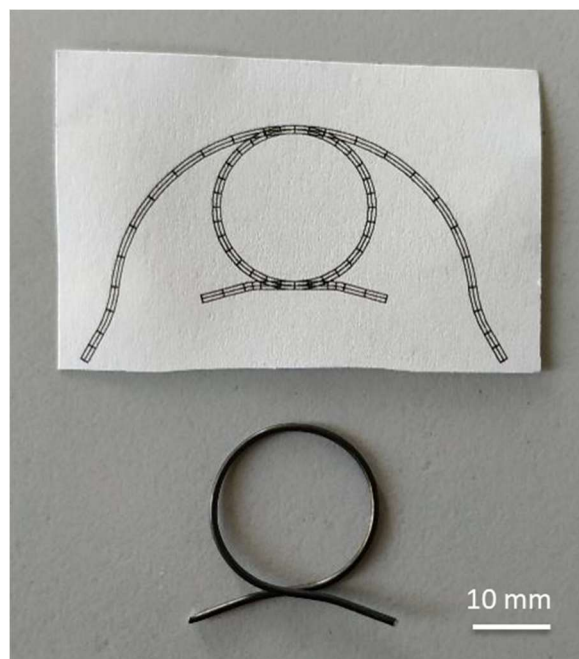


Figure 116 - Objective shape and shape-set SMA spring. The drawing of the spring design shows both the closed shape that the spring has been set in, and the open shape it will be deformed into, prior to being inserted into the final device.

9.2.2. Spring characterisation

The springs produced were stabilised by mechanical cycling and characterised. The objective was to verify the correct mechanical functioning, as well as evaluate the force exerted during thermal cycling.

The stabilisation was done in the dynamic mechanical analyser (DMA – Q800, TA Instruments) at constant temperature $A_f + 10$ °C, changing the distance between the tails from 9 to 20 mm for 50 cycles, holding the tails but letting them free to rotate.

For the characterisation, the spring has been constrained by the tails in a similar way, as shown in Figure 117, and in this case the tails were not free to rotate.

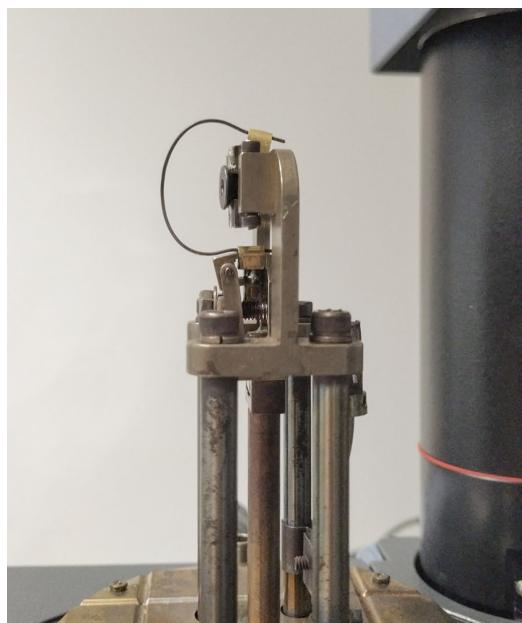


Figure 117 – Measurement set-up for the characterisation of the SMA springs in the DMA. The spring tails are held in clamps parallel to one another.

The spring was characterised in fixed positions, i.e. for set tail separations of 9, 12 and 15 mm, by subjecting it to thermal cycling between 25 °C and 90 °C. The first measurements were performed with a temperature gradient of 2 °C/min (Figure 118). The characteristic curve changes with the tail distance. For larger distances the spring exerts a slightly higher force. It is interesting to note that the spring produced a negative force during the end of the cooling phase. This behaviour, probably due to the two-way memory effect, may assist in reopening the final device.

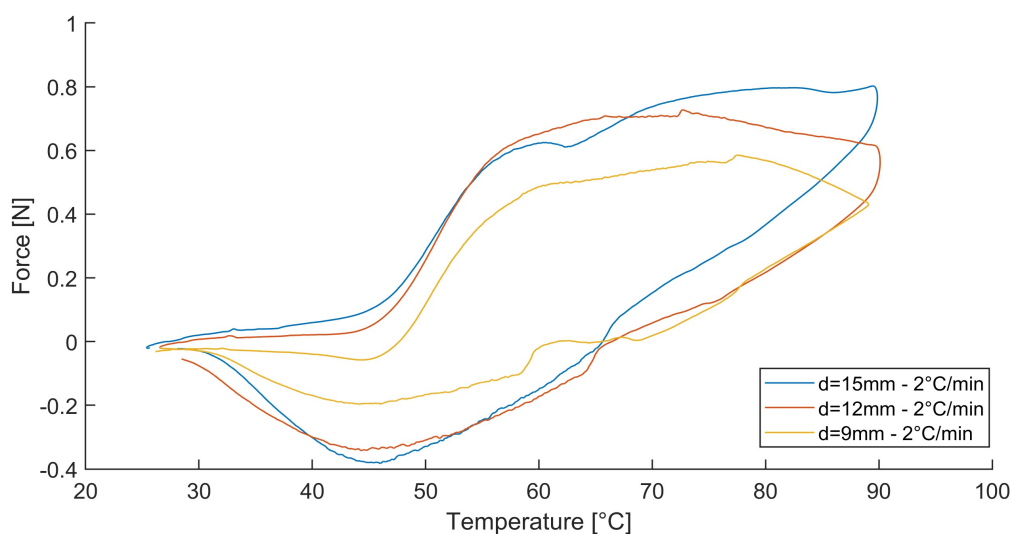


Figure 118 - Measurement of the closing, force exerted by the spring on fixed clamps held at different distances (d) during complete thermal cycles at 2 °C/min.

The behaviour of the spring for different heating (cooling) rates at a constant opening of 15 mm was then verified. As the heating rate increases, the spring exerts more force (Figure 119). The maximum heating speed at which it was possible to carry out the measurements is equal to 10 °C/min. This value is much lower than the real value obtainable by heating the wire through Joule's effect. However, I do not expect that the force exerted in a situation of real use can increase much further compared to that measured at 10 °C/min. We can therefore assume, conservatively, that 1.5 N is the maximum gripping force that can be developed by the actuator.

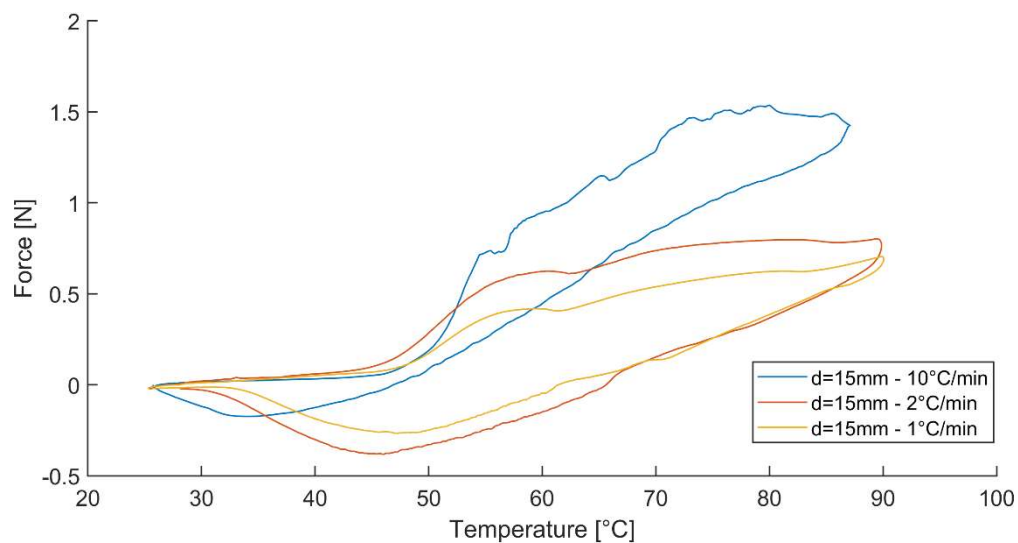


Figure 119 - Measurement of the closing force exerted by the spring on fixed clamps at a distance $d=15$ mm during complete thermal cycles conducted at different heating rates.

9.2.3. Production of the Orca gripper by stepwise moulding-and-assembling

After producing the spring, the electrical connection with the copper wires was made. Since it was not possible to solder or weld the electric wires directly to the SMA wire (NiTi-based alloys are notoriously very difficult to join), a crimping process was used. The copper wires were soldered to aluminium pin terminals, which were then filled with thermally-conductive silver paste. Then, the SMA spring tails were also inserted into the terminals. Finally, the terminals were tightened with special crimping pliers.

The following step was to virtually prototype and fabricate the moulds needed to make the gripper. For this scope were used a 3D CAD software (Rhinoceros 5) and a 3D printer (Dimension Elite, Stratsys). Multiple moulds to pour the PDMS matrix were designed and produced in ABS.

The first mould was necessary primarily to create a lining for the spring ends, where the electric wire connections are made. Another function of the first mould is to impart on the spring the correct open-jawed curvature. Therefore, SMA spring has been deformed in the central part to follow the curvature of the mould (Figure 120a) and then the end cavities were filled with the stiffer PDMS (Shore A-28) to cover the crimped electric connections. In Figure 120b it is possible to see the mould and the result of the first step of pouring the silicone into the mould. After complete curing, the device was manually removed from the moulds (Figure 120c). Another mould was created for the second assembling step.

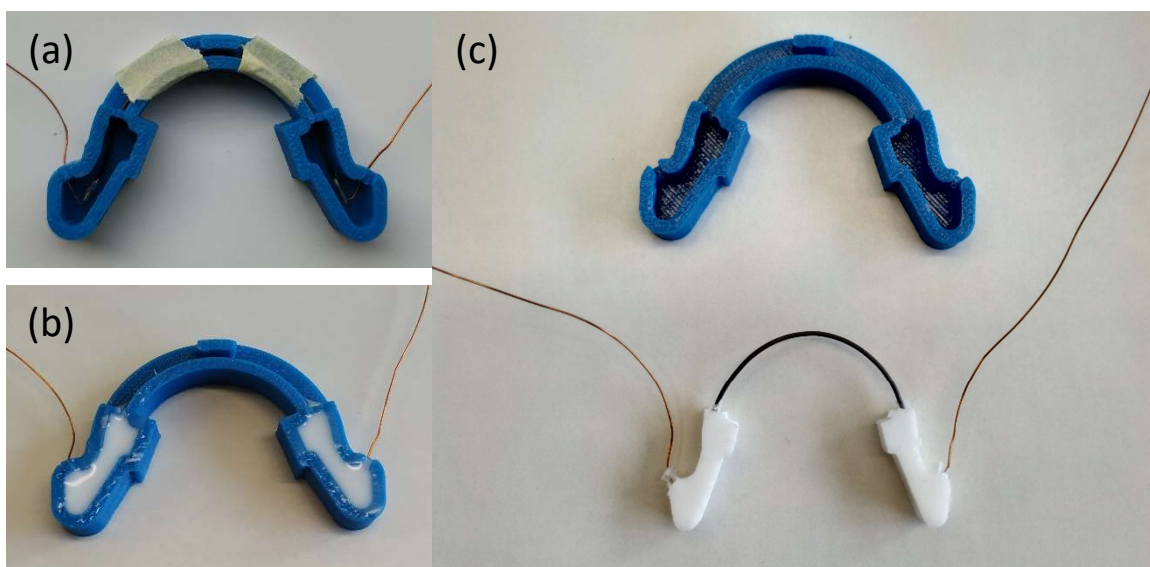


Figure 120 - Creation of the linings for the spring ends by means of the first mould. They are made with plain stiffer PDMS to protect the electric connections and provide bearing resistance during gripping.

The second mould (Figure 121) has the function to create the actuator body and, crucially, shape the lining of softer PDMS (or modified PDMS) around the spring arch. The part created in the previous step has been carefully inserted into it (Figure 121). The two copper electric wires were manually deformed into the right shape to follow a path along the centreline of the peripheral mould cavities and towards the gripper handle. All the cables have been brought out from the handle part of the device. A heat shrink sleeve was used to constrain the four wires at the point of exit from the soft actuator, to prevent them from cutting the PDMS.



Figure 121 - Insertion of the parts created in the first step into the second mould that forms the body of the actuator.

During the second step, the softer PDMS is cast over the spring and pre-covered ends to form the main structure. In order to remove the device, the second mould, unlike the first one, had to be broken, taking care not to damage the actuator. A picture of the first device with the non-functionalised matrix can be seen in Figure 122. The silicone rubbers revealed to have the right self-adhesion property needed, so the tail lining in stiffer PDMS attached perfectly and solidly to the over-cast softer matrix.

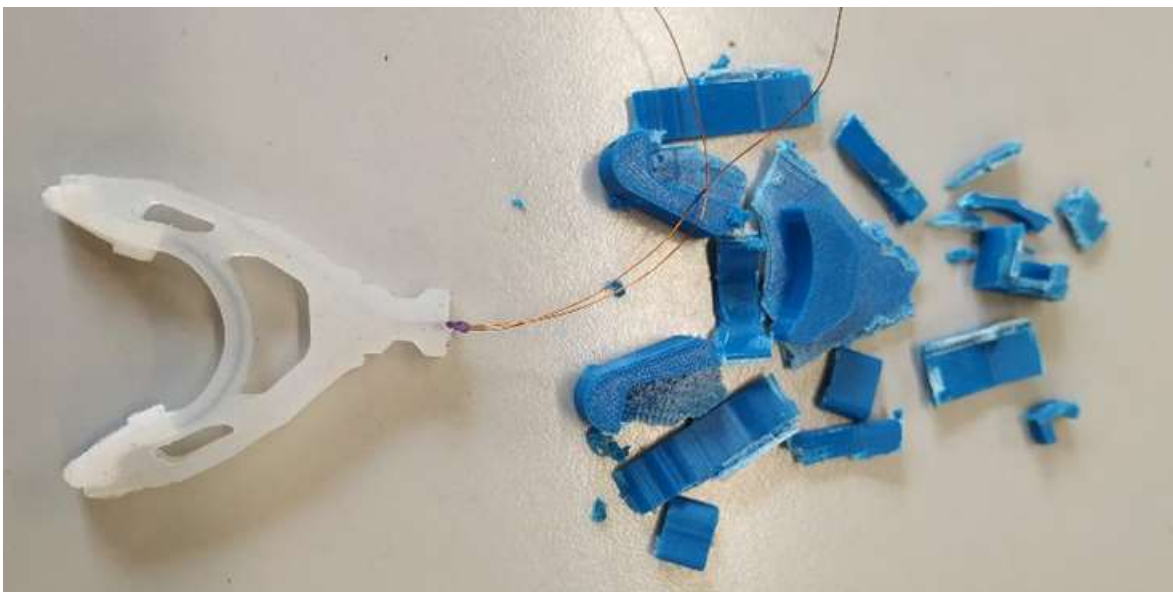


Figure 122 - Removing the device made with non-functionalised matrix from the second mould.

The second device, made with the functionalised matrix, is shown in Figure 123. The two-step process was identical to the one described, with the important difference that in this case the soft PDMS used in the second step was modified by addition of 5 wt% AO-2 GNPs.

This gripper was named *Orca*, by its black-and-white looks, and also as the acronym of “Optimised Rate-of-Cooling Actuator”.

Thanks to the successful construction of two devices, the production by stepwise moulding-and-assembling has been verified.



Figure 123 - Orca: “Optimised Rate-of-Cooling Actuator”, displaying the black modified PDMS matrix used for the body, cast over the plain stiffer white PDMS used to cover the electric connections in the tails.

9.3. Actuator characterisation and assessment of the effects of optimisation

The grippers based on the plain or modified matrix were characterised with the aim to evaluate differences in their performance. The two grippers were actuated during a grasp, hold and release cycle, starting from a stable temperature condition equal to T_{amb} (25 °C).

In both conditions, PDMS heating has been optimised (minimised) by applying a closed loop control on the gripping force exerted during the holding phase.

The next sections explain how the tests were implemented and show results of the comparison between the performance of the two design solutions.

9.3.1. Testing set-up and protocol

An *ad-hoc* set-up was designed and built to test and compare the actuation functionality of the two grippers (Figure 124). The set-up comprises a load cell (full scale 200 N, 8523-200 Burster), a pair of special fixtures 3D printed in ABS with adjustable distance, a high-precision programmable supply current generator (AimTTi CPX400DP) and a National Instrument acquisition station (NI cDAQ-9174). The load cell signal was amplified with a Burster 9243 module and then filtered with a 5 Hz RC low-pass filter (Total gain = 0.03 mV/mN).

A 200 m Ω shunt resistor (50 W) was used to measure precisely the electric current during the power supply of the SMA wire. The NI-9223 module (± 10 V, 16 bit) was used to acquire at 100Hz the force, current and voltage.

The force signal was fed to a computer (PC) running an *ad-hoc* closed-loop controller implemented in Labview, whose feedback variable is the output force error. The AimTTi CPX400DP power supply, connected via USB to the PC, allowed to set the current value with an update frequency of 10 Hz.

The distance between the fixtures was fixed at 8 mm.



Figure 124 - The *ad-hoc* set-up designed to test the devices with a closed-loop control of the gripping force exerted. A load cell (left side of the image) and a pair of special fixtures 3D printed in ABS with adjustable distance were used.

To achieve the gripping operation, the actuator was initially supplied a constant current. Its value, different for the two devices, was chosen after some preliminary tests in order to reach the target gripping force of 1 N in a time equal to 6.0 s. Subsequently, during the holding phase, the gripping force exerted on the fixtures was maintained constant for 6.0 s by the closed-loop control. The implemented purely proportional controller, was adjusted to a constant gain $K_p = 60$. After the holding phase, the power was switched off, which initiated the release phase. The opening of the actuator was monitored with the use of a video camera.

9.3.2. Results of the comparison

The comparison of the electric currents supplied and generated forces by the two different devices is shown in Figure 125. From the current graph it can be seen that the energy consumption is some 40 % higher with the modified matrix, as a consequence of the larger dissipation. This happens in both the grasping phase and the holding phase, where the level of the force is maintained similar. When the power is turned off, the graphene-modified device shows a much faster decrease in the exerted force. The time to reach null force is 10 s vs. 88 s, i.e. just over a ninth. That the thermal inertia is much smaller and the controllability is higher with the GNPs-modified matrix can also be appreciated from the greater variability of the controlled current during the holding phase.

These observations demonstrate that the cooling and release time are significantly reduced by the addition of GNP fillers.

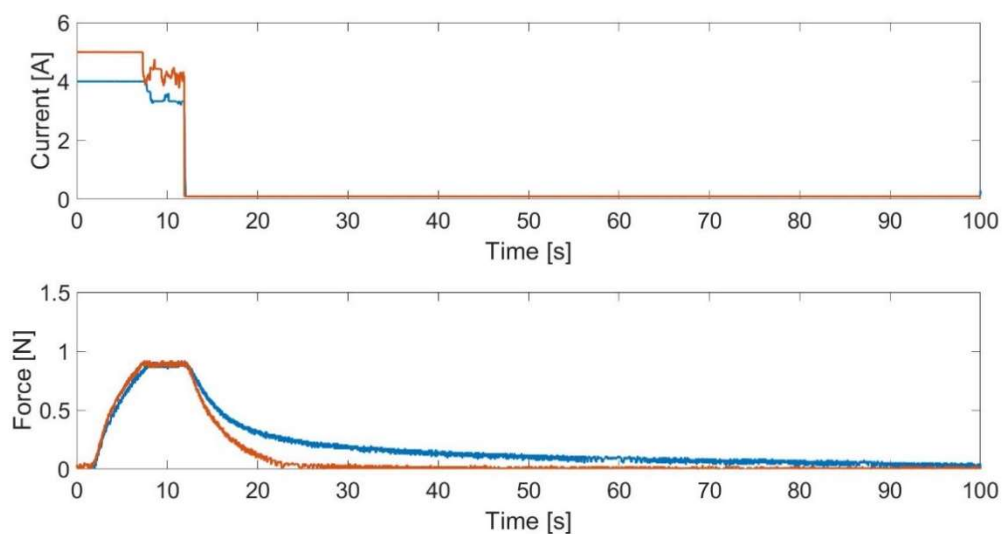


Figure 125 - Comparison of electric current requirement and generated force by the two different grippers, i.e. with plain PDMS matrix (blue) and 5 wt% graphene-modified matrix (red). The cycle includes fast activation, holding, and deactivation of the SMA wire. Note the feedback control acting on the current to maintain the target force constant during the holding phase.

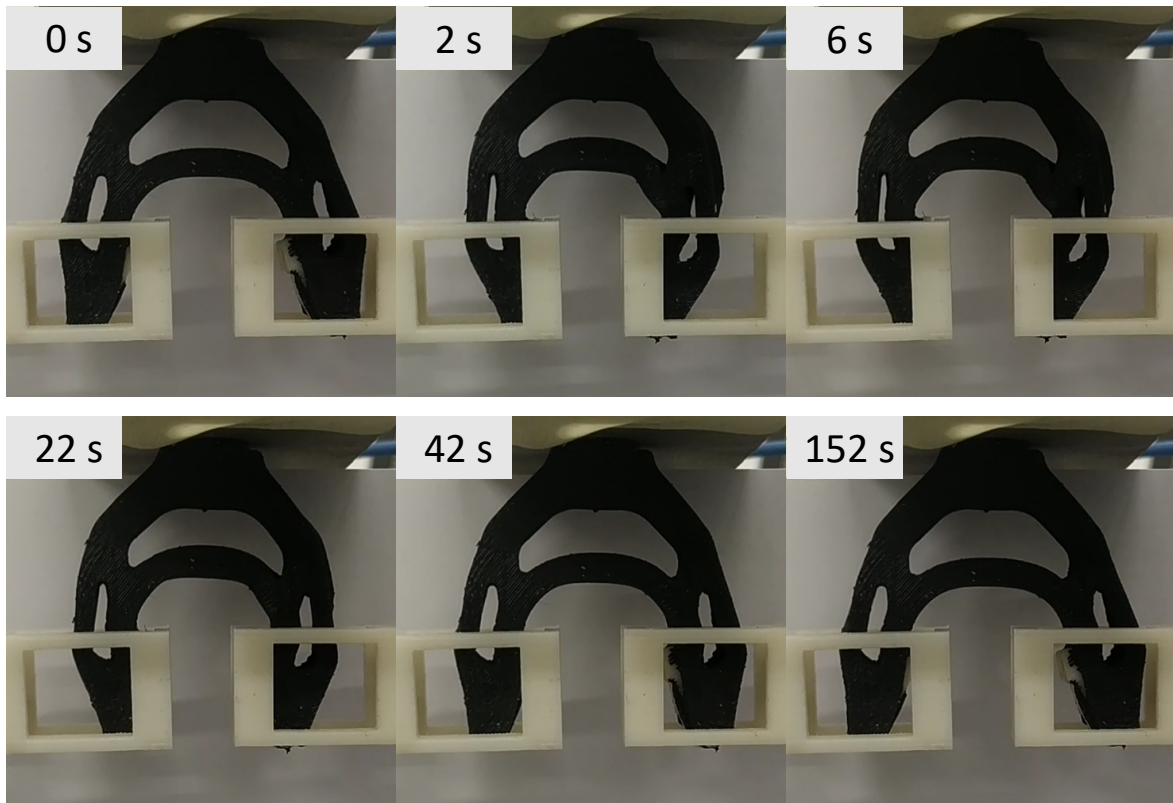


Figure 126 - Some frames of the recorded video showing the actuation sequence of the device with 5 wt% graphene-modified matrix. After two seconds the gripper is closed and the increase in the force exerted begins. Between 6 and 12 seconds the force is kept constant, then the release takes place, which ends with the annulment of the force exerted at second 22 (10 s after the interruption of the power supply). The device is almost fully open at second 42.

From the analysis of the video images (Figure 126) it was possible to estimate also the total reset time (complete martensitic transformation duration), which is equivalent to approximately 140 s for the modified PDMS actuator. For the plain PDMS matrix the total reset time was 175 s, so a 20 % improvement is obtained even on this value.

Furthermore, it was possible to observe that the GNPs-modified device reaches a good level of opening after about 30s from the interruption of the power supply, a time which for the standard device is not even sufficient to reset the force exerted.

Finally, during the experimental tests it was possible to observe that the reset position is more open for the optimised device, which reflects the stronger bias action of the graphene-modified PDMS since it is stiffer than the plain one.

9.4. Future developments

The most interesting development may concern the sensorisation of the actuator. The production by successive moulding opens many opportunities in this sense. One may be to insert pressure sensors in the gripping points as shown in Figure 127. Those sensors could be directly integrated in the PDMS matrix by optimising and exploiting piezoresistivity in a differently modified GNP/PDMS (cf. Section 5.4.2), or CNT/PDMS formulation.

Another development could be the addition of a further step in the production in order to form an inner arch for the gripper to provide extra insulation or optimise bias force. Possible future developments may also concern the SMA actuator element. In particular, it may be of interest to evaluate the replacement of the current SMA spring with another one with a hollow cross section, so as to empty it of the inefficient material from its centre. In [140] a compression spring with a hollow cross section was designed, produced and tested, to ensure the same stiffness and the same load capacity as a competitor helical spring with conventional solid round section. It shows better performances than a solid spring especially in terms of the reduced mass (37 % lighter) and cooling time (four times lower).

A similar strategy could be attempted also for our actuator because the material close to the neutral axis is of secondary importance also under bending conditions. What is difficult to anticipate is if the benefits in terms of performance would be replicated also in the presence of the matrix that surrounds and might even feel the meatus of the tube.

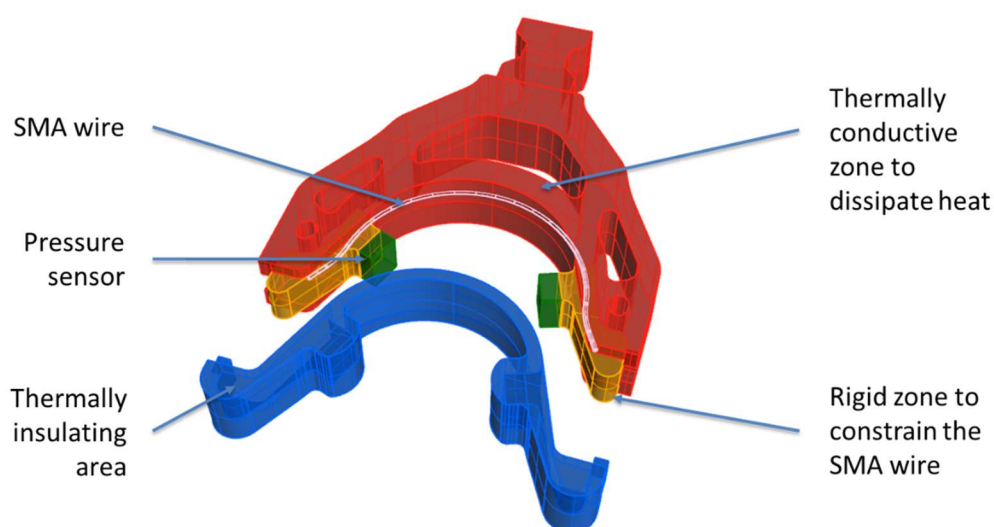


Figure 127 - Scheme representing the developed actuator together with some possible evolutions. The thermally conductive but electrically insulating matrix can allow easy integration of piezoresistive sensors for measuring the gripping force. Additionally, an inner arch can be added to provide extra bias force or insulation, if required.

Finally, another development may concern the creation of an actuator containing several springs laid in parallel in order to increase the gripping force. In this case the thermal problem becomes more complicated and will have to be studied in detail.

9.5. Conclusions

The present results demonstrate that it was possible to optimise a soft actuator based on SMA by creating zones with different functionalisation, viz. including GNP-modified matrix in of appropriate characteristics and size around the SMA element. Matrix modification by reducing thermal inertia, provides increased controllability and drastically decreases cooling time. Moreover, it induces mechanical stiffening, which had positive effects on cooling speed and opening width. A drawback is the higher energy consumption, that could be reduced by optimising (by a slight increase, see Section 8.3.1) specifically the thermal interface resistance between SMA and matrix. This is left as an open question for future investigation.

The fabricating procedure of the proposed gripper based on 3D printing and PDMS casting is simple and convenient. The Ecoflex™ 00-30 PDMS modified by the addition of 5 wt% AO-2 GNP flowed well and the pot life was sufficient to cast the composite matrix in the moulds. The adhesion between the different grades of PDMS utilised was good and mechanically sound.

Finally, and importantly, the fabrication of a gripper showed that the optimisation guidelines developed in the previous chapters by studying the case of a straight wire are robust and can be generalised to more complex actuator configurations, at least those sharing some basic size constraints, even though the geometry and loading patterns differ to some extent.

CHAPTER 10

Conclusions

Summary of achievements

This study developed models, procedures and methods to study and achieve objectives ranging from the comprehension of underlying phenomena, and the preparation of materials, to the characterisation of multimaterial systems and devices.

Starting from the key element of these devices, a ternary NiTiCu₆ alloy has been selected and optimised through a specific heat treatment which allowed to obtain a stable wire with small hysteresis in order to have fast transformation and low energy losses. The identification of the material functional parameters by physical and mechanical characterisation has been carried out completely and forms a basis for the modelling of the SMA wire.

As regards the soft matrix, silicone rubber was selected as the reference elastomer. Its functional modification was obtained through the use of high-quality large-aspect-ratio GNPs, which have been homogeneously dispersed in the elastomer, up to a loading of 10 wt%. The sample characterisations showed a moderate increase in both thermal properties and thermal diffusivity. A significant increase in thermal conductance, a mild increase in mass density, and a decrease in specific heat capacity were obtained with increasing loading of GNPs. The modification of the electrical properties was extremely small, limited to samples with a percentage of GNPs of 10 wt%.

An actuator made up of a straight SMA wire enclosed in a PDMS sheath was then defined as our reference scenario, with the intention of studying a specific case, free from morphological complexity, that could give universal - and potentially robust - indications on the optimisation of a general SMA/PDMS multimaterial actuator.

Two numerical models of the multimaterial actuator have been developed, which differ essentially in the treatment of heat transfer, and which are both based on a specially-modified version of Brinson's SMA phenomenological model in order to include important phenomena such as partial cycles and two-way shape memory, besides the addition of the effects of the outer matrix. The two implementations were compared to ensure that their overall predictions in simple case scenarios were consistent.

A 1-D model implementation was used for multiphysics simulations, which through the development of a parametric study, has allowed to investigate how the behaviour of a multimaterial actuator changes upon variation of some of its construction characteristics and also with the changes in operating conditions.

The simpler 0-D thermal model, faster-to-compute but similarly robust, was employed for running automatic control simulations, which can potentially be executed in real time.

An estimator, based on an Extended Kalman filter (EKF), and an advanced nonlinear controller were developed and tested in different scenarios, as applied on a digital twin of the multimaterial actuator, based on the SMA wire model. This was essential to address the optimisation of performance recognising the effect of the addition of an enveloping matrix on the controllability of SMA. The control action was adjusted according to the current strain error by some coefficients, which change depending on the current SMA operating range estimated by the EKF, as well as the estimation of the mean SMA wire temperature T_1 , and the temperature of the matrix T_2 . The EKF filter used to estimate the state variables showed high performance, with reduced errors calculated against the model variables. In particular, the mean temperature of the SMA wire T_1 was estimated with an error of less than 2 °C.

Finally, with the materials produced and optimised, and using the indications obtained from the numerical simulations, a functionalised multimaterial actuator for gripping objects was designed and characterised as a proof of feasibility.

Answer to the research question and guidelines for optimised SMA/PDMS actuators

The research question that the project proposed to investigate can be now answered.

The role of the matrix is very important in SMA/elastomer soft actuators and through the developed methods it was possible to show how keeping the matrix cooler is absolutely necessary to make these systems performant. Appropriate dimensioning, moderate matrix modification and optimised control strategies can help in achieving this goal, reducing energy waste and playing a fundamental part in establishing the dynamic working properties

of the system. While the study focussed mainly on a specific actuator layout, I argue that the wide variety of parameters analysed may lead to general insights that could inform universally the design of other SMA-based soft actuators. The following principles can be recommended when designing an SMA/PDMS soft actuator:

1. The choice of SMA material is important, and so is its processing. Selecting composition and treatments to decrease hysteresis, match the desired working ranges without overloading the material, and inducing two-way shape memory can favour speed of actuation and minimisation of energy cost.
2. Matrix modification by thermally conductive particles can be pursued, while it must be recognised that the dependency of the actuator functionality on material properties such as heat conductivity is not simple, but is strongly mediated by other inherent and operating factors. When using GNPs, large-aspect-ratio particles provided sufficient improvement in thermal diffusivity and moderate increase in mechanical properties that could be exploited for bias action. It is important to verify the quality of the GNP, considering the degree of exfoliation, the integrity of the graphene sheets and issues related to the formation of large aggregates.
3. Simulating of the interplay of material and operating factors even with low-dimensionality models can provide invaluable general insight in the multimaterial optimisation and device design process. As I derived from the simulations, modifying the matrix to increase thermal conductivity can help reduce cooling times, provided that this does not lead to overheating in operating conditions. The main drawback is the degrading of energy efficiency, but that can be limited with proper design. For one-shot activations, especially if long holding times are needed, matrices of at least 4 mm of thickness are recommended using a 0.65 mm NiTiCu₆ wire. The greater the thickness, the lower the risk of overheating the matrix, the greater can be the improvement introduced with the thermal modification of the matrix. For consecutive activations, thicknesses of the order of 4 mm are suggested since showed the best balance between improving in deactivation speed and risk of overheating. The development of methods to reduce the thermal contact resistance R_c between the SMA and the matrix does not seem to be a further optimisation route, especially if the elastomeric material has been modified to obtain a greater thermal conductivity. The wear of the interface between the two materials is an aspect that has not been

treated experimentally, but this work will still be able to give indications in this sense, given that a worsening of the adhesion can bring with it a variation of the thermal contact resistance R_c .

4. Advanced control strategies can be advantageous to optimise the performance of the multimaterial actuator. The tests conducted with an EKF-informed variable PI nonlinear controller have shown superior performance over a standard non-variable controller, in particular with better energy management, better ability to follow the reference strain and a reduction in cooling times that can reach of 40-60 %. It appears that taking into account the physical properties of both materials and their interplay to adjust dynamically the intensity of the control action is useful. It can be done estimating the state of the complex system by a nonlinear mode-based state estimator like the EKF.
5. The results and indications, obtained on a simpler system void of morphological complexity like a sheathed wire, helped in the dimensioning of an optimised specific actuator with more complex geometry, such as a gripper. The construction of a SMA/PDMS gripper with functionalised-matrix has proved that the matrix modification with graphene is feasible and can be effectively integrated in designs as a means to optimise actuation. It provided increased controllability and drastically decreased cooling time, and induced mechanical stiffening, which has positive effects on cooling speed and opening width. It was observed that, thanks to the thermally-modified matrix possessing electrically insulating characteristics, the optimisation of this device will be able to advance in the future by introducing more actuator elements in parallel or other functional parts such as integrated sensors.

Limitations and future prospects

Some limitations and future outlooks have been included in the conclusions of the different chapters. Here are summarised the most meaningful in a general sense.

The thesis approach was to cover multiple aspects of the SMA/PDMS systems in order to capture effects depending on various different phenomena with the purpose to gain a broad overview of the possibilities at hand to optimise these multimaterials. The varied spectrum of tests and analyses carried out inevitably implies the need for a large amount of methodological validation, which could only be carried out partially in the available time.

The validation of the numerical models has been conducted so far by comparing the prediction of the 0-D with those of the 1-D simulations, and verifying a good similarity of the SMA-related part of the model with experimental measurements. A further validation of both models against measurements carried out on a physical sheathed wire actuator is still to be produced, and is part of my research plans.

So far, only a single type of actuation has been used to test the proof-of-concept gripper that I fabricated, and a coupling of the actuator with a complete version of the proposed controller in real-time has not been carried out yet. Besides being a limitation of this work, the need to implement new experiments with complex working paths for the actuator to follow is certainly an interesting goal to be tackled early in future.

More limitations include the need to test the repeatability of the matrix modification with different batches of GNP, and possibly a comparison of the performance of the selected type of particles versus other types of fillers. This is also seen as an interesting development.

What is ultimately left for the future is the possibility to replicate successful applications of the suggested guidelines to produce other complex SMA/PDMS based devices, thus verifying the overall robustness of the suggested approach to optimisation, which is considered to be the main upshot of this work. Among such systems, there is the vast and very interesting class of flexible actuators in which the matrix bends under the action of a non-axial wire operating in tension. I expect that most of the design principles exposed would still be valid. In this respect, a future development would include establishing what effective radius has to be used for the heat transfer through the matrix in case of strong geometrical asymmetries.

-
- [1] L. Hines, K. Petersen, G. Zhan Lum, e M. Sitti, «Soft Actuators for Small-Scale Robotics», *Adv. Mater.*, vol. 29, fasc. 13, 2017.
- [2] M. Cianchetti, C. Laschi, A. Menciassi, e P. Dario, «Biomedical applications of soft robotics», *Nat. Rev. Mater.*, vol. 3, fasc. 6, pp. 143–153, mag. 2018, doi: 10.1038/s41578-018-0022-y.
- [3] H. Banerjee, Z. T. H. Tse, e H. Ren, «SOFT ROBOTICS WITH COMPLIANCE AND ADAPTATION FOR BIOMEDICAL APPLICATIONS AND FORTHCOMING CHALLENGES», *Int. J. Robot. Autom.*, vol. 33, fasc. 1, 2018, doi: 10.2316/Journal.206.2018.1.206-4981.
- [4] Y. Zhang e M. Lu, «A review of recent advancements in soft and flexible robots for medical applications», *Int. J. Med. Robot.*, vol. 16, fasc. 3, giu. 2020, doi: 10.1002/res.2096.
- [5] J. Kim, J. W. Kim, H. C. Kim, L. Zhai, H.-U. Ko, e R. M. Muthoka, «Review of Soft Actuator Materials», *Int. J. Precis. Eng. Manuf.*, vol. 20, fasc. 12, pp. 2221–2241, dic. 2019, doi: 10.1007/s12541-019-00255-1.
- [6] N. El-Atab *et al.*, «Soft Actuators for Soft Robotic Applications: A Review», *Adv. Intell. Syst.*, vol. 2, fasc. 10, p. 2000128, ott. 2020, doi: 10.1002/aisy.202000128.
- [7] T. Mirfakhrai, J. D. W. Madden, e R. H. Baughman, «Polymer artificial muscles», *Mater. Today*, vol. 10, fasc. 4, pp. 30–38, apr. 2007, doi: 10.1016/S1369-7021(07)70048-2.
- [8] A. Gonzalez-Vazquez, L. Garcia, J. Kilby, e P. McNair, «Soft Wearable Rehabilitation Robots with Artificial Muscles based on Smart Materials: A Review», *Adv. Intell. Syst.*, p. 2200159, mar. 2023, doi: 10.1002/aisy.202200159.
- [9] J. Mohd Jani, M. Leary, A. Subic, e M. A. Gibson, «A review of shape memory alloy research, applications and opportunities», *Mater. Des. 1980-2015*, vol. 56, pp. 1078–1113, apr. 2014, doi: 10.1016/j.matdes.2013.11.084.
- [10] M. M. Kheirikhah, S. Rabiee, e M. E. Edalat, «A Review of Shape Memory Alloy Actuators in Robotics», in *RoboCup 2010: Robot Soccer World Cup XIV*, J. Ruiz-del-Solar, E. Chown, e P. G. Plöger, A c. di, in *Lecture Notes in Computer Science*, vol. 6556. Berlin, Heidelberg: Springer Berlin Heidelberg, 2011, pp. 206–217. doi: 10.1007/978-3-642-20217-9_18.
- [11] X. Huang *et al.*, «Highly Dynamic Shape Memory Alloy Actuator for Fast Moving Soft Robots», *Adv. Mater. Technol.*, vol. 4, fasc. 4, p. 1800540, apr. 2019, doi: 10.1002/admt.201800540.
- [12] L. Fumagalli, F. Butera, e A. Coda, «SmartFlex® NiTi Wires for Shape Memory Actuators», *J. Mater. Eng. Perform.*, vol. 18, fasc. 5–6, pp. 691–695, ago. 2009, doi: 10.1007/s11665-009-9407-9.
- [13] H. Rodrigue, W. Wang, M.-W. Han, T. J. Y. Kim, e S.-H. Ahn, «An Overview of Shape Memory Alloy-Coupled Actuators and Robots», *Soft Robot.*, vol. 4, fasc. 1, pp. 3–15, mar. 2017, doi: 10.1089/soro.2016.0008.
- [14] H. Rodrigue, W. Wang, D.-R. Kim, e S.-H. Ahn, «Curved shape memory alloy-based soft actuators and application to soft gripper», *Compos. Struct.*, vol. 176, pp. 398–406, set. 2017, doi: 10.1016/j.compstruct.2017.05.056.
- [15] H. Rodrigue, W. Wang, B. Bhandari, M.-W. Han, e S.-H. Ahn, «Cross-shaped twisting structure using SMA-based smart soft composite», *Int. J. Precis. Eng. Manuf.-Green Technol.*, vol. 1, fasc. 2, pp. 153–156, apr. 2014, doi: 10.1007/s40684-014-0020-5.
- [16] H. Rodrigue, W. Wang, B. Bhandari, M.-W. Han, e S.-H. Ahn, «SMA-based smart soft composite structure capable of multiple modes of actuation», *Compos. Part B Eng.*, vol. 82, pp. 152–158, dic. 2015, doi: 10.1016/j.compositesb.2015.08.020.

- [17] H. Rodrigue, W. Wei, B. Bhandari, e S.-H. Ahn, «Fabrication of wrist-like SMA-based actuator by double smart soft composite casting», *Smart Mater. Struct.*, vol. 24, fasc. 12, p. 125003, dic. 2015, doi: 10.1088/0964-1726/24/12/125003.
- [18] H. Yuan, F. Chapelle, J.-C. Fauroux, e X. Balandraud, «Concept for a 3D-printed soft rotary actuator driven by a shape-memory alloy», *Smart Mater. Struct.*, vol. 27, fasc. 5, p. 055005, mag. 2018, doi: 10.1088/1361-665X/aab56f.
- [19] H.-I. Kim, M.-W. Han, S.-H. Song, e S.-H. Ahn, «Soft morphing hand driven by SMA tendon wire», *Compos. Part B Eng.*, vol. 105, pp. 138–148, nov. 2016, doi: 10.1016/j.compositesb.2016.09.004.
- [20] H. Jin, E. Dong, M. Xu, C. Liu, G. Alici, e Y. Jie, «Soft and smart modular structures actuated by shape memory alloy (SMA) wires as tentacles of soft robots», *Smart Mater. Struct.*, vol. 25, fasc. 8, p. 085026, ago. 2016, doi: 10.1088/0964-1726/25/8/085026.
- [21] W. Wang, H. Rodrigue, H.-I. Kim, M.-W. Han, e S.-H. Ahn, «Soft composite hinge actuator and application to compliant robotic gripper», *Compos. Part B Eng.*, vol. 98, pp. 397–405, ago. 2016, doi: 10.1016/j.compositesb.2016.05.030.
- [22] J.-H. Lee, Y. S. Chung, e H. Rodrigue, «Long Shape Memory Alloy Tendon-based Soft Robotic Actuators and Implementation as a Soft Gripper», *Sci. Rep.*, vol. 9, fasc. 1, p. 11251, ago. 2019, doi: 10.1038/s41598-019-47794-1.
- [23] Y. Zhang, M. Su, M. Li, R. Xie, H. Zhu, e Y. Guan, «A spatial soft module actuated by SMA coil», in *2017 IEEE International Conference on Mechatronics and Automation (ICMA)*, Takamatsu, Japan: IEEE, ago. 2017, pp. 677–682. doi: 10.1109/ICMA.2017.8015897.
- [24] C. Laschi, M. Cianchetti, B. Mazzolai, L. Margheri, M. Follador, e P. Dario, «Soft Robot Arm Inspired by the Octopus», *Adv. Robot.*, vol. 26, fasc. 7, pp. 709–727, gen. 2012, doi: 10.1163/156855312X626343.
- [25] M. Cianchetti, A. Licofonte, M. Follador, F. Rogai, e C. Laschi, «Bioinspired Soft Actuation System Using Shape Memory Alloys», *Actuators*, vol. 3, fasc. 3, pp. 226–244, lug. 2014, doi: 10.3390/act3030226.
- [26] M. Cianchetti, M. Calisti, L. Margheri, M. Kuba, e C. Laschi, «Bioinspired locomotion and grasping in water: the soft eight-arm OCTOPUS robot», *Bioinspir. Biomim.*, vol. 10, fasc. 3, p. 035003, mag. 2015, doi: 10.1088/1748-3190/10/3/035003.
- [27] T. Umedachi e B. A. Trimmer, «Design of a 3D-printed soft robot with posture and steering control», in *2014 IEEE International Conference on Robotics and Automation (ICRA)*, Hong Kong, China: IEEE, mag. 2014, pp. 2874–2879. doi: 10.1109/ICRA.2014.6907272.
- [28] J. O. Alcaide, L. Pearson, e M. E. Rentschler, «Design, modeling and control of a SMA-actuated biomimetic robot with novel functional skin», in *2017 IEEE International Conference on Robotics and Automation (ICRA)*, Singapore, Singapore: IEEE, mag. 2017, pp. 4338–4345. doi: 10.1109/ICRA.2017.7989500.
- [29] L. Mizzi, A. Spaggiari, e E. Dragoni, «Design-oriented modelling of composite actuators with embedded shape memory alloy», *Compos. Struct.*, vol. 213, pp. 37–46, apr. 2019, doi: 10.1016/j.compstruct.2019.01.057.
- [30] A. A. Villanueva, K. B. Joshi, J. B. Blottman, e S. Priya, «A bio-inspired shape memory alloy composite (BISMAL) actuator», *Smart Mater. Struct.*, vol. 19, fasc. 2, p. 025013, feb. 2010, doi: 10.1088/0964-1726/19/2/025013.
- [31] S. Akbari, A. H. Sakhaei, S. Panjwani, K. Kowsari, A. Serjouei, e Q. Ge, «Multimaterial 3D Printed Soft Actuators Powered by Shape Memory Alloy Wires», *Sens. Actuators Phys.*, vol. 290, pp. 177–189, mag. 2019, doi: 10.1016/j.sna.2019.03.015.

-
- [32] Y. Haibin, K. Cheng, L. Junfeng, e Y. Guilin, «Modeling of grasping force for a soft robotic gripper with variable stiffness», *Mech. Mach. Theory*, vol. 128, pp. 254–274, ott. 2018, doi: 10.1016/j.mechmachtheory.2018.05.005.
- [33] M. Liu, L. Hao, W. Zhang, e Z. Zhao, «A novel design of shape-memory alloy-based soft robotic gripper with variable stiffness», *Int. J. Adv. Robot. Syst.*, vol. 17, fasc. 1, p. 172988142090781, gen. 2020, doi: 10.1177/1729881420907813.
- [34] B. Mazzolai *et al.*, «Roadmap on soft robotics: multifunctionality, adaptability and growth without borders», *Multifunct. Mater.*, vol. 5, fasc. 3, p. 032001, set. 2022, doi: 10.1088/2399-7532/ac4c95.
- [35] R. Dauksher, Z. Patterson, e C. Majidi, «Characterization and Analysis of a Flexural Shape Memory Alloy Actuator», *Actuators*, vol. 10, fasc. 8, p. 202, ago. 2021, doi: 10.3390/act10080202.
- [36] X. Huang, Z. Ren, e C. Majidi, «Soft Thermal Actuators with Embedded Liquid Metal Microdroplets for Improved Heat Management», in *2020 3rd IEEE International Conference on Soft Robotics (RoboSoft)*, New Haven, CT, USA: IEEE, mag. 2020, pp. 367–372. doi: 10.1109/RoboSoft48309.2020.9115972.
- [37] Y. She, C. Li, J. Cleary, e H.-J. Su, «Design and Fabrication of a Soft Robotic Hand With Embedded Actuators and Sensors», *J. Mech. Robot.*, vol. 7, fasc. 2, p. 021007, mag. 2015, doi: 10.1115/1.4029497.
- [38] J. Mersch, M. Bruns, A. Nocke, C. Cherif, e G. Gerlach, «High-Displacement, Fiber-Reinforced Shape Memory Alloy Soft Actuator with Integrated Sensors and Its Equivalent Network Model», *Adv. Intell. Syst.*, vol. 3, fasc. 7, p. 2000221, lug. 2021, doi: 10.1002/aisy.202000221.
- [39] Z. Ren, M. Zarepoor, X. Huang, A. P. Sabelhaus, e C. Majidi, «Shape Memory Alloy (SMA) Actuator With Embedded Liquid Metal Curvature Sensor for Closed-Loop Control», *Front. Robot. AI*, vol. 8, p. 599650, mar. 2021, doi: 10.3389/frobt.2021.599650.
- [40] G. Stano, S. M. A. I. Ovy, J. R. Edwards, M. Cianchetti, G. Percoco, e Y. Tadesse, «One-shot additive manufacturing of robotic finger with embedded sensing and actuation», *Int. J. Adv. Manuf. Technol.*, vol. 124, fasc. 1–2, pp. 467–485, gen. 2023, doi: 10.1007/s00170-022-10556-x.
- [41] N. Ma e G. Song, «Control of shape memory alloy actuator using pulse width modulation», *Smart Mater. Struct.*, vol. 12, fasc. 5, pp. 712–719, ott. 2003, doi: 10.1088/0964-1726/12/5/007.
- [42] M. Kim, Y.-J. Shin, J.-Y. Lee, W.-S. Chu, e S.-H. Ahn, «Pulse width modulation as energy-saving strategy of shape memory alloy based smart soft composite actuator», *Int. J. Precis. Eng. Manuf.*, vol. 18, fasc. 6, pp. 895–901, giu. 2017, doi: 10.1007/s12541-017-0106-4.
- [43] X. An, Y. Cui, H. Sun, Q. Shao, e H. Zhao, «Active-Cooling-in-the-Loop Controller Design and Implementation for an SMA-Driven Soft Robotic Tentacle», *IEEE Trans. Robot.*, pp. 1–17, 2023, doi: 10.1109/TRO.2023.3234801.
- [44] A. Villoslada, A. Flores, D. Copaci, D. Blanco, e L. Moreno, «High-displacement flexible Shape Memory Alloy actuator for soft wearable robots», *Robot. Auton. Syst.*, vol. 73, pp. 91–101, nov. 2015, doi: 10.1016/j.robot.2014.09.026.
- [45] D. Copaci, D. Blanco, e L. E. Moreno, «Flexible Shape-Memory Alloy-Based Actuator: Mechanical Design Optimization According to Application», *Actuators*, vol. 8, fasc. 3, p. 63, ago. 2019, doi: 10.3390/act8030063.
- [46] D. C. Lagoudas, *Shape Memory Alloys: Modeling and Engineering Applications*. Boston, MA: Springer US, 2008. doi: 10.1007/978-0-387-47685-8.

- [47] W. Huang, «Shape Memory Alloys and their Application to Actuators for Deployable Structures», 1998.
- [48] J. M. McCracken, B. R. Donovan, e T. J. White, «Materials as Machines», *Adv. Mater.*, vol. 32, fasc. 20, p. 1906564, mag. 2020, doi: 10.1002/adma.201906564.
- [49] J. Ma, I. Karaman, e R. D. Noebe, «High temperature shape memory alloys», *Int. Mater. Rev.*, vol. 55, fasc. 5, pp. 257–315, set. 2010, doi: 10.1179/095066010X12646898728363.
- [50] K. Otsuka e X. Ren, «Physical metallurgy of Ti–Ni-based shape memory alloys», *Prog. Mater. Sci.*, vol. 50, fasc. 5, pp. 511–678, lug. 2005, doi: 10.1016/j.pmatsci.2004.10.001.
- [51] K. Otsuka e C. M. Wayman, *SHAPE MEMORY MATERIALS*. Cambridge university press, 1999.
- [52] F. J. J. van Loo, J. W. G. A. Vrolijk, e G. F. Bastin, «Phase relations and diffusion paths in the Ti–Ni–Fe system at 900 °C», *J. Common Met.*, vol. 77, fasc. 1, pp. 121–130, gen. 1981, doi: 10.1016/0022-5088(81)90014-X.
- [53] Y. Zhan, L. He, X. Lu, X. Zhu, e Q. Chen, «The Effect of Ageing Treatment on Shape-Setting and Shape Memory Effect of a NiTi SMA Corrugated Structure», *Adv. Mater. Sci. Eng.*, vol. 2020, pp. 1–11, giu. 2020, doi: 10.1155/2020/2846721.
- [54] C. Cisse, W. Zaki, e T. Ben Zineb, «A review of constitutive models and modeling techniques for shape memory alloys», *Int. J. Plast.*, vol. 76, pp. 244–284, gen. 2016, doi: 10.1016/j.ijplas.2015.08.006.
- [55] R. C. Smith, *Smart Material Systems Model developement*. SIAM, 2005.
- [56] J. Ortín e L. Delaey, «Hysteresis in shape-memory alloys», *Int. J. Non-Linear Mech.*, vol. 37, fasc. 8, pp. 1275–1281, dic. 2002, doi: 10.1016/S0020-7462(02)00027-6.
- [57] J. Ortín, «Preisach modeling of hysteresis for a pseudoelastic Cu–Zn–Al single crystal», *J. Appl. Phys.*, vol. 71, fasc. 3, pp. 1454–1461, feb. 1992, doi: 10.1063/1.351238.
- [58] Y. Ivshin e T. Pence, «A constitutive model for hysteretic phase transition behavior.», *Int. J. Eng. Sci.*, vol. 32, fasc. 4, pp. 681–704, 1994.
- [59] E. Fried e M. E. Gurtin, «Dynamic solid-solid transitions with phase characterized by an order parameter», *Phys. Nonlinear Phenom.*, vol. 72, fasc. 4, pp. 287–308, mag. 1994, doi: 10.1016/0167-2789(94)90234-8.
- [60] A. Srinivasa e K. Rajagopal, «On the thermomechanics of shape memory wires», *Z. Für Angew. Math. Phys.*, vol. 50, fasc. 3, p. 459, 1999, doi: 10.1007/s000330050028.
- [61] S. Seelecke e I. Muller, «Shape memory alloy actuators in smart structures: Modeling and simulation», *Appl. Mech. Rev.*, vol. 57, fasc. 1, pp. 23–46, gen. 2004, doi: 10.1115/1.1584064.
- [62] K. Tanaka, «A thermomechanical sketch of shape memory effect: one dimensional tensile behavior.», *Res Mech.*, vol. 18, fasc. 3, pp. 251–263, 1986.
- [63] C. Liang e C. A. Rogers, «One-dimensional thermomechanical constitutive relations for shape memory materials.», *J. Intell. Mater. Syst. Struct.*, vol. 8, fasc. 4, pp. 285–302, 1990.
- [64] L. C. Brinson, «One-Dimensional Constitutive Behavior of Shape Memory Alloys: Thermomechanical Derivation with Non-Constant Material Functions and Redefined Martensite Internal Variable», *J. Intell. Mater. Syst. Struct.*, vol. 4, fasc. 2, pp. 229–242, apr. 1993, doi: 10.1177/1045389X9300400213.
- [65] M. A. Ahmed, A. H. Bassiuny, e E. M. Bakr, «Design and Implementation of Gains Scheduled PI Control System for Shape Memory Alloy Actuator», *Int. J. Model. Optim.*, pp. 120–124, 2013, doi: 10.7763/IJMO.2013.V3.249.

-
- [66] S.-H. Lee e S.-W. Kim, «Improved position control of shape memory alloy actuator using the self-sensing model», *Sens. Actuators Phys.*, vol. 297, p. 111529, ott. 2019, doi: 10.1016/j.sna.2019.111529.
- [67] E. Ayvali e J. P. Desai, «Pulse width modulation–based temperature tracking for feedback control of a shape memory alloy actuator», *J. Intell. Mater. Syst. Struct.*, vol. 25, fasc. 6, pp. 720–730, apr. 2014, doi: 10.1177/1045389X13502576.
- [68] C. Mavroidis, «Development of Advanced Actuators Using Shape Memory Alloys and Electrorheological Fluids», *Res. Nondestruct. Eval.*, vol. 14, fasc. 1, pp. 1–32, mar. 2002, doi: 10.1080/09349840209409701.
- [69] Z. Guo, Y. Pan, L. B. Wee, e H. Yu, «Design and control of a novel compliant differential shape memory alloy actuator», *Sens. Actuators Phys.*, vol. 225, pp. 71–80, apr. 2015, doi: 10.1016/j.sna.2015.01.016.
- [70] G. Lange, A. Lachmann, A. H. A. Rahim, M. H. Ismail, e C. Y. Low, «Shape Memory Alloys as Linear Drives in Robot Hand Actuation», *Procedia Comput. Sci.*, vol. 76, pp. 168–173, 2015, doi: 10.1016/j.procs.2015.12.335.
- [71] S.-H. Liu, T.-S. Huang, e J.-Y. Yen, «Tracking Control of Shape-Memory-Alloy Actuators Based on Self-Sensing Feedback and Inverse Hysteresis Compensation», *Sensors*, vol. 10, fasc. 1, pp. 112–127, dic. 2009, doi: 10.3390/s100100112.
- [72] J. H. Lilly, *Fuzzy Control and Identification*, 1^a ed. Wiley, 2010. doi: 10.1002/9780470874240.
- [73] A. Kumagai, T.-I. Liu, e P. Hozian, «Control of Shape Memory Alloy Actuators with a Neuro-fuzzy Feedforward Model Element», *J. Intell. Manuf.*, vol. 17, fasc. 1, pp. 45–56, feb. 2006, doi: 10.1007/s10845-005-5512-2.
- [74] K. K. Ahn e N. B. Kha, «Modeling and control of shape memory alloy actuators using Preisach model, genetic algorithm and fuzzy logic», *Mechatronics*, vol. 18, fasc. 3, pp. 141–152, apr. 2008, doi: 10.1016/j.mechatronics.2007.10.008.
- [75] V. Utkin e Jingxin Shi, «Integral sliding mode in systems operating under uncertainty conditions», in *Proceedings of 35th IEEE Conference on Decision and Control*, Kobe, Japan: IEEE, 1996, pp. 4591–4596. doi: 10.1109/CDC.1996.577594.
- [76] N. D., A. Nandakumar, A. Sampath, e D. K., «Fuzzy based active stiffness control of a synergistically compliant variable stiffness shape memory actuator», in *2019 IEEE 5th International Conference for Convergence in Technology (I2CT)*, Bombay, India: IEEE, mar. 2019, pp. 1–5. doi: 10.1109/I2CT45611.2019.9033710.
- [77] A. M. Khan, Y. Kim, B. Shin, M. H. Moghadam, e N. A. Mansour, «Modeling and control analysis of an arc-shaped SMA actuator using PID, sliding and integral sliding mode controllers», *Sens. Actuators Phys.*, vol. 340, p. 113523, giu. 2022, doi: 10.1016/j.sna.2022.113523.
- [78] M. H. Elahinia e H. Ashrafioun, «Nonlinear Control of a Shape Memory Alloy Actuated Manipulator», *J. Vib. Acoust.*, vol. 124, fasc. 4, pp. 566–575, ott. 2002, doi: 10.1115/1.1501285.
- [79] R. Abiri, I. Kardan, R. Nadafi, e M. Kabganian, «Nonlinear State Space Modeling and Control of a Shape Memory Alloy Spring Actuator», 2016.
- [80] D. Zhang, X. Zhao, J. Han, X. Li, e B. Zhang, «Active Modeling and Control for Shape Memory Alloy Actuators», *IEEE Access*, vol. 7, pp. 162549–162558, 2019, doi: 10.1109/ACCESS.2019.2936256.
- [81] S. Pittaccio e L. Garavaglia, «Electric resistance monitoring as a method for controlling shape memory alloy characteristics during shape-setting treatments in the furnace», *Mater. Sci. Eng. A*, vol. 599, pp. 92–104, apr. 2014, doi: 10.1016/j.msea.2014.01.075.

- [82] C. L. Moore e H. A. Bruck, «A fundamental investigation into large strain recovery of one-way shape memory alloy wires embedded in flexible polyurethanes», *Smart Mater. Struct.*, vol. 11, fasc. 1, pp. 130–139, feb. 2002, doi: 10.1088/0964-1726/11/1/315.
- [83] H. A. Bruck, C. L. Moore, e T. L. Valentine, «Repeatable bending actuation in polyurethanes using opposing embedded one-way shape memory alloy wires exhibiting large deformation recovery», *Smart Mater. Struct.*, vol. 11, fasc. 4, pp. 509–518, ago. 2002, doi: 10.1088/0964-1726/11/4/305.
- [84] L. N. Lewis, J. Stein, Y. Gao, R. E. Colborn, e G. Hutchins, «Platinum Catalysts Used in the Silicones Industry», 1997.
- [85] G. Socrates, *Infrared and Raman characteristic group frequencies: tables and charts*. 2001.
- [86] P. Liu *et al.*, «Transfer function and working principle of a pressure/temperature sensor based on carbon black/silicone rubber composites», *J. Appl. Polym. Sci.*, vol. 133, fasc. 7, p. n/a-n/a, feb. 2016, doi: 10.1002/app.42979.
- [87] H. Devaraj *et al.*, «Highly elastic and flexible multi-layered carbon black/elastomer composite based capacitive sensor arrays for soft robotics», *Meas. Sens.*, vol. 2–4, p. 100004, ago. 2019, doi: 10.1016/j.measen.2020.100004.
- [88] C. H. Liu, H. Huang, Y. Wu, e S. S. Fan, «Thermal conductivity improvement of silicone elastomer with carbon nanotube loading», *Appl. Phys. Lett.*, vol. 84, fasc. 21, pp. 4248–4250, mag. 2004, doi: 10.1063/1.1756680.
- [89] D. Ponnamma, K. K. Sadasivuni, Y. Grohens, Q. Guo, e S. Thomas, «Carbon nanotube based elastomer composites – an approach towards multifunctional materials», *J Mater Chem C*, vol. 2, fasc. 40, pp. 8446–8485, 2014, doi: 10.1039/C4TC01037J.
- [90] M. Amjadi e I. Park, «Carbon nanotubes-ecoflex nanocomposite for strain sensing with ultra-high stretchability», in *2015 28th IEEE International Conference on Micro Electro Mechanical Systems (MEMS)*, Estoril, Portugal: IEEE, gen. 2015, pp. 744–747. doi: 10.1109/MEMSYS.2015.7051065.
- [91] J. Kong *et al.*, «Electrically conductive PDMS-grafted CNTs-reinforced silicone elastomer», *Compos. Sci. Technol.*, vol. 159, pp. 208–215, mag. 2018, doi: 10.1016/j.compscitech.2018.02.018.
- [92] H. Mai, R. Mutlu, C. Tawk, G. Alici, e V. Sencadas, «Ultra-stretchable MWCNT–Ecoflex piezoresistive sensors for human motion detection applications», *Compos. Sci. Technol.*, vol. 173, pp. 118–124, mar. 2019, doi: 10.1016/j.compscitech.2019.02.001.
- [93] B. Wang, B.-K. Lee, M.-J. Kwak, e D.-W. Lee, «Graphene/polydimethylsiloxane nanocomposite strain sensor», *Rev. Sci. Instrum.*, vol. 84, fasc. 10, p. 105005, ott. 2013, doi: 10.1063/1.4826496.
- [94] H. Yang *et al.*, «Highly sensitive and stretchable graphene-silicone rubber composites for strain sensing», *Compos. Sci. Technol.*, vol. 167, pp. 371–378, ott. 2018, doi: 10.1016/j.compscitech.2018.08.022.
- [95] D. T. Beruto, M. Capurro, e G. Marro, «Piezoresistance behavior of silicone–graphite composites in the proximity of the electric percolation threshold», *Sens. Actuators Phys.*, vol. 117, fasc. 2, pp. 301–308, gen. 2005, doi: 10.1016/j.sna.2004.06.027.
- [96] Q. Mu e S. Feng, «Thermal conductivity of graphite/silicone rubber prepared by solution intercalation», *Thermochim. Acta*, vol. 462, fasc. 1–2, pp. 70–75, ott. 2007, doi: 10.1016/j.tca.2007.06.006.
- [97] P. S. Sarath *et al.*, «Fabrication of exfoliated graphite reinforced silicone rubber composites - Mechanical, tribological and dielectric properties», *Polym. Test.*, vol. 89, p. 106601, set. 2020, doi: 10.1016/j.polymertesting.2020.106601.

-
- [98] J. Y. Woo, K. K. Kim, J. Lee, J. T. Kim, e C.-S. Han, «Highly conductive and stretchable Ag nanowire/carbon nanotube hybrid conductors», *Nanotechnology*, vol. 25, fasc. 28, p. 285203, lug. 2014, doi: 10.1088/0957-4484/25/28/285203.
- [99] S.-C. Lin *et al.*, «Preparation of a graphene–silver nanowire hybrid/silicone rubber composite for thermal interface materials», *J. Taiwan Inst. Chem. Eng.*, vol. 68, pp. 396–406, nov. 2016, doi: 10.1016/j.jtice.2016.08.009.
- [100] L. C. Sim, S. R. Ramanan, H. Ismail, K. N. Seetharamu, e T. J. Goh, «Thermal characterization of Al₂O₃ and ZnO reinforced silicone rubber as thermal pads for heat dissipation purposes», *Thermochim. Acta*, vol. 430, fasc. 1–2, pp. 155–165, giu. 2005, doi: 10.1016/j.tca.2004.12.024.
- [101] D. Yang *et al.*, «Mussel Inspired Modification for Aluminum Oxide/Silicone Elastomer Composites with Largely Improved Thermal Conductivity and Low Dielectric Constant», *Ind. Eng. Chem. Res.*, vol. 57, fasc. 9, pp. 3255–3262, mar. 2018, doi: 10.1021/acs.iecr.7b04970.
- [102] J. Lin, S. Su, Y. He, e F. Kang, «Improving thermal and mechanical properties of the alumina filled silicone rubber composite by incorporating carbon nanotubes», *New Carbon Mater.*, vol. 35, fasc. 1, pp. 66–72, feb. 2020, doi: 10.1016/S1872-5805(20)60476-0.
- [103] M. D. Bartlett *et al.*, «High thermal conductivity in soft elastomers with elongated liquid metal inclusions», *Proc. Natl. Acad. Sci.*, vol. 114, fasc. 9, pp. 2143–2148, feb. 2017, doi: 10.1073/pnas.1616377114.
- [104] A. Li, C. Zhang, e Y.-F. Zhang, «Thermal Conductivity of Graphene-Polymer Composites: Mechanisms, Properties, and Applications», *Polymers*, vol. 9, fasc. 9, p. 437, set. 2017, doi: 10.3390/polym9090437.
- [105] J. Zhao, G.-Y. Zhang, e D.-X. Shi, «Review of graphene-based strain sensors», *Chin. Phys. B*, vol. 22, fasc. 5, p. 057701, mag. 2013, doi: 10.1088/1674-1056/22/5/057701.
- [106] B. Alemour e M. H. Yaacob, «Review of Electrical Properties of Graphene Conductive Composites», vol. 11, fasc. 4, 2018.
- [107] D. G. Papageorgiou, Z. Li, M. Liu, I. A. Kinloch, e R. J. Young, «Mechanisms of mechanical reinforcement by graphene and carbon nanotubes in polymer nanocomposites», *Nanoscale*, vol. 12, fasc. 4, pp. 2228–2267, 2020, doi: 10.1039/C9NR06952F.
- [108] E. Pop, V. Varshney, e A. K. Roy, «Thermal properties of graphene: Fundamentals and applications», *MRS Bull.*, vol. 37, fasc. 12, pp. 1273–1281, dic. 2012, doi: 10.1557/mrs.2012.203.
- [109] A. A. Balandin, «Thermal properties of graphene and nanostructured carbon materials», *Nat. Mater.*, vol. 10, fasc. 8, pp. 569–581, ago. 2011, doi: 10.1038/nmat3064.
- [110] H. Malekpour *et al.*, «Thermal conductivity of graphene with defects induced by electron beam irradiation», *Nanoscale*, vol. 8, fasc. 30, pp. 14608–14616, 2016, doi: 10.1039/C6NR03470E.
- [111] Y. Xu, X. Wang, e Q. Hao, «A mini review on thermally conductive polymers and polymer-based composites», *Compos. Commun.*, vol. 24, p. 100617, apr. 2021, doi: 10.1016/j.coco.2020.100617.
- [112] Y. Su, J. J. Li, e G. J. Weng, «Theory of thermal conductivity of graphene-polymer nanocomposites with interfacial Kapitza resistance and graphene-graphene contact resistance», *Carbon*, vol. 137, pp. 222–233, ott. 2018, doi: 10.1016/j.carbon.2018.05.033.

- [113] X. Shen, Z. Wang, Y. Wu, X. Liu, Y.-B. He, e J.-K. Kim, «Multilayer Graphene Enables Higher Efficiency in Improving Thermal Conductivities of Graphene/Epoxy Composites», *Nano Lett.*, vol. 16, fasc. 6, pp. 3585–3593, giu. 2016, doi: 10.1021/acs.nanolett.6b00722.
- [114] H. S. Kim, H. S. Bae, J. Yu, e S. Y. Kim, «Thermal conductivity of polymer composites with the geometrical characteristics of graphene nanoplatelets», *Sci. Rep.*, vol. 6, fasc. 1, p. 26825, mag. 2016, doi: 10.1038/srep26825.
- [115] K. Chu, W. Li, e H. Dong, «Role of graphene waviness on the thermal conductivity of graphene composites», *Appl. Phys. A*, vol. 111, fasc. 1, pp. 221–225, apr. 2013, doi: 10.1007/s00339-012-7497-y.
- [116] Y. Guo, K. Ruan, X. Shi, X. Yang, e J. Gu, «Factors affecting thermal conductivities of the polymers and polymer composites: A review», *Compos. Sci. Technol.*, vol. 193, p. 108134, giu. 2020, doi: 10.1016/j.compscitech.2020.108134.
- [117] F. Zhang, Y. Feng, e W. Feng, «Three-dimensional interconnected networks for thermally conductive polymer composites: Design, preparation, properties, and mechanisms», *Mater. Sci. Eng. R Rep.*, vol. 142, p. 100580, ott. 2020, doi: 10.1016/j.mser.2020.100580.
- [118] G. Speranza, «The Role of Functionalization in the Applications of Carbon Materials: An Overview», *C — J. Carbon Res.*, vol. 5, fasc. 4, p. 84, dic. 2019, doi: 10.3390/c5040084.
- [119] T. Ge, M. Zhang, K. Tang, e H. Tang, «Diisocyanate-modified graphene oxide/hydroxyl-terminated silicone rubber composites for improved thermal conductivity», *Mater. Chem. Phys.*, vol. 252, p. 123250, set. 2020, doi: 10.1016/j.matchemphys.2020.123250.
- [120] R. Saito, M. Hofmann, G. Dresselhaus, A. Jorio, e M. S. Dresselhaus, «Raman spectroscopy of graphene and carbon nanotubes», *Adv. Phys.*, vol. 60, fasc. 3, pp. 413–550, 2011.
- [121] A. C. Ferrari, «Raman spectroscopy of graphene and graphite: Disorder, electron–phonon coupling, doping and nonadiabatic effects», *Solid State Commun.*, vol. 143, fasc. 1–2, pp. 47–57, lug. 2007, doi: 10.1016/j.ssc.2007.03.052.
- [122] A. C. Ferrari e J. Robertson, «Interpretation of Raman spectra of disordered and amorphous carbon», *Phys. Rev. B*, vol. 61, fasc. 20, pp. 14095–14107, mag. 2000, doi: 10.1103/PhysRevB.61.14095.
- [123] K. Hu *et al.*, «Development of Tailored Graphene Nanoparticles: Preparation, Sorting and Structure Assessment by Complementary Techniques», *Molecules*, vol. 28, fasc. 2, p. 565, gen. 2023, doi: 10.3390/molecules28020565.
- [124] I. Pócsik, M. Hundhausen, M. Koós, e L. Ley, «Origin of the D peak in the Raman spectrum of microcrystalline graphite», *J. Non-Cryst. Solids*, vol. 227–230, pp. 1083–1086, mag. 1998, doi: 10.1016/S0022-3093(98)00349-4.
- [125] M. Wall, «The Raman Spectroscopy of Graphene and the Determination of Layer Thickness», *Appl. Note 52252*.
- [126] F. Tuinstra e J. L. Koenig, «Raman Spectrum of Graphite», *J. Chem. Phys.*, vol. 53, fasc. 3, pp. 1126–1130, ago. 1970, doi: 10.1063/1.1674108.
- [127] M. M. Lucchese *et al.*, «Quantifying ion-induced defects and Raman relaxation length in graphene», *Carbon*, vol. 48, fasc. 5, pp. 1592–1597, apr. 2010, doi: 10.1016/j.carbon.2009.12.057.
- [128] A. Eckmann *et al.*, «Probing the Nature of Defects in Graphene by Raman Spectroscopy», *Nano Lett.*, vol. 12, fasc. 8, pp. 3925–3930, ago. 2012, doi: 10.1021/nl300901a.

-
- [129] M. Merzlyakov e C. Schick, «Thermal conductivity from dynamic response of DSC», *Thermochim. Acta*, vol. 377, fasc. 1–2, pp. 183–191, ott. 2001, doi: 10.1016/S0040-6031(01)00553-6.
- [130] P. S. Lobo, J. Almeida, e L. Guerreiro, «Shape Memory Alloys Behaviour: A Review», *Procedia Eng.*, vol. 114, pp. 776–783, 2015, doi: 10.1016/j.proeng.2015.08.025.
- [131] «<https://matthey.com/products-and-markets/other-markets/medical-components/resource-library/nitinol-technical-properties>».
- [132] S. Vollach e D. Shilo, «The Mechanical Response of Shape Memory Alloys Under a Rapid Heating Pulse», *Exp. Mech.*, vol. 50, fasc. 6, pp. 803–811, lug. 2010, doi: 10.1007/s11340-009-9320-z.
- [133] M. Bahrami, M. M. Yovanovich, e E. E. Marotta, «Thermal Joint Resistance of Polymer-Metal Rough Interfaces», *J. Electron. Packag.*, vol. 128, fasc. 1, pp. 23–29, mar. 2006, doi: 10.1115/1.2159005.
- [134] S. K. Parihar e N. T. Wright, «Thermal contact resistance at elastomer to metal interfaces», *Int. Commun. Heat Mass Transf.*, vol. 24, fasc. 8, pp. 1083–1092, dic. 1997, doi: 10.1016/S0735-1933(97)00102-4.
- [135] F. Scarpa e M. De Rosa, «Transient heat conduction in wires with heat sources; lumped and distributed solution techniques.», *Heat Transf. Res.*, vol. 47, fasc. 8, pp. 753–765, 2016, doi: 10.1615/HeatTransRes.2016012206.
- [136] P. C. C. Monteiro, L. L. Silva, T. A. Netto, e M. A. Savi, «Experimental investigation of the influence of the heating rate in an SMA actuator performance», *Sens. Actuators Phys.*, vol. 199, pp. 254–259, set. 2013, doi: 10.1016/j.sna.2013.05.016.
- [137] G. Scirè Mammano e E. Dragoni, «Effect of Stress, Heating Rate, and Degree of Transformation on the Functional Fatigue of Ni-Ti Shape Memory Wires», *J. Mater. Eng. Perform.*, vol. 24, fasc. 7, pp. 2709–2719, lug. 2015, doi: 10.1007/s11665-015-1561-7.
- [138] D. Magrin, «Modeling and state estimation for the advanced control of a multimaterial shape memory based actuator», Politecnico di Milano, 2021.
- [139] H. Cho, T. Yamamoto, Y. Takeda, A. Suzuki, e T. Sakuma, «Exploitation of shape memory alloy actuator using resistance feedback control and its development», *Prog. Nat. Sci. Mater. Int.*, vol. 20, pp. 97–103, nov. 2010, doi: 10.1016/S1002-0071(12)60013-6.
- [140] I. Spinella, E. Dragoni, e F. Stortiero, «Modeling, Prototyping, and Testing of Helical Shape Memory Compression Springs With Hollow Cross Section», *J. Mech. Des.*, vol. 132, fasc. 6, p. 061008, giu. 2010, doi: 10.1115/1.4001601.